Spectroscopy and Chemistry of Interstellar Ice Analogues

Spectroscopy and Chemistry of Interstellar Ice Analogues – Jordy Bouwman
Thesis Universiteit Leiden - Illustrated - With summary in Dutch - With references
ISBN/EAN 978-90-9025686-3
Printed by Ipskamp Drukkers
Cover by Ruud Engelsdorp
This work is part of the research programme of the Foundation for Fundamental Research on Matter (FOM), which is part of the Netherlands Organisation for Scientific Research (NWO).

Spectroscopy and Chemistry of Interstellar Ice Analogues

PROEFSCHRIFT

ter verkrijging van
de graad van Doctor aan de Universiteit Leiden,
op gezag van de Rector Magnificus prof. mr. P. F. van der Heijden,
volgens besluit van het College voor Promoties
te verdedigen op dinsdag 12 oktober 2010
klokke 13.45 uur

door

Jordy Bouwman
geboren te Haarlem
in 1979

Promotiecommissie:

Promotor:	Prof. dr. H. V. J. Linnartz	
Copromotor:	Dr. L. J. Allamandola	NASA Ames Research Center
Overige Leden:	Prof. dr. K. Kuijken	
	Prof. dr. A. G. G. M. Tielens	
	Prof. dr. M. R. S. McCoustra	Heriot-Watt University
	Prof. dr. J. Oomens	FOM Rijnhuizen
	Dr. H. M. Cuppen	

Contents

CHAPTER 1

Introduction

The pressures in space are much lower than one can reach in the best vacuum chamber in a laboratory on Earth and the temperatures vary from extremely high to close to absolute zero. Despite these extreme circumstances there is a surprisingly active chemistry which enriches the vast regions in space, leaving a large puzzle for mankind to solve.

Most molecules detected in the interstellar medium (ISM) are unambiguously identified by their rovibrational (infrared), or purely rotational (microwave) fingerprint absorption or emission spectra. One particular family of molecules — the so-called Polycyclic Aromatic Hydrocarbons (PAHs) — is detected as a class by its characteristic mid-infrared (mid-IR) emission spectrum. Although these molecules have not been uniquely identified, because of their common spectral signature, their presence in photon-dominated regions (PDRs) is now widely accepted in the astrochemical community.

Besides gas phase species, molecules are also detected in solid form, as interstellar ices. Ices are formed in cold and dark regions in space, known as molecular clouds, by accretion of gas phase species on cold carbonaceous or silicate dust grains. The thin layers of ice contain rather simple molecules, such as H_2O, CO, CO_2, CH_3OH, CH_4, and NH_3. The constituents of icy grain mantles are further energetically processed by heat, cosmic rays, or ultraviolet (VUV) radiation, leading to more complex molecules. Interstellar ices are now regarded as important catalytic sites for the formation of complex (organic) molecules during the evolution of an interstellar cloud and are considered crucial in astrochemistry.

This thesis describes laboratory and observational studies which are aimed to understand physical interactions and abundances of species in, and the VUV induced chemical evolution of, interstellar ices in a laboratory setting using mid-IR and near-ultraviolet/ visible (near-UV/VIS) spectroscopic techniques. The remainder of the introduction is used to put the thesis work into context.

1.1 Astrochemistry

The formation and detection of polyatomic molecules in the interstellar medium had long been unexpected because of the harsh UV fields and low densities ($\sim$ 1–10^2 molecules

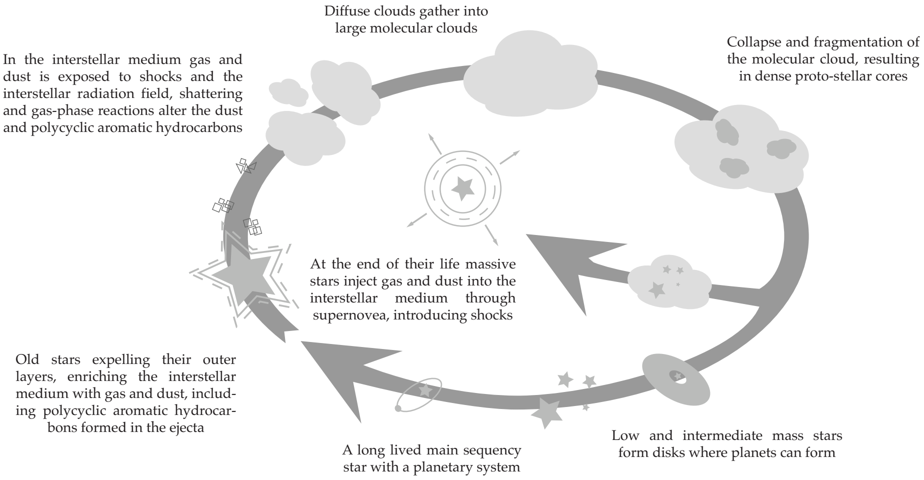

Figure 1.1 Cartoon of the Galactic life cycle. After Steven Simpson (Verschuur 1992, Sky & Telescope Magazine), by Christiaan Boersma.

cm^{-3}). However, in 1937 the first molecules, CH, CN, and CH$^+$ were detected in diffuse clouds [Swings & Rosenfeld 1937]. The detection of only transient species confirmed the idea that the unfavorable conditions would preclude the presence of more complex chemistry. The detection of more complex molecules in the ISM such as NH_3 and H_2CO in the 1960s opened up a new field in astronomy, astrochemistry, in which the abundances and reactions of chemical elements and molecules, and their interaction with light are studied. Up to now, as many as 152 molecules[1] have been detected in the gas of inter- and circumstellar clouds and every year some new species are detected. Amongst the detected molecules are simple species, such as H_2 and CO, but also rather complex and exotic species, such as $HC_{11}N$ [Bell et al. 1997] with the largest unambiguously detected molecules being C_{60} and C_{70}. The detection of a large variety of species in the strongly UV processed medium implies that chemical reactions are very efficient. It is mostly ion-molecule reactions that are responsible for the high production rates of these molecular species in the gas. In cold regions, such as dense clouds, chemistry is now known to proceed via grain catalyzed reactions in which species released from interstellar ices play a key role.

New ground-based and space-borne observatories with improved sensitivity and spectral resolution combined with advances in laboratory techniques shed new light on the molecular diversity. The detected species continue giving us insight in the complex chemistry that takes place in the vast regions of space and perhaps even clues to the formation of life on Earth, or even life outside of our own solar system.

---

[1] `http://www.astrochymist.org`

1.2 The interstellar cycle of matter

Although what triggered the formation of the first stars in the Universe after the occurrence of the big bang about 14 billion years ago is still a big mystery, the life cycle of low-mass stars, such as our own sun, is now quite well understood [e.g. Evans 1999, van Dishoeck 2004, and references therein]. Disregarding the birth of the first stars, the evolution of gas and dust in the ISM from stellar birth to death can be depicted as a cyclic event as seen in Fig. 1.1. The building blocks of the newly formed stars are the remnants of the old dead stars; the diffuse interstellar medium is enriched by its previous inhabitants. Stellar remnants, however, are mostly destroyed by the omnipresent strong ultraviolet (UV) radiation, leaving only heavy elements, large molecules such as PAHs, and dust grains intact. New stars are formed from these basic ingredients and the complex chemistry involved in star-formation starts all over again.

The process of low-mass star formation is schematically displayed in Fig. 1.2. In the first stage, the diffuse medium is disturbed by a process, such as a stellar wind or a supernova explosion. This causes dense clouds to form out of the material in the diffuse medium. Once formed, these dense cloud cores, mainly consisting of hydrogen, helium, heavier elements, dust and some larger molecules, are held together by gravitational forces. The densities in these clouds reach a point at which the core of the

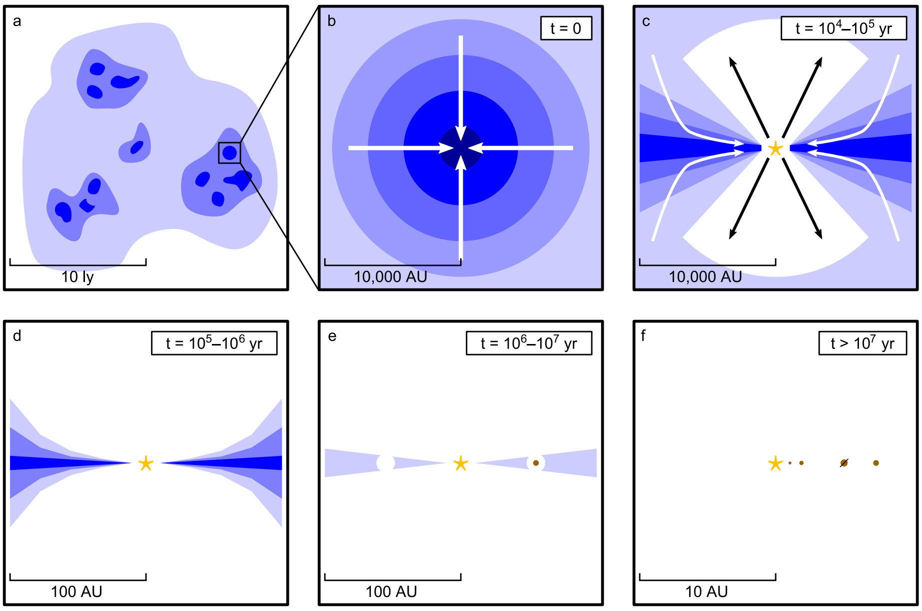

Figure 1.2 Schematic illustration of the different stages of low-mass star formation. Figure taken from Visser [2009].

cloud is completely shielded from intense UV radiation and molecules can form. The temperatures in these dense clouds are low (T ~10 K) and the densities rather high by interstellar standards (~ 10^4–10^5 molecules cm^{-3}), causing molecules to freeze out efficiently on nanometer sized dust particles or possibly on large PAH molecules or clusters of PAH molecules. Thin layers of ice which act as catalytic sites for chemical reactions are formed. Ice abundances, formation, and chemistry will be described in more detail in §1.3.

Within the dense molecular clouds, cores of even higher densities (>10^5 molecules cm^{-3}) are formed. If the density in such a core gets high enough, the core will collapse under its own gravity, forming a so-called protostellar core, i.e. a region of the cloud that will eventually become a star. The collapse releases a large amount of energy and the pressure building up in the core prevents it from collapsing further. At this stage, molecules play a key role in the process of star formation; they convert translational energy via collisions into IR radiation which is emitted at the molecule's specific wavelengths. Some of this radiation can escape the collapsing cloud, resulting in efficient cooling and a continuation of the collapse of the core.

In the next stage, the protostar starts losing angular momentum by expelling mass in bipolar outflows. Additionally, a protoplanetary disk is formed around the central object from which material continues to accrete onto the protostar. In this disk small grains coagulate, forming larger and larger rocks and eventually planets. The outside of the disk is processed by the strong UV irradiation from the new born star and becomes heated and chemically processed. The center of the disk, however, remains cold and the chemical evolution of matter in this part of the disk will be dominated by ice grain chemistry. For low-mass stars, the disk will slowly evolve into a planetary system such as our own.

The formation process of high-mass stars is not yet fully understood, but most likely has many similarities to the formation of low-mass stars. The final stages of the lifecycle of both high- and low-mass stars, on the other hand, are well understood. At the end of its life, the star enriches the interstellar medium by expelling its contents into its surroundings. Stars with a mass smaller than 2.5 Solar masses ($M \leq 2.5M_{\odot}$) such as our own Sun expel their mass in relatively gentle stellar winds, the so-called protoplanetary nebula phase, after which only the hot core of the star will remain; a white dwarf. Stars with a large mass ($M \geq 2.5M_{\odot}$) end their life in a less gentle manner. They return their mass to the ISM in a violent event, a so-called supernova explosion, which can again trigger the formation of new stars as described above.

1.3 Mid-IR absorption bands – Interstellar ices

The presence of ices in the interstellar medium was already proposed in 1937, even before the detection of the first interstellar molecule [Eddington 1937]. The detection of an interstellar ice absorption feature was a fact in 1973, nearly four decades after the presence of ices was proposed. A strong and broad mid-IR absorption band located at ~3 μm was detected and assigned to the H_2O ice stretching mode [Gillett et al. 1973]. The spectroscopic signatures of interstellar ices fall in the mid-IR as absorption profiles which are superimposed on the black body radiation curve of a background star, or embedded object. Since the molecules are confined within the ice, they do not have translational, nor rotational degrees of freedom and absorption of a mid-IR photon by a molecule results in vibration of the molecule only. While interstellar species in the gas phase can be detected in absorption or emission, ices are only detected in absorption. This comes from the fact that the temperature corresponding to mid-IR radiation is higher than the temperature of the ice.

Interstellar ices have been detected either using ground-based, airborne, or space based observatories. Ground based mid-IR observatories, such as the powerful Very Large Telescope (VLT), have a limited spectral window because nearly half of the mid-IR spectrum is blocked by telluric absorptions, primarily H_2O and CO_2. Sophisticated observatories were built to extend wavelength coverage, push the detection limit and to obtain higher resolution spectra. First, the Kuiper Airborne Observatory (KAO) was constructed. Observations with the KAO were conducted at high altitude (40,000 to 45,000 feet), well above most of the H_2O in the atmosphere. This opened up a very important 5 to 10 μm portion of the infrared fingerprint region [Haas et al. 1995]. The combination of airborne with ground based observations provided the first access to nearly all of the mid-IR spectrum for a handful of objects. By the early 1990s, interstellar ices were known to be water-rich mixtures containing species such as CH_3OH, NH_3, H_2CO, etc. The complete mid-IR spectrum of the cosmos was opened up with the launch of the Infrared Space Observatory (ISO), an observatory that revolutionized our understanding of interstellar ices. Free of telluric absorptions, the eyes of ISO revealed many secrets of ices in dense clouds and around star forming regions. The number of detected interstellar ices nearly doubled. While ISO probed quiescent lines of site as well as star forming regions, due to its low sensitivity, however, ISO was limited to observing bright, high-mass, star-forming regions [e.g., van Dishoeck 2004, and references therein]. Its successor, NASA's very sensitive *Spitzer Space Telescope*, opened up the window of opportunity further. It offered the high sensitivity needed to observe faint objects such as low-mass protostars, without being limited by the transmission of the Earth's atmosphere [Chapter 3, Pontoppidan et al. 2008, Boogert et al. 2008, Öberg et al. 2008]. These very successful observatories offered a sensitive view into the kitchen of newborn high- and low-mass stars.

1.3.1 Composition of interstellar ices

It is now established that water is the first molecule to form and freeze out on interstellar grains in the evolution from a diffuse cloud to a dense cloud and that H_2O is the most abundant species in ice toward most sources [e.g. Sonnentrucker et al. 2008]. Typical *Spitzer* absorption spectra combined with L and M band VLT data toward two low-mass protostars with the identified ice absorption bands marked out is shown in Fig. 1.3. The ice absorption profiles are always accompanied by a feature at 10 μm which is typical for the silicate Si–O stretching mode originating from the grain core. Table 1.1 gives an overview of ice abundances with respect to H_2O ice detected towards the high-mass object W33A.

Besides the identified species indicated in Fig. 1.3, the detections of some other molecules based on absorptions in the 5 to 8 μm spectral region have been suggested and are given in parenthesis in Table 1.1. The dominant absorption profile in this region is the 6 μm H_2O bending mode on which a substructure is superimposed. Besides the H_2O bending mode and an absorption band at 7.68 μm, which can confidently be attributed to the CH_4 deformation mode. Assignments of other bands in this spectral region remain controversial. For example, the detection of species such as formaldehyde (H_2CO), formic acid (HCOOH) and the ammonium ion (NH_4^+) have been claimed. Experiments on the formation route of these molecules indeed point out that these molecules are the likely formed under interstellar conditions and thus these species are plausible carriers of these absorption bands [Fuchs et al. 2009, Ioppolo et al. 2010]. An absorption located at 6.2 μm has been tentatively assigned to the CC stretching mode of aromatic molecules trapped in the interstellar ice based on proximity to an interstellar emission band attributed to aromatic species [Keane et al. 2001a]. Experimental data on the spectroscopy of these species in interstellar ice analogues, however, is lacking in the literature. Chapter 4 deals with the spectroscopy of aromatic molecules in ices and their possible contribution to several absorption features in the 5 to 9 μm region.

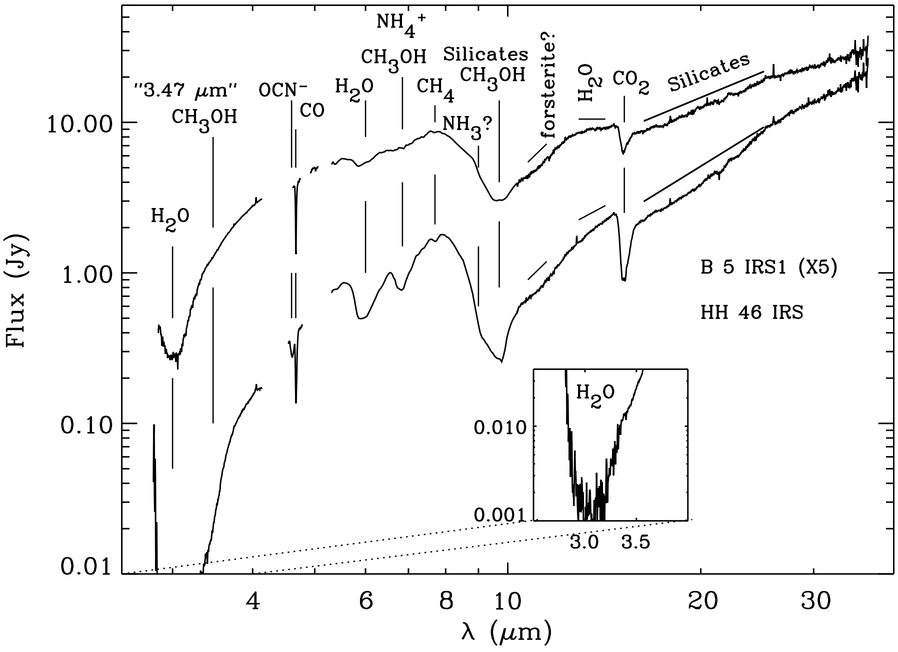

Figure 1.3 *Spitzer* infrared absorption spectrum combined with L and M band observations of low-mass embedded protostars B5 IRS1 (top, multiplied by factor of 5 for clarification) and HH46 IRS (bottom). Identifications and possible identifications are indicated. Spectrum is adopted from Boogert et al. [2004]

Table 1.1 Ice abundances with respect to H_2O ice towards the high-mass protostar W33A taken from Gibb et al. [2000]. The NH_4^+ abundance is taken from Boogert & Ehrenfreund [2004].

Species	Abundance % of H_2O	Species	Abundance % of H_2O
H_2O	100	(HCOOH)	7
CO (polar)	6	(H_2CO)	6
CO (non-polar)	2	(NH_3)	15
CO_2 (polar)	11	(NH_4^+)	12
CO_2 (non-polar)	2	OCN^-	3.5
CH_4	1.5	(SO_2)	2.4
CH_3OH	18	OCS	0.2

The detection of NH_3 ice has been claimed in some studies [e.g. Gibb et al. 2000, Lacy et al. 1998] and upper limits of its abundance towards massive YSO's have been reported in others [e.g. Dartois & d'Hendecourt 2001]. Detections towards low-mass Young Stellar Objects (YSO's), however, remain controversial [Taban et al. 2003]. Most of the NH_3 vibrations overlap with other prominent bands in the spectrum. The most isolated band, the umbrella mode at ~9 μm, overlaps with the strong 10 μm silicate absorption band. The detection of NH_3 in low-mass star forming regions is confirmed and investigated in detail in Chapter 3 of this thesis.

Apart from the identification of frozen out species, mid-IR absorption spectra also allow one to obtain information on physical properties of the ice, such as ice temperature, degree of mixing, and interactions between species. Precise peak positions and band profiles directly reflect the composition and complex physical interplay between the species in ices. This allows observers to discriminate, for example, between polar ices (H_2O-rich) and non-polar ices (H_2O-poor) [Sandford et al. 1988] ice composition, in turn, reflects the formation mechanisms and accretion history of molecules on cold grains. To this end, the interaction between CO and H_2O in binary ices and the effect of mixing rations on band shapes and band strengths is studied in detail in Chapter 2. A similar extensive laboratory study on the effects of mixing H_2O, NH_3, CH_3OH , CO_2 and CO is presented in Chapter 3, where the data are used to interpret *Spitzer* spectra towards 41 low-mass objects.

1.3.2 Ice formation and grain chemistry

Ice covered grains are crucial for the interstellar chemistry leading to the formation of complex molecules. As the embedded object starts nuclear fusion, the ices in the surrounding region are processed energetically by heating, by cosmic ray induced processes and by ultraviolet processing. The rather simple mixtures of ices evolve to more complex ices. When the temperature reaches a high enough value the ices are desorbed and molecules are brought back into the gas phase. Gas phase observations of this stage of star formation indeed exhibit a large variety of complex species that originate from interstellar grains and thus confirm the importance of chemical reactions catalyzed on very cold ices. Chemistry in the gas phase and on grains are thus strongly coupled.

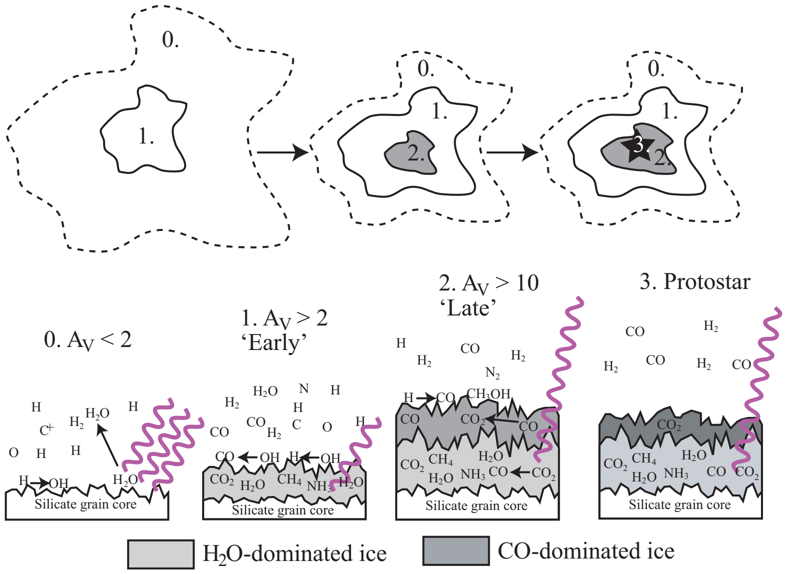

Figure 1.4 A proposed route of ice formation in the evolution from a diffuse to a dense cloud. Figure is taken from Öberg [2009].

The formation of ices in the evolution from a diffuse cloud toward a protostar is illustrated in Fig. 1.4. Tielens & Hagen [1982] proposed a chemical network in which molecules are formed from atoms which are accreted to the grain surface. In their model, the desorption energy of the atom is larger than the energy needed for the atom to hop from one site on the surface to the next. The atom scans the grain surface for a certain amount of time, depending on the grain temperature and desorption energy of the atom. Meanwhile the atom may find a (radical) reaction partner on the surface, react, and form a new species. Since hydrogen atoms are the most mobile species present on the grain, simple H-rich species such as H_2O, CH_4, NH_3 can be formed. Observations towards protostars and dense clouds indeed point to ice layers containing H-rich molecules, dominated by H_2O (polar ices).

Carbon monoxide is, as opposed to the other species mentioned above, efficiently produced in the gas phase. Therefore, CO ice is formed by the freeze-out of CO directly from the gas phase, rather than by reactions on the surface [Pontoppidan 2006]. The CO ice forms on top of the other species in a rather pure layer, forming the so-called non-polar ice. On the grain CO can be further processed by hydrogen addition reaction, resulting in formaldehyde (H_2CO) and eventually methanol (CH_3OH) [Watanabe & Kouchi 2002, Fuchs et al. 2009].

This is not the end of the ice chemistry. Ice species, such as CH_3OH, are also subjected to VUV radiation powerful enough to photodissociate the molecules, leading to radical species in the ice layer [e.g. Öberg et al. 2009c]. The fragments can diffuse on the surface of the ice and react with other radical species or molecules. This system is thought to be responsible for the formation of larger organic molecules such as methyl formate ($HCOOCH_3$), formic acid (HCOOH) and (CH_3OCH_3) [e.g. Garrod & Herbst 2006]. These species have been detected in the gas phase in regions where ices are released in the gas phase by thermal or photo-desorption.

1.4 Mid-IR emission bands – Polycyclic Aromatic Hydrocarbons

The initial ground-based detection of the first of a family mid-IR emission features that are now attributed to polycyclic aromatic hydrocarbons (PAHs) dates back to 1973, when Gillett et al. discovered an unexpectedly broad emission feature peaking near 11.3 μm. Over the next twenty years it was found that this family of bands was surprisingly widespread and associated with a wide variety of different types of astronomical objects including galactic HII regions, reflection nebulae, young stellar objects, planetary nebulae, and post-asymptotic giant branch (AGB) objects. With the launch of ISO, and later *Spitzer*,

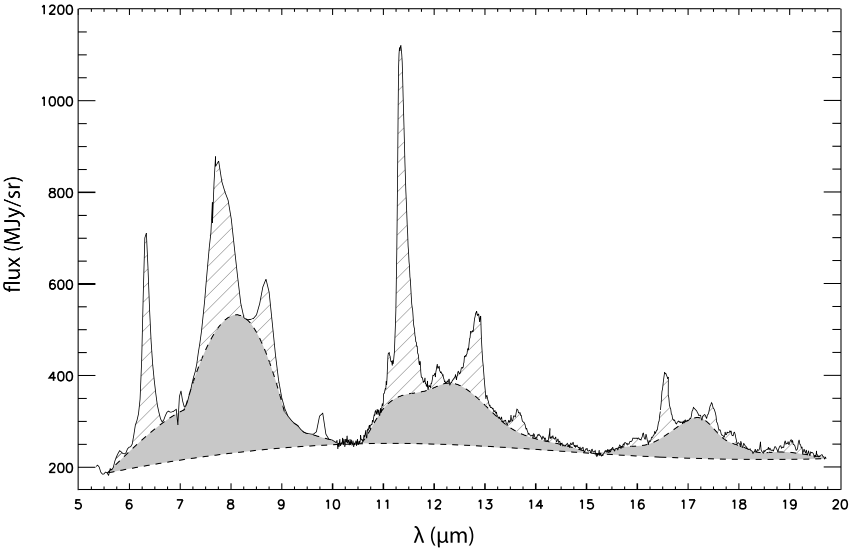

Figure 1.5 Mid-infrared spectrum of the reflection nebula NGC 7023 observed by NASA's *Spitzer* space telescope, illustrating the richness and dominance of the UIR bands. The hatched areas are the distinct UIR bands, the shaded area are UIR plateaus. (Spectrum from Sellgren et al. [2007], shadings courtesy Boersma)

mapping of these features in extended objects became possible and their detection was pushed out to galaxies across the Universe [Peeters et al. 2004b, van Dishoeck 2004, Tielens 2008].

The most prominent of these mid-IR emission bands occur at 3.3, 6.2, 7.7, 8.6, 11.2, and 12.7 μm and are often superimposed on broad plateaus (see Fig. 1.5). The bands originate from regions where material is too cold to be emitting mid-IR radiation. This requires that the carrier emits the bands upon excitation by a single photon of higher energy (UV–near IR) and that the molecules are free gas phase species. Strong correlation between the mid-IR emission bands and the available carbon suggests that carbon is the main building block of the carrier. Additionally, the emission bands also originate from regions which are dominated by harsh UV radiation, implying that the carrier must be highly photostable. The origin of the emission features was long debated, but after more than two decades the hypothesis that they are emitted from highly vibrationally excited PAHs [Allamandola et al. 1989, Puget & Leger 1989] is gaining wide acceptance [e.g. van Dishoeck 2004, Tielens 2008].

PAHs are the largest molecules known in space and contain about 10–20% of the total available cosmic carbon. They have been found in objects, such as meteotites, and in interplanetary dust particles, indicating their prescence in the early stages of the formation of our solar system. PAHs may even play an important role in the formation and evolution of life on Earth [Bernstein et al. 1999, Ehrenfreund et al. 2006].

1.4.1 The PAH building block – Carbon

Carbon is abundantly produced in stars by the triple alpha nuclear fusion process of helium, making it the sixth most abundant species in the ISM. The ability to form 4 bonds makes carbon an important material both in a terrestrial setting as well as in space; carbon acts as a building block from which complex organic molecules can be formed. The carbon atom contains 4 electrons which can participate in molecular bonding; two electrons reside in the 2s atomic orbital and two electrons reside in the atomic 2p orbitals. These atomic orbitals can mix, forming the hybridised orbitals sp, sp^2 and sp^3. In the case of the sp^3 bonded form, one of the 2s electrons is promoted to the empty 2p orbital. The 2s and three 2p electron atomic electron wavefunctions mix to form sp^3 atomic orbitals, giving rise to a tetrahedral structure with the ability to form four covalent σ bonds. This form of hybridisation is found in structures such as diamond, or in molecules such as diamondoids (diamantane, iceane, adamantane, etc.), and alkanes (methane, ethane, etc.). In the sp^2 hybridised form only two of the three 2p orbitals mix with the 2s orbital, resulting in the ability to form three σ bonds and one π bond. This type of bonding occurs in nanotubes, graphene, or PAHs. In the last hybridised form, sp hybridisation, the 2s electron wavefunction only mixes with one of the p electrons. The C atom can form two σ bonds and two π bonds. This occurs in the ethynes, such as acetylene (C_2H_2), or carbon chain radicals (e.g. C_6H). Summarizing, carbon can reside in many different forms, ranging from very stable configurations to highly reactive molecules. Figure 1.6 shows some examples of the forms in which carbon atoms can be found.

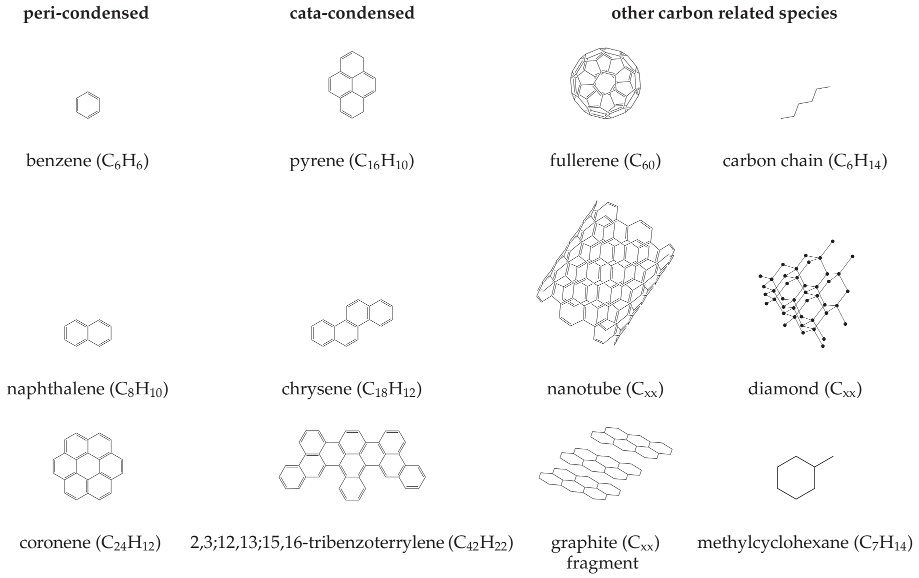

Figure 1.6 Some examples of the various types of carbon containing material. (Figure taken from Boersma [2009])

Aromatic molecules are planar structures with the atoms arranged in one or more rings and a conjugate π-system which consists of a number of delocalized π-electrons given by Hückels rule ($4n + 2$, where $n = 0, 1, 2..$). Polycyclic aromatic hydrocarbons, a class of aromatic molecules, are characterized by carbon atoms arranged in chickenwire shaped ring structures of 6 carbon atoms with 3 electrons participating in sigma-bonds and the left over electron participating in a delocalized π-bond, resulting in a highly stable structure. The simplest member of the stable aromatic family is benzene (C_6H_6). The 6 carbon atom containing hexagon of the benzene molecule forms the building block of larger aromatic molecules consisting of 2 or more rings fused together, the PAHs. PAHs can exist in two main forms; the peri-condensed and cata-condensed PAHs. Peri-condensed PAHs are those which contain C atoms that are part of three fused rings of the aromatic network. Peri-condensed PAHs are therefore centrally condensed and allow for full delocalization of the π electron, resulting in highly stable molecules. Cata-condensed PAH molecules do not have any carbon atoms bonded to more than two rings and therefore have a more open structure which restricts electron delocalization making them less stable.

1.4.2 The origin of interstellar PAHs

In the ISM, PAH molecules are most likely formed in carbon-rich Asymptotic Giant Branch (AGB) stars [Latter 1991, Cherchneff et al. 1992]. Until recently, direct evidence for this was lacking. In general, carbon-rich AGB stars are namely too cold to efficiently excite the PAHs and therefore no strong PAH mid-IR emission is found towards these objects. However, the presence of PAHs in planetary nebulae and post-AGB carbon-rich stars, objects sampling the next stage of stellar ejecta, is unequivocal [Cerrigone et al. 2009]. Stars at this stage of their life are hotter and brighter in the near-UV and hence pump the PAHs more efficiently, making them fluoresce in the mid-IR. Recently, *Spitzer* observations of carbon-rich AGB stars have shown emission from what appears to be a mixture of aromatic species. This mixture seems to include less stable PAH related species that have not yet been ‘weeded out’ to the more robust PAH forms which can survive the rigors of the UV rich radiation from the hotter stars and general ISM and which produce the well-known emission spectra.

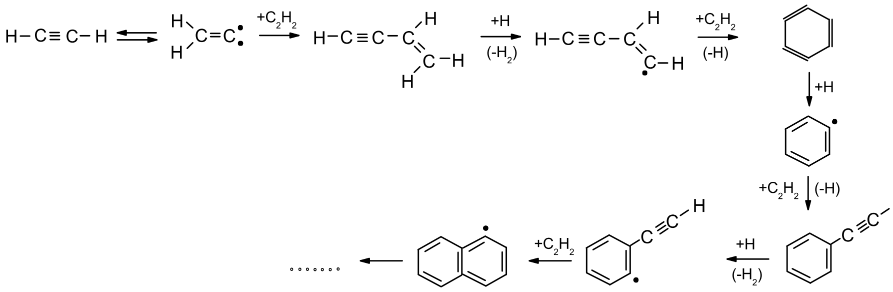

Figure 1.7 Chemical reaction scheme thought to be responsible for the production of the first aromatic ring, from which larger PAH species grow. Figure is reproduced from Frenklach & Feigelson [1989].

The formation process of interstellar PAHs is thought to be similar to the formation of soot in a terrestrial setting [Frenklach & Feigelson 1989, Allamandola et al. 1989, and Fig. 1.7]. The carbon in the outflow of carbon-rich AGB stars is mainly locked up in CO and acetylene (C_2H_2). Since CO is highly stable, the molecule that is most likely responsible for the formation of PAHs in the the outflow of these stars is acetylene and its radical derivatives. The creation of the first aromatic ring is the most problematic step in the formation of PAHs. Hydrogen addition to a C_2H_2 molecule yields the C_2H_3 radical, which can react with a second C_2H_2 molecule, forming C_4H_5. Two reactions involving H abstraction followed by reactions with two acetylene molecules yields C_6H_5, which after a reaction of the remaining triple bond and the unpaired electron forms the first fused ring. From here, more rings can be fused to the aromatic ring by similar acetylene addition reactions. After their formation, they are brought into the ISM by dust-driven winds [Speck & Barlow 1997, Boersma et al. 2006]. They can be regarded as an extension of the grain-size distribution into the molecular (sub nanometer size) domain and are the building blocks from which larger agglomerations — soot particles — of PAHs can be formed.

1.4.3 PAHs in interstellar ices?

The mid-IR emission bands are omnipresent in space, however, the strength of these bands varies strongly. Towards dense clouds the bands have much lower intensity. There are two contributing factors for the quenching of the emission bands as one probes deeper into dense clouds. The first being that the emission bands lose intensity in dense clouds because the extinction increases and there are not enough high energy photons to excite the PAH. The second is that the highly non-volatile PAHs condense out on grains and are incorporated in interstellar ices.

PAHs are not expected to fluoresce in their typical mid-IR modes when incorporated in ices, since the energy is quickly dissipated into the phonon modes of the ice lattice [Allamandola et al. 1985, 1989]. Thus, when trapped in ices PAHs are expected to exhibit mid-IR absorption bands instead. There are lines of evidence that support the existence of PAHs in ices covering interstellar grains. Absorption bands *likely* caused by PAH feature have been reported [Smith et al. 1989, Chiar et al. 2000, Bregman et al. 2000], but extensive laboratory studies are still lacking in the literature. Chapter 4 of this thesis describes a study of the mid-IR spectroscopy of PAH species trapped and photolyzed in H_2O ice with the aim to understand: 1) the roles that PAHs might play in ice processing and astrochemistry, 2) the signature PAHs add to the mid-IR spectra of embedded protostars, and 3) identify PAH:H_2O ice photoproducts and to obtain first order estimates of their abundances in the ices surrounding both low- and high-mass protostars.

Additional spectroscopic studies are performed in the near-UV/VIS regime on PAH containing H_2O and CO ice in order to obtain rate constants for photoreactions of PAHs in ices as a function of temperature. These studies are presented in Chapter 5–7. The studies indicate that PAH are efficiently ionized and react with other ice constituent photoproducts. PAHs are thus shown to have a great impact on the interstellar ice radical budget and charge state, particularly during the early stages of star formation and possibly also in later stages. Although much is now known about the formation of organic molecules on interstellar ices, very little is known about the chemical processes involving the abundantly present and largest organic molecules in the ISM, the PAHs.

1.5 Laboratory spectroscopic ice studies

Laboratory astrophysics aims to understand the physical interactions between and chemical evolution of molecular species in the interstellar medium. The physical interplay of mixed molecular ices and their chemistry have been studied for some decades and are reasonably well understood. The first experiments were extensions of a technique called “Matrix Isolation Spectroscopy” [e.g. Hagen et al. 1979, 1980, Hudgins et al. 1993] and aimed to measure band positions, FWHM and band strengths of the simplest molecular species at cryogenic temperatures. Quickly the field evolved and more realistic “dirty ices” — ice mixtures consisting of 2 or more species with specific mixing ratios — were studied with the aim to understand the complex mid-IR spectra that new observatories were discovering. Even now, these rather simple experiments still offer a wealth of infor-

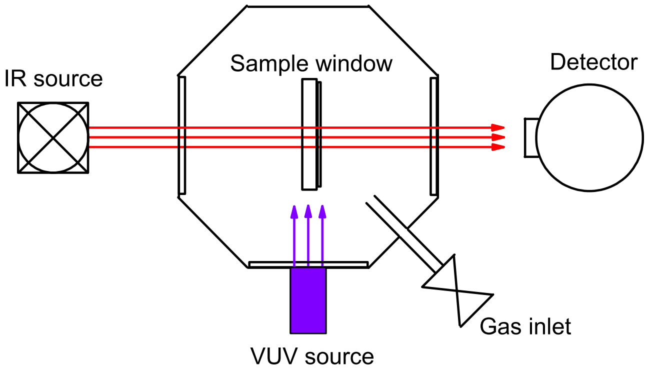

Figure 1.8 A schematic of the high vacuum setup used for monitoring physical interactions and VUV induced chemical reactions in interstellar ices with mid-IR spectroscopy.

mation on the physical interactions between molecules condensed on a cold surface and gain insight in physical parameters — such as temperature and composition — in actual interstellar ices.

Since molecules are brought in close contact in interstellar ices, the grains act as catalytic sites for chemical reactions. These reactions are important for the overall chemistry in the ISM. Many laboratory studies have been devoted to understanding the chemical evolution of ices upon energetic input. Up to date, most experimental studies have employed mid-IR absorption spectroscopy on ice covered cryogenic sample windows or gold surfaces suspended in either high- or ultrahigh vacuum systems. Recently, experimental setups employing near-UV/VIS absorption spectroscopy have become available [Gudipati & Allamandola 2003, and Chapter 5 of this thesis]. Both the mid-IR and near-UV/VIS spectroscopic techniques are the subject of this thesis work and will be described shortly in this section.

1.5.1 Mid-IR ice spectroscopy

A typical mid-IR spectroscopic setup is schematically depicted in Fig. 1.8. A sample window is suspended in the center of a vacuum chamber, which is pumped down by a turbomolecular pump to a pressure of 10^{-7} mbar. The sample window is cooled down by a closed-cycle Helium refrigerator and the sample window temperature can be controlled by means of resistive heating. The (mixed) gas sample is prepared off-line in a glass bulb which can be connected to the vacuumchamber gas inlet. Ice samples are grown by vapor depositing this gas sample onto the cold window. Subsequently, spectra are taken with a Fourier Transform InfraRed (FTIR) spectrometer on samples of different mixing ratios and sample window temperatures. For some of the mid-IR experiments in this thesis, energetic H_2 emission is generated using a Hydrogen flow microwave (MW) discharge lamp, to simulate energetic processing of the ices in the ISM. The resulting vacuum ultraviolet

(VUV) photons at 121.6 nm (Ly-α 10.2 eV) together with a broad molecular H_2 emission band at 160 nm (7.8 eV). Ices are subject to photons of high energy which may alter their chemical identity and the chemical evolution of the photoproducts is tracked as a function of VUV photolysis time. Typically, the FTIR spectroscopic technique has a time resolution of roughly 1 spectrum per 20 minutes for good signal to noise and a resolution of 0.5 cm^{-1}. Furthermore, the sample window needs to be rotated by 90° when changing from the performing spectroscopy to the VUV photolysis position. Thus, this experiment does not allow the possibility of monitoring changes in real-time nor without disturbing the optics; requirements that must be met to fully understand the photochemistry and determine reaction rates. This mid-IR system, however, is ideal for the identification of functional groups in the newly formed photoproducts.

1.5.2 Near-UV/VIS absorption ice spectroscopy

Although some gas phase spectra of small PAH members are available, most of our knowledge on PAHs and related species is based on matrix isolation experiments in which the species of interest are doped in an argon or neon matrix at low temperature, after which the spectra — in both the mid-IR and near-UV/VIS — of the cryogenic samples are taken. These experiments have allowed for comparison of experimental data with theoretical calculations. In addition, the experiments mentioned above using a H_2 microwave powered discharge VUV sources also allow for measuring the spectra of cationic and an-

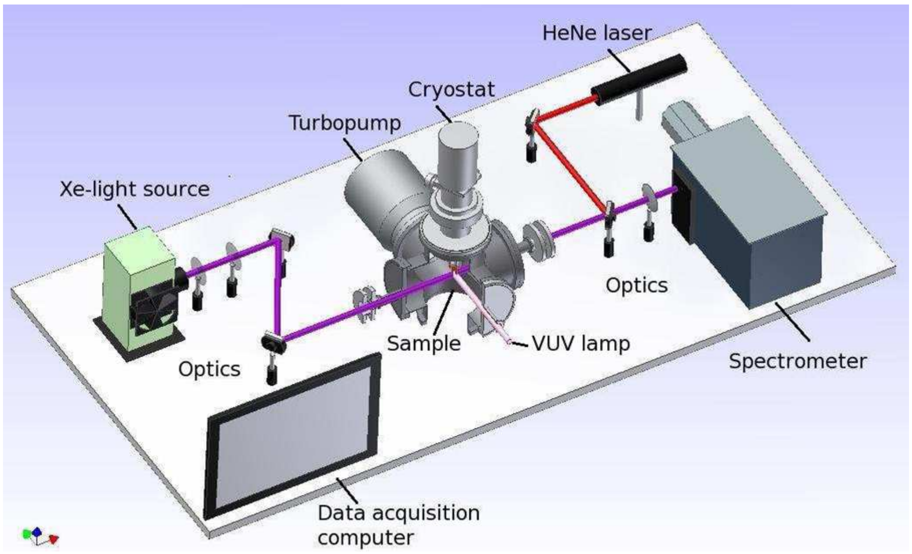

Figure 1.9 A schematic of *OASIS*; the experimental setup for measuring spectroscopy and chemical kinetics of VUV processed PAH:H_2O ice mixtures.

ionic species. Recently, researchers realized that in the ISM PAHs should also condense on cold grains and should be incorporated in ices. Subsequently, they can participate in VUV induced chemical reactions and form more complex species.

The field of PAH photochemistry in realistic interstellar ice analogues was opened by Bernstein et al. in 1999. However, it was soon realized that because PAHs have very weak bands compared to the bands of dominant interstellar species such as, e.g., H_2O, it was difficult to disentangle their chemistry in the laboratory with traditional IR techniques and equally difficult to interpret the role PAHs played in the spectra of astronomical observations. The dominant interstellar ice species, however, do not have electronic transitions and are thus largely transparent in the near-UV and visible spectral range. PAHs on the other hand, because of their delocalized π-electrons, exhibit very strong transitions in this part of the electromagnetic spectrum. Subsequently, an experimental setup — Optical Absorption Setup for Ice Spectroscopy (*OASIS*) — aimed to study PAH electronic transitions in interstellar ice analogues was developed. A schematic the setup is displayed in Fig. 1.9.

The new measurement technique has two major advantages compared to measurements made using mid-IR FTIR spectroscopic techniques. The first is that PAH absorptions in this wavelength regime are much stronger compared to the (very) weak PAH absorptions in the IR (band strengths of $\sim 10^{-13}$ cm molecule^{-1} for near-UV/VIS compared to $\sim 10^{-17}$ cm molecule^{-1} for mid-IR bands). The other advantage of near-UV/VIS studies of ices compared to IR studies is in the time resolution of the spectroscopic measurement. *OASIS*, on the other hand, is capable of measuring one spectrum per 5 ms. The technique is described in more detail in Chapter 5.

1.6 Outline of this thesis

In the work presented here, two laboratory methods are employed to investigate the physical interactions and chemistry in laboratory analogues of astrophysical ices. The first measurements are performed by FTIR studies of ices. These data are almost one-to-one comparable to observational spectra and give good insight in the physical state of the interstellar ice, i.e., its mixing ratio and temperature. Additionally, measurements are performed in the near-UV/VIS spectral regime. This type of spectroscopy is perfectly suited to investigate the fast chemical reactions taking place within laboratory ice analogs of interstellar ices with in situ VUV photolysis. This thesis is thus divided into two parts. Part I of this thesis aims to interpret infrared laboratory measurements to explain the detection, or non-detection, of absorption bands in observational spectra. Part II aims to qualitatively and quantitatively understand VUV driven chemical processes in PAH containing interstellar ices by means of near-UV/VIS absorption spectroscopy.

Part I: Mid-IR absorption spectroscopy

- **Chapter 2** Absorption profiles and band strengths of the H_2O fundamental vibrations change in a mixed H_2O:CO ice. These changes are investigated as a function of the amount of mixed in CO. Additionally, the appearance of a CO stretching mode band at 2152 cm^{-1} is quantified as a function of two physical parameters; the amount of mixed in H_2O and the sample temperature.

- **Chapter 3** The detection of NH_3 ice towards low-mass protostars has long been debated. This chapter aims to detect the NH_3 umbrella mode in a set of 41 *Spitzer* spectra and to derive the abundance of NH_3 with respect to H_2O. Additionally, the CH_3OH abundance is also determined from the CO stretch mode. The obtained CH_3OH abundances are compared to previously obtained data based on the CH_3OH ν_2 C-H stretching mode.

- **Chapter 4:** PAHs are known to be ubiquitous in many phases of the ISM. Spectroscopy and chemistry of PAHs in H_2O ices, however, is poorly understood. This chapter aims to obtain mid-IR spectroscopic information on PAHs trapped in H_2O and to identify the photoproducts resulting from VUV processing of these ices. The data are used to derive upper limits of PAH abundances in interstellar ices towards a low- and high-mass protostar.

Part II: Near-UV/VIS absorption spectroscopy

- **Chapter 5:** This chapter describes a new experimental setup for performing near-UV/VIS spectroscopy on VUV processed interstellar ice analogues. The spectral and temporal performance of the experimental setup is described by means of measurements on pyrene trapped in water ice.

- **Chapter 6:** The system, pyrene trapped and photolyzed in H_2O and CO ice, is described in detail in this chapter. The chemical reactions are quantified by fitting rate constants to the experimental data. The data are used to calculate the limit for detecting Pyrene:H_2O ice and its photoproducts in near-UV/VIS spectra towards dense clouds.

- **Chapter 7:** A set of four PAH:H_2O ice mixtures is investigated spectroscopically. Rate constants are fitted to the experimental and a general conclusion is drawn on the ionization of PAHs in interstellar ices. The findings are incorporated in an astrochemical model demonstrating the importance of these processes in interstellar environments.

- **Chapter 8:** This chapter is dedicated to the future prospects of the experiments on PAH:ice spectroscopy in the Sackler Laboratory for Astrophysics and the future prospects of the near-UV/VIS absorption spectrometer in particular. Open research questions and possible future measurements are briefly discussed.

Part I

Mid-IR absorption spectroscopy

CHAPTER 2

Band profiles and band strengths in mixed H_2O:CO ices[1]

Laboratory spectroscopic research plays a key role in the identification and analysis of interstellar ices and their structure. To date, a number of molecules have been positively identified in interstellar ices, either as pure, mixed or layered ice structures. Previous laboratory studies on H_2O:CO ices have employed a ‘mix and match’ principle and describe qualitatively how absorption bands behave for different physical conditions. The aim of this study is to quantitatively characterize the absorption bands of solid CO and H_2O, both pure and in their binary mixtures, as a function of partner concentration and temperature. Laboratory measurements based on Fourier transform infrared transmission spectroscopy are performed on binary mixtures of H_2O and CO ranging from 1:4 to 4:1. A quantitative analysis of the band profiles and band strengths of H_2O in CO ice, and vice versa, is presented and interpreted in terms of two models. The results show that a mutual interaction takes place between the two species in the solid, which alters the band positions and band strengths. It is found that the band strengths of the H_2O bulk stretch, bending and libration vibrational bands decrease linearly by a factor of up to 2 when the CO concentration is increased from 0 to 80%. By contrast, the band strength of the free OH stretch increases linearly. The results are compared to a recently performed quantitative study on H_2O:CO_2 ice mixtures. It is shown that for mixing ratios of 1:0.5 H_2O:X and higher, the H_2O bending mode offers a good tracer to distinguish between CO_2 or CO in H_2O ice. Additionally, it is found that the band strength of the CO fundamental remains constant when the water concentration is increased in the ice. The integrated absorbance of the 2152 cm^{-1} CO feature, with respect to the total integrated CO absorption feature, is found to be a good indicator of the degree of mixing of CO in the H_2O:CO laboratory ice system. From the change in the H_2O absorption band strength in laboratory ices upon mixing we conclude that astronomical water ice column densities on various lines of sight can be underestimated by up to 25% if significant amounts of CO and CO_2 are mixed in.

---

[1] Based on: J. Bouwman, W. Ludwig, Z. Awad, K. I. Öberg, G. W. Fuchs, E. F. van Dishoeck, H. Linnartz, Astronomy and Astrophysics, 476, 995-1003 (2007)

2.1 Introduction

Water and carbon monoxide are common constituents in vast regions of space, both in the gas phase and in ices. Interstellar water ice was first identified in 1973 via a strong band at 3.05 μm and unambiguously assigned to water ice following comprehensive laboratory work [Merrill et al. 1976, Léger et al. 1979, Hagen et al. 1979]. Meanwhile, it has become clear that H_2O ice is the most abundant ice in space. The OH stretching mode at 3.05 μm and the H_2O bending mode at 6.0 μm are detected in many lines of sight [e.g. Willner et al. 1982, Tanaka et al. 1990, Murakawa et al. 2000, Boogert et al. 2000, Keane et al. 2001a, Gibb et al. 2004, Knez et al. 2005] and in many different environments, ranging from quiescent dark clouds to dense star forming regions and protoplanetary disks [Whittet et al. 1988, Tanaka et al. 1994]. It has been a long-standing problem that the intensity ratio of these two water bands in astrophysical observations is substantially different from values derived from laboratory spectra of pure H_2O ice. In recent years it has been proposed that this discrepancy may be due to contributions of other species, in particular more complex organic ices, to the overall intensity of the 6 μm band [Gibb & Whittet 2002]. An alternative explanation is that the band strengths change due to interaction of H_2O molecules with other constituents in the ice. In both high-mass and low-mass star forming regions, CO is — together with CO_2 — the most dominant species that could mix with H_2O. In a recent study on H_2O:CO_2 ices, Öberg et al. [2007a] showed indeed significant band strength differences between pure and mixed H_2O ices. The present study extends this work to CO containing water ice.

CO accretes onto dust grains around 20 K [Sandford et al. 1988, Acharyya et al. 2007] and plays a key role in solid state astrochemical processes, e.g., as a starting point in hydrogenation reactions that result in the formation of formaldehyde and methanol [Watanabe & Kouchi 2002, Hiraoka et al. 2002, Watanabe et al. 2004, Fuchs et al. 2009]. A strong absorption centered around 2139 cm^{-1} was assigned to solid CO by Soifer et al. [1979], again following thorough laboratory infrared work. Further efforts in the laboratory have shown that CO molecules can be intimately mixed, either with molecules that possess the ability to form hydrogen bonds, such as H_2O, NH_3 and CH_3OH — often referred to as “polar” ices — or with molecules that can only participate in a van der Waals type of bond, such as CO itself, CO_2 and possibly N_2 and O_2 — so-called “non-polar” ices. In laboratory mixtures with H_2O and CO, the two forms are distinguished spectroscopically; the double Gaussian peak structure for the CO stretch fundamental can be decomposed in Gaussian profiles at 4.647 μm (2152 cm^{-1}) and 4.675 μm (2139 cm^{-1}), attributed to the polar and non-polar component, respectively [Sandford et al. 1988, Jenniskens et al. 1995]. On the contrary, pure CO measured in the laboratory exhibits a single Lorentzian band, which is located around 2139 cm^{-1}. This Lorentzian absorption profile can be further decomposed into three Lorentzian components centered around 2138.7, 2139.7 and 2141.5 cm^{-1} [H. J. Fraser, private communication].

In astronomical spectra, the 2139 cm^{-1} feature has been considered as an indicator of CO in H_2O poor ice, and the 2136 cm^{-1} feature as CO in H_2O rich environments [Tielens et al. 1991]. More recently it was found that the astronomical CO profiles can be decomposed into three components at 2136.5 cm^{-1}, 2139.9 cm^{-1} and 2143.7 cm^{-1}, with the 2139.9 cm^{-1} feature ascribed to pure CO ice, and the 2143.7 cm^{-1} feature ascribed to the longitudinal optical (LO) component of the vibrational transition in pure crystalline CO [Pontoppidan et al. 2003b]. Boogert et al. [2002] proposed that the astronomically observed peak at 2143 cm^{-1} can originate from CO:CO$_2$ mixtures, but this identification is still controversial [van Broekhuizen et al. 2006]. The assignment of the 2136.5 cm^{-1} feature in these phenomenological fits remains unclear. It should be noted that laboratory and astronomical data differ slightly in peak position, largely due to the fact that grain shape effects play a role for abundant ice molecules like CO and H_2O.

Recently, elaborate laboratory work and ab initio calculations on mixtures of CO and H_2O have shown that the absorption around 2152 cm^{-1} results from CO being bound to the dangling OH site in H_2O ice [Al-Halabi et al. 2004]. Surprisingly enough, this absorption has never been observed in the interstellar medium [e.g. Pontoppidan et al. 2003b]. The non-detection of this feature has been explained by other molecules blocking the dangling OH site, which is therefore unavailable to CO. An extension of this explanation is that the binding sites are originally populated by CO, but that this has been processed to other molecules, such as CO$_2$ or methanol [Fraser et al. 2004]. Furthermore, it has been shown that the number of dangling OH sites decreases upon ion irradiation, which in turn results in a reduction of the integrated intensity of the 2152 cm^{-1} feature [Palumbo 2006, and references therein]. The 2136–2139 cm^{-1} feature is ascribed to CO bound to fully hydrogen bonded water molecules [Al-Halabi et al. 2004].

Since CO and H_2O are among the most abundant molecules in the interstellar medium, mixed CO and H_2O ices have been subject to many experimental and theoretical studies [e.g. Jiang et al. 1975, Hagen & Tielens 1981, Hagen et al. 1983, Al-Halabi et al. 2004, Fraser et al. 2005]. For example, the behavior of the 2136–2139 cm^{-1} CO stretching band has been quantitatively studied as a function of temperature and its band width and position have been studied as a function of H_2O concentration in binary mixtures, but containing only up to 25% of CO [Schmitt et al. 1989a,b]. Furthermore, water clusters have been studied in a matrix of CO molecules with a ratio of 1:200 H_2O:CO. This has resulted in a tentative assignment of H_2O monomers and dimers and the conclusion that H_2O forms a bifurcated dimer structure in CO [Hagen & Tielens 1981]. Other studies have focussed on Temperature Programmed Desorption (TPD) combined with Reflection Absorption Infrared Spectroscopy (RAIRS) of mixed and layered CO/H_2O systems, enhancing greatly our knowledge on their structures and phase transitions [Collings et al. 2003a,b]. Nevertheless, a full quantitative and systematic study on the behavior of H_2O in CO ice, and vice versa, with straight applications to astronomical spectra, is lacking in the literature. This is the topic of the present work.

The desorption temperatures of CO and H_2O differ by as much as 145 K under laboratory conditions. However, H_2O/CO ices are expected to play a role in astronomical environments at temperatures not only well below the desorption temperature of CO at 20 K [Fuchs et al. 2009], but also well above the desorption temperature of pure CO ice, since CO can be trapped in the pores of H_2O ice [Collings et al. 2003a]. Thus far, both species have been observed together in lines of sight. It is often concluded from the non-detection of the 2152 cm^{-1} feature that H_2O and CO are not intimately mixed in interstellar ices. On the other hand, in some lines of sight CO is trapped in pores of a host

Table 2.1 Ice mixtures and resulting deposition thicknesses used in this work. Column A denotes the molecule of which the deposited amount is kept constant, and column B indicates the molecule that is mixed in. The first series is used for determining the effect of CO on the H_2O band strengths and profiles. The second series is used to determine the effects of H_2O on the CO band strengths and profiles.

Composition	A (ML)	B (ML)	Total ice thickness (ML)
pure H_2O	3000	0	3000
pure CO	0	3000	3000
H_2O:CO 1:0.25	3000	750	3750
H_2O:CO 1:0.5	3000	1500	4500
H_2O:CO 1:1	3000	3000	6000
H_2O:CO 1:2	3000	6000	9000
H_2O:CO 1:4	3000	12000	15000
H_2O:CO 1:1	10000	10000	20000
H_2O:CO 1:1	1000	1000	2000
CO:H_2O 1:0.25	3000	750	3750
CO:H_2O 1:0.5	3000	1500	4500
CO:H_2O 1:1	3000	3000	6000
CO:H_2O 1:2	3000	6000	9000
CO:H_2O 1:4	3000	12000	15000
CO:H_2O 1:1	10000	10000	20000
CO:H_2O 1:1	1000	1000	2000

matrix, as evidenced by the detection of the 2136 cm^{-1} CO feature [Pontoppidan et al. 2003b]. It is plausible that this trapping results from heating of a mixture of CO and a host molecule. Accordingly, we have also performed some experiments as a function of temperature.

In this work, the effect of CO on the H_2O vibrational fundamentals is compared to the effect of CO_2 on these modes, as studied recently by Öberg et al. [2007a]. A comparison between the H_2O bending mode characteristics in CO and CO_2 containing ices illustrates the sensitivity of this mode to the molecular environment. In addition, this work provides a unique laboratory tool for investigating the amount of CO mixed with water.

The outline of this chapter is as follows. In §2.2 the experimental setup is described and the data analysis is explained. §2.3 is dedicated to the influence of CO on the water vibrational modes, as well as the influence of water on the CO bands. In §2.4, the astrophysical relevance is discussed and the conclusions are summarized in §2.5.

2.2 Experiment and data analysis

The experimental setup used for the measurements has been described in detail in Gerakines et al. [1995]. It consists of a high vacuum setup ($\approx 10^{-7}$ Torr) in which ices are grown on a CsI window at a temperature of 15 K. The window is cooled down by a closed cycle He refrigerator and the sample temperature is controlled by resistive heating. A Fourier Transform InfraRed (FTIR) spectrometer is used to record ice spectra in transmission mode from 4000 to 400 cm^{-1} (2.5–25 μm) with a resolution of 1 cm^{-1}.

The sample gas mixtures are prepared in glass bulbs, using a glass vacuum manifold. The bulbs are filled to a total pressure of 10 mbar, which is well below the water vapor pressure. The base pressure of the manifold is better than 10^{-4} mbar, resulting in negligible contamination levels. A sample of CO (Praxair 99,999%) is used without further purification. Deionized water, further purified by three freeze-pump-thaw cycles, is used for the H_2O:CO mixtures. Mixtures with different ratios H_2O:CO are prepared in the vacuum manifold and the resulting depositions are listed in Table 2.1. The growth rate onto the ice is determined by setting the exposure to $\sim 10^{16}$ molecules $cm^{-2}s^{-1}$. Assuming a monolayer surface coverage of 10^{15} molecules cm^{-2} and a sticking probability of 1, this results in a growth rate of 10 $ML \cdot s^{-1}$ (ML=Monolayer). In the experiments where the effect of CO on the water ice vibrational modes is investigated, the water exposure has been kept constant with about 3000 ML of water ice for the different mixtures to facilitate a one-on-one comparison between all samples. In the experiments where the effect of the H_2O on the CO modes has been investigated, the total amount of deposited CO is kept constant at 3000 ML (Table 2.1).

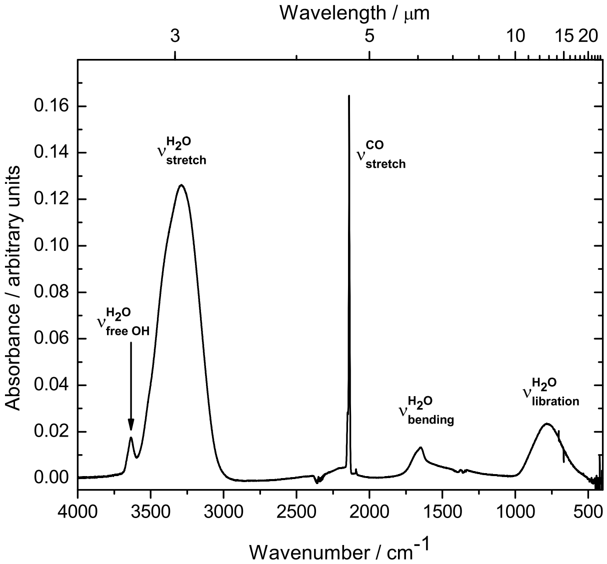

Figure 2.1 A typical baseline and background corrected ice spectrum for a H_2O:CO=1:1 mixture. The measurement is performed at 15 K. The vibrational modes in the H_2O:CO ice are indicated.

Three independent measurements are performed for 1:1 H_2O:CO mixtures. These measurements allow for an estimate of the error in the experiment due to mixing of the gas, deposition of the sample and other errors that may occur. A conservative error of ~10% on the mixing ratios is deduced from these experiments. Additionally, two test measurements are performed for samples of 1000 and 10000 ML, to check for layer thickness dependencies (Table 2.1).

The infrared spectra are taken in absorbance mode ($\ln(I/I_0)$) using a Biorad FTS40

Table 2.2 The measured peak positions and the integration boundaries in cm^{-1} used to compute the integrated intensities of the H_2O bands. The values between brackets indicate the μm values.

			Integration bounds	
Species	Assignment	Peak	Lower	Upper
H_2O	$\nu_{\text{libration}}$	780 (12.8)	500 (20.0)	1100 (9.09)
	ν_{bend}	1655 (6.04)	1100 (9.09)	1900 (5.26)
	ν_{stretch}	3279 (3.05)	3000 (3.33)	3600 (2.78)
	$\nu_{\text{free OH}}$	3655 (2.73)	3600 (2.78)	3730 (2.68)
CO [a]	$\nu_{\text{'stretch'}}$	2139 (4.68)	2120 (4.72)	2170 (4.61)
	$\nu_{\text{'polar'}}$	2152 (4.65)	2120 (4.72)	2170 (4.61)

[a] The integrations for the two CO bands are performed using Gaussian fits.

spectrometer. A total of 256 spectra are acquired and averaged for each sample measurement. The spectra are further processed using IDL (Interactive Data Language) in order to flatten the baseline. This is done by fitting a second order polynomial through a set of five points, which are visually chosen well away from absorption features. The data reduction does not lead to a distortion of the absorption profiles. A typical absorption spectrum is shown in Fig. 2.1.

The absorption band strengths for the three modes of pure water ice at 15 K are well known from literature [Gerakines et al. 1995]. The adopted values are 2×10^{-16}, 1.2×10^{-17} and 3.1×10^{-17} cm molecule^{-1} for the stretching ($\nu_{\text{stretch}} = 3279\ \text{cm}^{-1}$ or 3.05 μm), bending ($\nu_{\text{bend}} = 1655\ \text{cm}^{-1}$ or 6.04 μm) and libration mode ($\nu_{\text{lib}} = 780\ \text{cm}^{-1}$ or 12.8 μm), respectively (see Fig. 2.1). Calculating the integrated absorption bands over the intervals listed in Table 2.2 for the mixtures and scaling them to the integrated band strength for pure water ice, allows for a deduction of the band strengths for the water ice bands in the mixture via:

$$A^{\text{band}}_{\text{H}_2\text{O:CO=1:x}} = \int_{\text{band}} I_{\text{H}_2\text{O:CO=1:x}} \times \frac{A^{\text{band}}_{\text{H}_2\text{O}}}{\int_{\text{band}} I_{\text{H}_2\text{O}}}, \tag{2.1}$$

where $A^{\text{band}}_{\text{H}_2\text{O:CO=1:x}}$ is the calculated band strength for the vibrational water mode in the 1:x mixture, $\int_{\text{band}} I_{\text{H}_2\text{O:CO=1:x}}$ its integrated area, $A^{\text{band}}_{\text{H}_2\text{O}}$ the band strengths for the water modes as available from literature and $\int_{\text{band}} I_{\text{H}_2\text{O}}$ the integrated area under the vibrational mode for the pure water sample. The free OH stretching mode, “the fourth band”, is scaled to the stretching mode for pure water since this absorption is absent in the spectrum of pure H_2O ice.

Integration limits used throughout the experiment are listed in Table 2.2. Integrated areas relative to the integrated area of the pure water stretching mode, $A/A_{\text{pure H}_2\text{O stretch}}$, are investigated as a function of CO concentration. For the sample with the most mixed in CO, i.e. the 1:4 H_2O:CO mixture, an analysis in terms of cluster formation is given. In addition, the influence of temperature on the water stretching mode is studied. The measured spectra for the H_2O:CO mixtures are available online at the Leiden ice database.

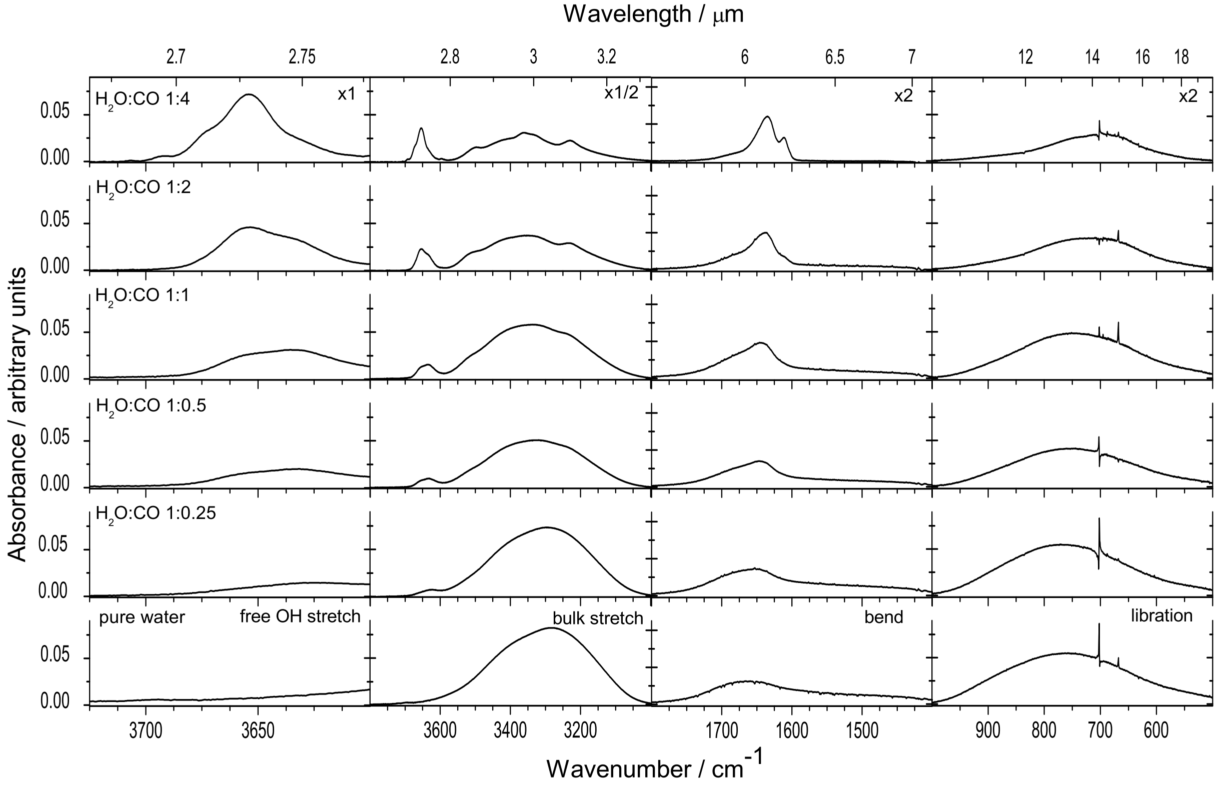

Figure 2.2 Combined spectra of the four modes for water ice for the six measured compositions (see Table 2.1), ranging from pure water ice (bottom) to a 1:4 H_2O:CO mixture (top figures). The spectra are taken at a temperature of 15 K. Note that the wavelength ranges for separate modes are different. The small structures on the libration mode are experimental artifacts.

2.3 Results

2.3.1 Influence of CO on water bands

In Fig. 2.2 the four H_2O ice fundamentals are shown for different compositions. Similar to CO_2 [Öberg et al. 2007a], CO has a clear influence on the water ice absorption bands compared to the pure H_2O ice. This effect is different for each of the four bands. The bulk stretch mode is most strongly affected; the band strength for this mode decreases by more than a factor of 2 when the CO fraction is raised from 0% to 80%. The band strength of the free OH stretch, which is absent when no CO is mixed in, is greatly enhanced with concentration. The libration mode gradually looses intensity when the amount of CO in the ice is increased and the peak of the absorption band shifts to lower energy. The integrated areas of the four water modes are scaled to the pure water stretching mode and plotted versus the CO concentration in Fig. 2.3.

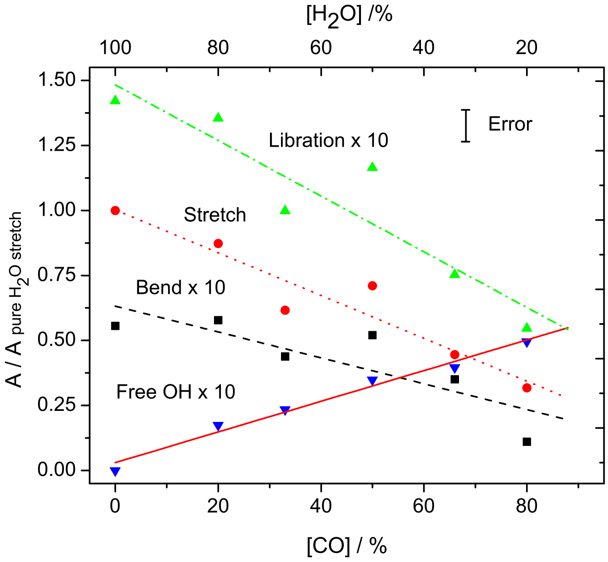

Figure 2.3 The integrated intensity of the water vibration modes relative to the integrated intensity of the pure water stretch mode plotted versus the concentration of CO in the sample ice. It should be noted that the plots for the bending, free OH and libration mode have been multiplied by a factor of ten to facilitate the display and that the stretch mode is the one actually most depending on the concentration. The four water modes show to first order a linear dependence on the CO concentration. The estimated error in the data amounts to 10%.

A linear function $A_{\mathrm{eff}} = a \cdot [\mathrm{CO}] + b$ is fitted through the data points of the four water modes. The a coefficient indicates the strength of increase/decrease of the band strength, and the b coefficient indicates the band strength of water relative to the pure stretching

Table 2.3 Resulting linear fit coefficients for the H_2O:CO mixtures. The coefficients indicate the strength of the interaction between CO and the H_2O host molecules in the matrix for mixtures which are deposited at a temperature of 15 K. The corresponding values for H_2O:CO_2 ice mixtures from Öberg et al. [2007a] are listed for a comparison.

		Linear Coefficients		
mixture	H_2O mode	constant (b) $[10^{-16}$ cm molecule$^{-1}]$	slope (a) $[10^{-19}$ cm molecule$^{-1}]$	R^2
H_2O:CO	$\nu_{\mathrm{libration}}$	0.30±0.02	−2.1±0.4	0.93
	ν_{bend}	0.13±0.02	−1.0±0.3	0.84
	ν_{stretch}	2.0±0.1	−16±3	0.95
	$\nu_{\mathrm{free\ OH}}$	0	1.2±0.1	0.99
H_2O:CO_2	$\nu_{\mathrm{libration}}$	0.32±0.02	−3.2±0.4	0.99
	ν_{bend}	0.14±0.01	−0.5±0.2	0.81
	ν_{stretch}	2.1±0.1	−22±2	0.99
	$\nu_{\mathrm{free\ OH}}$	0	1.62±0.07	0.99

mode when no impurities are mixed in. There exists some deviation between the data points and the fit function which is most probably due to the deposition accuracy, but this deviation is within the experimental error of 10%. A clear trend in all four modes is observed. In Table 2.3, the linear fit coefficients are listed for the H_2O:CO binary mixtures. The linear coefficient for the H_2O stretching mode is highest and negative, indicating the strongest decrease in band strength. The free OH stretching mode has a positive linear coefficient indicating that this is the only mode to increase in intensity upon CO increase. A comparison with recently obtained data for H_2O:CO_2 ices shows the same trend. Apart from the bending mode, all effects are more pronounced in the CO_2 mixtures, i.e., the absolute values of the a coefficient are larger by a factor of 1.3–2. This is related to the actual interactions in the ice and work is in progress to study such effects in more detail for a large number of species from a chemical physics perspective.

The free OH mode, the water stretching mode and the water bending mode start showing substructure superposed onto the bulk absorption profile upon increase of the fraction of CO in the ice mixture (Fig. 2.4). The absorptions of the bulk modes are still clearly apparent beneath the substructure. For the stretching mode this absorption shifts from 3279 cm^{-1} to a higher frequency of 3300 cm^{-1}. The peak absorption for the bulk bending mode shifts from 1655 cm^{-1} for pure H_2O to 1635 cm^{-1} for the 1:4 H_2O:CO mixture. The libration mode is also red-shifted upon CO concentration increase. For the pure H_2O ice spectrum this mode is located at 780 cm^{-1}, while for the highest partner concentration it appears at 705 cm^{-1}. The free OH stretch gradually increases in frequency. The peak absorption shifts from 3636 cm^{-1} for the 1:0.25 to 3655 cm^{-1} for the 1:4 H_2O:CO mixture, which corresponds to a blue shift of 19 cm^{-1}.

The substructure which is superimposed on the bulk stretching mode around 3300 cm^{-1} has been previously assigned to $(H_2O)_n$ water clusters in the ice. These assignments are based on matrix spectroscopic data of H_2O in a matrix of N_2 + O_2 (75:25) [Ohno et al. 2005]. Comparable data for H_2O in a matrix of CO are not available. Nevertheless, in Fig. 2.4 it is shown that an excellent fit is obtained when peak positions from matrix spectroscopic data are used, assuming that the peak positions are shifted which is indicative for the difference in interaction between H_2O and CO compared to H_2O and N_2 + O_2. For each of the contributions the peak position, bandwidths (Full-Width-at-Half-Maximum (FWHM)) and integrated area are summarized in Table 2.4 and compared to previous results obtained by Ohno et al. [2005]. Some absorptions are red-shifted and other absorptions are blue-shifted compared to absorptions of H_2O clusters in a N_2 + O_2 matrix. Note that the relative H_2O concentrations in the present work are substantially higher than in the matrix experiments by Ohno et al. [2005]. As a consequence larger H_2O clusters are more pronounced in our spectra.

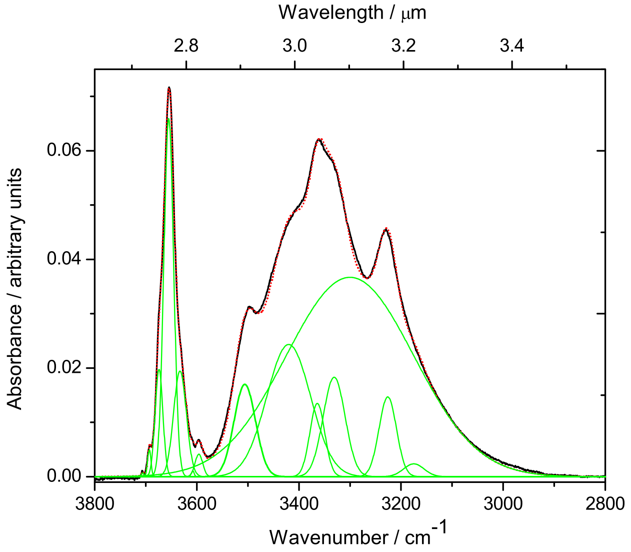

Figure 2.4 Measured and fitted spectrum of a 1:4 H_2O:CO mixture in the frequency range of the H_2O bulk stretch and free OH stretch modes at a temperature of 15 K. The water stretching mode clearly shows substructure. An excellent fit is obtained by a superposition of the bulk stretch mode and Gaussian functions representing smaller H_2O clusters in the matrix material [Ohno et al. 2005]. The fitted peak positions and the positions from Ohno et al. [2005] are listed in Table 2.4.

Additionally, the temperature of the sample plays a role on the band strengths. A clear effect is encountered when the temperature is slightly increased, i.e., from 15 to 25 K, close to the desorption temperature of CO. At this temperature, the CO molecules in the matrix start gaining enough energy to become mobile. The mobility in the matrix allows water clusters to find partners for hydrogen bonding and to reorganize themselves to form a stronger bulk hydrogen bonded network, as indicated by the increased bulk stretch mode band strength and decreasing intensity of the substructure. Figure 2.5 nicely shows the transition from H_2O clusters embedded in a matrix of CO to the formation of a bulk hydrogen bonded network.

Table 2.4 Line positions, FWHMs and integrated areas of the Gaussian functions fitted to the 1:4 H_2O:CO water bulk stretch and free OH stretch spectrum. The assignment is based on both Density Functional Theory (DFT) calculations and experimental values from Ohno et al. [2005] obtained in a N_2/O_2 matrix.

Mode	Position^a (cm^{-1})	Position^b (cm^{-1})	Δ Position^b (cm^{-1})	FWHM^b (cm^{-1})	Area^b (a.u. $\cdot$ cm^{-1})
Free OH (ring) cyclic-pentamer, cyclic-trimer free OH, clusters hexamer	3688	3674	15	15	0.371
Asymmetric stretch H-acceptor dimer	3715	3693	22	7	0.040
Asymmetric stretch monomer	3715	3706	9	5	0.043
Symmetric stretch monomer	3635	3608	27	5	0.074
Symmetric stretch H-acceptor dimer	3629	3596	33	15	0.078
Bulk free OH stretch	—–	3655	—–	19	1.57
Bulk free OH stretch	—–	3633	—–	25	0.609
H-bonded OH stretch "chair" hexamer	3330	3331	-1	43	0.987
H-bonded OH stretch "cage" hexamer	3224	3226	-2	34	0.626
H-bonded OH stretch "prism" hexamer	3161	3175	-14	40	0.119
H-bonded OH stretch pentamer	3368	3364	4	29	0.491
H-bonded OH stretch "book1, cage" hexamer	3450	3420	30	86	2.62
Bulk stretching mode	—–	3300	—–	250	11.5
H-bonded OH stretch ring cyclic trimer	3507	3506	1	42	0.894

[a] Ohno et al. [2005], [b] This work.

Figure 2.6 shows the different effect of CO and CO_2 on the H_2O bending mode in ice for the 1:4 H_2O:CO_2 and 1:4 H_2O:CO mixtures. The intensity ratio of the main peaks is actually reversed in the two mixtures. The differences between the two mixtures start showing up from a mixing ratio of 1:0.5 H_2O:X and become more pronounced for higher CO and CO_2 concentrations. In addition, the CO mixtures exhibit a stronger broad underlying feature, which is visualized by the Gaussian fit in Fig. 2.6. In other words, a detailed study of the H_2O bending and stretching modes may provide additional information on whether CO or CO_2 dominates in the ice. The free OH stretching mode is also affected differently by the two molecules. In the H_2O:CO_2 mixtures, the mode is more shifted to higher wavenumbers. For the 1:1 H_2O:CO_2 mixture the peak position is 3661 cm^{-1}, compared to 3635 cm^{-1} for the H_2O:CO mixtures.

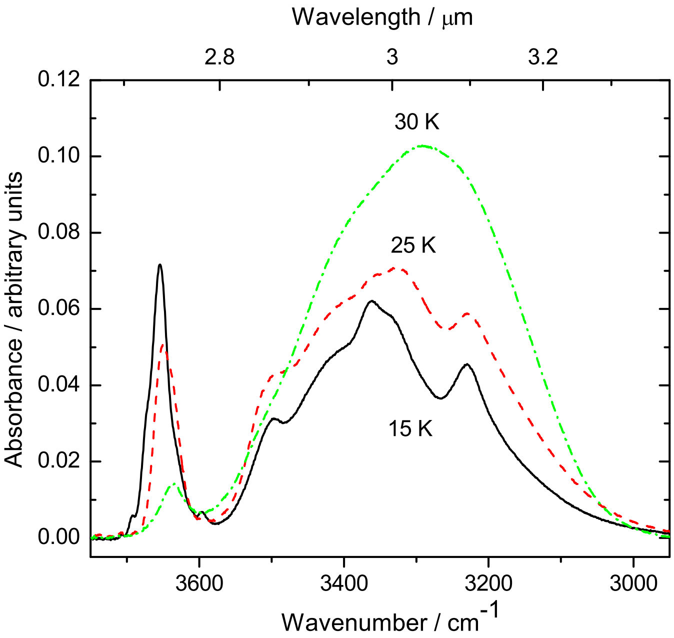

Figure 2.5 Temperature dependence of larger clusters of water molecules in a matrix of H_2O CO = 1:4. For increasing temperature the substructure gives way to the bulk stretch mode when CO evaporates.

Thicker and thinner layers of the mixtures have been measured to check for thickness dependence. We conclude that within our experimental error limit, ice thickness does not play a significant role in the behavior of the relative band strengths. This conclusion is supported by the observation that identical mixing ratios in the two measurement series (H_2O/CO and CO/H_2O) show the same (scaled) spectroscopic behavior for different total ice thicknesses (Table 2.1).

2.3.2 Influence on the CO band

Paragraph 2.3.1 shows that mixing CO into a water mixture affects the band strengths of the water vibrational modes. Vice versa, the CO stretch mode is also altered when water is added to CO ice. This is seen in the experiments where the amount of deposited CO is kept constant (Table 2.1). When water is mixed into the CO ice, the absorption changes from a Lorentzian profile to a Gaussian profile. Furthermore, the second CO absorption at 2152 cm^{-1} ascribed to CO bound to the H_2O dangling OH sites [Fraser et al. 2004] manifests itself as a Gaussian profile and increases in integrated intensity upon increase of water concentration. The transition from the pure CO Lorentzian shaped profile to two Gaussian shaped profiles for the mixed CO:H_2O ices is illustrated in Fig. 2.7. We have not further decomposed the 2139 cm^{-1} component.

Gaussian fits for both CO absorption components are made for the range of mixtures as listed in Table 2.1 at a temperature of 15 K. One typical fit is shown in Fig. 2.8. With this example it is demonstrated that excellent fits are obtained by using the fit parameters as listed in Table 2.5. The behavior of the integrated area of the 2152 cm^{-1} compared with the total integrated CO absorption is plotted as a function of CO and H_2O concentration

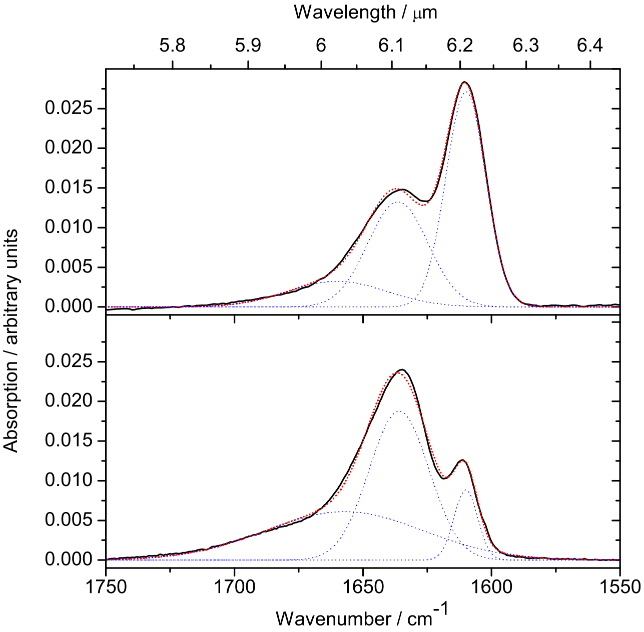

Figure 2.6 The spectral differences in the water bending mode profile for a 1:4 H_2O:CO_2 ice mixture (top) [Öberg et al. 2007a] and a 1:4 H_2O:CO mixture (bottom). The bold (overall) spectra indicate the laboratory spectra and coincide with the fitted spectra consisting of the three Gaussian curves as indicated by the dotted lines.

in Fig. 2.9. The integrated area for the 2152 cm^{-1} component decreases while increasing the CO content, and is undetectable for a pure CO ice. A second order polynomial describes how the polar component behaves with respect to the CO concentration [x] or water concentration [$100 - x$] in the ice over the interval spanning from 20% CO up to a pure CO ice. Note that the total amount of deposited CO is kept constant. The coefficients of the second order polynomial of the form $y = a \cdot x^2 + b \cdot x + c$ are $a = -0.005$, $b = 0.23$ and $c = 26.6$. For a decreasing amount of water in the sample the peak position of the 2152 cm^{-1} absorption feature is most strongly affected and decreases gradually to lower wavenumbers, until it reaches 2148 cm^{-1} for the 1:0.25 CO:H_2O mixture. The FWHM of this band is also affected. It starts at a width of 10.5 cm^{-1} for the 1:4 CO:H_2O mixture and decreases to 7.5 cm^{-1} for the 1:0.25 CO:H_2O mixture. The position of the main absorption feature at 2139 cm^{-1} is only slightly affected by increasing the amount of water in the sample and decreases by 1.3 cm^{-1} when going from pure CO ice to the 1:4 CO:H_2O mixture, i.e., a shift toward the 2136 cm^{-1} feature is observed upon dilution (see Fig. 2.10). Its position is expected to shift even more, to 2136 cm^{-1} for H_2O concentrations above 80%. The FWHM of this absorption feature decreases from 8 cm^{-1} for the 1:4 CO:H_2O

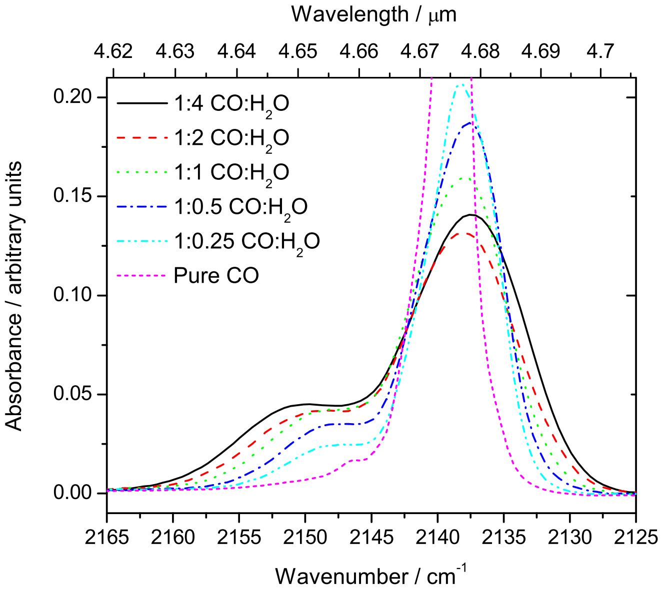

Figure 2.7 Illustration of the behavior of the CO stretch fundamental upon increase of the concentration of H_2O in CO. The total integrated band strength remains unchanged within the experimental error, although the maximum intensity of the absorption decreases strongly. The y-axis is cut off for the pure CO mode to make a clearer distinction between 'non-polar'and 'polar'components of the CO absorption for the CO:H_2O mixtures.

to 5 cm^{-1} for the 1:0.25 CO:H_2O sample. The Lorentzian peak profile of the pure CO absorption exhibits an even smaller FWHM of 2 cm^{-1}. An overview of the changes in peak position, FWHM and integrated intensity is given in Table 2.5.

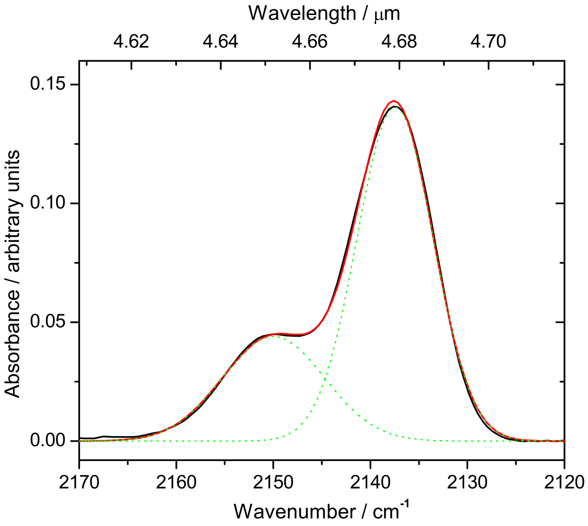

Figure 2.8 Gaussian fit of the CO stretch mode in a CO:H_2O = 1:0.25 mixture. The bold (overall) spectrum is the measured laboratory spectrum that is reproduced by adding the two Gaussian components (dotted lines) centered around 2138.2 cm^{-1} and 2147.5 cm^{-1}. These are attributed to CO in a ‘non-polar’and ‘polar’environment, respectively.

Table 2.5 Lorentzian and Gaussian fit parameters for the CO stretching mode for a constant amount of CO in ice mixtures ranging from 100% CO to a 1:4 CO:H_2O mixture.

Composition	Position (cm^{-1})	FWHM (cm^{-1})	Area (a.u.·cm^{-1})
Pure CO [a]	2138.8	2.2	1.9
1:0.25 CO:H_2O	2138.2	5.0	1.31
	2147.5	7.5	0.23
1:0.5 CO:H_2O	2138.0	5.8	1.40
	2148.1	7.8	0.34
1:1 CO:H_2O	2138.2	6.5	1.28
	2148.3	9.0	0.44
1:2 CO:H_2O	2137.9	7.6	1.24
	2149.5	9.8	0.49
1:4 CO:H_2O	2137.5	7.9	1.38
	2150.0	10.5	0.58

[a] Lorentzian profile

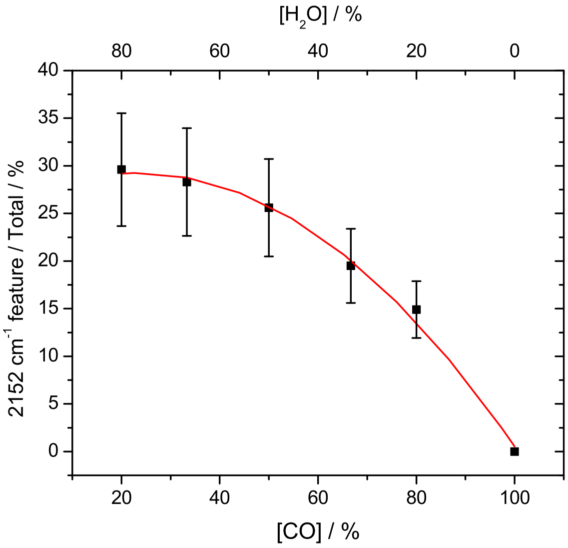

Figure 2.9 Absorbance of the 2152 cm^{-1} component relative to the total CO absorption as a function of CO concentration.

The position of the 2139 cm^{-1} absorption feature is also strongly dependent on the temperature of the ice as illustrated in Fig. 2.10. The majority of the CO will desorb as the ice is heated above the CO desorption temperature. The remaining CO shows an absorption that is shifted toward 2135 cm^{-1}. Thus, a shift from 2139 to 2136 cm^{-1} occurs both by mixing with significant amounts of H_2O and by heating of CO:H_2O above 40 K, even for mixtures with modest amounts of H_2O. From Fig. 2.10 it becomes clear that the latter effect (i.e. heating) is the more critical one. One should note that the laboratory data presented here can not be compared one-to-one with the observational data because of shifts caused by grain shape effects.

2.4 Discussion

CO and H_2O ice abundances are often derived using the well known constants from the literature. The experimental work presented here shows that band strengths deduced from pure ices cannot be used to derive column densities in interstellar ices without further knowledge on the environmental conditions in the ice. Concentrations of CO and CO_2 ice as high as 15 and 21%, respectively, relative to H_2O have been reported towards GL7009S [Keane et al. 2001a]. If we assume a polar fraction of 75%, as reported towards W33A, and that the polar fraction of both CO and CO_2 ice are in close contact with the water, the band strength for the H_2O bending mode is reduced by a factor of ~1.25. In other words, the band strength for H_2O will be smaller and hence the column density of H_2O will be underestimated if the laboratory data from pure H_2O ice are adopted from the literature.

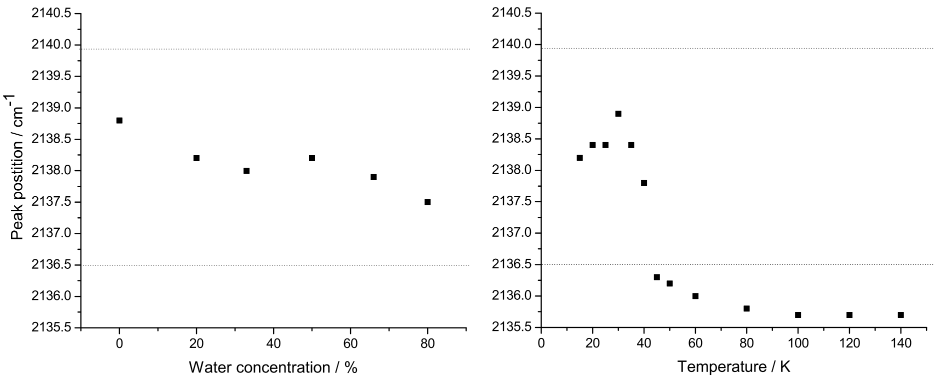

Figure 2.10 Change in peak position of the 2139 cm^{-1} CO absorption feature as a function of both H_2O concentration and as a function of temperature for the 1:4 H_2O:CO mixture. The dotted lines indicate the band positions measured for CO in the interstellar medium.

Vice versa, for deriving the column density of CO ice one should also consider the influence of other molecules in its vicinity. The integrated absorbance of CO, however, is less strongly influenced by the presence of H_2O. The CO absorption decreases in absolute intensity when water is mixed in, but the total integrated band strength is compensated by a broadening of the absorption and the appearing of the 2152 cm^{-1} component, at least in the laboratory spectra. Upon heating, the CO molecules become trapped into pores as indicated by the 2136 cm^{-1} feature. The absorption strength of this band is very sensitive to temperature [Schmitt et al. 1989a]. The CO absorption profile is indicative for the amount of water that is mixed. The percentage of CO mixed into the H_2O ice is derived in the laboratory from the ratio between the 2152 cm^{-1} feature and the total CO absorption (Fig. 2.9) in §2.3.2. This allows for a derivation of the effective band strength $A_{\rm eff}^{\rm band}$ for H_2O in a mixture with CO using the linear model proposed in § 2.3.1 and thus an estimate of the column density for H_2O via the equation [Sandford et al. 1988]:

$$N_{\rm corr}=\frac{\int \tau_\nu d\nu}{A_{\rm eff}}. \tag{2.2}$$

Temperature also affects the band strength as shown in Fig. 2.5. The applications of the model presented in Fig. 2.9 are restricted to deduction of column densities for ices with a temperature of about 15 K and that have not been thermally processed. It should also be noted, as recently demonstrated by Bisschop et al. [2007b], that beside binary also tertiary mixtures have to be taken into account to compare laboratory data with astronomical spectra.

2.5 Conclusions

Based on the experiments described in this manuscript and in recent work on H_2O:CO_2 mixed ices we draw the following conclusions regarding the interaction between H_2O and CO in a solid environment:

1. The general trend on the band strengths of the four vibrational modes in water ices is similar for H_2O:CO and H_2O:CO_2 mixtures with increasing CO or CO_2 concentration. However, quantitative differences exist, reflecting differences in the strength of the interaction, which allow to distinguish between CO and CO_2 in H_2O ice, explicitly assuming that the main constituents of the ice are H_2O, CO_2 and CO.

2. The position of the water free OH stretching mode is particularly indicative of the molecule that is interacting in the matrix (CO vs CO_2), again under the assumption that we only consider H_2O/CO_2/CO ices. The peak position of this mode is 26 cm^{-1} red-shifted for a 1:1 H_2O:CO ice mixture compared to a 1:1 H_2O:CO_2 ice mixture.

3. In addition, the water bending mode is indicative of the molecule, i.e., CO or CO_2, that is interacting with the water ice. The relative integrated intensity of the Gaussian components reveals whether CO_2 or CO is mixed into the H_2O ice. The same restriction as mentioned in conclusions 1 and 2 applies.

4. Upon increasing the relative amount of CO in the mixture, a clear substructure starts showing up in the bending, free OH stretch and bulk stretching mode. The arising substructure indicates the onset of H_2O cluster formation in the H_2O:CO ice. An assignment of the clusters has been possible following matrix isolation spectroscopy.

5. The substructure on the stretching mode quickly gives way to the bulk water mode when the temperature is increased close to the desorption temperature of CO. This can easily be depicted by CO molecules becoming mobile and hence allowing single water molecules and larger water clusters to find partners for bulk hydrogen bonding.

6. The ratio 2152 cm^{-1}total integrated CO absorption intensity is a tracer of the amount of CO that is mixed into the laboratory water ice, or vice versa. In astronomical spectra this band has not been observed.

7. H_2O column densities derived from astronomical spectra can easily be underestimated by as much as 25% when environmental influences, i.e., CO or CO_2 presence, are not taken into account.

The present systematic study of CO:H_2O ice, together with recent work on CO_2:H_2O ice, provide the tools to estimate on the mixing ratios of the three most abundant molecules in interstellar ices.

CHAPTER 3

The c2d *Spitzer* spectroscopic survey of ices around low-mass young stellar objects. IV. NH_3 and CH_3OH [1]

NH_3 and CH_3OH are key molecules in astrochemical networks leading to the formation of more complex N- and O-bearing molecules, such as CH_3CN and CH_3OCH_3. Despite a number of recent studies, little is known about their abundances in the solid state. This is particularly the case for low-mass protostars, for which only the launch of the *Spitzer* Space Telescope has permitted high sensitivity observations of the ices around these objects. In this work, we investigate the 8 – 10 μm region in the *Spitzer* IRS (InfraRed Spectrograph) spectra of 41 low-mass young stellar objects (YSOs). These data are part of a survey of interstellar ices in a sample of low-mass YSOs studied in earlier papers in this series. We used both an empirical and a local continuum method to correct for the contribution from the 10 μm silicate absorption in the recorded spectra. In addition, we conducted a systematic laboratory study of NH_3- and CH_3OH-containing ices to help interpret the astronomical spectra. We detected the NH_3 ν_2 umbrella mode at ~9 μm in low-mass YSOs for the first time. We identified this feature in 24 sources, with abundances with respect to water between ~2 and 15%. Simultaneously, we also revisited the case of CH_3OH ice by studying the ν_4 C–O stretch mode of this molecule at ~9.7 μm in 16 objects, yielding abundances consistent with those derived by Boogert et al. [2008] (hereafter paper I) based on a simultaneous 9.75 and 3.53 μm data analysis. Our study indicates that NH_3 is present primarily in H_2O-rich ices, but that in some cases, such ices are insufficient to explain the observed narrow FWHM. The laboratory data point to CH_3OH being in an almost pure methanol ice, or mixed mainly with CO or CO_2, consistent with its formation through hydrogenation on grains. Finally, we use our derived NH_3 abundances in combination with previously published abundances of other solid N-bearing species to find that up to 10–20% of nitrogen is locked up in known ices.

---

[1] Based on: S. Bottinelli, A. C. A Boogert, J. Bouwman, M. Beckwith, E. F. van Dishoeck, K I. Öberg, K. M. Pontoppidan, H. Linnartz, G. A. Blake, N. J. Evans II and F. Lahuis, Astrophysical Journal, 718, 1100-1117 (2010)

3.1 Introduction

Ammonia and methanol are among the most ubiquitous and abundant (after H_2 and CO) molecules in space. Gaseous NH_3 and CH_3OH are found in a variety of environments such as infrared dark clouds, dense gas surrounding ultra-compact H II regions, massive hot cores, hot corinos, and comets. Solid CH_3OH has been observed in the ices surrounding massive YSOs [e.g. Schutte et al. 1991, Dartois et al. 1999, Gibb et al. 2004] and more recently toward low-mass protostars [Pontoppidan et al. 2003a]. The presence of solid NH_3 has been claimed toward massive YSOs only [Lacy et al. 1998, Dartois et al. 2002, Gibb et al. 2004, Gürtler et al. 2002], with the exception of a possible detection in the low-mass object IRAS 03445+3242 [Gürtler et al. 2002]. However, these detections are still controversial and ambiguous [Taban et al. 2003].

Both molecules are key participants in gas-grain chemical networks resulting in the formation of more complex N- and O-bearing molecules, such as CH_3CN and CH_3OCH_3 [e.g. Rodgers & Charnley 2001]. Moreover, UV processing of NH_3- and CH_3OH-containing ices has been proposed as a way to produce aminoacids and other complex organic molecules [e.g. Muñoz Caro & Schutte 2003, Bernstein et al. 2002a, Öberg et al. 2009a]. In addition, the amount of NH_3 in ices has a direct impact on the content of ions such as NH_4^+ and OCN^-, which form reactive intermediates in solid-state chemical networks. A better knowledge of the NH_3 and CH_3OH content in interstellar ices will thus help to constrain chemical models and to gain a better understanding of the formation of more complex, prebiotic, molecules.

During the pre-stellar phase, NH_3 is known to freeze out on grains (if the core remains starless long enough – Lee et al. 2004). Moreover, CH_3OH is known to have gas-phase abundances with respect to H_2 in hot cores/corinos that are much larger than in cold dense clouds: $\sim (1-10) \times 10^{-6}$ vs. $\leq 10^{-7}$, with the former values most likely representing evaporated ices in warm regions [e.g. Genzel et al. 1982, Blake et al. 1987, Federman et al. 1990]. Together, these findings suggest that ices are an important reservoir of NH_3 and CH_3OH and that prominent features should be seen in the absorption spectra toward high- and low-mass protostars. Unfortunately, as summarized in Table 3.1, NH_3 and CH_3OH bands, with the exception of the 3.53 μm CH_3OH feature, are often blended with deep water and/or silicate absorptions, complicating unambiguous identifications and column density measurements. This is particularly true for NH_3 whose abundance determination based on the presence of an ammonium hydrate feature at 3.47 μm remains controversial [e.g. Dartois & d'Hendecourt 2001].

Nonetheless, it is important to use all available constraints to accurately determine the abundances of these two molecules. Despite the overlap with the 10 μm silicate (Si–O stretch) feature, the NH_3 ν_2 umbrella mode at ~9 μm (~1110 cm^{-1}) offers a strong intrinsic absorption cross section and appears as the most promising feature to determine the abundance of this species in the solid phase. Moreover, the CH_3OH ν_4 C–O stretch at ~9.7 μm (~1030 cm^{-1}) provides a good check on the validity of the different methods we will use to subtract the 10 μm silicate absorption, since the abundance of this molecule has been accurately determined previously from both the 3.53 and 9.75 μm features (see Boogert et al. [2008]).

Table 3.1. Selected near- and mid-infrared features of NH_3 and CH_3OH.

Mode	λ (μm)	$\bar{\nu}$ (cm^{-1})	Problem
NH_3 features:			
ν_3 N–H stretch	2.96	3375	Blended with H_2O (O–H stretch, 3.05 μm/3275 cm^{-1})
ν_4 H–N–H bend	6.16	1624	Blended with H_2O (H–O–H bend, 5.99 μm/1670 cm^{-1}), HCOOH
ν_2 umbrella	**9.00**	**1110**	**Blended with silicate**
CH_3OH features:			
ν_2 C–H stretch	3.53	2827	–
ν_6 & ν_3 –CH_3 deformation	6.85	1460	Blended (e.g. with NH_4^+)
ν_7 –CH_3 rock	8.87	1128	Weak; blended with silicate
ν_4 C–O stretch	**9.75**	**1026**	**Blended with silicate**
Torsion	14.39	695	Blended with H_2O libration mode

Note. — The bold-faced lines indicate the features studied here.

Note. — The nomenclature for the NH_3 and CH_3OH vibrational modes are adopted from Herzberg [1945].

More detailed spectroscopic information is particularly interesting for low-mass protostars as the ice composition reflects the conditions during the formation of Sun-like stars. Such detections have only become possible with *Spitzer*, whose sensitivity is necessary to observe low luminosity objects even in the nearest star-forming clouds.

The gain in sensitivity offered by *Spitzer* compared to previous space-based observatory, as well as the spectral resolution of the data analyzed here ($\Delta\lambda/\lambda \sim 100$), imply that the interpretation of the astronomical spectra should be supported by a systematic laboratory study of interstellar ice analogues containing NH_3 and CH_3OH. The spectral appearance of ice absorption features, such as band shape, band position and integrated band strength, is rather sensitive to the molecular environment. Changes in the lattice geometry and physical conditions of an ice are directly reflected by variations in these spectral properties. In the laboratory, it is possible to record dependencies over a wide range of astrophysically relevant parameters, most obviously ice composition, mixing ratios, and temperature. Such laboratory data exist for pure and some H_2O-rich NH_3- and CH_3OH-containing ices [e.g. D'Hendecourt & Allamandola 1986, Hudgins et al. 1993, Kerkhof et al. 1999, Taban et al. 2003], but a systematic study and comparison with observational spectra is lacking.

In principle, the molecular environment also provides information on the formation pathway of the molecule. For example, NH_3 ice is expected to form simultaneously with H_2O and CH_4 ice in the early, low-density molecular cloud phase from hydrogenation of N atoms [e.g. Tielens & Hagen 1982]. In contrast, solid CH_3OH is thought to result primarily from hydrogenation of solid CO, a process which has been confirmed to be rapid at low temperatures in several laboratory experiments [e.g. Watanabe & Kouchi 2002, Hidaka et al. 2004, Fuchs et al. 2009]. A separate, water-poor layer of CO ice is often found on top of the water-rich ice layer in low-mass star-forming regions due to the 'catastrophic' freeze-out of gas-phase CO at high densities [Pontoppidan et al. 2003a, Pontoppidan 2006]. Hydrogenation of this CO layer should lead to a nearly pure CH_3OH ice layer [e.g. Cuppen et al. 2009], which will have a different spectroscopic signature from that of CH_3OH embedded in a water-rich matrix. The latter signature would be expected if CH_3OH ice were formed by hydrogenation of CO in a water-rich environment or by photoprocessing of H_2O:CO ice mixtures, another proposed route [e.g. Moore & Hudson 1998].

Here, we present *Spitzer* spectra between 5 and 35 μm of ices surrounding 41 low-mass protostars, focusing on the 8 – 10 μm region that contains the ν_2 umbrella and ν_4 C–O stretch modes of NH_3 and CH_3OH, respectively. This chapter is part of a series of ice studies [Boogert et al. 2008, Pontoppidan et al. 2008, Öberg et al. 2008] carried out in the context of the *Spitzer* Legacy Program "From Molecular Cores to Planet-Forming Disks" ("c2d"; Evans et al. 2003). In §3.2, we carry out the analysis of the *Spitzer* data in 8 – 10 μm range. In §3.3, we present the laboratory data specifically obtained to help interpret the data that are discussed in §3.4. Finally, we conclude in §3.5 with a short discussion of the joint astronomy-laboratory work (including the overall continuum determination).

3.2 Astronomical observations and analysis

The source sample consists of 41 low-mass YSOs that were selected based on the presence of ice absorption features. The entire sample spans a wide range of spectral indices $\alpha = -0.25$ to $+2.70$, with α defined as $d\log(\lambda F_\lambda)/d\log(\lambda)$, where d indicates the derivative, and F_λ represents all the photometric fluxes available between $\lambda = 2.17$ μm (2MASS K_s-band) and $\lambda = 24$ μm (*Spitzer*/MIPS band). In the infrared broad-band classification scheme, 35 out of 41 objects fall in the embedded Class 0/I category ($\alpha > 0.3$). The remaining 6 objects are flat-spectrum type objects [$-0.3 < \alpha < 0.3$; Greene et al. 1994]. *Spitzer*/IRS spectra (5-35 μm) were obtained as part of the c2d Legacy program (PIDs 172 and 179), as well as a dedicated open time program (PID 20604), and several previously published GTO spectra [Watson et al. 2004]. We refer the reader to Table 1 and Section 3 of Boogert et al. [2008] for the source coordinates and a description of the data reduction process (including overall continuum determination).

As mentioned previously, spectral signatures in the 8 – 10 μm region are dominated by the Si–O stretching mode of silicates. The overall shape as well as the sub-structure of the silicate feature depend on grain size, mineralogy, level of crystallinity. These effects are degenerate and so these different factors cannot be easily separated. For example, large grains and the presence of SiC both produce a shoulder at 11.2 μm [e.g. Min et al. 2007]. Therefore, trying to fit the 10 μm silicate feature by determining the composition and size of the grains is a complex process. For this reason, we use two alternative methods to model the silicate profile and extract the NH_3 (and CH_3OH) feature(s) from the underlying silicate absorption.

3.2.1 Local continuum

The first method uses a local continuum to fit the shape of the silicate absorption. For this, we fit a fourth order polynomial over the wavelength ranges 8.25–8.75, 9.23–9.37, and 9.98–10.4 μm, avoiding the positions where NH_3 and CH_3OH absorb around 9 and 9.7 μm. These fits are shown with thick black lines in Fig. 3.1. After subtraction of the local continuum from the observations, we fit a Gaussian to the remaining NH_3 and/or CH_3OH feature, when present, as shown in Fig. 3.2. The results of the Gaussian fits are listed in Table 3.5 of Appendix 3.6.

3.2.2 Template

The second method assumes that the 8–10 μm continuum can be represented by a template silicate absorption feature, selected among the observed sources. A comparison of the results obtained using a template to those obtained using a simple local continuum provides an estimate of the influence of the continuum choice on the shape and depth of the NH_3 and CH_3OH features. The templates were chosen using an empirical method. Upon examination of the 10 μm feature of the entire sample, the sources could be separated into three general categories, depending on the shape of the wing of the silicate absorption between ~8 and 8.7 μm (which we will refer to as the 8 μm wing): (i) sources with a straight 8 μm wing (Fig. 3.3-a), (ii) sources with a curved 8 μm wing (Fig. 3.3-b), and (iii) sources with a rising 8 μm wing (“emission” sources, Fig. 3.3-c).

Note that, since radiative transfer in the 8–10 μm region can be complicated by the presence of silicate emission, we only consider sources that are the least affected by emission, that is those falling in one of the first two categories. Nevertheless, non-rising silicate profiles might still suffer from the presence of emission. To try and estimate the impact of this potential effect, we used two silicate emission sources from Kessler-Silacci et al. [2006], and subtracted these emission profiles from our absorption profiles, assuming that the emission represented 10 to 50% of the observed absorption. After removal of a local continuum, we determined the integrated optical depths of the NH_3 and CH_3OH features in the spectra corrected for emission, and compared these to the integrated optical depths of the uncorrected spectra. We find that the difference can be up to a factor of two and therefore identify this possible presence of underlying emission as the largest source of uncertainty in our abundance determinations.

For each of the straight and curved 8 μm wings, two sources (in order to test for template-dependent effects) were selected as possible templates for the silicate feature. The selection criteria were: (i) a silicate feature as deep as possible to minimize the effects

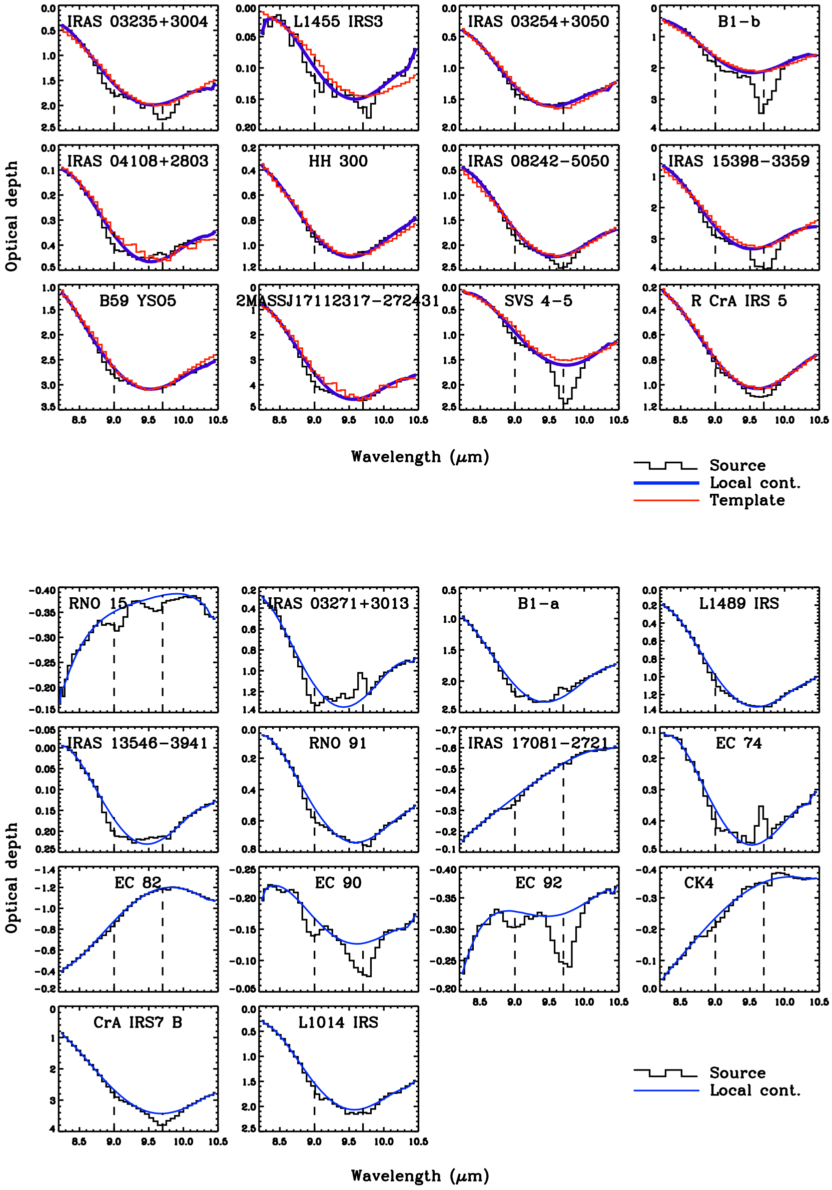

Figure 3.1 (*Top*) Local continuum (thick blue/black lines) and template (red/grey lines) fits to all sources for which a template could be found. (See §3.2.2 for details) — (*Bottom*) Local continuum fits to emission sources or sources for which no reasonable template could be found.

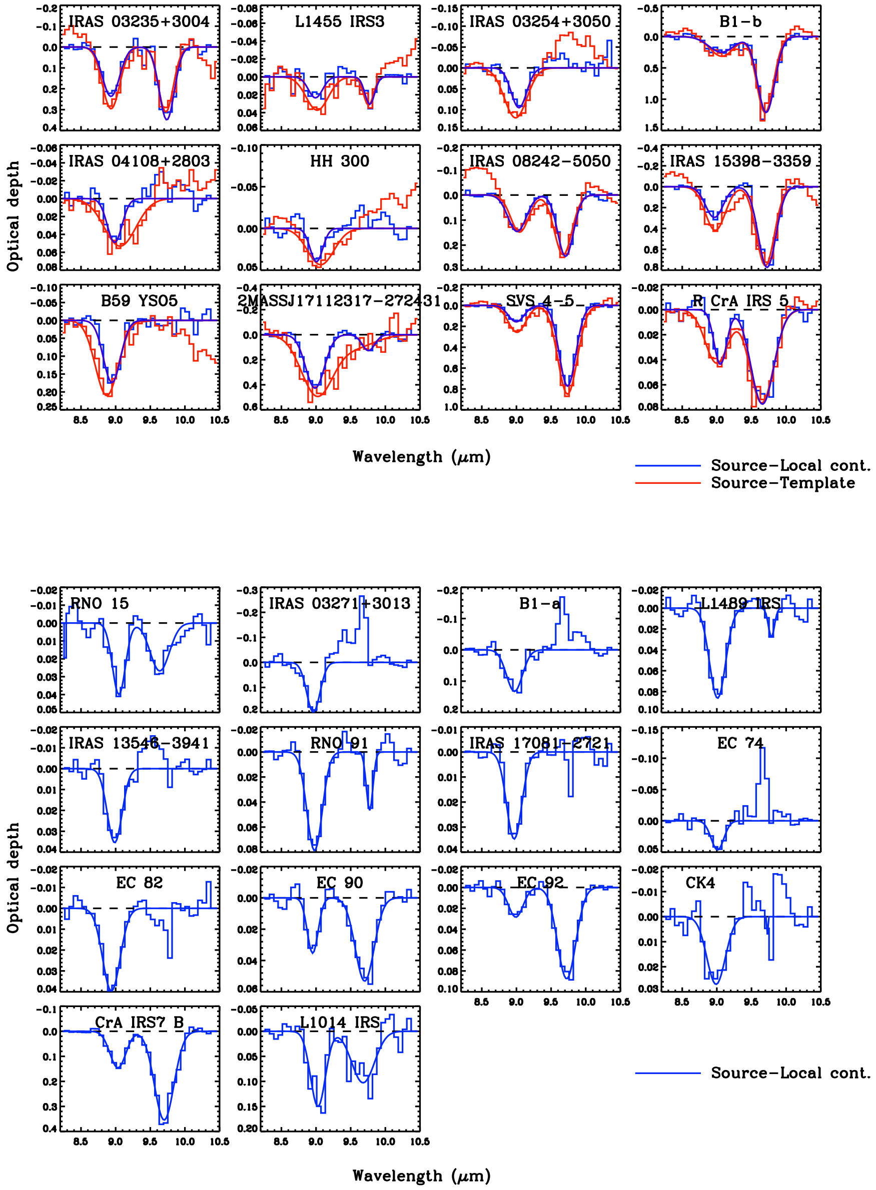

Figure 3.2 (*Top*) Residual after removal of local continuum and template fits for all sources for which a template could be found. (See §3.2.2 for details) — (*Bottom*) Residual after removal of local continuum fits for emission sources or sources for which no reasonable template could be found.

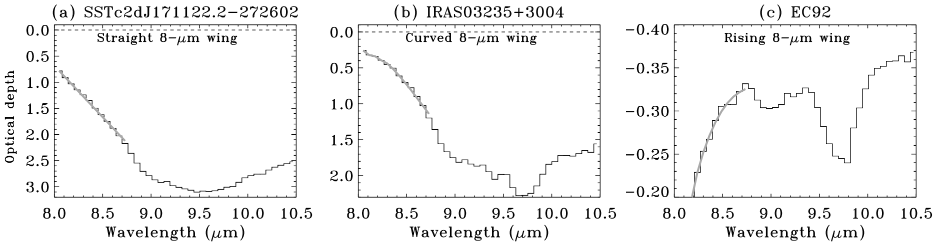

Figure 3.3 Examples illustrating the three shapes of the 8 μm wing shown by the thick grey line: (a) straight, (b) curved, and (c) rising.

of silicate emission and (ii) little NH_3 and CH_3OH signal, as estimated after subtraction of a local continuum. Additionally, we added to this list the GCS3 spectrum observed by Kemper et al. [2004] toward the Galactic Center. The spectra of these templates in the 8–10 μm region are displayed in Fig. 3.4.

For all the other sources in our sample, the best template was determined by scaling the possible templates to the observed optical depth at different wavelengths (8.75, 9.30, 9.37, 9.70, 9.98 μm) and finding the combination (template + scaling point) that gave the least residuals over the same wavelength ranges used to estimate the local continuum (8.25–8.75, 9.23–9.37, 9.98–10.4 μm). The result of this process is displayed for each source in the top part of Fig. 3.1, where the best template is shown by a grey line. The bottom panels of Fig. 3.1 show sources for which no reasonable template could be found, as well as emission sources, in which case only the local continuum is overlaid. As in the case of the local continuum method, the spectra obtained after subtraction of the templates are shown in Fig. 3.2. Taken together, NH_3 features are detected in 24 out of 41 sources.

The top panel of Figure 3.2 shows that the CH_3OH feature is not affected by the continuum choice, whereas the width of the NH_3 band is somewhat sensitive to this choice, especially if there is no CH_3OH absorption, in which case the local continuum yields a wider NH_3 profile. For both continua, there is clearly a feature around 9 μm, which we attribute to NH_3, with the characteristics and limitations given and discussed in the following sections.

3.2.3 NH_3 ice column densities and abundances

Gaussian fits were performed to the NH_3 and/or CH_3OH features when present, and derived parameters for NH_3 are listed in Table 3.5 (Appendix 3.6). Table 3.2 gives the column densities derived for NH_3 for each of the two methods employed to determine the continuum, using a band strength of 1.3×10^{-17} cm molecule^{-1} for the NH_3 ν_2 umbrella mode appropriate for a water-rich ice [D'Hendecourt & Allamandola 1986, Kerkhof et al. 1999]. The two methods generally agree to within a factor of 2 or better. A similar factor of ≤2 overall uncertainty is estimated for those sources for which only the local continuum has been used.

The position of the NH_3 ν_2 umbrella mode is very close to that of the ν_7 CH_3-rock mode of CH_3OH. As illustrated by our laboratory data (see §3.3), sources with an absorption depth at ~9.7 μm (CO-stretch mode of CH_3OH) at least twice as large as the absorption depth at ~9 μm (blend of CH_3-rock mode of CH_3OH and NH_3 umbrella mode) have a significant contribution to the 9 μm integrated optical depth from the CH_3-rock mode of CH_3OH. In these cases (sources followed by an asterisk in Table 3.2 and in Table 3.5 of Appendix 3.6), we performed the following correction: we scaled a H_2O:CH_3OH=9:1 laboratory spectrum to the observed optical depth of the CO-stretch mode of CH_3OH, determined the integrated optical depth of the CH_3-rock mode of CH_3OH in that scaled spectrum, and subtracted it from the total observed optical depth at 9 μm. This correction is justified by the fact that the H_2O:CH_3OH:NH_3=10:4:1 spectrum, a typical interstellar abundance mixture, is well reproduced around 8–10 μm by a combination of H_2O:CH_3OH=9:1 and H_2O:NH_3=9:1 (see § 3.3).

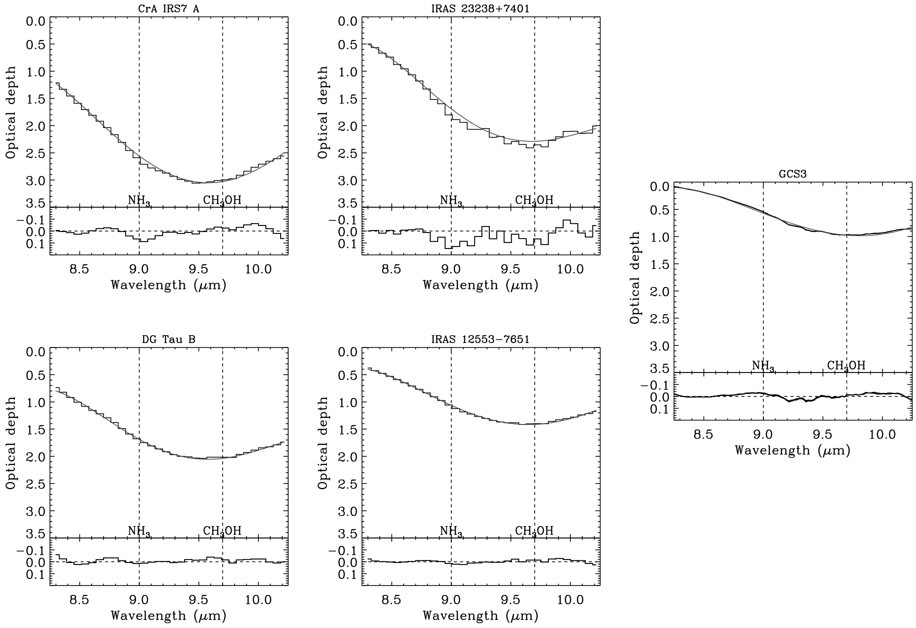

Figure 3.4 Silicate features of the sources used as templates for a straight 8 μm wing (left), curved 8-μm wing (middle), and GCS3 (right). The bottom panels of each plot are the residuals after removal of the local continuum shown in grey in the top panels. The optical depth scale is kept fixed for comparison. These sources are selected to have no or at most weak NH_3 and CH_3OH absorptions.

Table 3.2. NH_3 column densities[a] and abundances with respect to H_2O ice[b]

Source	NH_3, local		NH_3, template		Template	Scaling point
	$\times 10^{17}$ cm^{-2}	% H_2O^b	$\times 10^{17}$ cm^{-2}	% H_2O^b		μm
IRAS 03235+3004	6.83 (0.98)	4.71 (1.00)	8.94 (1.03)	6.17 (1.20)	IRAS 12553	9.30
L1455 IRS3	0.57 (0.23)	6.21 (3.51)	1.41 (0.27)	15.37 (6.86)	GCS3	9.37
IRAS 03254+3050	2.44 (0.39)	6.66 (1.37)	4.58 (0.49)	12.52 (2.10)	IRAS 12553	10.40
B1-b*	~7.3	~4.2	~9.8	~5.6	IRAS 12553	9.70
IRAS 04108+2803	1.23 (0.24)	4.29 (1.03)	2.07 (0.39)	7.21 (1.69)	IRAS 23238	9.70
HH 300	0.90 (0.22)	3.46 (0.90)	2.23 (0.37)	8.60 (1.65)	DG Tau B	9.70
IRAS 08242−5050	4.77 (0.46)	6.13 (0.85)	4.41 (0.54)	5.66 (0.89)	IRAS 12553	9.70
IRAS 15398−3359	8.73 (1.18)	5.90 (1.77)	13.80 (1.35)	9.33 (2.65)	IRAS 12553	9.70
B59 YSO5	4.92 (0.72)	3.53 (0.88)	6.37 (0.99)	4.57 (1.17)	CrA IRS7 A	9.70
2MASSJ17112317−272431	13.10 (1.06)	6.70 (0.54)	20.60 (2.76)	10.58 (1.42)	IRAS 23238	9.70
SVS 4-5*	~2.4	~4.3	~5.8	~10.3	GCS3	8.75
R CrA IRS 5	0.91 (0.23)	2.54 (0.67)	1.49 (0.31)	4.15 (0.92)	IRAS 12553	9.70
RNO 15[c]	0.80 (0.21)	11.58 (3.18)	–	–	–	–
IRAS 03271+3013	4.90 (0.88)	6.37 (1.86)	–	–	–	–
B1-a	3.46 (0.69)	3.33 (0.98)	–	–	–	–
L1489 IRS	2.31 (0.30)	5.42 (0.96)	–	–	–	–
IRAS 13546−3941	0.94 (0.16)	4.56 (0.87)	–	–	–	–
RNO 91	2.03 (0.30)	4.78 (0.81)	–	–	–	–
IRAS 17081−2721	0.86 (0.16)	6.54 (1.39)	–	–	–	–
EC 74[c]	1.00 (0.29)	9.35 (3.13)	–	–	–	–
EC 82	1.22 (0.14)	31.31 (6.65)	–	–	–	–
EC 90	0.67 (0.20)	3.94 (1.24)	–	–	–	–
EC 92*	~0.5	~3.0	–	–	–	–
CrA IRS7 B*	~3.0	~2.8	–	–	–	–
L1014 IRS	3.72 (0.91)	5.20 (1.43)	–	–	–	–
CK4	0.84 (0.13)	5.37 (0.86)	–	–	–	–

Table 3.2. Cont'd

Source	NH_3, local		NH_3, template		Template	Scaling point
	$\times 10^{17}$ cm^{-2}	% H_2O^b	$\times 10^{17}$ cm^{-2}	% H_2O^b		μm
3-σ upper limits						
LDN 1448 IRS1	0.20	4.15	–	–	–	–
IRAS 03245+3002	17.28	4.40	–	–	–	–
L1455 SMM1	15.10	8.29	–	–	–	–
IRAS 03301+3111	0.24	5.93	–	–	–	–
B1-c	11.93	4.04	–	–	–	–
IRAS 03439+3233	0.31	3.10	–	–	–	–
IRAS 03445+3242	0.47	2.09	–	–	–	–
DG Tau B	0.47	2.05	–	–	–	–
IRAS 12553-7651	0.61	2.04	–	–	–	–
Elias 29	0.28	0.93	–	–	–	–
CRBR 2422.8−342	0.52	1.23	–	–	–	–
HH 100 IRS	0.46	1.89	–	–	–	–
CrA IRS7 A	0.97	0.89	–	–	–	–
CrA IRAS32	5.44	10.35	–	–	–	–
IRAS 23238+7401	1.60	1.24	–	–	–	–

Note. — Sources in bold were used as templates. Uncertainties quoted in parenthesis are statistical errors from the Gaussian fits while absolute errors are up to a factor of 2.

[a] Derived using a band strength of 1.3×10^{-17} cm molecule^{-1}.

[b] Using the H_2O ice column densities listed in Paper I.

[c] Values are likely upper limits (see §3.4.2 for details).

[*] Sources with $\tau_{9.7\mu m} > 2 \times \tau_{9.0\mu m}$, for which an estimated contribution from the CH_3-rock mode of CH_3OH was subtracted (see text for details).

The inferred NH_3 ice abundances range from $\lesssim$ 1% to 15% with respect to H_2O ice, excluding the abnormally high value of EC 82. When considering all values (except that of EC 82) determined with the local continuum method, this relative abundance is centered on 5.3% with a standard deviation of 2.0%. If we use values determined with the template method whenever available, we find a mean of 7.0±3.2%. Either way, within the errors, this is similar to what was obtained by Öberg et al. [2008] for CH_4 (4.7±1.6%), another ice component that should form via hydrogenation. For 6 out of the 8 sources where both NH_3 and CH_4 are detected, the NH_3-to-CH_4 ratio is slightly larger than 1 (~1.2). Based on elemental abundance ratios, one would expect NH_3/CH_4 smaller than 1, but since two thirds of the carbon is in refractory grains and some fraction of the gaseous CO locked up in CO at the ice formation threshold, NH_3-to-CH_4 ratios larger than 1 are consistent with both NH_3 and CH_4 being formed by hydrogenation of N and C, respectively.

Here, we only report values for the Gaussian parameters and derived column densities in the appendix (see Table 3.5), to show that the numbers we obtain in this independent study are consistent with those reported in Paper I. Our recommended abundances are those from paper I, based on the combined 9.75 and 3.53 μm analysis. The inferred CH_3OH abundances range from < 1% to > 25% with respect to H_2O ice, indicating significant CH_3OH/NH_3 abundance variations from source-to-source. Such relative abundance variations can already be clearly seen from the changing relative depths of the 9.0 and 9.7 μm features (see also Paper I). Thus, NH_3 and CH_3OH ice are likely formed through different formation pathways and/or in different ice environments.

3.3 Laboratory work and analysis

The band profiles presented in Fig. 3.2 contain information on the ice environment in which NH_3 and CH_3OH are located, and thus their formation and processing history. To extract this information, a systematic laboratory study of the NH_3 and CH_3OH features in a variety of ices has been carried out. Specifically, three features between 8 and 10 μm have been analyzed:

1. the NH_3 ν_2 umbrella mode, at ~9.35 μm or 1070 cm^{-1} in pure NH_3 ice, and with band strength $A_{\rm pure}$ =1.7×10^{-17} cm molecule^{-1} [D'Hendecourt & Allamandola 1986],

2. the CH_3OH ν_4 CO– stretching mode, at ~9.74 μm or 1027 cm^{-1} in pure CH_3OH ice, and with $A_{\rm pure}$ = 1.8×10^{-17} cm molecule^{-1} [D'Hendecourt & Allamandola 1986],

3. the CH_3OH ν_7 CH_3 rocking mode, at ~8.87 μm or 1128 cm^{-1} in pure CH_3OH ice, and with $A_{\rm pure}$ = 1.8×10^{-18} cm molecule^{-1} [Hudgins et al. 1993].

It should be noted that, as mentioned in the above list, the quoted positions are for pure ices only and therefore slightly deviate from the astronomical values given in Table 3.1.

This laboratory study targeted pure, binary and tertiary interstellar ice analogs consisting of different mixtures of H_2O, NH_3, CH_3OH, CO and CO_2, the major ice components. All measurements were performed under high vacuum conditions ($\sim 10^{-7}$ mbar) using an experimental approach described in Gerakines et al. [1995], Chapter 2 of this thesis, and Öberg et al. [2007a]. The ice spectra were recorded in transmission using a Fourier transform infrared spectrometer covering 25–2.5 μm (400–4000 cm^{-1}) with 1 cm^{-1} resolution and by sampling relatively thick ices, typically several thousands monolayers (ML)[1] thick. These ices were grown at a speed of $\sim 10^{16}$ molecules cm^{-2} s^{-1} (10 MLs^{-1} on a temperature-controlled CsI window.

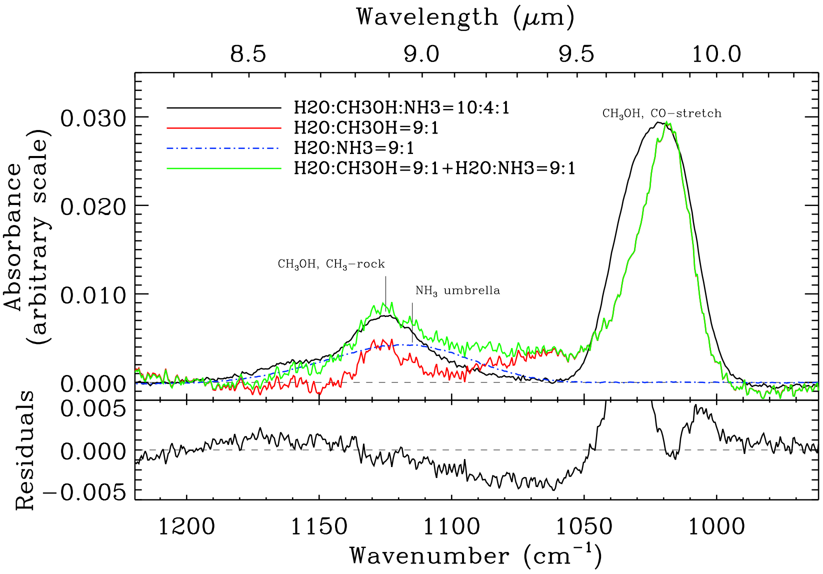

Figure 3.5 Example of a reduced laboratory spectrum (solid black line) for a $H_2O:CH_3OH:NH_3$= 10:4:1 ice mixture at 15 K, in the 8–10 μm / 960–1220 cm^{-1} range. This spectrum can be approximated as the sum (solid green/dark grey line) of $H_2O:CH_3OH$=9:1 (solid red/light grey line) and $H_2O:NH_3$=9:1 (dash-dot blue/grey line). The bottom plot is the difference between the two, showing that the feature at 9 μm (blend of NH_3 and CH_3OH CH_3-rock modes) is well reproduced by the sum of the two individual signatures. This figure also illustrates the fact that the positions of the features in mixed ices differ from that in pure ices (see list at the beginning of this section).

A typical reduced spectrum for an ice mixture containing $H_2O:CH_3OH:NH_3$= 10:4:1 at 15 K is shown in Fig. 3.5. Since band profiles and strengths change with ice composition and also with temperature, the three fundamentals mentioned above were investigated as a function of temperature ranging from 15 to 140 K with regular temperature steps for

---

[1] One ML corresponds to the layer thickness resulting from an exposure for 1 second at a pressure of 10^{-6} torr assuming a sticking probability of one. One ML is equivalent to about 10^{15} molecules cm^{-2}.

a number of binary and tertiary mixtures (listed in Appendix 3.6). An IDL routine was used to determine the location of the band maximum, FWHM and integrated absorbance of the individual absorption bands. For the asymmetric NH_3 ν_2 umbrella mode the band position has been determined by the maximum absorbance and for the symmetric profiles the spectral parameters have been determined from Gaussian fits of baseline subtracted spectra. The resulting absolute frequency uncertainty is of the order of 1 cm^{-1}. The measurements are presented in Table 3.6 of Appendix B, and are included in the Leiden laboratory database[2].

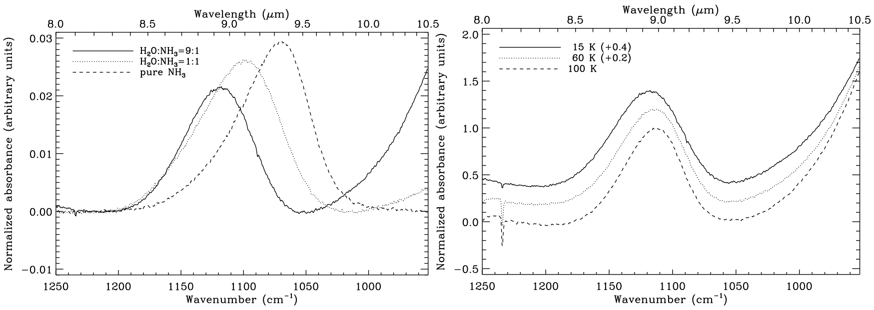

Figure 3.6 (*Left*) FTIR ice spectra of the ν_{NH3} mode for pure NH_3, a H_2O:NH_3=1:1 and a H_2O:NH_3=9:1 mixture at a temperature of 15 K. At the low frequency side of the spectrum the H_2O libration mode (centered around 770 cm^{-1}, or 13 μm) starts showing up for the H_2O-containing mixtures. — (*Right*) Temperature effect on a H_2O:NH_3=9:1 mixture: decreasing FWHM with increasing temperature.

NH_3 and CH_3OH both have the ability to form hydrogen bonds in water-rich matrices, so it is not surprising that the band profile changes compared with pure ices because of the various molecular interactions [e.g., D'Hendecourt & Allamandola 1986]. In addition to profiles, band strengths can change with environment and with temperature, as discussed for the cases of CO and CO_2 in water-rich ices in Kerkhof et al. [1999], Öberg et al. [2007a], and Chapter 2 of this thesis. Figure 3.6 shows how the NH_3 ν_2 umbrella mode absorption maximum shifts from 1070 cm^{-1} (9.35 μm) for pure NH_3 ice to 1118 cm^{-1} (8.94 μm) for an astronomically more realistic H_2O:NH_3=9:1 (hereafter 9:1) mixture, for which the FWHM and integrated band strength also change significantly. For example, the band strength is lowered in the 9:1 mixture to 70% of its initial value in pure NH_3 ice. This is in good agreement with previous experiments performed by Kerkhof et al. [1999]. The spectral appearance also depends on temperature; for the 9:1 mixture a temperature increase from 15 to 120 K results in a redshift of the peak position from 1118 to 1112 cm^{-1} (8.94 to 8.99 μm) and the FWHM decreases from 62 to 52 cm^{-1} (0.50 to 0.42 μm) (see Fig. 3.7). The NH_3 band strength, on the other hand, does not show any temperature dependence.

---

[2] `http://www.strw.leidenuniv.nl/~lab/`

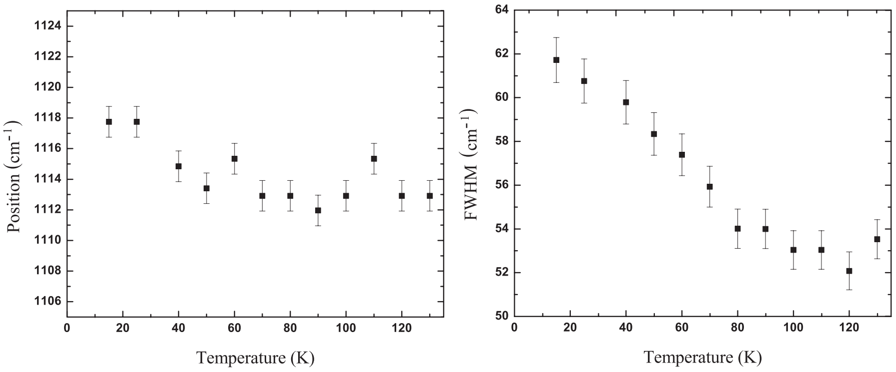

Figure 3.7 A plot indicating the changes in peak position (left) and FWHM (right) of the NH_3 ν_2 umbrella mode as a function of temperature in a 9:1 H_2O:NH_3 ice.

If NH_3 is in a water-poor environment with CO and/or CO_2, the ν_2 peak position shifts to the red compared with pure NH_3, to as much as 1062 cm^{-1} (9.41 μm). The FWHM is not much affected whereas the band strength is lowered by 20%. Because of the intrinsically large difference in band maximum position between NH_3 in a water-poor and water-rich environment, the astronomical observations can distinguish between these two scenarios.

Methanol-containing ices have been studied in a similar way (see Fig. 3.8). The weakly absorbing ν_7 CH_3 rocking mode at ~1125 cm^{-1} (8.89 μm) is rather insensitive

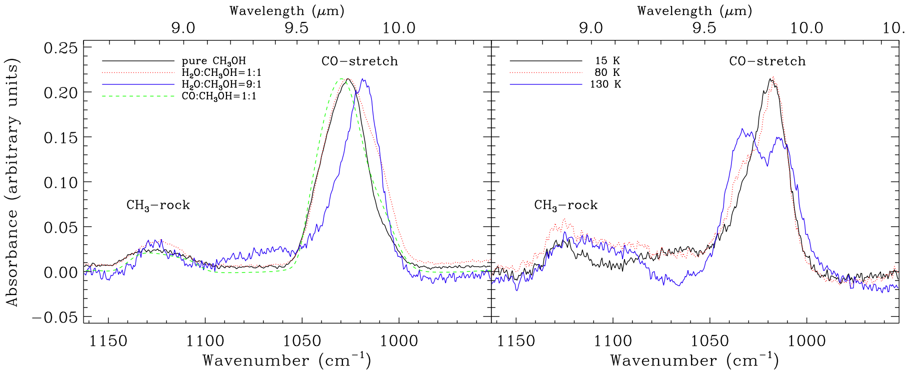

Figure 3.8 (*Left*) Spectra of the CH_3OH ν_{CO} modes and ν_{CH3} modes for pure CH_3OH, a H_2O:CH_3OH=1:1, a H_2O:CH_3OH=9:1 and a CO:CH_3OH=1:1 ice mixture at a temperature of 15 K. — (*Right*) Temperature effect on the CO-stretch mode of a H_2O:CH_3OH=9:1 mixture.

to H_2O mixing, but the ν_4 CO stretch vibration shifts to the red from 1028 to 1020 cm^{-1} (9.73 to 9.80 μm) when changing from a pure CH_3OH ice to a H_2O:CH_3OH=9:1 mixture. In the latter spectrum the CH_3OH ν_4 CO stretch mode needs to be fitted with a double Gaussians. A substructure appears for a temperature of 80 K (right panel of Fig. 3.8) while for even higher temperatures, a clearly double peaked structure becomes visible (as previously seen in e.g. Fig. 2 of Schutte et al. 1991). This splitting hints at different physical sites and has been previously ascribed to type II clathrate formation in the ice [Blake et al. 1991].

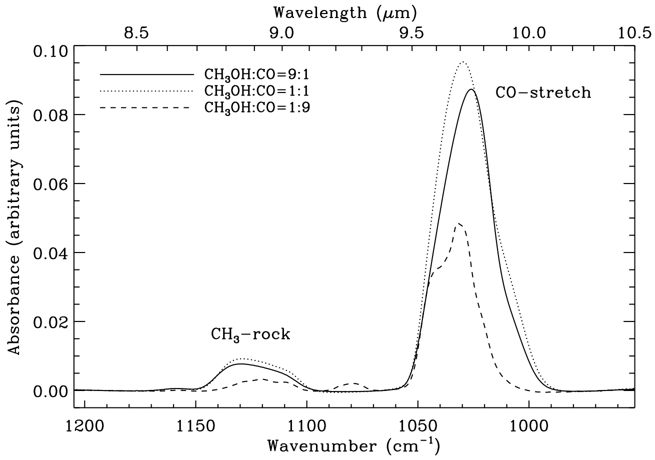

Figure 3.9 Spectra of CH_3OH:CO mixtures in the range of the methanol CO stretch mode and the methanol CH_3 rock mode. A small blue shift together with a clear substructure are seen upon mixing in more CO.

When CH_3OH is mixed with CO, the band maximum shifts from 1028 to 1034 cm^{-1} (9.73 to 9.67 μm) when going from a 9:1 to a 1:9 CH_3OH:CO mixture. When 50% or more CO is mixed in, the CH_3OH ν_4 CO stretch mode starts to show a shoulder and cannot be fitted correctly by a single Gaussian component (see Fig. 3.9). Such a two-component profile would not be recognized, however, at the spectral resolution and signal/noise of our *Spitzer* data, so for the comparison between laboratory and observational data a single Gaussian is used. Overall, the shifts of the CH_3OH ν_4 mode between water-rich and CO-rich mixtures are much smaller than in the case of the NH_3 ν_2 mode.

The effect of CH_3OH on the 4.7μm ν_1 stretch mode of CO has also been investigated. The band maximum shifts from 2139 cm^{-1} (4.68 μm) for the nearly pure 9:1 CO:CH_3OH mixture to 2136 and 2135 cm^{-1} for the 1:1 and 1:9 mixtures, respectively. The CO band located at 2136 cm^{-1} is often referred to as CO residing in a polar, mainly H_2O ice, environment. Clearly, the polar CH_3OH molecules can also contribute to CO absorption at 2136 cm^{-1} when intimately mixed in an astronomical ice.

Binary mixtures of NH_3 and CH_3OH have been studied as well. The CH_3OH modes behave very much as they do in a pure methanol ice, but the NH_3 ν_2 umbrella mode is clearly suppressed. Its integrated absorbance is readily reduced to 70% of the integrated absorbance of pure NH_3 in a CH_3OH:NH_3=1:1 mixture and becomes even lower for a 4:1 binary composition. The NH_3 band also broadens compared to pure NH_3 or H_2O:NH_3 mixtures and strongly overlaps with the CO stretching mode of CH_3OH, to the level that it becomes difficult to measure.

A qualitative comparison with the astronomical data (see §3.4) indicates that neither pure NH_3, CH_3OH, nor mixed CH_3OH:NH_3 or H_2O-diluted binary ices can simultaneously explain the different NH_3 profiles in the recorded *Spitzer* spectra. Thus, a series of tertiary mixtures with H_2O:CH_3OH:NH_3 in ratios 10:4:1, 10:1:1 and 10:0.25:1 have been measured, because CH_3OH is the next major ice component. These ratios roughly span the range of observed interstellar column density ratios. In Fig. 3.10, the spectra of H_2O:CH_3OH:NH_3 tertiary mixtures are plotted and compared to binary H_2O:CH_3OH and H_2O:NH_3 data. The NH_3 ν_2 umbrella mode shifts slightly to the blue in the presence of both H_2O and CH_3OH, with an absorption maximum at 1125 cm^{-1} (8.90 μm) for the 10:4:1 H_2O:CH_3OH:NH_3 mixture (compared to 1118 cm^{-1} (8.94 μm) in the H_2O:NH_3=9:1 mixture). The peak intensity of the NH_3 ν_2 umbrella mode band in this tertiary mixture is small compared with that of the CH_3OH CH_3 rock mode, but its integrated intensity is a factor of two larger because of the larger NH_3 width.

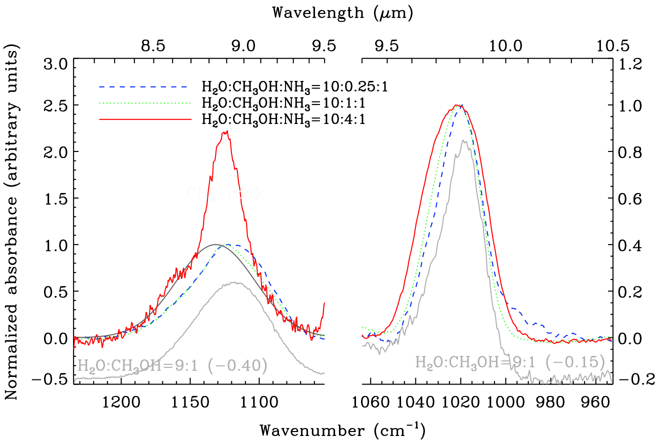

Figure 3.10 Normalized spectra of the CH_3OH ν_4 C–O mode (right panel), and NH_3 ν_2 umbrella mode (left panel) for a H_2O:CH_3OH:NH_3=10:0.25:1, a H_2O:CH_3OH:NH_3=10:1:1 and a H_2O:CH_3OH:NH_3=10:4:1 mixture at a temperature of 15 K. These mixture ratios span the range of observed interstellar column density ratios. Spectra were normalized to better show the changes in band maximum position and FWHM of each feature. Spectra of a H_2O:CH_3OH=9:1 and a H_2O:NH_3=1:1 mixture were offset and overlaid in light grey in the right and left panel, respectively. In the case of H_2O:CH_3OH:NH_3=10:4:1, the NH_3 ν_2 umbrella mode is heavily blended with the CH_3OH ν_7 CH_3 rocking mode, so that the dark grey line actually shows the Gaussian fit to the underlying NH_3 feature, whereas the full 9 μm feature is shown in black.

The ν_4 C–O stretching vibration profile of CH_3OH in the tertiary mixture does not differ much from the binary values for the highest water content. The position of the absorption maximum is also only marginally affected by the temperature. The FWHM decreases from 30 cm^{-1} (0.29 μm) for the 10:4:1 mixture to 22 cm^{-1} (0.21 μm) for the 10:0.25:1 mixture.

Besides H_2O, other species may also be regarded as potential candidates for changing the spectral appearance of the NH_3 and/or CH_3OH features. Chemically linked is HCOOH [Bisschop et al. 2007a] which unfortunately cannot be deposited in the present setup because of its reactive behavior when mixed with NH_3. Tertiary mixtures with CO and CO_2, two other important constituents in interstellar ices, have been measured (see Appendix 3.6) but here the differences are small compared with the observed binary water-rich or CO-rich mixtures, and do not offer an alternative explanation.

3.4 Comparison between astronomical and laboratory data

3.4.1 8–10 μm range

The FWHM and band positions of the NH_3 and CH_3OH features measured in the laboratory and astronomical spectra are shown in Figs. 3.11 (for NH_3) and 3.12 (for CH_3OH). For the YSOs, the values obtained after removal of the silicate absorption (see §3.2) using the local continuum method are indicated by filled squares, whereas those obtained from the template method are plotted with open squares. Note that the presence of significant amounts of CH_3OH may artificially lower the inferred NH_3 ν_2 width in CH_3OH rich sources (indicated with * in Table 3.2) because of the contribution of the narrower ν_7 CH_3-rock mode.

Regardless of the method used to subtract the continuum, or the type of source (CH_3OH-rich/poor), we find that the observational band positions of the ν_2 NH_3 umbrella mode absorptions vary, within the errors, between 8.9 and 9.1 μm. This position is not well reproduced by any of the investigated mixtures, but the positions measured in water-rich ice mixtures are the closest, whereas the positions in pure NH_3 or CO/CO_2 rich ices are too far away to be representative of the astronomical positions. The derived *Spitzer* FWHM values range between 0.23 and 0.32 μm (except for B1-b : 0.39 μm), when using the local continuum method, not depending on whether the target is CH_3OH-rich or -poor. For the template method, CH_3OH-rich sources generally tend to have a narrower inferred FWHM, 0.3–0.5 μm, contrary to what would be expected if the NH_3 mode is contaminated by the CH_3-rock feature. In any case, most of these widths are still narrower than the laboratory FWHM values. To investigate further the effect of the continuum on the positions and widths of the bands, we performed the following calculation to check whether a continuum could be found that would yield NH_3 and CH_3OH features with parameters within the laboratory measurements. To do that, we fitted the data between 8.25 and 10.4 μm with a function that is the sum of a 4th order polynomial and two Gaussians;

positions and widths of the Gaussians were constrained with limits taken from the laboratory data of binary water mixtures (8.9–8.95 μm for the NH_3 position, 0.42–0.52 μm for its width; 9.67–9.77 μm for the CH_3OH position, 0.2–0.3 μm for its width). We found that the continuum derived in this way is different from those determined via the other two methods. This result supports the fact that the difference between astronomical and laboratory data could be attributed to the uncertainty in the continuum determination.

Taking the above considerations into account, Figs. 3.11 and 3.12 suggest that the template method for subtraction of the 10 μm silicate absorption is more consistent with the laboratory measurements, but both methods probably miss some weak NH_3 absorption features in the broad line wings where they blend with the continuum at the S/N of the data. If so, the too small line widths inferred from the data (most probably due to the uncertainty in the continuum determination) would mean that we have underestimated NH_3 abundances by a up to a factor of 2.

The observational band position and FWHM of the CH_3OH features derived with either the local continuum or template method are clustered around 9.7–9.75 μm, with the exception of R CrA IRS 5 at 9.66 μm. Similarly the FWHM of the CH_3OH features are all very similar between ~0.22 and 0.32 μm, except for R CrA IRS 5 with 0.39 μm. These values agree (with a few exceptions) with the values obtained from the laboratory spectra. Note that the observed positions of the CH_3OH feature are all on the low side of the laboratory range. Since the position of this feature shifts to higher wavelengths with increasing water content, the observed low values could therefore indicate that CH_3OH and H_2O are not well mixed and that there exists a separate CH_3OH-rich component, as suggested in previous work [e.g. Pontoppidan et al. 2003a, Skinner et al. 1992]. Alternatively, the low values could be due to the presence of CO as indicated by the CH_3OH feature shift to 9.70 μm in CH_3OH:CO=1:1. Both interpretations would be consistent with the bulk of the CH_3OH formation coming from hydrogenation of a CO-rich layer, rather than photochemistry in a water-rich matrix. However, the shift from the water-rich mixtures is small, and some water-rich fraction cannot be excluded with the current spectral resolution.

3.4.2 The 3 and 6 μm ranges

Dartois & d'Hendecourt [2001] discussed the possibility of a 3.47 μm absorption band which could be related to the formation of an ammonia hydrate in the ice mantles: they found that if this band were mostly due to this hydrate, then ammonia abundances would be at most 5% with respect to water ice. Considering the fact that our derived abundances are larger than 10% in some sources, it is necessary to investigate the effect of such a high abundance on the ammonia features in other spectral ranges. For this, depending on the NH_3-to-CH_3OH abundance ratio observed in the *Spitzer* spectra, we scale one of the following laboratory spectra to the 9 μm NH_3 feature: H_2O:NH_3=9:1, H_2O:NH_3=4:1, H_2O:CH_3OH:NH_3=10:1:1, H_2O:CH_3OH:NH_3=10:4:1. Figure 3.13 illustrates the comparison between the *Spitzer* and scaled laboratory spectra for the relevant wavelength ranges for a couple of sources, while Figs. 3.14 and 3.15 (see Appendix 3.6) show the

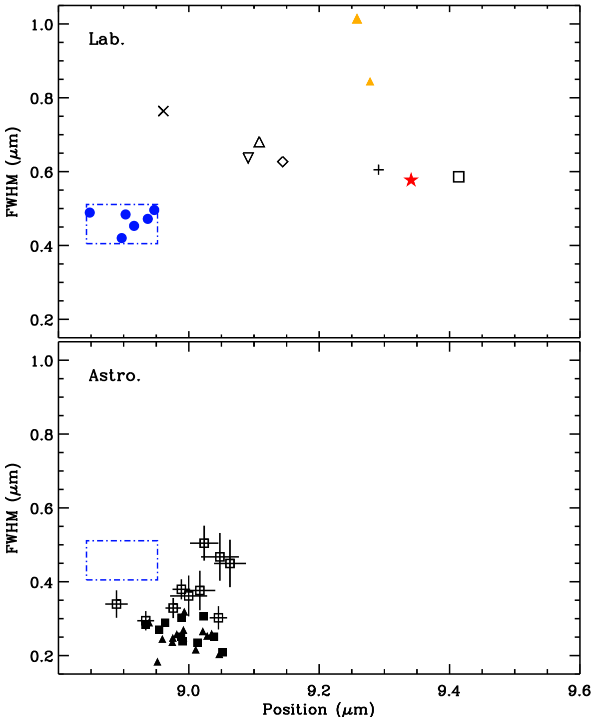

Figure 3.11 FWHM and band maximum position of the NH_3 feature measured in the laboratory mixtures at 15 K ("Lab.", top panel) and in the *Spitzer* spectra ("Astro.", bottom panel). In the top panel, the filled star indicates pure NH_3, filled circles represent H_2O-rich mixtures and filled triangles are for NH_3:CH_3OH mixtures (an increasing symbol size indicative of increasing CH_3OH content). Other symbols are as follows: + for NH_3:H_2O=1:0.11, ▽ for NH_3:H_2O=1:1, ◇ for NH_3:H_2O:CO=1:1:1, △ for NH_3:H_2O:CO_2=1:1:1, □ for NH_3:CO:CO_2=1:1:1, × for NH_3:CH_3OH:H_2O=1:1:1. In the bottom panel, open and filled squares indicate values obtained with the template and local continuum method, respectively. The dash-dot polygons delimitate the parameter space of FWHM and positions corresponding to H_2O-rich mixtures.

comparison for all sources where NH_3 was detected. For further comparison, in Appendix 3.6 we also overplotted in Figs. 3.14 and 3.15 the following spectra: (i) the pure H_2O ice spectrum derived from the H_2O column density quoted in Boogert et al. [2008] (deep blue); and (ii) for sources with 3 μm data, the pure H_2O spectrum scaled to the optical depth of the 3 μm feature of the mixed ice laboratory spectrum (purple-dotted). The difference between this scaled pure water spectrum and the mixed ice spectrum gives an indication of the contribution of ammonia features around 3.47 and 6.1 μm.

We then determined the contributions from the NH_3 features to the integrated optical depths of the 3 and 6 μm bands and to the optical depth of component C2, a feature at

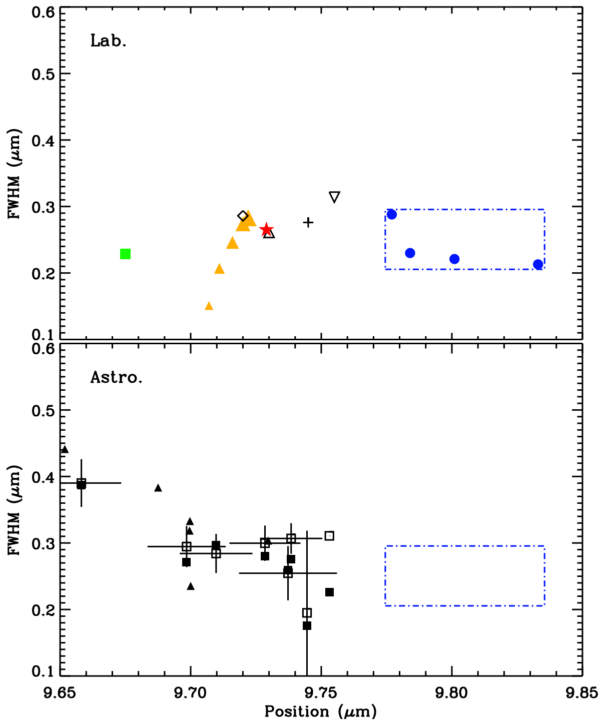

Figure 3.12 Same as Fig. 3.11 but for CH_3OH. In the top panel, the filled star is for pure CH_3OH, the filled square is representative of a CO-rich mixture. All other symbols (top and bottom panels) have the same meaning as in Fig. 3.11, except for the following in the top panel: + for NH_3:CH_3OH:H_2O=1:1:1, ▿ for CH_3OH:H_2O=1:1, ⋄ for CH_3OH:CO=1:1, ▵ for CH_3OH:CO=9:1.

6.0-6.4 μm arising from a blend of several species, including NH_3, H_2O, CO_2, $HCOO^-$ (see Paper I for more details). These contributions are reported in Tables 3.3 and 3.4.

Figures 3.14 and 3.15 (Appendix 3.6), and Tables 3.3 and 3.4 show that (i) the scaled laboratory spectra generally do not overestimate the observed absorption features, and (ii) for most sources, the presence of NH_3 at the level we determine from the 9 μm feature does not explain by itself the depth of the C2 component and of the red wing of the 3 μm band. Hence, our inferred NH_3 abundances up to 15% from the 9.7 μm data are not in conflict with the lack of other NH_3 features. The only exceptions are two sources (RNO 15 and EC 74), for which the scaled mixed ice spectrum exceeds the data in the 3 μm range. In the case of RNO 15, the NH_3 abundance could have been overestimated due to the contribution of the CH_3OH CH_3-rock feature at ~9 μm. For EC 74, this overestimate and the presence of emission weakens the identification of the NH_3 signature. In both cases, the quoted NH_3 abundances should be considered as upper limits.

Table 3.3. NH_3 contribution to the 3 and 6 μm bands for sources with a template

Source	$\frac{\int \tau_{H_2O,3.0}}{\int \tau_{3.0}}$	$\frac{\int \tau_{mix,3.0}}{\int \tau_{3.0}}$	$\frac{\int_{1562}^{1785} \tau_{H_2O}}{\int_{1562}^{1785} \tau}$	$\frac{\int_{1562}^{1785} \tau_{mix}}{\int_{1562}^{1785} \tau}$	$\frac{\int \tau_{NH_3,6.16}}{\int_{1562}^{1785} \tau_{H_2O}}$	$\frac{\tau_{NH_3,6.16}}{\tau_{C2}}$
IRAS 03235+3004	–	–	0.50	0.24	0.02	0.61
IRAS 03254+3050	0.73	1.30	0.56	0.92	0.12	1.72
IRAS 04108+2803	0.70	0.67	0.58	0.53	0.06	0.49
HH 300	0.70	0.57	0.50	0.39	0.05	0.45
IRAS 08242-5050	0.76	0.72	0.50	0.45	0.06	0.46
IRAS 08242-5050	0.76	0.56	0.50	0.35	0.05	0.36
2MASSJ17112317-272431	–	–	0.69	0.53	0.05	4.23
SVS 4-5	0.91	0.94	0.42	0.29	0.00	0.08
R CrA IRS 5	0.85	0.42	0.63	0.29	0.03	0.21

Note. — A dash indicates that the ratio was not calculated due to the high noise in the 3 μm spectrum.
Parameters are:
$\int \tau_{H_2O,3.0}$ = integrated optical depth of pure water at 3 μm, determined from the column density of paper I and a band strength of 2.0×10^{-16} cm^{-1}.
$\int \tau_{3.0}$, $\int \tau_{mix,3.0}$ = integrated optical depth over the entire 3 μm region for, respectively, the considered source and the corresponding laboratory mixture (selected from the NH_3 feature at 9 μm).
$\int_{1562}^{1785} \tau_{H_2O}$, $\int_{1562}^{1785} \tau$, $\int_{1562}^{1785} \tau_{mix}$ = integrated optical depth of, respectively, pure water, source spectrum, and laboratory mixture, between 1562 and 1785 cm^{-1} (5.6 to 6.4 μm).
$\int \tau_{NH_3,6.16}$, $\tau_{NH_3,6.16}$ = integrated and peak optical depth of the 6.16 μm feature of ammonia obtained after subtraction of a pure water spectrum scaled to the optical depth at 3 μm of the laboratory mixture.
τ_{C2} = peak optical depth of the C2 component from paper I.

Table 3.4. NH_3 contribution to the 3 and 6 μm bands for sources with no associated template

Source	$\frac{\int \tau_{H_2O,3.0}}{\int \tau_{3.0}}$	$\frac{\int \tau_{mix,3.0}}{\int \tau_{3.0}}$	$\frac{\int_{1562}^{1785} \tau_{H_2O}}{\int_{1562}^{1785} \tau}$	$\frac{\int_{1562}^{1785} \tau_{mix}}{\int_{1562}^{1785} \tau}$	$\frac{\int \tau_{NH_3,6.16}}{\int_{1562}^{1785} \tau_{H_2O}}$	$\frac{\tau_{NH_3,6.16}}{\tau_{C2}}$
RNO 15	0.80	1.97	0.53	1.23	0.16	0.45
IRAS 03271+3013	–	–	0.36	0.44	0.05	0.60
B1-a	–	–	0.67	0.43	0.03	0.57
L1489 IRS	0.78	0.88	0.60	0.56	0.04	0.83
RNO 91	0.94	0.94	0.53	0.45	0.04	0.53
IRAS 17081-2721	0.65	0.95	0.62	0.75	0.05	1.64
EC 74	0.95	2.34	0.57	1.18	0.09	0.76
EC 92	0.90	0.35	0.38	0.10	0.00	0.01
CrA IRS7 B	–	–	0.81	0.19	0.00	0.08
L1014 IRS	–	–	0.62	0.55	0.06	0.34

Note. — A dash indicates that the ratio was not calculated due to the high noise in the 3 μm spectrum.
Parameters are:
$\int \tau_{H_2O,3.0}$ = integrated optical depth of pure water at 3 μm, determined from the column density of paper I and a band strength of 2.0×10^{-16} cm^{-1}.
$\int \tau_{3.0}$, $\int \tau_{mix,3.0}$ = integrated optical depth over the entire 3 μm region for, respectively, the considered source and the corresponding laboratory mixture (selected from the NH_3 feature at 9 μm).
$\int_{1562}^{1785} \tau_{H_2O}$, $\int_{1562}^{1785} \tau$, $\int_{1562}^{1785} \tau_{mix}$ = integrated optical depth of, respectively, pure water, source spectrum, and laboratory mixture, between 1562 and 1785 cm^{-1} (5.6 to 6.4 μm).
$\int \tau_{NH_3,6.16}$, $\tau_{NH_3,6.16}$ = integrated and peak optical depth of the 6.16 μm feature of ammonia obtained after subtraction of a pure water spectrum scaled to the optical depth at 3 μm of the laboratory mixture.
τ_{C2} = peak optical depth of the C2 component from paper I.

Overall, our reported NH_3 abundances are up to a factor of three larger than the upper limits derived by Dartois & d'Hendecourt [2001]. Firstly, let's recall that the conclusions in their study and in ours are drawn from the analysis of different samples. Secondly, Dartois & d'Hendecourt made an assumption that does not apply to our sample: indeed, they considered a grain size distribution including also scattering from larger grains, producing an enhanced 3 μm wing, whereas the results presented here can be taken as representative of NH_3 absorption from small grains. It is beyond the scope of this paper to investigate the effects of grain size distribution and scattering in as much detail as did Dartois & d'Hendecourt [2001].

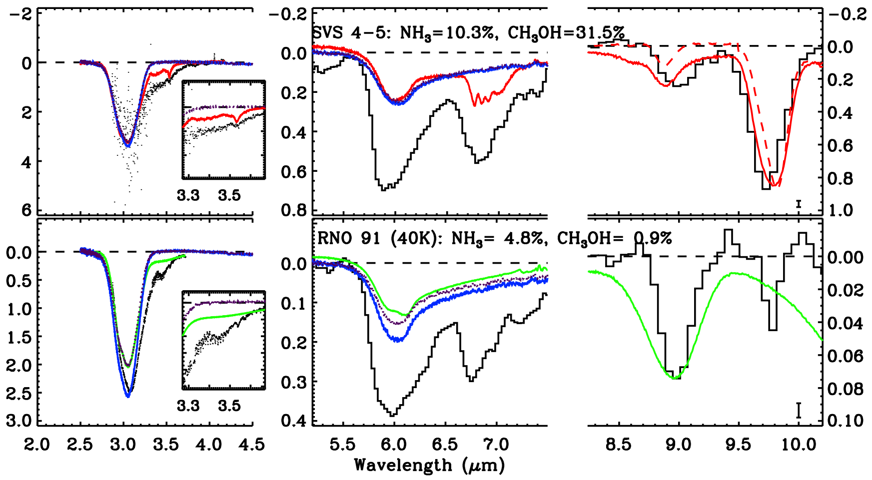

Figure 3.13 Comparison of astronomical data (VLT or Keck measurements at short wavelengths, IRS *Spitzer* observations elsewhere) and laboratory spectra in selected wavelength ranges: 2.0–4.5 μm (left panels), 5.2–7.5 μm (middle panels) and 8.2–10.2 μm (right panels, silicate absorption subtracted via the template method). Error bars are indicated in the bottom-right corner. Overlaid in red and green are laboratory spectra corresponding to $H_2O:CH_3OH:NH_3=10:4:1$ and $H_2O:NH_3=9:1$, respectively, scaled to the 9 μm NH_3 umbrella mode. The dark blue line represents the pure water laboratory spectrum scaled to the water column density taken in paper I. The dotted purple line corresponds to a pure water spectrum scaled to the 3 μm water feature of the mixed ice spectrum, showing the contribution of NH_3 features around 3.47 and 6.1 μm. Finally, the red dashed line in the right panel of SVS 4-5 represents a $H_2O:CH_3OH=9:1$ laboratory spectrum scaled to the 9.7 μm CH_3OH CO-stretch mode: this gives an indication of the contribution of the 9 μm CH_3OH CH_3-rock mode to the total 9 μm feature. The laboratory spectra are recorded at 15 K unless indicated differently.

3.4.3 Nitrogen ice inventory

The confirmation of the presence of relatively large amounts of solid NH_3, up to 15%, in interstellar ices solves a long-standing problem. Indeed, the detection of solid NH_3 has remained elusive and/or controversial, despite a number of clues suggesting its presence:

- High cosmic abundance of atomic nitrogen : $N_{\rm N}/N_{\rm H} = 7.76 \times 10^{-5}$ [Savage & Sembach 1996], only a factor of a few below those of oxygen and carbon. Here N_H indicates the total number of hydrogen nuclei, N_H=N(H)+2N(H_2).
- High abundances of gaseous NH_3 of $N_{\rm NH_3}/N_{\rm H_2} \sim 10^{-6} - 10^{-5}$ in the Orion-KL nebula [Barrett et al. 1977, Genzel et al. 1982] and in other hot cores such as G9.62+0.19, G29.96−0.02, G31.41+0.31 [Cesaroni et al. 1994], and G10.47+0.03 [Cesaroni et al. 1994, Osorio et al. 2009].
- Identification of substantial amounts of OCN^- [e.g. van Broekhuizen et al. 2004, 2005] and NH_4^+ in ices [e.g. Schutte & Khanna 2003, Boogert et al. 2008]: considering that these ions form via reactions involving NH_3, the non-detection of solid NH_3 would be puzzling.

Our results can be used to draw up a possible nitrogen budget. Assuming $N_{\rm H_2O}/N_{\rm H} \sim 5{\times}10^{-5}$ [Pontoppidan et al. 2004, Boogert et al. 2004], and average abundances w.r.t. H_2O of 5.5% for NH_3 (see §3.2.3), 7% for NH_4^+ (from Table 3 of Paper I), and 0.6% for OCN^- [van Broekhuizen et al. 2005], then the NH_3, NH_4^+ and OCN^- abundances with respect to total H are 2.8, 3.5, and 0.3 $\times 10^{-6}$ respectively. This corresponds to, respectively, 3.4, 4.4 and 0.4% of the atomic nitrogen cosmic abundance so that, in total, about 10% of the cosmically available nitrogen would be locked up in ices, leaving solid and gaseous N_2, N and HCN as other substantial nitrogen carriers. The main uncertainty in this determination is the adopted H_2O ice abundance with respect to total H; in several sources this may well be a factor of 2 larger, leading to about 20% of the nitrogen accounted for in ices.

3.5 Conclusion

We have analyzed in detail the 8-10 μm range of the spectra of 41 low-mass YSOs obtained with *Spitzer* and presented in Boogert et al. [2008]. The sources are categorized into three types: straight, curved and rising 8 μm silicate wings, and for each category template sources with little or no absorption from ices around 9–10 μm have been determined. This has led to two ways of subtracting the contribution from the 10 μm silicate absorption: first, by determining a local continuum, and second, by scaling the templates to the optical depth at 9.7 μm. The two methods give consistent band positions of the NH_3 features, but the resulting widths can be up to a factor of two larger using the template continuum method. Taking into account the uncertainty in continuum determination, NH_3 ice is most likely detected in 24 of the 41 sources with abundances of ~2 to 15% w.r.t. H_2O, with an average abundance of 5.5±2.0%. These abundances have estimated uncertainties up to a factor of two and are not inconsistent with other features in the 3 and 6 μm ranges. CH_3OH is often detected as well, but the NH_3/CH_3OH abundance ratio changes strongly from source to source. Our inferred CH_3OH column densities are consistent with the values derived in paper I.

Targeted laboratory experiments have been carried out to characterize the NH_3 and CH_3OH profiles (position, FWHM, integrated absorbance). Comparison with the observational data shows reasonable agreement (within ~1%) for the position of the NH_3 feature in H_2O-rich ices, but the observed widths are systematically smaller than the laboratory ones for nearly all sources. The silicate template continuum method gives widths that come closest to the laboratory values. This difference in width (i.e. widths derived from astronomical spectra smaller than those in the laboratory spectra) suggests that the NH_3 abundances determined here may be on the low side.

The CH_3OH profile is most consistent with a significant fraction of the CH_3OH in a relatively pure or CO-rich phase, consistent with its formation by the hydrogenation of CO ice. In contrast, the most likely formation route of NH_3 ice remains hydrogenation of atomic N together with water ice formation in a relatively low density molecular phase. Finally, the nitrogen budget indicates that up to 10 to 20% of nitrogen is locked up in known ices.

3.6 Appendix

Parameters of Gaussian fits

Table 3.5. (a) Parameters of Gaussian fits to the NH_3 feature.

Source	NH_3, local			NH_3, template		
	λ (μm)	FWHM (μm)	$\tau_{\rm peak}$	λ (μm)	FWHM (μm)	$\tau_{\rm peak}$
IRAS 03235+3004	8.93±0.02	0.28±0.03	0.23±0.02	8.93±0.01	0.29±0.03	0.30±0.02
L1455 IRS3	8.99±0.03	0.24±0.07	0.02±0.01	9.02±0.02	0.38±0.05	0.04±0.01
IRAS 03254+3050	9.04±0.01	0.25±0.03	0.10±0.01	8.99±0.01	0.38±0.03	0.12±0.01
B1-b*	9.05±0.03	0.39±0.06	0.25±0.02	9.07±0.03	0.40±0.06	0.31±0.03
IRAS 04108+2803	8.99±0.02	0.25±0.04	0.05±0.01	9.05±0.03	0.47±0.06	0.04±0.01
HH 300	9.01±0.02	0.23±0.05	0.04±0.01	9.06±0.02	0.45±0.06	0.05±0.01
IRAS 08242-5050	9.02±0.01	0.31±0.03	0.15±0.01	9.05±0.01	0.30±0.03	0.15±0.01
IRAS 15398-3359	8.96±0.01	0.29±0.03	0.30±0.02	8.98±0.01	0.33±0.03	0.41±0.02
B59 YSO5	8.95±0.01	0.27±0.03	0.18±0.02	8.89±0.02	0.34±0.04	0.18±0.02
2MASSJ17112317-272431	8.99±0.01	0.30±0.02	0.43±0.02	9.02±0.02	0.50±0.05	0.41±0.04
SVS 4-5*	9.00±0.01	0.26±0.03	0.16±0.02	9.01±0.01	0.30±0.03	0.26±0.02
R CrA IRS 5	9.05±0.02	0.21±0.04	0.04±0.01	9.00±0.03	0.36±0.06	0.04±0.01

Table 3.5. (a) Cont'd

Source	NH_3, local			NH_3, template		
	λ (μm)	FWHM (μm)	τ_{peak}	λ (μm)	FWHM (μm)	τ_{peak}
RNO 15	9.05±0.02	0.20±0.04	0.04±0.01	–	–	–
IRAS 03271+3013	8.96±0.02	0.25±0.04	0.20±0.02	–	–	–
B1-a	8.98±0.02	0.25±0.04	0.14±0.02	–	–	–
L1489 IRS	9.02±0.01	0.27±0.03	0.09±0.01	–	–	–
IRAS 13546-3941	8.99±0.02	0.27±0.03	0.03±0.00	–	–	–
RNO 91	8.98±0.01	0.26±0.03	0.08±0.01	–	–	–
IRAS 17081-2721	8.97±0.02	0.24±0.04	0.04±0.00	–	–	–
EC 74	9.01±0.02	0.22±0.05	0.05±0.01	–	–	–
EC 82	8.94±0.01	0.29±0.03	0.04±0.00	–	–	–
EC 90	8.95±0.02	0.18±0.05	0.04±0.01	–	–	–
EC 92*	8.99±0.02	0.25±0.05	0.03±0.00	–	–	–
CK4	8.99±0.02	0.32±0.04	0.03±0.00	–	–	–
CrA IRS7 B*	9.04±0.01	0.26±0.03	0.15±0.01	–	–	–
L1014 IRS	9.03±0.02	0.25±0.05	0.15±0.02	–	–	–

Note. — Uncertainties are statistical errors from the Gaussian fits.

*Sources with $\tau_{9.7\mu m} > 2 \times \tau_{9.0\mu m}$, for which the contribution from the CH_3OH CH_3-rock mode is significant. Since the latter and the NH_3 umbrella mode were difficult to disentangle, a single fit was performed (the reported parameters) and the integrated optical depth of the ammonia feature was then obtained from the total integrated optical depth at 9 μmby subtracting the estimated contribution of the CH_3OH CH_3-rock mode (see §3.2.2).

Table 3.5. (b) Parameters of Gaussian fits to the CH_3OH C-O stretch mode (after subtraction of the continuum with the local and/or template method), and CH_3OH column densities (or 3-σ upper limits).

Source	Local continuum				Template continuum				Paper I
	λ (μm)	FWHM (μm)	$\tau_{\rm peak}$	X (% H_2O)	λ (μm)	FWHM (μm)	$\tau_{\rm peak}$	X (% H_2O)	X (% H_2O)
IRAS 03235+3004	9.74±0.02	0.26±0.03	0.35±0.04	4.40±1.04	9.74±0.02	0.25±0.04	0.31±0.04	3.84±0.99	4.20±1.20
L1455 IRS3	9.78±0.01	0.14±0.03	0.03±0.01	3.67±1.80	9.78±0.02	0.26±0.04	0.04±0.01	7.71±3.46	<12.5
IRAS 03254+3050	···	···	···	< 5.4	···	···	···	< 5.4	< 4.6
B1-b	9.71±0.01	0.30±0.03	1.19±0.11	14.15±3.16	9.71±0.01	0.28±0.03	1.21±0.11	13.75±3.12	11.20±0.70
IRAS 04108+2803	···	···	···	< 2.7	9.75±0.00	0.06±0.04	0.04±0.03	0.58±0.62	< 3.5
HH 300	···	···	···	< 4.7	9.74±0.00	0.19±0.12	0.01±0.01	0.78±0.52	< 6.7
IRAS 08242-5050	9.70±0.01	0.27±0.03	0.25±0.02	6.12±1.01	9.70±0.01	0.29±0.03	0.24±0.02	6.39±1.09	5.50±0.30
IRAS 15398-3359	9.73±0.01	0.28±0.03	0.77±0.06	10.26±3.02	9.73±0.01	0.30±0.03	0.75±0.06	10.69±3.14	10.30±0.80
B59 YSO5	···	···	···	< 1.2	···	···	···	< 1.2	< 1.3
2MASSJ17112317-272431	9.75±0.02	0.23±0.04	0.13±0.02	1.03±0.22	···	···	···	< 2.0	< 3.2
SVS 4-5	9.74±0.01	0.28±0.03	0.77±0.06	26.38±6.17	9.74±0.01	0.31±0.02	0.83±0.06	31.50±7.12	25.20±3.50
R CrA IRS 5	9.66±0.01	0.39±0.03	0.07±0.00	5.68±0.60	9.66±0.02	0.39±0.04	0.07±0.00	5.51±0.72	6.60±1.60

Table 3.5. (b) Cont'd.

Source	Local continuum				Template continuum				Paper I
	λ (μm)	FWHM (μm)	$\tau_{\rm peak}$	X (% H_2O)	λ (μm)	FWHM (μm)	$\tau_{\rm peak}$	X (% H_2O)	X (% H_2O)
RNO 15	9.65±0.03	0.44±0.07	0.02±0.00	11.13±2.16	···	···	···	···	< 5.0
IRAS 03271+3013	···	···	···	< 4.3	···	···	···	···	< 5.6
B1-a	···	···	···	< 2.4	···	···	···	···	< 1.9
L1489 IRS	9.78±0.02	0.10±0.03	0.03±0.01	0.44±0.22	···	···	···	···	4.90±1.50
IRAS 13546-3941	···	···	···	< 2.0	···	···	···	···	< 3.9
RNO 91	9.77±0.01	0.11±0.03	0.05±0.01	0.87±0.32	···	···	···	···	< 5.6
IRAS 17081-2721	···	···	···	< 6.6	···	···	···	···	3.30±0.80
EC 74	···	···	···	<13.5	···	···	···	···	< 9.3
EC 82	···	···	···	<24.6	···	···	···	···	<14.2
EC 90	9.70±0.01	0.32±0.03	0.05±0.00	6.91±0.99	···	···	···	···	6.80±1.60
EC 92	9.73±0.01	0.30±0.02	0.09±0.01	11.16±1.46	···	···	···	···	11.70±3.50
CK4	···	···	···	···	···	···	···	···	···
CrA IRS7 B	9.70±0.01	0.33±0.02	0.36±0.02	7.74±1.56	···	···	···	···	6.80±0.30
L1014 IRS	9.69±0.03	0.38±0.08	0.10±0.01	3.61±0.99	···	···	···	···	3.10±0.80

Note. — This table shows that CH_3OH column densities obtained in this paper are consistent with those in Paper I, which are our recommended values.

Note. — Uncertainties are statistical errors from the Gaussian fits.

Additional laboratory data

The table presented here (Table 3.6) gives an overview of all the ice mixtures measured in the laboratory. The table contains only spectra taken at a sample temperature of 15 K. The focus in the table is on the band position of the NH_3 ν_2 umbrella mode, the CH_3OH ν_4 C-O stretch mode and the CH_3OH ν_7 CH_3 rock mode. Full width at half maximum (FWHM) and the position of the maximum of the absorption profile of these modes are indicated in both cm^{-1} and μm for each mixture. For the NH_3 ν_2 umbrella mode, the band strength relative to that of the pure NH_3 mixture is also indicated.

Table 3.6. Ice composition, band maximum position (“peak position”), FWHM and band strength relative to the pure ice ($A_{rel.}$), listed for a set of ice mixtures under investigation.

Ice mixture					Molecule	Peak position		FWHM		$A_{rel.}$	Mode	
NH_3	CH_3OH	H_2O	CO	CO_2		cm^{-1}	μm	cm^{-1}	μm			
1	0	0	0	0	NH_3	1070	9.341	66	0.577	1	ν_2	umbrella
1	0	0.11	0	0	NH_3	1076	9.291	70	0.605	1	ν_2	umbrella
1	0	1	0	0	NH_3	1100	9.091	77	0.637	1	ν_2	umbrella
1	0	9	0	0	NH_3	1118	8.947	62	0.496	0.7	ν_2	umbrella
1	0	10	1	0	NH_3	1124	8.897	53	0.420	0.7	ν_2	umbrella
1	0	1	1	0	NH_3	1094	9.144	75	0.627	1	ν_2	umbrella
1	0	10	0	2	NH_3	1122	8.916	57	0.453	0.8	ν_2	umbrella
1	0	1	0	1	NH_3	1098	9.108	82	0.681	0.9	ν_2	umbrella
1	0	0	1	1	NH_3	1062	9.414	66	0.586	0.8	ν_2	umbrella
1	4	0	0	0	NH_3	1129[a]	8.856[a]	108[a]	0.849	0.4[a]	ν_2	umbrella
1	4	0	0	0	CH_3OH	1029	9.722	30	0.283	–	ν_4	C-O stretch
1	4	0	0	0	CH_3OH	1128	9.707	35	0.275	–	ν_7	CH_3 rock
1	4	0	0	0	CH_3OH	2823	3.543	28	0.035	–	ν_2	C-H stretch
1	2	0	0	0	NH_3	1111[a]	8.994[a]	115[a]	0.934	0.6[a]	ν_2	umbrella
1	2	0	0	0	CH_3OH	1029	9.720	29	0.274	–	ν_4	C-O stretch
1	2	0	0	0	CH_3OH	1132	8.833	35	0.273	–	ν_7	CH_3 rock
1	2	0	0	0	CH_3OH	2820	3.546	26	0.033	–	ν_2	C-H stretch
1	1	0	0	0	NH_3	1086	9.209	137	1.166	0.8	ν_2	umbrella
1	1	0	0	0	CH_3OH	1029	9.716	26	0.246	–	ν_4	C-O stretch
1	1	0	0	0	CH_3OH	1135	8.813	44	0.342	–	ν_7	CH_3 rock
1	1	0	0	0	CH_3OH	2817	3.550	26	0.033	–	ν_2	C-H stretch
1	0.5	0	0	0	NH_3	1080	9.258	118	1.015	0.8	ν_2	umbrella
1	0.5	0	0	0	CH_3OH	1030	9.711	22	0.207	–	ν_4	C-O stretch
1	0.5	0	0	0	CH_3OH	1128[a]	8.865[a]	35[a]	0.275	–	ν_7	CH_3 rock
1	0.5	0	0	0	CH_3OH	2813	3.555	27	0.034	–	ν_2	C-H stretch
1	0.25	0	0	0	NH_3	1078	9.278	98	0.845	0.9	ν_2	umbrella
1	0.25	0	0	0	CH_3OH	1030	9.707	16	0.151	–	ν_4	C-O stretch
1	0.25	0	0	0	CH_3OH	–[a]	–[a]	–[a]	–[a]	–	ν_7	CH_3 rock
1	0.25	0	0	0	CH_3OH	2808[a]	3.561[a]	17[a]	0.022	–[a]	ν_2	C-H stretch

[a] Band is weak and spectral overlap prohibits accurate fitting.

Table 3.6. (cont'd)

Ice mixture					Molecule	Peak position		FWHM		$A_{\mathrm{rel.}}$	Mode	
NH_3	CH_3OH	H_2O	CO	CO_2		cm^{-1}	μm	cm^{-1}	μm			
1	1	1	0	0	NH_3	1116[a]	8.961	95	0.764	0.7	ν_2	umbrella
1	1	1	0	0	CH_3OH	1026	9.745	29	0.276	–	ν_4	C-O stretch
1	1	1	0	0	CH_3OH	1125[a]	8.888[a]	32[a]	0.253	–	ν_7	CH_3 rock
1	1	1	0	0	CH_3OH	2824	3.541	26	0.033	–	ν_2	C-H stretch
1	0.25	10	0	0	NH_3	1119	8.937	59	0.472	1	ν_2	umbrella
1	0.25	10	0	0	CH_3OH	1017	9.833	22	0.213	–	ν_4	C-O stretch
1	0.25	10	0	0	CH_3OH	–[a]	–[a]	–[a]	–[a]	–	ν_7	CH_3 rock
1	0.25	10	0	0	CH_3OH	2829[a]	3.534[a]	30[a]	0.037	–	ν_2	C-H stretch
1	1	10	0	0	NH_3	1123	8.903	61	0.484	1	ν_2	umbrella
1	1	10	0	0	CH_3OH	1022	9.784	24	0.230	–	ν_4	C-O stretch
1	1	10	0	0	CH_3OH	–[a]	–[a]	–[a]	–[a]	–	ν_7	CH_3 rock
1	1	10	0	0	CH_3OH	2830	3.533	15	0.019	–	ν_2	C-H stretch
1	4	10	0	0	NH_3	1130	8.848	62	0.489	–	ν_2	umbrella
1	4	10	0	0	CH_3OH	1023	9.777	30	0.288	–	ν_4	C-O stretch
1	4	10	0	0	CH_3OH	1124	8.896	23	0.183	–	ν_7	CH_3 rock
1	4	10	0	0	CH_3OH	2830	3.534	14	0.017	–	ν_2	C-H stretch
0	1	0	0	0	CH_3OH	1028	9.729	28	0.265	1	ν_4	C-O stretch
0	1	0	0	0	CH_3OH	1125	8.888	34	0.269	1	ν_7	CH_3 rock
0	1	0	0	0	CH_3OH	2828	3.536	33	0.041	1	ν_2	C-H stretch
0	1	1	0	0	CH_3OH	1025	9.755	33	0.314	–	ν_4	C-O stretch
0	1	1	0	0	CH_3OH	1124	8.897	40	0.317	–	ν_7	CH_3 rock
0	1	1	0	0	CH_3OH	2828	3.536	23	0.029	–	ν_2	C-H stretch
0	1	9	0	0	CH_3OH	1020	9.801	23	0.221	–	ν_4	C-O stretch
0	1	9	0	0	CH_3OH	1126	8.883	13	0.103	–	ν_7	CH_3 rock
0	1	9	0	0	CH_3OH	2828	3.536	23	0.029	–	ν_2	C-H stretch

[a] Band is weak and spectral overlap prohibits accurate fitting.

Table 3.6. (cont'd)

Ice mixture					Molecule	Peak position		FWHM		$A_{\text{rel.}}$	Mode	
NH_3	CH_3OH	H_2O	CO	CO_2		cm^{-1}	μm	cm^{-1}	μm			
0	1	0	9	0	CH_3OH	1034	9.675	25	0.229	–	ν_4	C-O stretch
0	1	0	9	0	CH_3OH	1119	8.938	30	0.242	–	ν_7	CH_3 rock
0	1	0	9	0	CH_3OH	2831	3.532	–	–	–	ν_2	C-H stretch
0	1	0	9	0	CO	2138	4.677	7	0.014	–	ν_1	C-O stretch
0	1	0	1	0	CH_3OH	1029	9.720	30	0.286	–	ν_4	C-O stretch
0	1	0	1	0	CH_3OH	1124	8.898	32	0.258	–	ν_7	CH_3 rock
0	1	0	1	0	CH_3OH	2830	3.534	–	–	–	ν_2	C-H stretch
0	1	0	1	0	CO	2136	4.682	9	0.020	–	ν_1	C-O stretch
0	9	0	1	0	CH_3OH	1028	9.730	28	0.261	–	ν_4	C-O stretch
0	9	0	1	0	CH_3OH	1125	8.890	32	0.255	–	ν_7	CH_3 rock
0	9	0	1	0	CH_3OH	2824	3.541	–	–	–	ν_2	C-H stretch
0	9	0	1	0	CO	2135	4.685	9	0.021	–	ν_1	C-O stretch

[a] Band is weak and spectral overlap prohibits accurate fitting.

Comparison between astronomical and laboratory data

Comparison between astronomical and laboratory data for sources whose silicate absorption feature was fitted with a template. For a given source (displayed in either the left or right column of the figure), the middle and right panels show 5.2–7.5 and 8.2–10.2 μm regions from IRS *Spitzer* spectra overlaid with laboratory spectra, scaled to the 9 μm NH_3 umbrella mode. Error bars for the *Spitzer* spectra are indicated in the bottom-right corner. The dark blue line represents the pure water laboratory spectrum scaled to the water column density taken in paper I. Other colors are representative of laboratory spectra obtained for the following mixtures: H_2O:NH_3=9:1 (green), H_2O:CH_3OH:NH_3=10:0.25:1 (orange), H_2O:CH_3OH:NH_3=10:1:1 (cyan), and H_2O:CH_3OH:NH_3=10:4:1 (red). When available (see Boogert et al. 2008), VLT or Keck data (2.0–4.5 μm, left panel) are also plotted. In this case, we overplotted (dotted purple line) a pure water spectrum scaled to the 3 μm water feature of the mixed ice spectrum. Whenever present, a red dashed line in the right panel of a given source represents a H_2O:CH_3OH=9:1 laboratory spectrum scaled to the 9.7 μm CH_3OH CO-stretch mode: this gives an indication of the contribution of the 9 μm CH_3OH CH_3-rock mode to the total 9 μm feature. The laboratory spectra are recorded at 15 K unless indicated differently. Please refer to the on-line version for the color coding.

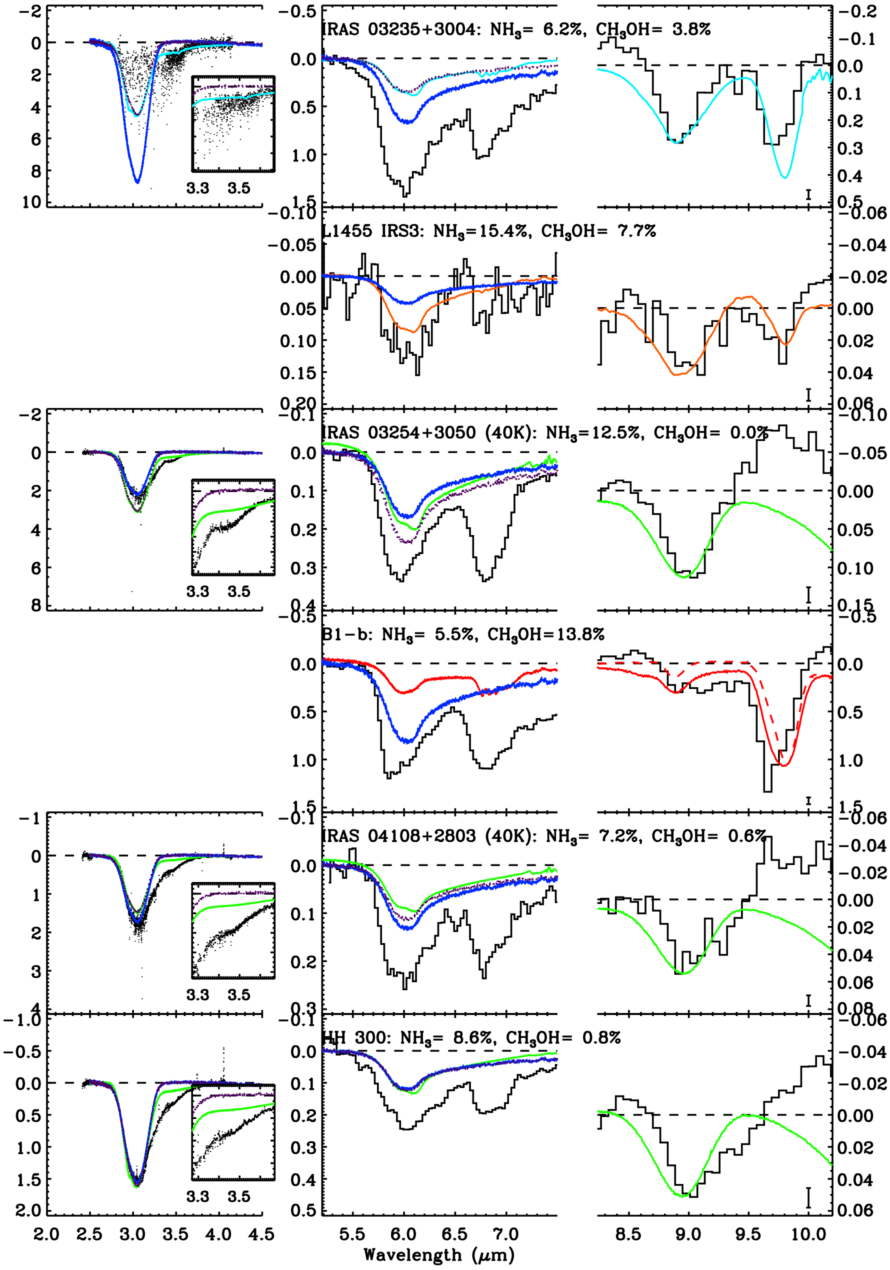

Figure 3.14 (a) Caption as described on the previous page

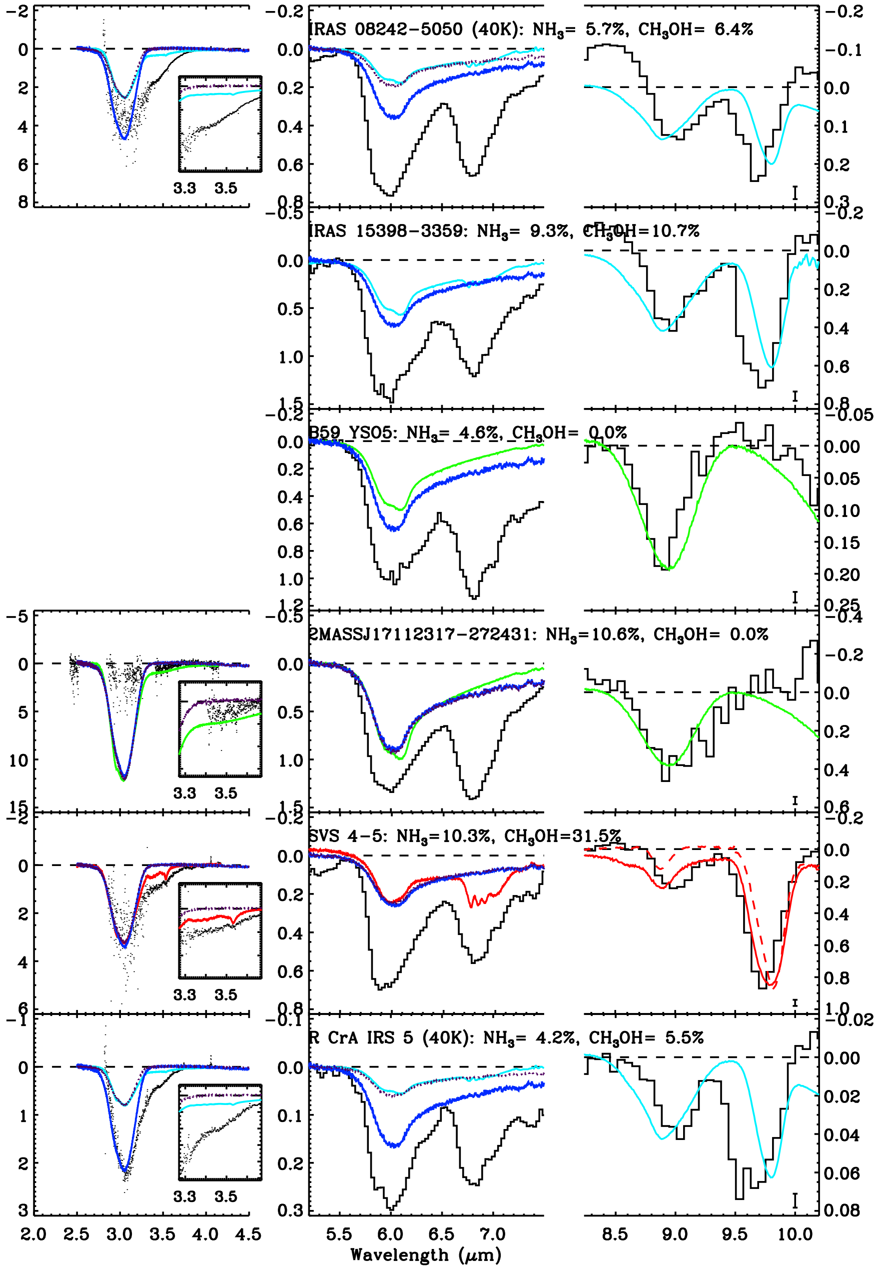

Figure 3.15 same as Fig. 3.14.

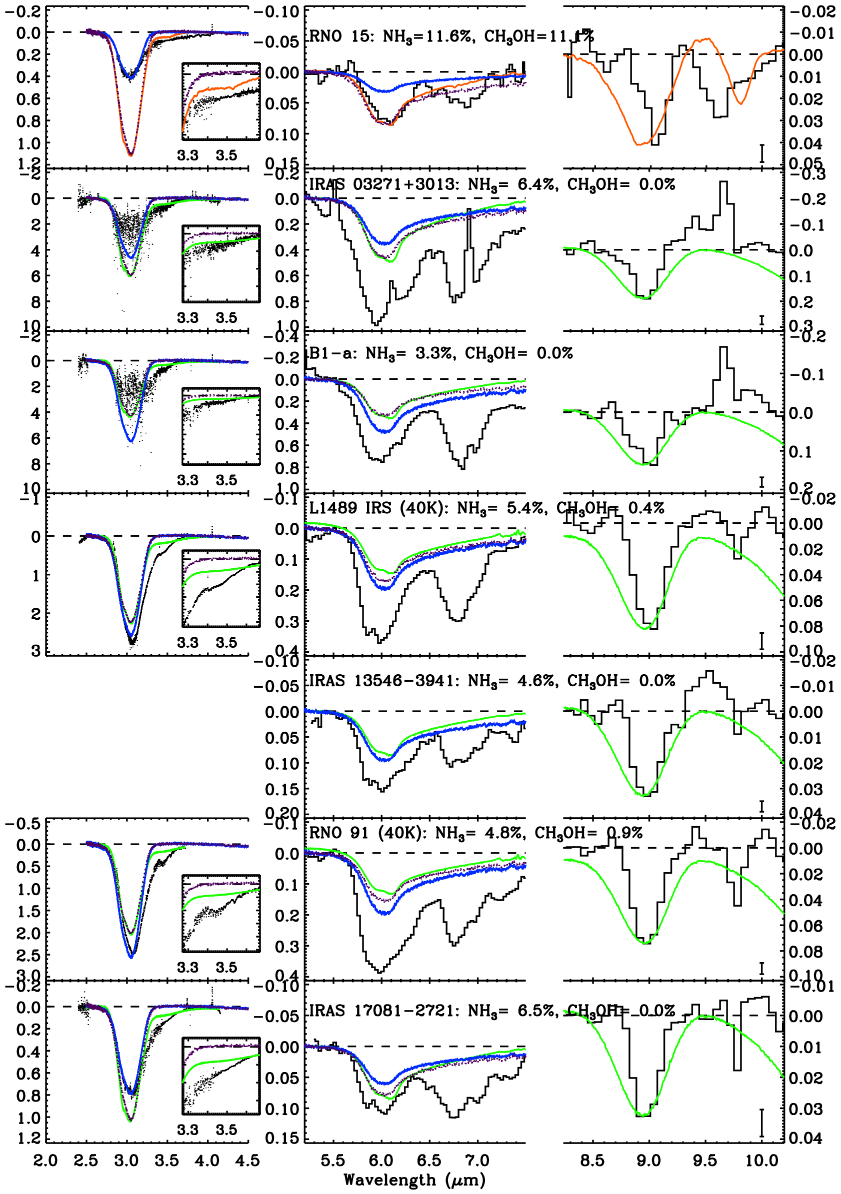

Figure 3.15 (b) As for Fig. 3.14 but for sources with no associated template, i.e. with the 10 μm silicate feature subtracted via the local continuum method. Additionally, yellow represents H_2O:NH_3=4:1 (H. Fraser, priv. comm.).

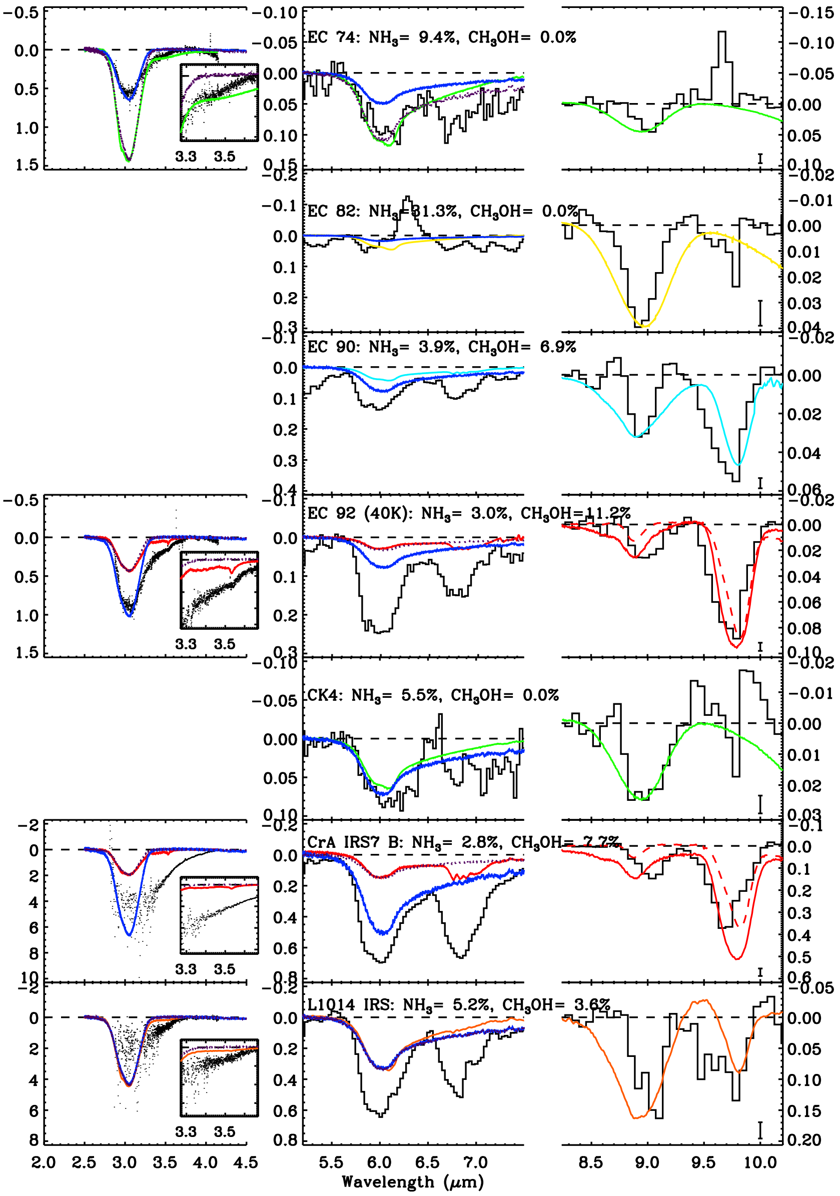

Figure 3.15 (b) As (a) but for sources with no associated template, i.e. with the 10 μm silicate feature subtracted via the local continuum method. Additionally, yellow represents H_2O:NH_3=4:1 (H. Fraser, priv. comm.).

CHAPTER 4

IR spectroscopy of VUV irradiated PAH containing interstellar ices[1]

Polycyclic aromatic hydrocarbons (PAHs) are known to be abundantly present in photon-dominated regions (PDRs), as evidenced by their ubiquitous mid-IR emission bands. Towards dense clouds, however, their IR emission bands are strongly suppressed. It is here where molecules are known to reside on very cold grains ($T \leq 30$ K) in the form of interstellar ices. Therefore, it is likely that non-volatile species, such as PAHs, also freeze out on grains. Such icy grains act as catalytic sites and, upon vacuum ultraviolet (VUV) irradiation, chemical reactions are initiated. These reactions and the resulting photoproducts are investigated in the study presented here for PAH containing water ices. The aim of this work is to monitor vacuum ultraviolet induced chemical reactions of PAHs in cosmic ice through their IR signatures, to characterize the families of species formed in these reactions, and to apply the results to astronomical observations. Mid-infrared Fourier transform absorption spectroscopic measurements ranging from 6500 to 450 cm^{-1} are performed on freshly deposited and vacuum ultraviolet processed PAH containing cosmic H_2O ices at low temperatures. The mid-IR spectroscopy of anthracene, pyrene and benzo[ghi]perylene containing H_2O ice is reported. Band strengths of the neutral PAH modes in H_2O ice are derived. Additionally, spectra of vacuum ultraviolet processed PAH containing H_2O ices are presented. These spectra are compared to spectra measured in VUV processed PAH:argon matrix isolation studies. It is concluded that the parent PAH species is ionized in H_2O ice and that other photoproducts, mainly more complex PAH derivatives, also form. The importance of PAHs and their PAH:H_2O photoproducts in astronomical mid-infrared spectroscopic studies, in particular in the 5–8 μm region, is discussed. As a test-case, the VUV photolyzed PAH:H_2O laboratory spectra are compared to a high resolution ISO-SWS spectrum of the high-mass embedded protostar W33A and to a *Spitzer* spectrum of the low-mass Young Stellar Object (YSO) RNO 91. For these objects, an upper limit of 2–3% with respect to H_2O ice is derived for the contribution of PAHs and PAH:H_2O photoproducts to the absorbance in the 5–8 μm region towards these objects.

---

[1] Based on: J. Bouwman, A. L. Mattioda, H. Linnartz, and L. J. Allamandola, Astronomy and Astrophysics, submitted (2010)

4.1 Introduction

Polycyclic aromatic hydrocarbons (PAHs) are known to be abundantly present in photon-dominated regions (PDRs) [Peeters et al. 2004a, van Dishoeck 2004, Tielens 2008]. The evidence for the ubiquity of astronomical PAHs is the widespread, well-known family of prominent emission bands at 3.28, 6.2, 7.6, 8.6, and 11.2 μm (3050, 1610, 1300, 1160, and 890 cm^{-1}) associated with many, if not most, galactic and extragalactic objects [Smith et al. 2007, Draine & Li 2007]. These bands dominate the mid-IR emission spectrum because of an intrinsically high efficiency of the fluorescent process and are most easily detected in regions where individual gas-phase PAH molecules (both neutrals and ions) become highly vibrationally excited by the ambient UV-VIS-NIR radiation field [Mattioda et al. 2005a, Li & Draine 2002]. They then energetically relax by emission of IR photons at frequencies corresponding to fundamental vibrational modes, resulting in these well known emission spectra.

PAHs and related aromatic materials are expected to be present both in optically thin, diffuse regions of the ISM and in dense environments. In dense regions, however, the highly efficient PAH fluorescence is found to be quenched. There are two reasons for this. First, the radiation which pumps the emission tapers off with extinction into dense regions, and second, in cold molecular clouds PAHs can serve as nucleation sites on which other species condense. In this way, neutral and/or charged PAHs can agglomerate to form (charged) PAH clusters, or very small grains (VSGs) [e.g., Allamandola et al. 1989, Rapacioli et al. 2006]. The VSGs can, subsequently, freeze out on grains or serve as nucleation sites for small molecules forming ice covered VSGs. Individual PAHs can also efficiently condense onto dust grains as ‘guest molecules’ in icy grain mantles, much as is the case for most other smaller interstellar molecules [e.g., Sandford & Allamandola 1993]. Vibrational energy of a PAH molecule which is part of a larger dust particle, either as a nucleation center or guest in a water-rich ice, efficiently dissipates into the phonon modes of the solid material on a time-scale orders of magnitude shorter than required to emit an IR photon [Allamandola et al. 1985, 1989]. Consequently, in dark, dense regions, PAHs and PAH derivatives are expected to give rise to IR *absorption* bands, not to *emission* features.

There are several lines of evidence that support the presence of PAHs in dense molecular clouds. Aromatics in primitive meteorites and interplanetary dust particles contain deuterium enrichments that are best explained by an interstellar cloud heritage [e.g., Sandford 2002,and references therein]. In addition, very weak absorption features attributed to aromatic hydrocarbons have been observed in the IR absorption spectra of objects embedded in dense clouds. These include a band near 3.3 μm (3030 cm^{-1}) [Smith et al. 1989, Sellgren et al. 1995, Brooke et al. 1999, Chiar et al. 2000], and bands near 6.2 μm (1600 cm^{-1}) [Chiar et al. 2000] and 11.2 μm (890 cm^{-1}) [Bregman et al. 2000]. These very weak features are severely blended with much stronger H_2O ice bands, consistent with the number of PAH molecules relative to the number of H_2O molecules along these lines of sight on the order of a few percent. So far, it has proven difficult to unambiguously interpret these absorption features in spite of the fact that there is a growing database of theoretically calculated and laboratory measured IR absorption spectra of both neutral and ionized PAHs in inert matrices [e.g., Szczepanski & Vala 1993, Szczepanski et al. 1993a,b, 1995a,b, Hudgins et al. 1994, Hudgins & Allamandola 1995a, 1997, Langhoff 1996, Mattioda et al. 2005b, Bauschlicher et al. 2009, 2010,and references therein]. Unfortunately, these spectra cannot be used directly to compare with PAHs in H_2O-rich ices, as rare gas matrix spectra will be different. Intermolecular interactions perturb the molecular vibrational energy levels, influencing IR band positions, widths, profiles, and intrinsic strengths. Consequently, it has not yet been possible to properly evaluate astronomical solid state PAH features, mainly because the corresponding laboratory data of *realistic ice analogs* are lacking.

Therefore, in the Astrochemistry Laboratory at NASA Ames Research Center a program to measure the IR spectra of PAHs in water ices was started. Earlier work focused on the IR band positions, band widths, and relative band strengths of neutral PAHs [Sandford et al. 2004, Bernstein et al. 2005a,b]. More recently, an exploratory study of the effects of vacuum ultraviolet (VUV) photolysis on several PAH:H_2O ice mixtures was carried out [Bernstein et al. 2007]. Unfortunately, at concentrations that are most appropriate for dense clouds, PAH bands are swamped in the mid-IR by overlapping H_2O ice bands and it has proven difficult to put these IR-only data on a solid quantitative footing. This situation has changed thanks to the development of a new apparatus at the Sackler Laboratory for Astrophysics at Leiden University which allows one to track the in situ, VUV photochemistry of low concentration PAH:H_2O ices using optical (i.e. electronic) spectroscopy (Chapter 5, 6, and 7). This approach makes it possible to simultaneously follow the VUV driven kinetic behavior of the neutral parent PAH and photoproducts on millisecond timescales with a concentration precision on the order of a few percent. Using this approach, it was possible characterized the VUV photochemistry of four PAHs anthracene, pyrene, benzo[ghi]perylene, and coronene in water ice at various concentrations and ice temperatures. This is described in detail in Chapter 7. The mid-IR study presented here is partially based on the quantitative results derived in the optical work.

This paper is laid out as follows. After the experimental technique is described in §7.2, the results are presented in §4.3 and §4.4. These include band profiles and band strengths for neutral anthracene, pyrene and benzo[ghi]perylene in H_2O ice, the IR spectroscopic properties of their VUV induced photoproducts, and the visualization of photochemical processes at play during extended photolysis. In §4.6 we extend our findings to the general IR properties of PAHs in ices and use these data to interpret observations of ices in dense clouds towards the high-mass protostar W33A and the low-mass young stellar object RNO 91. The conclusions are summarized in §4.7.

4.2 Experimental technique

The techniques employed in this study have been described in detail previously [Hudgins et al. 1994] and the relevant details are summarized briefly. The ices are prepared by vapor co-deposition of the PAH of interest with water vapor onto a 15 K CsI window which is suspended in a high vacuum chamber ($P \leq 10^{-8}$ Torr). The PAHs anthracene (Ant, $C_{14}H_{10}$, Aldrich, 99%) and pyrene (Py, $C_{16}H_{10}$, Aldrich, 99%) are used without further purifica-

Table 4.1 Ice mixture (PAH:X, where X indicates the ice matrix species), PAH vaporization temperatures, resulting concentrations (PAH:Z, where Z indicates the relative amount of the matrix species) for anthracene, pyrene, and benzo[ghi]perylene containing ices, and the ice temperature during photolysis for the ice mixtures under investigation.

Ice (PAH:X)	T_{dep} (°C)	Conc. (PAH:Z)	T_{ice} (K)
Ant:H_2O	32	1:450	15
	42	1:172	15
	53	1:60	15
	71	1:11	15
	51	1:100	125
Py:H_2O	41	1:200	15
	44	1:90	15
	50	1:65	15
	51	1:70	125
Py:CO	50	1:30	15
$B_{ghi}P$:H_2O	143	1:160	15
	156	1:60	15
	152	1:110	125

tion and vaporized from heated pyrex tubes. The PAH benzo[ghi]perylene ($B_{ghi}P$, $C_{22}H_{12}$, Aldrich, 98%) is kept at a temperature of 180°C for 20 minutes with a cold shield blocking the deposition onto the sample window to remove most of the contaminants and is subsequently deposited in a manner similar to that for Ant and Py. Simultaneously, water vapor — milli-Q grade, further purified by three freeze-pump-thaw cycles — is admitted through an adjacent deposition tube. To prepare PAH:H_2O ices with different concentrations, the PAH deposition temperature was varied from one experiment to the other, while the water flow was kept constant. Mid-infrared spectroscopy of the PAHs Ant, Py, and $B_{ghi}P$ in water ice and for Py:CO ice as a control experiment is performed for a range of concentrations. The PAH deposition temperature, the resulting PAH concentration, and the ice temperature during photolysis are summarized in Table 4.1.

VUV photolysis of the sample ices is accomplished with the combined 121.6 nm Lyman-α (10.6 eV) and 160 nm (7.8 eV) molecular hydrogen emission bands from a microwave powered discharge in a flowing H_2 gas at a dynamic pressure of 150 mTorr. The VUV radiation from the lamp enters the sample chamber through a MgF_2 window. The UV photon flux of the lamp is $\sim 10^{15}$ photons $cm^{-2}s^{-1}$ at the sample surface.

Spectra from 6500 to 450 cm^{-1} are measured with a Biorad Excalibur FTS 4000 FTIR spectrometer equipped with a KBr beamsplitter and a liquid N_2-cooled MCT detector. Spectra are taken in optical depth ($\tau = \ln I/I_0$), with the background spectrum (I_0) taken on the cold sample window before sample deposition, and the spectra (I) taken after deposition and VUV processing of the sample. Each spectrum represents a co-addition of 512 spectra at a resolution of 0.5 cm^{-1}. This level of resolution is necessary to distinguish photoproduct bands that are close to the position of the neutral band. The number of scans was chosen to optimize both the signal-to-noise ratio as well as the time requirements for each experiment. Spectra are taken at 15 K of the freshly deposited sample and after 5, 10, 15, 30, 60, 120, and 180 minutes of VUV photolysis. Similar measurements are also performed on PAH:H_2O ice samples at 125 K to check for differences in photochemistry between low and high temperature photolysis experiments.

We focus on the bands in the 1650–1000 cm^{-1} region because this is where the PAH mid-IR bands suffer the least from overlap with the strong H_2O ice features (Fig. 4.1). Hereafter we refer to this as the Region Of Interest (ROI). The absolute band strengths for the neutral PAH modes in H_2O ice are derived as follows. The H_2O bending and librational overtone modes are subtracted from the raw spectrum by fitting a spline function through a set of points where no PAH absorption occurs. Subsequently, the total theoretically calculated absolute intensity in the ROI is proportionally divided over the measured PAH modes in this frequency range, via:

$$A_i^{\mathrm{exp}} = \left[\sum_{j=0}^{M} A_j^{thy} \right] \frac{\int_{\nu_{i,1}}^{\nu_{i,2}} \tau_{i,\nu}\, d\nu}{\sum_{i=0}^{L} \int_{\nu_{i,1}}^{\nu_{i,2}} \tau_{i,\nu}\, d\nu}, \tag{4.1}$$

where A_i^{exp} is the experimentally measured band strength of PAH mode i in H_2O ice in cm molecule^{-1}, A_j^{thy} is the theoretically calculated absolute intensity of vibrational mode j in the ROI in cm molecule^{-1}, M is the number of theoretically calculated modes in the ROI, $\tau_{i,\nu}$ is the optical depth of mode i in H_2O ice at frequency ν (cm^{-1}), L is the number of measured modes in the ROI, and $\nu_{i,1}$ and $\nu_{i,2}$ are the lower and upper integration boundaries in cm^{-1}, respectively, for absorption feature i. This method takes advantage of the fact that, although there may be band-to-band variations in the accuracy of the calculated intensity for one band, the total theoretically calculated intensity is generally accurate to within 10–20%. Here we assume that the matrix material does not substantially influence the total integrated IR band intensity and, as will be shown later, this is only an approximation.

The PAH in H_2O concentrations are determined as follows. The optical depths (τ_ν) of the 3 μm stretching, 6 μm bending, and 13 μm libration modes of water are integrated over the frequency domain (ν in cm^{-1}) and converted into the column density (N in molecules cm^{-2}), using the well known H_2O band strength values A_{band} [Hudgins et al. 1993], via:

$$N = \frac{\int \tau_\nu d\nu}{A_{\mathrm{band}}}. \tag{4.2}$$

The adopted H_2O band strength values, A_{band}, are 2×10^{-16}, 1.2×10^{-17} and 3.1×10^{-17} cm molecule^{-1} for the stretching, bending and libration mode, respectively. The H_2O column density is determined by taking the average of these three strong H_2O bands. Similarly, at least four strong bands of the PAHs under investigation are integrated and converted to column densities using the band strengths for these modes as calculated above (Eq. 4.1). The average PAH column density is used to determine the concentration, which is given by the ratio of the PAH and H_2O column densities.

Comparison of the PAH:H_2O ice spectrum before photolysis to that measured after photolysis permits identification of photoproduct features, including cation absorption bands. The spectrum of the freshly deposited PAH:H_2O ice, multiplied by a factor, Y ($0 \leq Y \leq 1$), is used as a reference that is subtracted from the spectrum of the irradiated ice using the Resolutions Pro spectrometer software package provided by Biorad. The factor Y is varied until the neutral bands are removed from the spectrum. At this point, the resulting subtraction spectrum reveals *only* the photoproduct bands and the subtraction factor, Y, directly reflects the amount of neutral PAH consumed during photolysis. Additionally, the contributions from the H_2O librational overtone and H_2O bending mode are subtracted by a spline function, for which points are chosen at positions where no PAH photoproduct absorptions are observed. The resulting baseline corrected spectra are used for further analysis.

The sample window on which the ices are grown was thoroughly cleaned before commencing experiments on a different PAH. Thus, the background spectrum taken of the cold sample window before starting a series of measurements (I_0) was free of PAH absorptions. For one specific PAH, typically five individual PAH:H_2O photolysis experiments were performed for different concentrations and temperatures (Table 4.1), during which a residue built up, comprising unprocessed PAH, and presumably also PAH:H_2O photoproducts. After completion of the measurement series for this specific PAH, a spectrum (I) was taken of the room temperature “dirty” sample window. Subsequently, the system was cleaned and prepared for the next run. The ratio $\ln(I/I_0)$ reflects the optical depth spectrum of the non-volatile residue and is used to derive complementary information on the species formed in the ice. The non-volatile residues that built up during the Ant, Py, and $B_{ghi}P$ measurement series are discussed in §4.5.

4.3 PAH:H_2O spectroscopy

Earlier observations [Smith et al. 1989, Sellgren et al. 1995, Brooke et al. 1999, Chiar et al. 2000, Bregman et al. 2000] indicate that the ratio of the number of PAH molecules to the number of H_2O ice molecules is small along lines of sight towards protostars in dense clouds. Based on these observations, we deduce that this number seems to be on the order of a few percent. In a very careful study, Sellgren et al. [1995] reported the optical depth of the 3.25 μm aromatic C–H stretch band towards Mon R2/IRS 3 as 0.045 with a FWHM of 75 cm^{-1}. These values are similar to the range of values reported by Bregman & Temi [2001] towards other deeply embedded protostars. For the purposes of this analysis, we use the results from Sellgren et al. [1995]. Similar conclusions can be drawn using the observations from these other lines of sight.

Using the standard equation to determine the column density of absorbers along a given line of sight:

$$N = \frac{\tau \times \mathrm{FWHM}}{A}, \tag{4.3}$$

with the FWHM in cm^{-1} and an A value of 2.5×10^{-18} cm per aromatic C–H bond [e.g. Joblin et al. 1994, Bauschlicher et al. 2008] yields 1.3×10^{18} aromatic C–H groups per cm^2 along the line of sight to Mon R2/IRS 3. Astronomical PAHs are thought to range in size from roughly C_{25} to well over C_{100}. Reasonable formulae for such sized species are

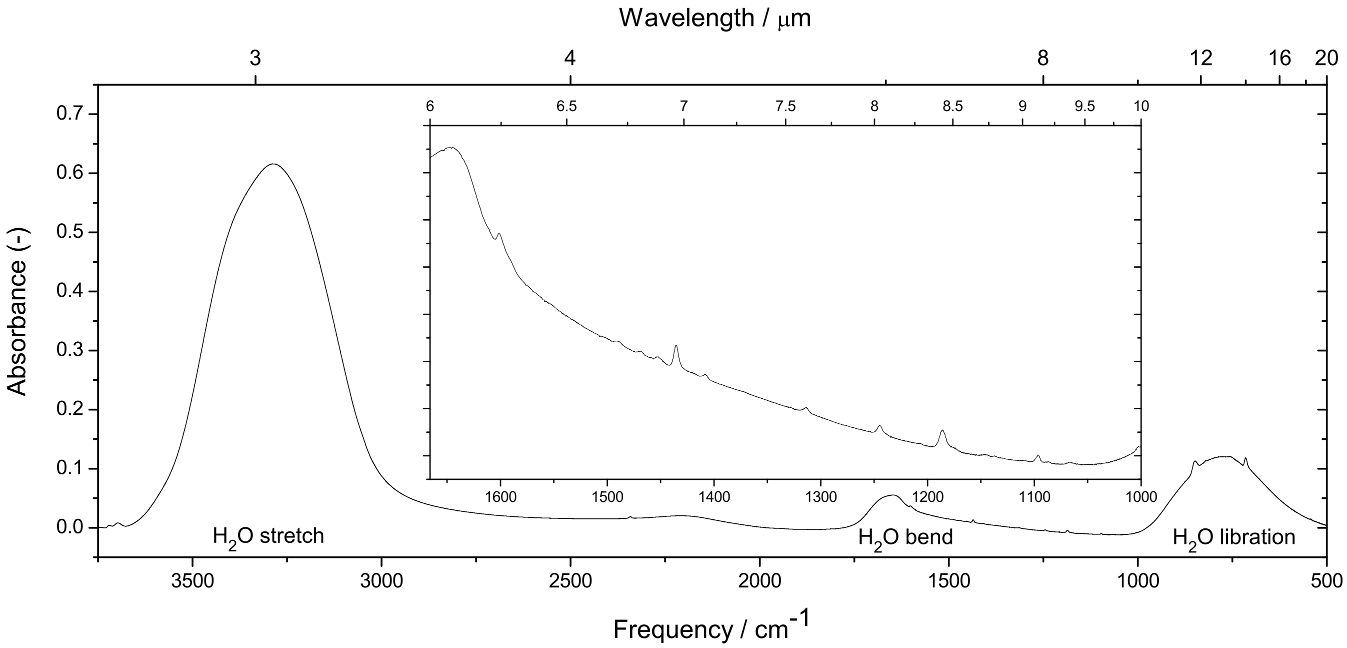

Figure 4.1 A typical absorption spectrum for a pyrene:H_2O (1:90) ice mixture at 15 K. The inset shows a blow-up of that part of the spectrum (region of interest) where Py absorptions are least affected by the water modes. The water modes are labeled in the spectrum.

$C_{32}H_{15}$ and $C_{130}H_{28}$. To take this into account, we estimate that the 'average' number of aromatic C–H bonds per astronomical PAH is 25. Dividing the column density of aromatic C–H bonds towards Mon R2/IRS 3 (1.3×10^{18}) by 25 yields the PAH column density, 7.2×10^{16} PAHs cm^{-2}. Likewise, for Mon R2/IRS 3 we derive 3.3×10^{18} H_2O ice molecules cm^{-2} from the O–H stretch band in Smith et al. [1989]. Thus, the PAH/H_2O ice ratio along this line of sight is $7.2 \times 10^{16}/3.3 \times 10^{18} = 0.022$, or 2%.

Figure 4.1 presents the 3750–500 cm^{-1} spectrum of a Py:H_2O (1:90) ice at 15 K, which clearly shows that the H_2O ice bands dominate the spectrum at these concentrations. In agreement with earlier findings on other PAHs at concentrations of a few percent in H_2O ice, the CH–stretch band near 3030 cm^{-1} (3.3 μm) is nearly imperceptible, while the strong C–H out-of-plane bending bands between 900–500 cm^{-1}(11–20 μm) suffer from severe blending with the H_2O ice libration mode [Sandford et al. 2004, Bernstein et al. 2005a]. This makes PAH bands between 1650–1000 cm^{-1} (~6.06–10 μm, the ROI) the most promising to study PAH:H_2O photochemistry, and to identify astronomical PAHs and PAH related photoproduct species in interstellar ices.

The spectroscopy of PAH:H_2O ice samples is discussed for Ant, Py, and $B_{ghi}P$ and compared to available PAH matrix isolation data. In Fig. 4.2 typical baseline corrected spectra of the three neutral PAHs in argon (trace A) are plotted together with the spectra of the neutral PAH:H_2O (trace B) ice (~1:60). The spectra are normalized to the strongest absorptions in the ROI. Clearly, the absorption bands are much broader in water ice compared to the argon matrix data, causing some of the absorption bands to overlap. Furthermore, the relative intensities of the bands differ for an argon or H_2O environment. The band positions and integrated absorbances relative to that of the strongest PAH absorption are listed in Table 4.2 for Ant, Py and $B_{ghi}P$ in H_2O ice and in an argon matrix [Hudgins & Sandford 1998a]. The corresponding Density Functional Theory (DFT) peak positions taken from Langhoff [1996] are given as well. The absolute band strengths for PAHs in H_2O ice, calculated under the assumptions described in Sect. 7.2, are also listed in Table 4.2. Within the errors, the FWHM, relative intensity, and position of the band maximum of absorptions of the three species studied here are found to be independent of concentration and temperature for the values listed in Table 4.1, even for the two most extreme Ant:H_2O ice concentrations (1:11 and 1:450). Thus, although we cannot fully exclude the presence of PAH aggregates in the ice, there is no spectral evidence for such species.

4.4 PAH ice photochemistry

All PAH:H_2O ice samples listed in Table 4.1 are VUV irradiated for 5, 10, 15, 30, 60, 120, and 180 minutes. Mid-IR spectra are taken after each VUV dose to look for changes in the spectrum. Spline baseline corrected spectra after 5 minutes of VUV irradiation of the Ant, Py, and $B_{ghi}P$ containing H_2O ice samples with a mixing ratio of ~1:60 are shown in trace (D) of Fig. 4.2. In this figure, the spectra are compared to those of the corresponding PAH^+ species produced and trapped in solid argon (trace C). Comparison of the traces (D) and (B) in Fig. 4.2 shows that new absorptions arise upon photolysis of

Table 4.2 The band positions and relative integrated absorbances for the PAHs antracene (Ant), pyrene (Py) and benzo[ghi]perylene ($B_{ghi}P$) in H_2O ice at 15 K, and in an argon matrix at 10 K. Band positions computed using Density Functional Theory are also listed. Absolute intensities (A_{band}) for the PAHs in H_2O ice are in units 10^{-19}cm/molecule.

PAH	Position (cm^{-1})			Relative I.A.		A_{band}
	H_2O	Ar	Theory[a]	H_2O	Ar	H_2O
Ant	1001.7	1000.9	1000.7	0.7	0.8	6.8
	1103.8			0.1		0.8
	1127.4			0.2		1.9
	1149.7	1149.2	1156.2	0.9	0.7	9.0
			1157.7			
	1168.2	1166.9	1169.3	0.6	0.5	6.2
	1186.8			0.1		1.0
	1272.3	1272.5	1274.6	0.5	0.6	5.7
	1316.0	1318.1	1311.2	1.0	1.0	10.4
	1328.3			0.2		2.1
	1347.7	1345.6,1346.4	1342.6	0.3	0.2	3.5
	1400.1			0.3		3.1
	1450.9	1450.5	1455.3	1.4	0.4	14.6
		1460.0	1456.1		0.3	
	1537.9	1542.0	1533.7	0.8	0.8	8.7
	1563.1			0.1		0.8
		1610.5	1620.0		0.2	
	1624.4	1627.8		0.8	0.4	7.9
Py	1065.5			0.1		2.8
	1096.4	1097.3	1092.3	0.2	0.2	5.1
	1136.6			0.1		2.1
	1176.3	1164.5	1160.8	0.3	0.1	6.1
	1185.6	1183.9	1188.3	1.0	1.0	21.7
	1244.0	1243.0	1253.1	0.5	0.2	10.3
	1313.7	1312.1	1314.6	0.2	0.2	5.3
	1435.1	1434.8	1427.0	0.8	0.6	17.3
			1427.5			
	1452.0			0.1		2.8
	1468.4	1471.0	1476.2	0.1	0.1	1.8
	1488.4			0.2		3.3
	1594.1		1586.1	0.6		12.7
	1600.5	1604.0	1597.0	0.6	0.4	12.0
$B_{ghi}P$	1038.3	1036.3	1037.6	0.2	0.1	4.4
	1085.9	1087.8	1082.2	0.2	0.0	3.6
		1093.4	1091.9		0.0	
	1132.0	1132.7	1136.6	0.4	0.3	8.5
	1148.0	1149.2	1152.7	0.8	0.1	17.8
	1186.5	1186.9	1171.1	0.3	0.0	6.2
			1206.6			
	1203.5	1206.7	1203.3	0.5	0.3	10.8
	1258.7	1259.1	1261.5	0.1	0.0	1.7
			1309.0			
	1305.6	1302.9,1307.0	1292.3	0.7	0.3	15.8
	1334.6		1338.6	0.3		6.3
	1342.2	1342.6	1336.0	1.0	1.0	22.5
	1374.9	1350.0	1375.8	0.1	0.2	1.6
			1398.9			
	1392.8	1394.7	1397.8	0.5	0.4	11.7
	1414.8	1416.0,1417.1	1426.2	0.5	0.3	11.4
	1447.8	1449.0,1451.1	1441.3	0.8	0.6	17.8
	1479.7			0.2		4.7
	1512.8	1517.8	1513.3	0.2	0.0	3.5
		1527.4			0.1	
	1582.8	1602.1	1586.4	0.4	0.2	9.1
	1598.5		1586.6	0.3		6.5
	1614.7			0.1		1.3
	1618.9			0.1		2.4

[a] Values taken from: Langhoff [1996]

the PAH:H_2O mixtures. The photoproduct features are, however, heavily blended with those of the remaining neutral PAH. To overcome this, spectra of freshly deposited PAHs are subtracted from their VUV photolyzed counterparts with a subtraction factor, Y, as described in §4.2. Subsequently, the contribution by the librational overtone and the H_2O bending mode are removed by fitting and subtracting a spline function. The resulting spectra are shown in trace (E) of Fig. 4.2 and show photoproducts only. The spectra are again scaled to the strongest absorption in the ROI. It has to be noted here, that the absorption bands of the photoproducts after 5 minutes of VUV irradiation are rather small compared to those of the neutral bands, as can be seen by comparing trace (B) and (D) from Fig. 4.2. While band intensities grow with longer irradiation time, the combination of spectral overlap and different photoproduct band growths and losses makes it difficult to track the precise photochemistry at longer photolysis times. This is discussed later in §4.4.2.

It is clear from Table 4.2 that the relative PAH band strengths in H_2O ice are different from those in an argon matrix, but the PAH cation band strengths measured in argon have to be used for further analysis, since band strength values for PAH cation vibrational modes in H_2O ice cannot be reliably determined for two reasons. First, the appearance of bands other than cation absorptions after 5 minutes of photolysis points out that there is no one-to-one conversion of the neutral PAH to the cation and, thus, the column density of used up neutral PAH molecules cannot be used as a reliable column density for cations in the ice on which to base a further band strength analysis. Secondly, spectral congestion and ill-defined baselines make it hard to obtain accurate band areas of photoproduct bands in irradiated mixtures. This choice induces additional errors in the absolute PAH^+ column density that can be as high as a factor of two.

4.4.1 PAH:H_2O photoproducts

VUV photoprocessed PAH containing H_2O ices spectra exhibit a set of broad absorption features (see trace E of Fig. 4.2). As with the neutral PAHs, the absorption profiles of PAH photoproducts in H_2O ice are much broader than those in an argon matrix (trace C). These PAH:H_2O photoproduct absorption bands are decomposed by multiple Gaussian fits and the peak positions of these bands are listed together with PAH^+ absorptions and band strengths measured in argon in Table 4.3. The solid lines along the top margin indicate the PAH cation band positions in Ar [Hudgins & Allamandola 1995a,b]. The photoproduct bands that fall within 10 cm^{-1} of these features are assigned to the PAH^+ bands in H_2O. Some of the newly formed absorption bands, however, occur at positions where no corresponding PAH^+ band is found in argon. These absorption bands reflect additional chemical reactions already at play in the early photolysis of PAH:H_2O ices.

It is well known that H_2O molecules photodissociate into radicals (H+OH) and that these radicals are mobile within H_2O ice, even at low temperatures [Andersson & van Dishoeck 2008, Öberg et al. 2009d]. At the concentrations under consideration here, it is therefore likely that these and other photoproducts react with the PAHs, forming more complex aromatic species containing functional groups that give rise to different peak

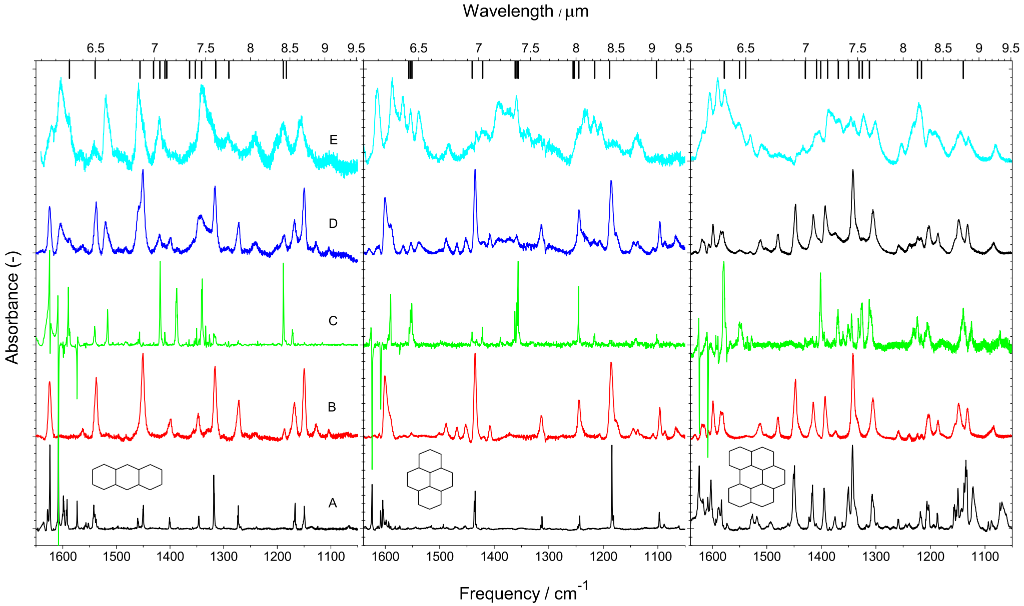

Figure 4.2 From left to right the 1640 to 1050 cm^{-1} spectra of the PAHs anthracene, pyrene, and benzo[ghi]perylene considered are shown here. A) Spectra of the neutral PAH in argon, B) spectra of the neutral PAH in water ice, C) spectra of the PAH cation in argon, D) spectra of the PAH:H_2O (1:60) mixture after 5 minutes of in-situ VUV photolysis, and E) spectra showing *only* the photoproduct features that appear after 5 minutes of in-situ VUV photolysis of the PAH:H_2O ice (spectrum ‘D’$-Y\times$‘B’). The tick marks connected to the top axis indicate the positions of PAH$^+$ features measured in argon. The PAH:matrix concentrations and temperatures for the spectra shown in A and B are: Ant:Ar $< 1 : 1000$, 10 K; Py:Ar $< 1 : 1000$, 10 K; $B_{ghi}P$:Ar $< 1 : 1000$, 10 K and Ant:H_2O=1:60, 15 K; Py:H_2O=1:65, 15 K; $B_{ghi}P$:H_2O=1:60, 15 K. Argon matrix spectra of neutral Ant and Py are reproduced from Hudgins & Sandford [1998a], neutral $B_{ghi}P$ from Hudgins & Sandford [1998b], ionized Ant from Hudgins & Allamandola [1995b], and ionized Py and $B_{ghi}P$ from Hudgins & Allamandola [1995a].

positions in the mid-IR spectra (see also Chapter 6 and the discussion in Gudipati & Allamandola [2006b]). While infrared spectroscopic data on PAH:H_2O photoproducts are largely lacking in the literature, analysis of the non-volatile photoproducts has shown that the O, OH and H additions to the parent PAH are the dominant reaction pathways [Ashbourn et al. 2007, Bernstein et al. 1999, 2002b]. Aromatic alcohols are among the known photoproducts, and the C–O stretching vibration in alcohols and phenols produces a strong band in the 1260–1000 cm^{-1} region [e.g., Silverstein & Bassler 1967]. Additionally, the alcohol OH wag falls in the 1420 to 1330 cm^{-1} region. Besides alcohols, aromatic ketones are also amongst the photoproducts. The C=O stretch vibration in ketones typically occurs at around 1700 cm^{-1}. Keeping this in mind, tentative identifications of unassigned bands, i.e. not due to PAH$^+$, are made below.

Anthracene:H_2O photoproducts

While most of the bands in the spectrum of the Ant:H_2O photoproducts can be attributed to Ant$^+$, some prominent bands cannot. Two such bands appear at 1156 and 1243 cm^{-1}. It is possible that both of these absorptions originate from the CO stretch of two different Ant–OH isomers. The 1243 cm^{-1} band was previously attributed to an unknown Ant:H_2O photoproduct [Bernstein et al. 2007]. Another prominent band that is not solely due to Ant$^+$ occurs at 1452 cm^{-1}. While a small cation band is present near this position in the argon matrix data, it is much less intense with respect to the other cation bands whereas the photoproduct band in trace (E) (Fig. 4.2) is one of the strongest in the spectrum. This band is likely a blend of the cation band with a much stronger product band. The absorption frequency suggests that it originates from an aromatic CC stretching and C–H in-plane bending mode. Two strong photoproduct bands also appear in the blue end of the ROI, one at 1518 cm^{-1}, the other at 1604 cm^{-1}. The moderately strong Ant$^+$ band at 1586.4 cm^{-1} is expected to contribute to the blue end of the 1604 cm^{-1} feature, but again seems to be too weak to explain the full feature. Both the 1518 cm^{-1} and most of the 1604 cm^{-1} bands are likely due to the aromatic CC stretch vibration of a newly formed species.

The detection of new bands in the 1260–1000 cm^{-1} region upon VUV photolysis of an Ant:H_2O mixture does agree with earlier findings by Ashbourn et al. [2007], who detected 1-anthrol and 2-anthrol using HPLC in a VUV irradiated Ant:H_2O ice ($>$ 1:100) after warm-up to room temperature. They also reported the formation of 1,4-anthraquinone, 9,10-anthraquinone and 9-anthrone. Anthraquinones contain two C=O bonds, which typically absorb at a frequency of 1676 cm^{-1}[Chumbalov et al. 1967]. This band position is outside of our ROI and detection is hampered by the strong H_2O bending mode. The other species detected by Ashbourn et al. [2007], 9-anthrone, belongs to the group of ketones and is expected to exhibit a C=O absorption at ~1700 cm^{-1}. The formation of this species can also not be confirmed for the same reason.

Table 4.3 Band positions of photoproducts appearing upon VUV photolysis of the PAHs antracene (Ant), pyrene (Py) and benzo[ghi]perylene ($B_{ghi}P$) in water ice at 15 K compared to cation absorption band positions and band strengths measured in an argon matrix. Band strengths are in units of 10^{-18} cm/molecule. Cation bands are marked with a '+'.

PAH	Position (cm^{-1}) H_2O	Position[a] (cm^{-1}) Argon	Band strength[a]	Ass.
Ant	1155.7			
	1190.5	1183.3	0.37	+
		1188.6	18	+
	1242.7			
	1292.8	1290.4	1.5	+
	1326.2	1314.6	1.5	+
	1340.5	1341	26	+
	1358.3	1352.6	8.0	+
		1364.4	1.0	+
	1412.1	1406.1	0.39	+
		1409.5	2.7	+
	1419.5	1418.4	22	+
	1424.7	1430.2	0.38	+
	1452.2			
	1459.6	1456.5	1.9	+
	1517.9			
	1541.0	1539.9	3.9	+
	1567.2			+
	1589.3	1586.4	3.6	+
	1603.6			
	1621.1			
Py	1137.3			
	1182.0	1188.7	0.56	+
	1205.2			
	1216.7	1216.0	1.7	+
	1232.2			
	1247.6	1245.1, 1253.7,1255.7	5.6	+
	1295.4			
	1319.0			
	1337.7			
	1359.0	1356.1,1358.4, 1361.8	16	+
	1372.8			
	1393.2			
	1422.2	1421.1	2.3	+
	1446.0	1440.3	1.5	+
	1484.0			
	1537.5			
	1553.4	1550.9,1553.4,1556.0	13	+
	1567.4			
	1586.4			
	1614.0			
$B_{ghi}P$	1080.2			
	1126.4			
	1146.7	1140.2	5.5	+
	1191.0			
	1223.6	1216.7	0.46	+
		1223.4	4.1	+
	1253.1			
	1303.0			
	1322.9	1311.9	1.9	+
		1324.4	10	+
	1339.8	1331.9	2.3	+
	1346.2			
	1352.9	1350.2	2.1	+
	1366.8	1369.0	8.6	+
	1380.3			
	1388.4	1388.3	0.44	+
	1406.1	1401.3	12	+
		1408.8	0.64	+
	1433.3	1429.4	1.3	+
	1479.7			
	1501.0			
	1510.4			
	1529.7			
	1550.5	1538.6	0.25	+
		1550.1	3.1	+
	1568.0			
	1578.0	1578.2	14	+
	1590.2			
	1604.7			
	1617.0			
	1624.3			

[a] Values taken from: Hudgins & Allamandola [1995a,b]

Pyrene:H_2O photoproducts

In the Py:H_2O case, the spectra in Fig. 4.2, trace (E) and photoproduct peak positions listed in Table 4.3 show that less than half of the new bands can be confidently assigned to Py^+. As discussed above for Ant, the new features between 1260 and 1000 cm^{-1} may be due to the CO stretch in various Py–OH isomers. Likewise, the prominent features at 1373 and 1393 cm^{-1} can be tentatively attributed to modes involving both aromatic CC stretch and C–H in-plane bends of new products. The large number of photoproduct bands between 1500 and 1650 cm^{-1} is striking, especially since only that at 1553 cm^{-1} can be confidently attributed to Py^+ based on matrix isolation spectra.

An attempt has been made to assign the unknown absorptions to more complex Py related species. Peak positions in the Py:H_2O photolysis experiments are compared to peak positions of 43 pyrene related species from the extensive theoretical database of PAH derivatives [Bauschlicher et al. 2010,www.astrochem.org/pahdb]. Some groups of molecules indeed do exhibit strong transitions around the peak positions where the absorption maxima are found for the undefined Py:H_2O photoproducts. These molecules include H, OH, and O added pyrene-based species, such as $C_{16}H_{11}O$, $C_{16}H_{10}O$, $C_{16}H_{12}$, and their cations, in a variety of possible configurations. Although some of these theoretical peak positions overlap with the photoproduct bands, accurate experimental spectral data for these molecules are needed for unambiguous identifications of the reaction products of Py in VUV photolyzed H_2O ice.

Benzo[ghi]perylene:H_2O photoproducts

As molecular size increases, the number of mid-IR transitions grows and, because of spectral congestion, subtraction of neutral precursor bands becomes increasingly difficult. This makes it hard to obtain clear-cut spectra of the products in the $B_{ghi}P$ photoprocessed ice and hence makes identification of individual bands difficult, if not impossible. As with Ant and Py, the spectra in Fig. 4.2 and photoproducts listed in Table 4.3 show that several absorption bands appear which clearly do not have a matrix cation counterband. Unassigned absorptions are found between 1470 and 1540 cm^{-1} and probably involve CC stretching and C–H in plane bending modes. The strong unidentified bands between 1600 and 1640 cm^{-1} are likely caused by the C=O stretching mode of $B_{ghi}P$ ketones formed in the ice.

Keeping the types of photoproducts in the Ant and Py ices in mind, it is most likely that $B_{ghi}P$ derivatives containing H, O, and OH groups are formed upon photolysis. As for the Ant:H_2O and Py:H_2O experiments, we cannot unambiguously assign the $B_{ghi}P$ photoproduct absorption bands. The non-volatile residue of a VUV irradiated $B_{ghi}P$:H_2O (<1:800) ice shows the addition of O, OH and H to the neutral parent [Bernstein et al. 1999]. Thus, as with the other PAH:H_2O systems studied to date, it is likely that many of these new bands in the mid-IR are due to various forms of $B_{ghi}P$–OH, $B_{ghi}P$–O, and $B_{ghi}P$–H_n and possibly their ionized counterparts.

4.4.2 Concentration effects and time dependent chemistry

PAH:H_2O photolysis experiments have been performed for a set of concentrations ranging from ∼ 1:11 to 1:200. Here only the Ant:H_2O experiments are described, but all three investigated PAHs exhibit a similar behavior. Figure 4.3 shows the decay in the amount of the neutral parent Ant in the ice as a function of photolysis time relative to the amount of the freshly deposited Ant before irradiation. Clearly, Ant loss is far more efficient for lower than for higher PAH concentration. Extrapolating these results, they are in good agreement with recent results that are described in Chapter 7 for PAH:H_2O ices at very low concentration (1:∼5,000 to 10,000), where it is found that all the neutral PAH was consumed at the end of a 4 hour photolysis experiment.

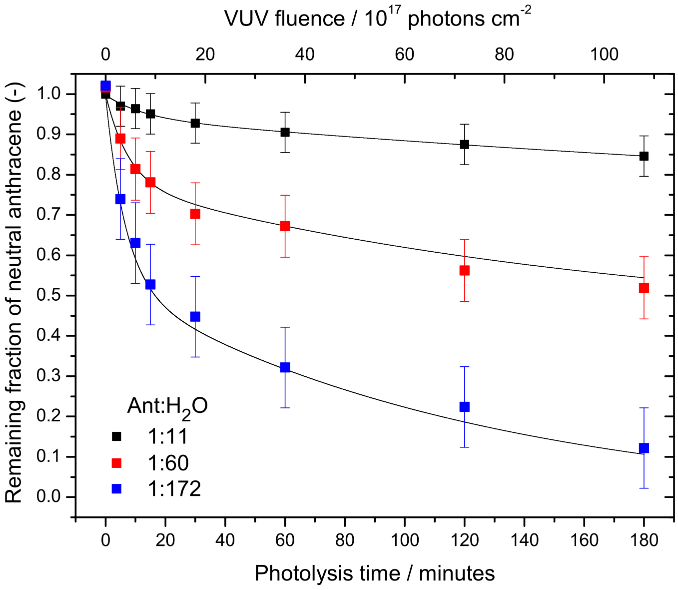

Figure 4.3 Neutral anthracene decay as a function of photolysis time (VUV fluence) and concentration for 1:11, 1:60, and 1:172 Ant:H_2O mixtures at 15 K. Conservative errors are ±5, ±7, and ±10%, respectively, of the initial amount of deposited neutral species. Second order exponential fits to the data (solid lines) are shown as well.

The 15 K neutral Ant decay data in Fig. 4.3 are co-plotted with a fit of the form $\Psi = C_1 \exp(-t/\tau_1) + C_2 \exp(-t/\tau_2)$. Fitting the experimental data required a sum of two exponentials. This indicates that more than one process is responsible for the neutral Ant loss. This is consistent with the optical work presented in Chapters 6 and 7 in which two photochemical reaction networks were described, one for PAH cation formation, the other involving H, O, and OH PAH addition reactions.

The time dependent PAH cation and other photoproduct signals are also studied as a function of photolysis time (VUV dose). For the lowest concentration Py:H_2O ice in our sample (1:200), the time dependent behavior of the photoproduct bands is compared to the optical results presented in Paper II. To this end, the behavior of the cation is traced as a function of VUV time by integrating two of the most isolated prominent Py^+ absorption bands in the spectra, located at 1359 and 1554 cm^{-1}. Figure 4.4 shows the time evolution of the column density of the Py^+ species derived from these bands (multiplied by a factor of 10 to facilitate the display and normalized to the initial amount of neutral Py) together with the time evolution of the relative amount of neutral Py in the ice based on the subtraction factor, Y. The photolytic behavior of the integrated absorption of the strongest undefined photoproduct band at 1567 cm^{-1} (multiplied by a factor of 100 to facilitate the display) is also shown. Because no information is available on the band strength of this species, we cannot convert this integrated absorbance into a column density relative to the amount of deposited neutral PAH. The Py^+ bands and 1567 cm^{-1}photoproduct band show a different time dependence and clearly do not correlate. While the integrated absorbance of Py^+ reaches a maximum after some 10 minutes and then declines, the photoproduct signal grows and levels slightly off towards the end of the experiment.

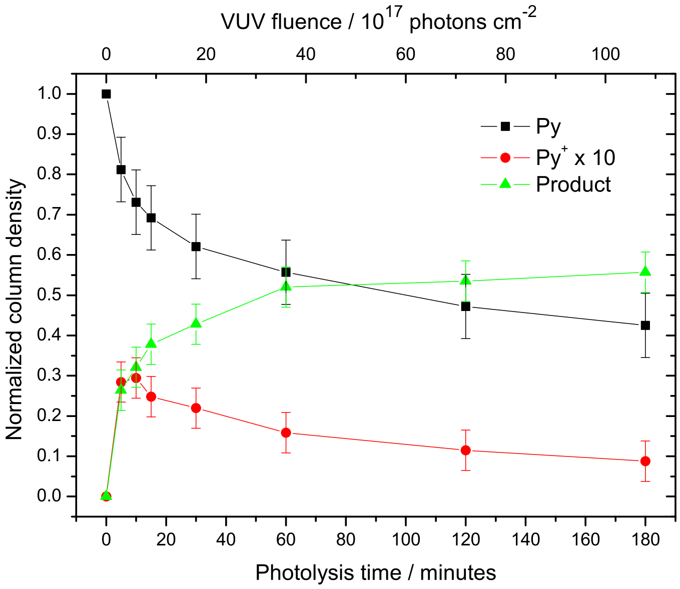

Figure 4.4 Evolution of Py, Py^+ and a single Py photoproduct for a 1:200 Py:H_2O ice at 15 K as a function of photolysis time (VUV fluence). Photoproduct species are tracked using the 1359 and 1553 cm^{-1} Py^+ and 1567 cm^{-1} Py photoproduct bands.

The error in the Py^+ column density is reduced by taking the average column density based on the two strongest cation absorptions located at 1359 and 1554 cm^{-1}. We estimate the error in the *relative* Py^+ abundance to be ±5% of the deposited amount of neutral Py and, thus, the shape of the time dependence curve is well defined. The error in the absolute number, however, is much larger because the argon band strength values from Table 4.3 have to be used for the analysis and because of ill-defined baselines caused by spectral congestion. Therefore, the error in the *absolute* amount of Py^+ produced can be quite high. For this reason, reliable quantitative time dependent data can only be obtained in the optical spectral regime, where cation absorptions are isolated and spectra are taken on a much shorter time scale. This is described in Chapter 7. The error in the absolute number of neutral Py molecules consumed, on the other hand, is low (±7%). Since no information is available on the band strength of the 1567 cm^{-1} unidentified photoproduct absorption band, no quantitative information can be obtained on the formation of the species responsible for this band.

Using the PAH cation in Ar band strengths values, it is also possible to derive N_{frac}, the first order estimate of the fraction of the used-up neutral PAH that is converted into cation species versus other photoproducts. The amount of deposited neutral, N_{PAH}, is known from concentration measurements (Eqns. 4.1 and 4.2) and the amount of consumed neutral is given by $(1 - Y)N_{\mathrm{PAH}}$. The cation column density, N_{PAH^+}, is calculated with Eq. 4.2 and the band strength values reported in Table 4.3. The difference between the two, $(1 - Y)N_{PAH} - N^+_{PAH}$, makes up the photoproduct column density. The fraction of consumed neutral PAH molecules converted into PAH^+ is given by:

$$N_{\mathrm{frac}} = \frac{N_{\mathrm{PAH^+}}}{[(1-Y)N_{\mathrm{PAH}}]}. \tag{4.4}$$

Values N_{frac} have been derived for different conditions for the three PAHs studied here. After 5 minutes of VUV photolysis of the Py:H_2O (1:200) mixture, roughly 15% of the used up neutral Py is converted into Py^+ and 85% in other charged and/or neutral photoproducts. The Py^+ absorption peaks at about 10 minutes of VUV photolysis, a value that is also found in the optical study for much lower PAH concentrations (1:5,000-1:10,000). A mid-IR experiment on an ice sample with a higher Py concentration (1:60) results in an even lower N_{frac} value of about 0.05, a trend that suggests that ionization is more important in low concentration ices. Similar trends are found for low concentration mixtures of $B_{\mathrm{ghi}}P$ — a (1:160) mixture gives $N_{\mathrm{frac}} \approx 0.20$ — and Ant — a (1:172) mixture gives $N_{\mathrm{frac}} \approx 0.10$ — after 5 minutes of VUV photolysis.

The quantitative analysis in Chapter 6 points out that there is a $Py^+ + e^-$ recombination channel. It is argued that the recombination reaction is most likely a local process, i.e., the electron released after ionization remains in the vicinity of its parent Py molecule. Putting this in perspective with the data presented here, this means that the recombination channel can well be more efficient in ices of higher concentration; the chance of recombination with an electron released from a neighboring Py molecule is larger. In the higher concentration experiments presented here, not all the neutral PAH is used up. Presumably some of the deposited PAHs are shielded from VUV irradiation and therefore not ionized. This may also explain the difference between the ionized fraction in low versus high concentration ices. Furthermore, as discussed before, ionization seems to be less efficient at high concentration ices, because chemical reactions between PAHs and radical species likely dominate the loss of the neutral species.

In summary, all PAH molecules trapped in H_2O ice exhibit a similar photoprocessing behavior. Ionization is more important in low concentration ices. However, after 5 minutes of VUV photolysis, most of the destroyed neutral species are converted into different PAH based photoproducts other than the cation. The concentration of the ice sample has a large influence on the efficiency of the chemical reactions. PAHs in lower concentration ices are used up faster and more efficiently, whereas in higher concentration ices, the PAH consumption is far less efficient. Although no mid-IR VUV photolysis measurements have been performed on coronene:H_2O ice mixtures, the near-UV/Vis study presented in Chapter 7 shows that also coronene exhibits a similar behavior.

4.4.3 Ionization efficiency in CO ice

A control experiment has been performed on a Py:CO ice sample at 15 K to investigate the ionization efficiency of PAHs upon photolysis in a CO matrix. After a short photolysis time (150 s), the ice exhibits weak absorptions at 1861 and 1090 cm^{-1}. These mid-IR absorption bands were previously assigned to the $HCO^{\cdot}$ radical by Milligan & Jacox [1969]. This observation is consistent with experiments reported in Chapter 6, where the electronic $HCO^{\cdot}$ signature is found in the 500 to 660 nm spectral range. There, it is also found that, in a CO matrix, the Py ionization efficiency is close to zero, unless a certain level of H_2O contamination in the CO matrix is reached. In the mid-IR experiment performed here, VUV photolysis of Py in a CO matrix indeed does not show any sign of pyrene ionization, but also does not show any other PAH:H_2O photoproduct bands. We do confirm the low ionization efficiency and the appearance of small $HCO^{\cdot}$ absorptions in a nearly pure CO ice, but no absorptions caused by $PyH^{\cdot}$ species, as in the optical study, are observed. The fact that PAH absorption band strengths typical of electronic transitions are 100 times stronger than those for vibrational transitions, and that the level of H_2O contamination, i.e. the source of H-atoms for the reaction $H^{\cdot} + CO^{\cdot} \rightarrow HCO^{\cdot}$, is lower in the experiments described here, probably explains why the $PyH^{\cdot}$ mid IR absorption bands were not detected. The important conclusion that follows from this control experiment is that H_2O catalyzes the ionization process. This is also consistent with the observation that ionization seems to be more efficient in low concentration PAH:H_2O ices.

4.4.4 Temperature effects

VUV photolysis experiments on PAH:H_2O samples (~1:60) were also conducted at a higher temperature (125 K). Consistent with the behavior reported in the optical studies Chapter 6, we find that the neutral PAH loss is still efficient, while the ionization channel is strongly suppressed. The less efficient formation of the cation can point to a lower rate of ionization, but it is also possible that the recombination channel becomes dominant at higher temperatures. The result is that, at higher temperatures, the parent PAHs are more efficiently converted into species other than the PAH cation.

In the high temperature Py:H_2O experiment, for example, some pronounced vibrational bands appear immediately upon VUV photolysis. These bands, located at 1137.8, 1216.7, 1386.1 cm^{-1} and a broad feature consisting of bands at 1553.5, 1566.1, and 1583.1 cm^{-1}, become strongest after 5 minutes of photolysis and then subside. Only the bands at 1216.7 and 1553.5 cm^{-1} are at positions of Py^{+} absorptions. The remaining bands are also apparent in the low temperature spectra, but shifted by up to 3 cm^{-1} and, in the absence of many of the other bands, seem to be more pronounced in the high temperature photolysis dataset.

For the PAH:H_2O ices irradiated at high temperatures there is a very broad overlapping substructure superimposed on the baseline of their mid-IR spectra. This is presumably caused by blended photoproducts and possibly PAH aggregates. Together with the knowledge that more complex species have been detected in other experiments [Bernstein et al. 1999, 2002b, Ashbourn et al. 2007], we conclude that predominantly a mixture of PAH–X_n species, with X being H, O, or OH, may have been formed and that only one or a few chemical reaction channels dominate, resulting in the observed bands.

Ices at a temperature of 125 K are known to be of different structure than ices at low temperature [Jenniskens & Blake 1994]. This structural difference — amorphous at 15 K vs. cubic crystalline at 125 K — may explain the different photochemical behavior. However, in Chapter 6 we investigated the influence of the ice structure on the photoionization and found that ices annealed at 125 K and subsequently cooled down to 25 K exhibit similar ionization behavior as those grown and photolyzed at 25 K. Hence, they ascribed the different behavior at high temperatures to the larger mobility of radical species in the ice. The experiments presented here, point out a similar behavior.

4.5 The non-volatile residue

Figure 4.5 shows the 4000 to 500 cm^{-1} room temperature spectra of the non-volatile residues produced by the photolysis of the three PAH:H_2O ices considered here. The spectra are measured as described in §7.2 and provide additional information on the photoproducts which have accumulated over a series of experiments for a particular PAH. These residues, complex mixtures of the non-volatile photoproducts, may also contain some of the parent PAH as well as some trapped H_2O or H_2O that accreted during the cooling of the sample window. Because the H_2O absorption bands in these spectra are much smaller than in the experiments on PAH:H_2O ice mixtures, the spectra can be investigated over the full range from 4000 to 500 cm^{-1}. In the ROI, the spectra show continuous, undulating absorptions from about 1750 to 1130 cm^{-1} with several distinct features superposed. Additional spectral features are found between 3750 and 2750 cm^{-1}. The chemical subgroups indicated by these features are consistent with the addition of O, H, and OH to the parent PAH.

The aromatic-rich nature of these residues makes their spectra qualitatively different from the 13 residue spectra previously analyzed to compare with the spectrum of the diffuse interstellar medium [Pendleton & Allamandola 2002]. While it is impossible to identify the molecules comprising the residues using infrared spectroscopy, it is possible to characterize the species and subgroups present by chemical type (i.e aliphatic versus aromatic hydrocarbons, carbonyl vs. alcohol carbon-oxygen links, etc.). The following analysis utilizes the characteristic group frequencies as well as relative and intrinsic band strengths as described in [Bellamy 1960, Silverstein & Bassler 1967, Wexler 1967]. The prominent features in these spectra are discussed systematically from higher to lower frequency.

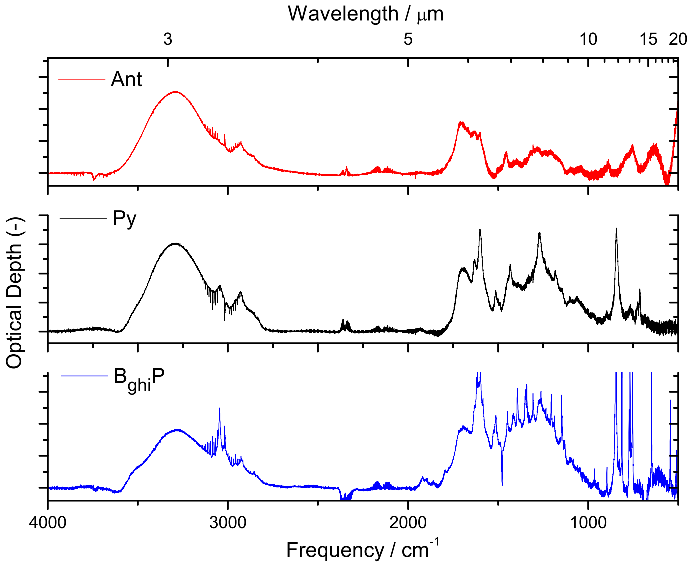

Figure 4.5 Overview of the room temperature spectra of the residues accumulated during the photolysis of Ant, Py, and $B_{ghi}P$ containing H_2O ices.

- *The 3300 cm^{-1}, O–H stretch:* A large part of this band can be ascribed to H_2O accretion to the cold sample, since the residue spectra are based on background spectra taken of a cold sample window. However, the weak sideband near 3550 cm^{-1} points to the O–H stretching mode in phenols and, thus, the presence of aromatic alcohols in the residues.

- *The 3060 cm^{-1} aromatic C–H stretch:* The next prominent band, peaking near 3060 cm^{-1}, is due to the aromatic C–H stretch belonging to either the parent PAH or PAH photoproducts.

- *The 2990–2850 cm^{-1} aliphatic C–H stretch:* The addition of H to the aromatic parent forms a new type of functional group, which is evident from the broad aliphatic C–H stretch feature between about 2850 and 2990 cm^{-1}. The two subpeaks at about 2925 and 2860 cm^{-1} are characteristic of methylene (–CH_2–) groups, showing that the major H-addition channel proceeds by addition, not ring opening. If ring opening had been an important channel, bands due to the C–H stretches of methyl (–CH_3) groups near 2960 and 2870 cm^{-1} would have been expected. The assignment to methylene groups is further supported by the prominent band near 1450–1460 cm^{-1} in the lower two spectra shown in Fig. 4.5. A band in this region indicates the –CH$_2$– scissoring mode in cyclic saturated compounds such as cyclohexane and cyclopentane. The spectrum of B$_{\mathrm{ghi}}$P is consistent with this analysis, but the bands are weaker. Given that the intrinsic strength of the aromatic C–H stretch is 10 times weaker than the intrinsic strength of the aliphatic C–H stretch per C–H [Wexler 1967], the increasing ratio of the aromatic band intensity to the aliphatic band intensity with PAH size indicates that H addition becomes less effective as the PAH size increases.

- *The 1700 cm^{-1} carbonyl C=O stretch:* As with the O–H stretching band near 3 μm, some of this band may be attributed to the bending mode of H_2O molecules frozen onto the cold sample window. However, it is likely that part of this band is caused by the C=O stretch in carbonyl groups. In this case, quinone-like structures would be expected with the double bond to O participating in the conjugation of the molecule as a whole.
- *The band at 1625 cm^{-1}:* A distinct feature is evident at this frequency in all three spectra. The value is low for isolated carbonyls, but is characteristic for the carbonyl C=O stretch in molecules with intramolecular hydrogen bonding with an OH group.
- *The 1600 cm^{-1} aromatic CC stretch:* A well defined, but generally weak band centered near 1600 cm^{-1} is characteristic of the CC skeletal stretch in aromatic molecules. The prominence of this band in all three residue spectra shows, not surprisingly, that they are primarily aromatic in nature.
- *The bands between 1520 and 1500 cm^{-1}:* Several features in this region become more prominent with parent PAH size. We are unable to attribute these bands to specific molecular vibrations.
- *The 1450 and 1440 cm^{-1} –CH$_2$– scissoring vibration:* This band has been discussed in the paragraph describing the aliphatic C–H vibrations above.
- *The 1260 cm^{-1} band in the pyrene photoproduct:* While this prominent band falls in the 1300–1000 cm^{-1} region which is characteristic of aromatic C–H in-plane bending vibrations, other likely compounds also absorb in this region. For example, the C–O stretch in aromatic alcohols has a strong band between 1260 and 1180 cm^{-1}.
- *The 900 to 500 cm^{-1} aromatic C–H out-of-plane bends:* This region encompasses the very strong C–H out of plane vibrations which are diagnostic of substitution patterns on the edge rings. In this case, these bands serve primarily as an indication of the presence of aromatic compounds.

All the pure PAHs under investigation here exhibit strong fluorescence upon excitation with a hand-held UV lamp. It is noteworthy, that after performing the experiments, the residues do not exhibit any fluorescence. This is consistent with the residues being processed PAHs with a different chemical identity.

4.6 Astrophysical implications

The 5–8 μm spectra of embedded low- and high-mass objects are generally dominated by two strong bands originating from interstellar ice, one centered near 6.0 μm and primarily attributed to the H_2O bending mode, and the other near 6.8 μm. Close inspection of the spectra of many different molecular clouds shows that, while features near 6.0 and 6.8 μm are nearly always present, band positions, profiles, and relative strengths of other features vary somewhat from one object to another, revealing changes in ice composition and structure [e.g. Keane et al. 2001b, Keane 2001, Gibb & Whittet 2002, Schutte & Khanna 2003, Boogert & Ehrenfreund 2004, Boogert et al. 2008]. Besides the two dominant absorptions, signals are also found from other species that absorb in the 5–8 μm region. An overview of absorptions by molecular species in this wavelength region is given in Table 4.4. The knowledge of interstellar ice composition and chemistry is based on over twenty five years of dedicated studies on laboratory ice analogs to interpret these observations [see references mentioned above and Ehrenfreund & Charnley 2000, van Dishoeck 2004,and references therein]. However, to date, such studies considering PAHs in ices and their contribution to the 5–8 μm absorption complex are lacking. Here, we discuss the possible contribution of PAHs in ices to the spectra of both high- and low-mass objects, using the laboratory data presented in the previous sections.

Table 4.4 Molecules, their vibrational modes and solid state absorption band positions thought to contribute to the 5–8 μm ice absorption complex towards low- and high-mass embedded objects

Molecule	Mode	λ (μm)	ν (cm^{-1})	Ref.
H_2O	H–O–H bend	5.4–9	1852–1111	1
	Libr. overtone			1
H_2CO	C=O stretch	5.83	1715	2
CH_3HCO	C=O stretch	5.83	1715	3
HCOOH	C=O stretch	5.85	1709	3,4
NH_3	H–N–H bend	6.16	1623	5
PAH?	**CC stretch**	**6.20**	**1613**	**6**
$HCOO^-$	C=O stretch	6.33	1580	3
H_2CO	H–C–H bend	6.68	1497	2
NH_4^+	Deformation	6.85	1460	7
HCOOH	C–H stretch	7.25	1379	3,4
$HCOO^-$	C–H deform.	7.40	1351	3
SO_2	Asymm. stretch	7.58	1319	8
CH_4	Deformation	7.68	1302	9

References: [1] D'Hendecourt & Allamandola [1986]; [2] Schutte et al. [1993]; [3] Schutte et al. [1999]; [4] Bisschop et al. [2007a]; [5] Kerkhof et al. [1999]; [6] Keane et al. [2001b] Kerkhof et al. [1999] ; [7] Schutte & Khanna [2003]; [8] Boogert et al. [1997]; [9] Boogert et al. [1996].

4.6.1 High-mass protostars

Figure 4.6 shows the ~5.3–8.7 μm (1900–1150 cm^{-1}) ISO SWS spectrum towards the high-mass protostar W33A (based on data from Keane et al. [2001b]) and the residual that remains after subtracting the H_2O bending and librational overtone bands in a manner similar to that described in §7.2. Based on a sample of five ISO spectra towards high-mass protostars, Keane et al. [2001b] attributed the bulk of the 6.0 μm ice band to amorphous H_2O ice, with additional absorptions on the short wavelength wing near 5.8 μm and on the long wavelength wing near 6.2 μm. They assigned the short wavelength absorption at 5.83 μm to the carbonyl CO stretch in formaldehyde and related species based on laboratory studies and tentatively suggested that the long wavelength absorption at 6.2 μm is due to the CC stretch of aromatic structures in PAHs or amorphous carbon particles. Keane et al. [2001b] also showed that the 6.85 μm band is comprised of two components, one centered near 6.75 μm, and the other at 6.95 μm, but they did not assign possible band carriers. Noteworthy in Fig. 4.6 are also the weak undulating features between ~7.2 and 7.9 μm. Assignments of these absorption features are discussed in Schutte & Khanna [2003].

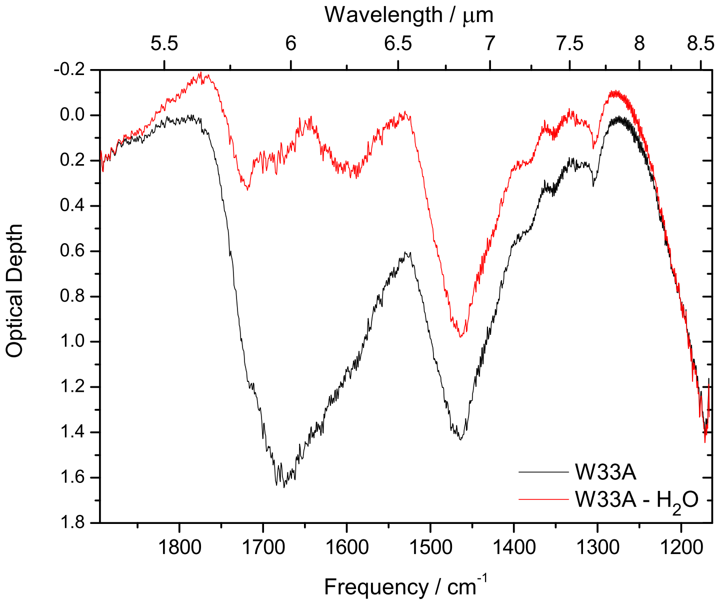

Figure 4.6 The 5.3 to 8.7 μm ISO SWS spectrum of the high-mass protostar W33A plotted in optical depth together with the spectrum obtained after subtraction of the H_2O bending and librational overtone modes. The figure is adapted, with permission, from Keane et al. [2001b].

4.6.2 Low-mass protostars

Figure 4.7 shows the ~5.3–8.1 μm (1900–1234 cm^{-1}) spectrum of the low-mass YSO RNO 91, reproduced from Boogert et al. [2008]. In this more recent, extensive spectroscopic study of the 5–8 μm region of 41 low luminosity, low-mass protostars measured with the *Spitzer* telescope, Boogert et al. [2008] showed that, once the contribution from H_2O ice is removed, the 5–8 μm residual spectrum can be split into five components (C1–C5). The large sample of objects permitted Boogert et al. to extract rough band profiles, although not uniquely assignable to specific band carriers, and to determine band to band variations for all five components. The positions of the C1 through C4 components are similar to those described in Keane et al. [2001b] and part of these bands can be attributed to the species mentioned in Table 4.4. C5, a very broad, underlying component that stretches from about 1725 to 1250 cm^{-1} (5.8–8 μm) cannot be explained by any of these species and is most likely a blend of more than one species. As with the spectrum of W33A, RNO 91 also shows several weaker features between 7.2 and 7.9 μm.

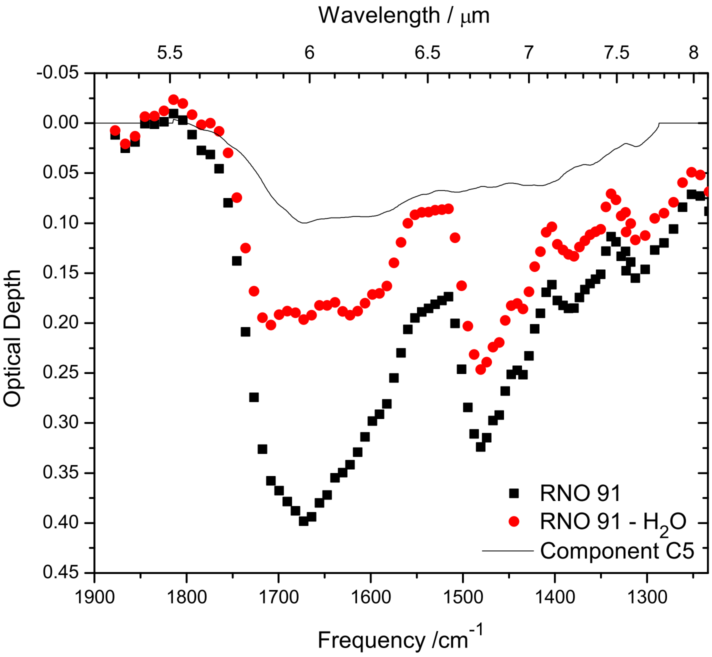

Figure 4.7 The 5.3 to 8.1 μm *Spitzer* spectrum of the low-mass YSO RNO 91 plotted in optical depth together with the spectrum obtained after subtraction of the H_2O bending, and librational overtone modes. The C5 complex absorption as described by Boogert et al. [2008] is also indicated (solid line). The figure is adapted, with permission, from Boogert et al. [2008].

4.6.3 PAH contributions to the 5–8 μm absorption

Here, we discuss the possible contribution that interstellar ices containing PAHs and their photoproducts could make to the spectra of molecular clouds in the 6.1–8.3 μm (1650–1200 cm^{-1}) region. The comparison is restricted to the three PAHs studied here. These three PAHs, Ant in particular, are on the low end of the PAH size distribution expected in space. As a consequence, the relative intensities of the modes are different than those expected for larger PAHs in the interstellar case. Infrared bands which result from the C–H functional group are expected to be less intense in space with respect to modes resulting from aromatic CC stretches, since astronomical PAHs are large and contain relatively more CC than CH bonds. Figure 4.8 shows the photoproduct bands that appear after 180 minutes of VUV photolysis of the PAHs considered here in H_2O ice. All VUV processed PAH:H_2O mixtures under investigation exhibit bands clustered around 1600 cm^{-1}. The band at 6.2 μm, observed towards both low- and high-mass sources and also shown in Fig. 4.8, could well be caused by a superposition of many different large PAH and

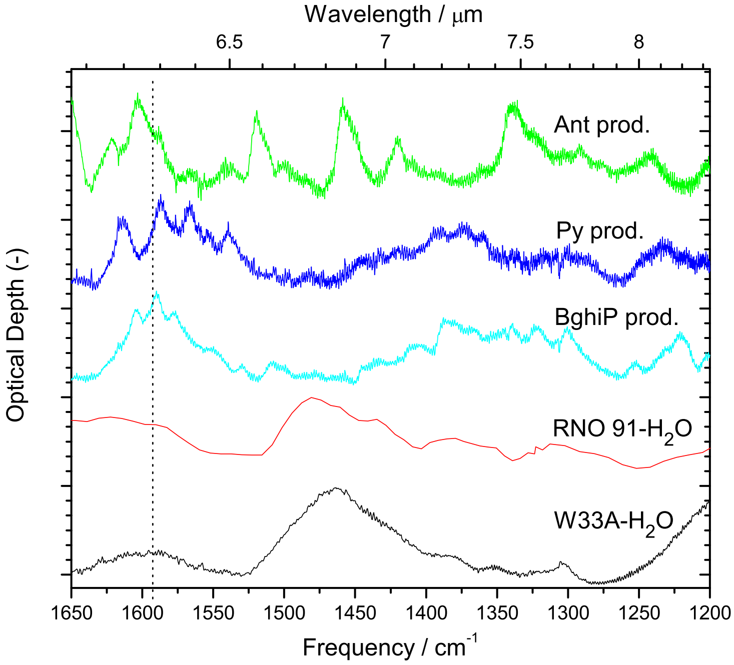

Figure 4.8 The 6.1–8.3 μm (1650 cm^{-1}–1200 cm^{-1}) region of the spectra of W33A and RNO 91 after subtraction of the H_2O bending and librational overtone contributions plotted in absorbance compared to the spectra of the products after 180 minutes of PAH:H_2O ice photolysis. The dotted line guides the eye to the ~6.2 μm ice absorption and main PAH:H_2O ice photoproduct bands.

PAH photoproduct absorption bands, or organic refractory material as discussed in §4.5. Additional minor PAH absorptions throughout the 6–10 μm spectrum can be (partly) responsible for the underlying C5 complex absorption which is also indicated in Fig. 4.5 as well as the weak undulating structure between 7.2 and 7.9 μm.

The observational data also permit one to put crude limits on the column densities of PAHs condensed in interstellar ice. Assuming that the 6.2 μm feature in the residual spectrum shown in Fig. 4.6 is due primarily to the aromatic CC stretching vibration in PAHs and closely related aromatic material frozen in H_2O-rich interstellar ice, one can estimate their column density (N_{PAH}) with Eq. 4.2. The integrated optical depths of the component are ~16 cm^{-1} for W33A and ~1.3 cm^{-1} for RNO 91. The experimental data indicate that a certain number of neutral PAH species is converted into PAH photoproduct species, as indicated by $(1 - Y)N_{\mathrm{neutral}}$, where N_{neutral} is the column density of deposited neutral molecules. This allows us to calculate an average band strength for the species responsible for the absorption band around 6.2 μm with Eq. 4.2. The resulting average band strength (A_{prod}) for the formed PAH products is 1.2×10^{-17} cm molecule^{-1}. With these assumptions, the column density of neutral PAHs and PAH photoproducts frozen in H_2O is 1.3×10^{18} molecules cm^{-2} for the high-mass object (W33A) and 7.6×10^{16} molecules cm^{-2} for the low-mass object (RNO 91). Given that the column densitiy of H_2O ice along the line of sight to these objects is 4×10^{19} molecules/cm^2 and 4.3×10^{18} molecules/cm^2 [Keane et al. 2001b, Boogert et al. 2008], respectively, this implies PAH and PAH photoproduct abundances between 2–3% with respect to water. This concentration range is reasonable given the PAH abundances derived from mid-IR emission features [Puget & Leger 1989, Allamandola et al. 1989].

4.7 Conclusions

The manuscript describes mid-IR absorption spectroscopy of PAH:H_2O ices, their VUV induced photochemistry and photoproducts. The main conclusions of this manuscript are summarized below.

1. Band positions, FWHMs, and relative intensities of anthracene, pyrene and benzo-[ghi]perylene in H_2O ice in the 1650–1000 cm^{-1} spectral window are compared to their matrix isolation data. Additionally, band strengths are derived for these species isolated in an astrophysically relevant H_2O ice at 15 K.

2. VUV photolysis of PAH containing H_2O ice causes the embedded PAH to ionize and react with H_2O photoproducts. The band positions of PAH cations trapped in H_2O ice are measured and compared to PAH cation values from previous argon matrix isolation studies. Additionally, peak positions of PAH:H_2O photoproducts other than the cation are determined and tentatively assigned to PAH–X_n species, with X being O, H or OH.

3. The PAH:H_2O ice photochemistry is tracked as a function of VUV fluence by monitoring the integrated absorbances of the parent PAH and PAH photoproduct bands

periodically during photolysis for several hours. In all cases, the PAH cation bands peak after some 5 to 10 minutes and then slowly decline while other photoproduct bands continue to grow steadily and starts to level off after about an hour of irradiation.

4. The VUV induced photochemistry of the PAH pyrene in a CO ice was also studied. In this case, PAH ionization is inefficient compared to a VUV irradiated PAH:H_2O ice and seems to depend on the presence of trace amounts of H_2O.

5. The photochemistry is also tracked as a function of PAH:H_2O ice concentration for PAH:H_2O ratios ~1:10 to 1:200. The fraction of neutral molecules converted into the cation is found to be larger in ices of lower concentration, consistent with the previous conclusion.

6. The ice photochemistry is monitored for two ice temperatures, 15 and 125 K. PAH cation formation is important and dominates the first few minutes in the low temperature case. However, ionization is far less efficient in the 125 K ice while the loss of the neutral parent PAH is equally efficient. It is concluded that reactions with H_2O photoproducts are the dominant channel at high temperatures.

7. Spectra from 4000 to 500 cm^{-1} of the non-volatile room temperature residue that builds up over the coarse of the experiments on each PAH species considered here are analyzed. These aromatic-rich residues contain OH, CO, and CH_2 groups as evidenced by absorptions in the OH stretching region (2.8 μm), CH stretching region (3.3–3.4 μm) and in the C=O, C–O, and aromatic CC region (5.6–10 μm).

8. The infrared data of the PAH photoproducts are compared to 5–8 μm ISO and *Spitzer* spectra of a high- and low-mass protostar. It is shown that PAH:H_2O ice photoproducts are plausible candidates for the 6.2 to 6.3 μm absorption band associated with interstellar ice and that these contribute to some of the weak structure between about 6.9 to 8 μm. The band strength of the 6.2 to 6.3 μm band of the PAH:H_2O ice photoproducts reported here is determined. From this we derive an upper limit for interstellar abundance of PAHs and PAH:H_2O ice photoproducts with respect to H_2O ice of 2–3%.

Part II

Near-UV/VIS absorption spectroscopy

CHAPTER 5

Real time optical spectroscopy of VUV irradiated pyrene:H_2O interstellar ice[1]

This chapter describes a near-UV/VIS study of a pyrene:H_2O interstellar ice analogue at 10 K using optical absorption spectroscopy. A new experimental approach makes it possible to irradiate the sample with vacuum ultraviolet (VUV) light (7–10.5 eV) while simultaneously recording spectra in the 240–1000 nm range with sub-second time resolution. Both spectroscopic and kinetic information on VUV processed ices are obtained in this way. This provides a powerful tool to follow, in situ and in real time, the photophysical and photochemical processes induced by VUV irradiation of a polycyclic aromatic hydrocarbon containing inter- and circumstellar ice analogue. Results on the VUV photolysis of a prototype sample — strongly diluted pyrene in H_2O ice — are presented. In addition to the pyrene cation (Py^+), other products — hydroxypyrene (PyOH), possibly hydroxypyrene cation ($PyOH^+$), and pyrene/pyrenolate anion (Py^-/PyO^-) — are observed. It is found that the charge remains localized in the ice, also after the VUV irradiation is stopped. The astrochemical implications and observational constraints are discussed.

---

[1] Based on: J. Bouwman, D. M. Paardekooper, H. M. Cuppen, H. Linnartz, L. J. Allamandola, Astrophysical Journal, 700, 56-62 (2009)

5.1 Introduction

At present, more than 150 different inter- and circumstellar molecules have been observed in space. The chemical diversity is striking, and both simple and very complex as well as stable and transient species have been detected. Among these unambiguously identified species polycyclic aromatic hydrocarbon molecules (or PAHs) are lacking even though PAHs are generally thought to be ubiquitous in space [e.g., van Dishoeck 2004]. Strong infrared emission features at 3.3, 6.2, 7.7, 8.6, and 11.2 μm are common in regions of, for example, massive star formation and have been explained by PAH emission upon electronic excitation by vacuum ultraviolet (VUV) radiation. Consequently, PAHs are expected to play a key role in the heating of neutral gas through the photoelectric effect. PAHs are also considered as important charge carriers inside dense molecular clouds, and relevant for molecule formation through ion — molecule interactions [Gillett et al. 1973, Puget & Leger 1989, Allamandola et al. 1989, Kim et al. 2001, Smith et al. 2007, Draine et al. 2007]. Nevertheless, the only aromatic species unambiguously identified in space is benzene, following infrared observations [Cernicharo et al. 2001].

In recent years electronic transitions of PAH cations have been studied in the gas phase with the goal to link laboratory data to unidentified optical absorption features observed through diffuse interstellar clouds. Following matrix isolation spectroscopic work [Salama & Allamandola 1991], gas phase optical spectra have been recorded for several PAH cations [Romanini et al. 1999, Bréchignac & Pino 1999] by combining sensitive spectroscopic techniques and special plasma expansions [Motylewski et al. 2000, Linnartz 2009]. Such optical spectra have unique features and therefore provide a powerful tool for identifying PAHs in space. So far, however, no overlap has been found between laboratory spectra of gaseous $PAHs^+$ and astronomical features.

In dense molecular clouds, most PAHs should quickly condense onto the H_2O- rich icy grain mantles, quenching the IR emission process. Here, they will participate in ice grain chemistry. More than 25 years of dedicated studies, mainly in the infrared, have proven that a direct comparison between laboratory and astronomical ice spectra paints an accurate picture of the composition and the presence of inter- and circumstellar ices, even though solid-state features are rather broad. The spectral features (band position, band width (FWHM) and the intensity ratio of fundamental vibrations) depend strongly on mixing ratio and ice matrix conditions and this provides a sensitive analytical tool to identify ice compositions in space [e.g., Boogert et al. 2008, Öberg et al. 2008].

In the past, several experiments have been reported in which the formation of new molecules was proven upon VUV irradiation of astronomical ice mixtures, typically under high vacuum conditions [e.g., Mendoza-Gomez et al. 1995, Bernstein et al. 1999, Gudipati & Allamandola 2003, Ruiterkamp et al. 2005, Peeters et al. 2005, Elsila et al. 2006]. Many of these studies were not in situ, i.e., reactants were determined after warm up of the ice, and although VUV-induced photochemistry at low temperatures is expected to take place, it is not possible to fully exclude that at least some of the observed reactants may have been formed during the warm-up stage. More recently, in situ studies have become possible using ultrahigh vacuum setups in which ices are grown with monolayer precision and reactions are monitored using reflection absorption infrared spectroscopy and temperature programmed desorption. Recent results show that H-atom bombardment of CO and O_2 ice results in the efficient formation of H_2CO/CH_3OH and H_2O_2/H_2O, respectively [Watanabe & Kouchi 2002, Ioppolo et al. 2008, Miyauchi et al. 2008]. Overall, such studies are still restricted to the formation of rather small species, with ethanol as the most complex molecule investigated in this way [Bisschop et al. 2007b]. Moreover, the reactants and products should not have overlapping bands in order to track them separately.

In the present work, a new approach is presented that extends our previous FTIR work on interstellar ice analogues to the UV/VIS. With the new setup it is possible to record, *in situ*, the VUV photochemistry of PAHs and PAH derivatives in water ice at 10 K in real time. In the next section, this new approach is discussed in detail. The first results for the PAH pyrene ($C_{16}H_{10}$, or Py) and its photoproducts, pyrene cation ($C_{16}H_{10}^+$, or Py^+), hydroxypyrene (PyOH), hydroxypyrene cation ($PyOH^+$), and pyrene/pyrenolate anion (Py^-/PyO^-) in H_2O ice are presented in §5.3. Finally, the astrophysical relevance of this work is discussed in §5.5. The latter is twofold. First, time-dependent results of VUV irradiated ice provide general insight into possible reaction pathways upon photoprocessing of PAH containing water ice. Second, the results provide a spectroscopic alternative to search for PAH and PAH-related optical features in the inter- and circumstellar medium (ISM/CSM) through electronic solid-state absorptions.

5.2 Experimental

A schematic of the experimental setup is shown in Fig. 5.1. The experiment consists of three units: a vacuum chamber in which the ice is grown, a special VUV irradiation source that is used for the photo-processing of the ice and a source emitting broadband light that is focused into the ice and subsequently detected using a monochromator equipped with a sensitive CCD camera.

The vacuum chamber consists of an ISO-160 6-cross piece. A 300 l s^{-1} turbomolecular pump, backed by a 10 m^3 hr^{-1} double stage rotary pump, is used to evacuate the chamber and to guarantee an operating pressure of $\sim 10^{-7}$ mbar. A catalytic trap is mounted on the pre-vacuum pump to prevent pump oil from entering the vacuum chamber.

The top flange of the cross piece holds a differentially pumped rotary flange on which is mounted a closed cycle helium refrigerator equipped with a cold finger. A MgF_2 sample window with a diameter of 14 mm, clamped into an oxygen free copper holder between indium gaskets, is mounted on the cold finger and centered on the optical axis of the setup. This allows for rotation of the sample window through 360° under vacuum. The sample window can be cooled down to 10 K and a thermocouple (Chromel-Au/Fe (0.07%)) and a temperature controller guarantee accurate temperature settings with 0.1 K precision.

The $Py{:}H_2O$ sample is prepared by vapor depositing pyrene from a solid sample (Aldrich 99%) heated to 40°C, together with milli-Q water vapor from a liquid sample. The entire inlet system is maintained at ≥40°C during deposition and comprises gas bulbs containing the sample material and tubing for directed deposition, approximately 15 mm from the sample window. The flow rate of the sample material is set by a high precision

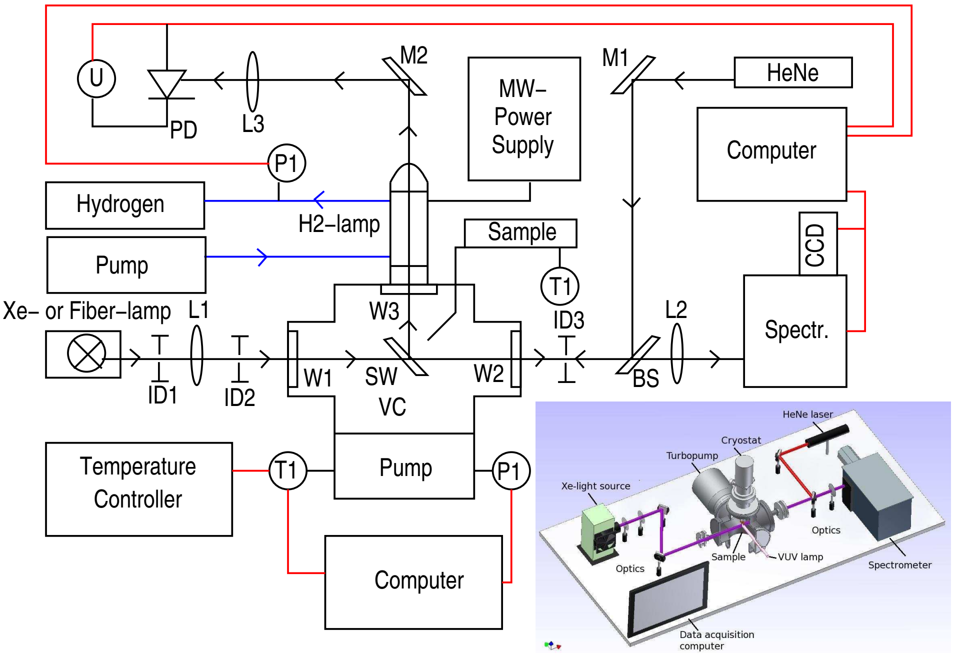

Figure 5.1 A schematic drawing of the experimental setup. BS: beam splitter; IDX: iris diaphragm X; LX: lens X; MX: mirror X; PD: photodiode to monitor interference fringes; PI: pressure indicator; SW: MgF_2 cold sample window; TI: temperature indicator; U: voltage meter; VC: Vacuum Chamber and WX: MgF_2 window X. The light paths are indicated by arrows, the data wiring is indicated in red lines, and the hydrogen flow is indicated by blue lines (see online color version). The inset shows a three-dimensional drawing of the experimental setup.

dosing valve. Condensation inside the tube is prohibited by additional resistive heating and the temperature settings are monitored by K-type thermocouples. The resulting ice film thickness is accurately measured by recording the number of interference fringe maxima (m) of a HeNe laser (λ =632.8 nm) which strikes the sample window at an angle of θ=45°. To monitor film growth and thickness, the intensity of the reflected laser light is measured with a sensitive photodiode. The ice thickness is subsequently determined by:

$$d = \frac{m\lambda_{\mathrm{HeNe}}}{2n_{\mathrm{ice}}\cos\theta}, \tag{5.1}$$

with the refractive index of the predominantly H_2O ice being $n_{\mathrm{ice}} \approx 1.3$ [Hudgins et al. 1993]. This is illustrated in Fig. 5.2 where both interference fringes produced during ice deposition and the simultaneous growth of the integrated neutral Py absorbance band are shown. The final ice thickness amounts to 1.7 μm and is reproducible to within 5% or better. Simultaneously, the number of pyrene molecules in the ice sample (N) is monitored by measuring the integrated absorbance of its strongest transition ($S_2 \leftarrow S_0$) (see Fig. 5.2). The number of pyrene molecules per cm^2 can be calculated via [Kjaergaard et al. 2000, Hudgins et al. 1993]:

$$N = \frac{\int_{\nu_1}^{\nu_2} \tau \, d\nu}{8.88 \times 10^{-13} f}, \tag{5.2}$$

where $f = 0.33$ is the known oscillator strength of the $S_2 \leftarrow S_0$ transition of pyrene [Bito et al. 2000, Wang et al. 2003]. The resulting column density of pyrene molecules amounts to about $4{\times}10^{14}$ cm^{-2}. For a typical sample with a thickness of 1.7 μm, the column density of H_2O molecules amounts to $4{\times}10^{18}$ cm^{-2}, using the value for the density of amorphous ice (ρ=0.94 g/cm^3; Sceats, M. G. and Rice, S., A. [1982]). Thus, the sample is calculated to consist of a 1:10,000 pyrene:H_2O mixture. This mixing ratio can be roughly varied by changing the H_2O flowrate or the pyrene sample temperature. The HeNe beam used here for monitoring the ice growth process also traces other elements along the optical path and is used to align all components.

The vacuum UV radiation from a special microwave (MW) powered hydrogen discharge lamp is used to simulate the interstellar radiation field [Muñoz Caro et al. 2002].

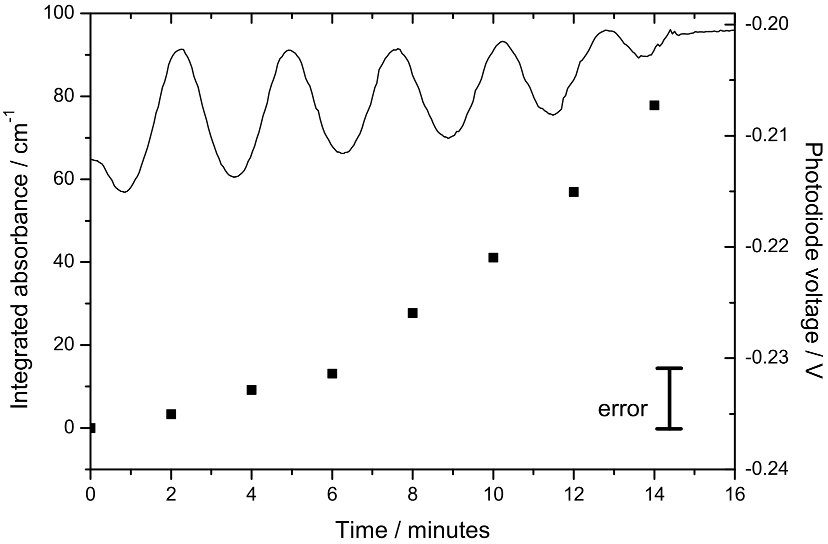

Figure 5.2 A plot showing both the growth of the integrated pyrene absorption band (squares and left axis) and the interference fringes measured by the photodiode (right axis). At t = 14 minutes, the deposition is stopped and the interference pattern diminishes. The error bar shown in the right lower corner applies to the pyrene-integrated absorbance.

The lamp consists of a flow tube clamped in a McCarroll cavity [McCarroll 1970] and emits mainly Ly-α radiation around 121.6 nm and, with less intensity, a band centered around 160 nm. The cavity is excited by a regular MW power supply (100 W, 2450 MHz). The H_2 pressure in the lamp is maintained at 0.4 mbar during operation (Praxair 5.0 H_2). This results in a VUV photon flux of $\sim10^{15}$ photons cm^{-2} s^{-1}. The lamp is centered onto the front flange and the VUV radiation enters the setup towards the ice sample through a MgF_2 window that also serves as a vacuum seal. A shutter is used to block the VUV until the moment that the ice processing should start. Besides eliminating the need to switch the H_2 lamp on and off during the course of an experiment, this allows the lamp to stabilize before irradiation starts. This is important when tracking photochemical behavior during extended periods of photolysis.

A 300 W ozone-free Xe-arc lamp serves as a broad band white light source to measure the spectral ice features in direct absorption. The lamp has a spectral energy distribution that covers the full detector range (200 nm $< \lambda <$ 2400 nm). Alternatively, the light from a halogen fiber lamp can be used when no UV coverage is desired. An optical system consisting of lenses and diaphragms is used to guide the light beam through a MgF_2 window along the optical axis — coinciding with the pre-aligned HeNe beam — and crossing the ice sample at a 45° angle. Light that is not absorbed exits the vacuum chamber through a second MgF_2 window after which it is focused onto the entrance slit of an ANDOR Shamrock spectrometer. The spectrometer is equipped with two interchangeable turrets which holds four gratings in total (2400, 1200, 600 and 150 lines mm^{-1}), allowing for a trade-off between wavelength coverage and spectral resolution, depending on the experimental needs. Since typical ice absorption bands exhibit a FWHM of 4–20 nm, most of the experiments are performed using the 600 lines mm^{-1} grating, resulting in an accessible wavelength range of $\sim$140 nm.

The light is dispersed onto a very sensitive 1024×256 pixel CCD camera with 16-bit digitization. The resulting signal is read out in the vertical binning mode by a data acquisition computer. Spectra are taken in absorbance mode (τ=-ln(I/I_0)) with respect to a reference spectrum (I_0) taken directly after depositing the sample. Recording a single spectrum typically takes about 5 ms and spectra are generally co-added to improve the signal-to-noise ratio (S/N). In a typical experiment more than 1000 individual spectra are recorded and are reduced using LabView routines. Data reduction consists of local linear baseline corrections, multiple Gaussian fitting of absorption profiles and absorption band integration.

5.3 Spectroscopic assignment

Figure 5.3 shows the 310 to 500 nm spectrum of a Py:H_2O ice at 10 K after 1200 s of in situ photolysis in absorbance mode. The spectrum is baseline subtracted and given in optical depth (OD). Since the spectrum recorded before VUV irradiation is taken as a reference (I_0), bands with positive OD values arise from species produced by photolysis while the carriers of negative OD bands decrease in density. It is noteworthy that S/N ratios are good even though the processes are studied in a very dilute mixture (Py:H_2O

~1:10,000). Previous work was on more concentrated samples (PAH:H_2O ~1:500, Gudipati & Allamandola [2003]; PAH:H_2O ~1:800 to 1:3200, Bernstein et al. [1999]).

A Gaussian fit to all of the features visible in the spectrum is indicated as well. Clearly, a number of new species are produced at the expense of neutral pyrene. The peak positions, FWHM and assignments of all the bands in Fig. 5.3 are summarized in Table 5.1, along with comparisons of earlier results found in other molecular environments. The assignments given in Fig. 5.3 were made as follows. Based on previous studies of pyrene in rare gas matrices [Vala et al. 1994, Halasinski et al. 2005], the strong, negative band peaking at 334 nm is readily assigned to the ${}^1B_{2u}{\leftarrow}{}^1A_g$ electronic transition of neutral pyrene ($S_2{\leftarrow}S_0$).

Similarly, the positive bands near 363, 446, and 490 nm are assigned as the strongest members of the pyrene cation ${}^2B_{1u}{\leftarrow}{}^2B_{3g}$, ${}^2A_u{\leftarrow}{}^2B_{3g}$ and ${}^2B_{1u}{\leftarrow}{}^2B_{3g}$ vibronic transitions, respectively [Vala et al. 1994, Hirata et al. 1999]. Table 5.1 shows that the bandwidth (FWHM) of the Py^+ bands is broader in the solid H_2O than in rare gas matrices, in accordance with the stronger interactions within the H_2O matrix network. Similarly, larger shifts in peak position may be expected.

In addition to the Py^+ bands, other new bands appear near 345, 367, 405, and 453 nm. We ascribe these to hydroxypyrene (PyOH), hydroxypyrene cation ($PyOH^+$), and pyrene/pyrenolate anion (Py^-/PyO^-) based on the work of Milosavljevic & Thomas [2002] who reported the spectra of 1-hydroxypyrene and its daughter products in various media. The suggestion of anion production in these ices is noteworthy in view of the astronomical detection of negative ions both in the solid state [van Broekhuizen et al. 2005] and in the gas phase [e.g., Agúndez et al. 2008].

The appearance of clear bands due to PyOH, $PyOH^+$, and Py^-/PyO^- after VUV radiation at 10 K is somewhat surprising. Previous optical studies of the VUV photolysis of three different PAHs in H_2O ice indicated that conversion of the parent neutral PAH to the cation was the major, and apparently only, photolytic step and that the cation remained stabilized in the ice to remarkably high temperatures (~100 K) for long periods [e.g., Gudipati & Allamandola 2006b]. Gudipati [2004] further showed that, in the case of naphthalene (Nap), subsequent reactions between Nap^+ and the H_2O matrix did indeed produce NapOH, but only during warm-up (~100 K). Using mass spectroscopy, Bernstein et al. [1999] showed that PAH oxides and hydroxides were part of the residues left *after* VUV photolyzed PAH:H_2O ices were warmed under vacuum. Furthermore, upon prolonged exposure, the VUV transmittance of the MgF_2 hydrogen lamp window drops and with this the PyOH and $PyOH^+$ production also decreases relative to the production of Py^+. This suggests that photolytic processes within the pyrene containing water ice change, perhaps because water dissociation becomes less effective with reduced hard UV flux while direct Py ionization still readily occurs with near UV photons [Gudipati & Allamandola 2004]. The influence of temperature and UV spectral energy distribution is currently under investigation.

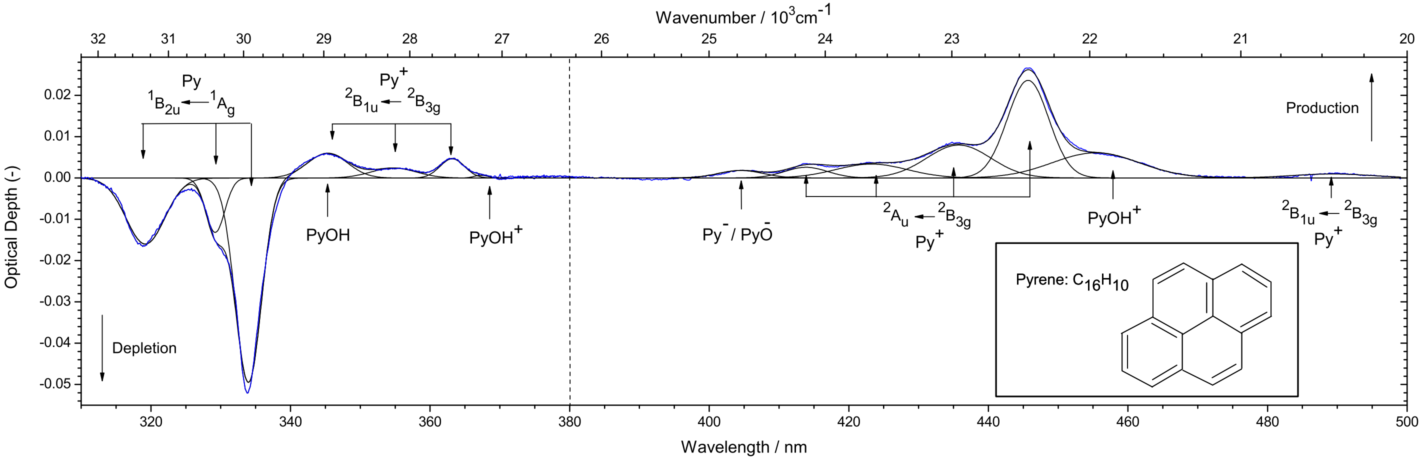

Figure 5.3 A baseline corrected spectrum obtained after 1200 s of VUV irradiation of a pyrene:H_2O ice at 10 K. The absorption features in the plot are assigned and fitted with Gaussian profiles. A negative OD indicates species destruction, a positive OD species formation. The left spectrum (up to 280 nm) is scaled down by 30% to facilitate comparison.

Table 5.1 Vibronic bands of pyrene and its photoproducts in a H_2O ice compared with rare gas matrix literature values.

Species	State	λ_{H_2O} (nm)	FWHM (nm)	$\lambda_{lit.}$ (nm)	FWHM$_{lit.}$ (nm)	$\lambda_{H_2O} - \lambda_{rg}$	ΔFWHM
Py	$^1B_{2u}$	334.0	4.4	323.3[a]	n.a.	10.7	-
		329.2	3.2	319.1[a]	n.a.	10.1	-
		319.2	6.5	309.4[a]	n.a.	9.8	-
Py^+	$^2B_{1u}$	363.2	3.6	362.6[b]	2.2	0.6	1.4
		354.0	6.5	355.1[b]	2.1	-1.1	4.4
		344.9	6.2	-	-	-	-
Py^+	^2A_u	445.6	6.6	443.8[b]	4.5	1.8	2.1
		435.5	10.2	433.2[b]	4.3	2.3	5.9
		423.0	12.2	422.9[b]	4.1	0.1	8.1
		413.8	5.3	412.1[b]	3.9	1.7	1.4
Py^+	$^2B_{1u}$	490.1	10.0	486.9[b]	5.5	3.2	4.5
PyOH		344.9	5.8	340[c]	-	-	-
Py^-/PyO^-		405.2	7.3	410[c]	-	-	-
$PyOH^+$		366.8	3.0	-	-	-	-
$PyOH^+$		452.9	18.2	465[c]	-	-	-

[a] Values measured in a Ne matrix taken from Halasinski et al. [2005]

[b] Values measured in an Ar matrix taken from Vala et al. [1994]

[c] Values measured in H_2O and 2-chlorobutane taken from Milosavljevic & Thomas [2002]

5.4 Chemical evolution of the ice

To further investigate the spectroscopy and the photochemistry of VUV irradiated H_2O-rich ices that contain PAHs, time-dependent optical studies were performed. Figure 5.4 shows the integrated OD behavior of the Py, Py^+ (for two bands), and PyOH absorptions as function of photolysis time. During the first 130 s of VUV irradiation, the Py decay is clearly correlated with Py^+ growth. This allows us to determine relative band strengths of the two species by investigation of the short timescale correlation. The sub-second time response of the present setup is a prerequisite for this to work. We derive a band strength of 2.9×10^{-13} cm molecule^{-1} for the $^2A_{2u} \leftarrow {}^2B_{3g}$ Py^+ transition in H_2O ice using Equation (5.2). As other chemical processes become important, the correlation disappears. The loss of Py slows significantly while the Py^+ starts a slow decline after the maximum is reached. The PyOH signal continues to grow slowly but steadily throughout the photolysis process and is most likely formed by Py/Py^+ reacting with photoproducts of H_2O. Its formation is consistent with the recent outcome of a quantitative VUV photodesorption study of H_2O ice under ultrahigh vacuum conditions, where a H+OH photodissociation channel was reported [Öberg et al. 2009d]. A reaction network connecting all of these species is presented in Fig. 5.5.

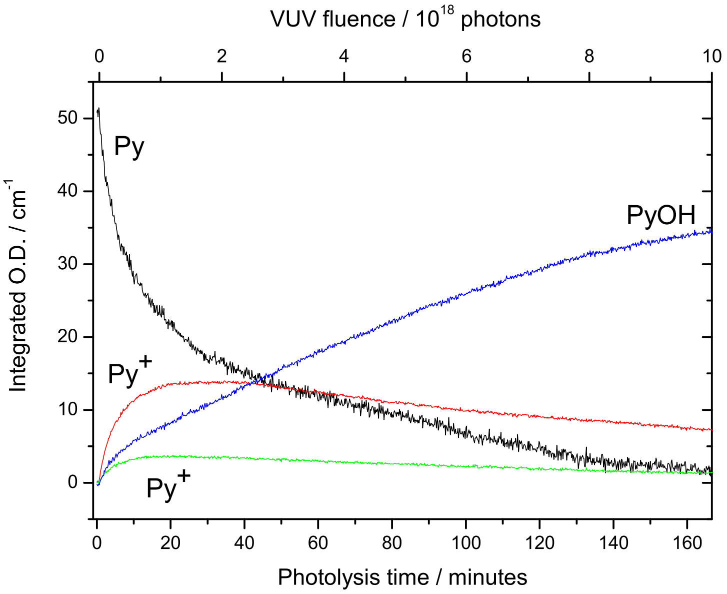

Figure 5.4 The behavior of Py, Py^+ (two transitions), and PyOH as a function of VUV photolysis time/VUV fluence.

In addition to Py^+ formation and reactivity during irradiation, we have also studied its stability within the ice when photolysis is stopped. Figure 5.6 plots the normalized integrated O.D. of the 445.6 nm Py^+ band as a function of time after VUV radiation is

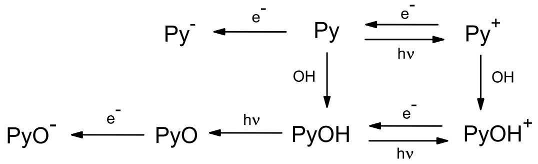

Figure 5.5 Possible reactions upon photolysis of Py:H_2O ice as derived from Fig. 5.3.

stopped. The figure spans 50 hr and shows that although the total Py^+ signal drops, 60% remains trapped in the ice after 2 days. The small wiggle at the 0.05 level is due to baseline variations. There are clearly two decay channels, one 'fast' and one 'slow'. The following expression is used to fit the experimental data:

$$y = A_1 \exp(-t/\tau_1) + A_2 \exp(-t/\tau_2) \tag{5.3}$$

with $A_1 = 0.70$, $\tau_1 = 351.3$ hr, $A_2 = 0.22$ and $\tau_2 = 1.7$ hr. This produces the red curve in Fig. 5.6. The processes responsible for these two decay rates are not yet clear. The Py^+ decay may be governed by recombination with trapped electrons. In considering these results, it is important to keep in mind that the ice processes described here are recorded for one temperature (10 K) and will most likely depend on temperature.

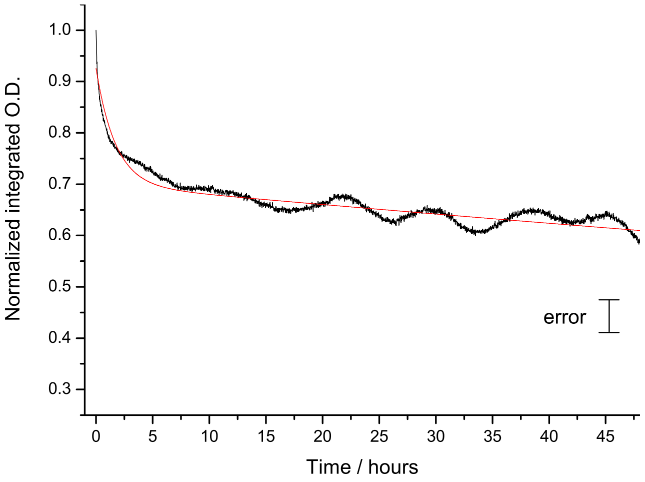

Figure 5.6 Normalized pyrene cation integrated O.D. as a function of time plotted together with a double exponential fit using Equation (5.3) (red curve). The wiggles superposed on the signal are caused by baseline effects and fall within the error of 5% as indicated by the error bar.

5.5 Astrophysical implications

Water is by far the dominant component of interstellar ices. Since PAHs are considered to be widespread throughout the ISM, they are likely to be frozen out wherever H_2O-rich ices are present. The photochemical kinetics observed here and the new spectroscopic information make two astrophysical points.

Astrochemically, this work shows that the effective photolytic production of PAH ions in PAH containing ice upon VUV irradiation should not be neglected *a priori* when modelling interstellar ice chemistry. The behavior of the various species that is shown in Fig. 5.4 suggests that a new set of solid-state reactions appears when irradiating PAH containing water ice. The present study is on a rather isolated ice system — typical for this type of laboratory study — comprising Py and H_2O. In a more realistic interstellar sample, containing other constituents, such as CO, CO_2 or NH_3, and other PAHs, chemical pathways will become more complicated, but since water is the most dominant component in these extraterrestrial ices, we expect that the trends observed here will generally apply. Another important point to note is that reactions involving ions are not included in any of the current astrochemical grain chemistry networks. The present study shows that positive ions can reside in the ice mantle for a substantial time. This is particularly interesting since an astronomical dust grain is a truly isolated system, whereas the laboratory analogue is grown on the tip of a cold finger.

Observationally, the spectroscopic results provide an alternative route to search for PAH features in space. Astrophysical searches to identify PAHs and PAH cations in the ISM/CSM have focused on vibrational and electronic transitions in the gas phase as well as solid-state PAH features in the infrared. As stated previously, these searches have been largely unsuccessful. The infrared work suffers from spectral congestion and spectral overlap of vibrational modes. This prohibits an unambiguous identification of an emission feature to a specific carrier. In the UV/VIS this is partly overcome as electronic excitations are unique for different PAHs. However, electronic spectra of gas phase PAHs showed no overlap with absorption features recorded through diffuse interstellar clouds, presumably of too low column densities [Romanini et al. 1999, Bréchignac & Pino 1999]. A different situation applies in the solid state; PAHs are refractory material and accumulate in time onto cold grains that offer a reservoir. Therefore, the specific embedding of PAHs in water ice as presented here provides an alternative starting point for an astronomical search. However, one has to realize that this idea has both pros and cons.

Table 5.1 shows that under the present experimental conditions the bands are rather broad. The FWHM of the Py^+ absorption feature at 445.6 nm is 66 Å. From an observational point of view this has the advantage that profiles can be studied at medium resolution, but also goes with the challenge to correct very accurately for possible background signals and in the end spectral overlaps may still exist, e.g., with silicate or carbonaceous features. Nevertheless, overlapping broad bands can contribute to the very broad structure (VBS) superposed on the interstellar extinction curve [Hayes et al. 1973, van Breda & Whittet 1981, Krelowski et al. 1986] and simply may have been overlooked in the past.

As stated before, the electronic excitation energy is unique. This is good for selectivity, but bad for sensitivity, since spectral features of different PAHs do not add up (as in the infrared) and consequently an individual optical band strength is, in principle, directly determined by the actual abundance of one specific PAH in space. It is difficult, however, to predict the percentage of the total interstellar PAH population that might exist in the form of one specific PAH, e.g., pyrene. Nevertheless, electronic PAH transitions are typically 2–3 orders of magnitude stronger than their IR bands and from this point of view, we expect that PAH bands may be observable in the visible even though IR bands are barely discernible on the strong H_2O bands [Brooke et al. 1999]. This is also reflected by the very good S/N ratios as visible in Fig. 5.2 for a very diluted mixture. We expect PAHs to be sufficiently abundant in ices in regions of molecular clouds with $A_v \geq 8$ to permit detection in the optical. Infrared ice bands have been detected along such lines of sight and the visible extinction is low enough to permit UV from the interstellar radiation field to process these ices.

We have estimated the expected Py and Py^+ absorption band strength towards an example source, MWC297. This is an early-type B1.5V star with a well-characterized stellar spectrum, a B magnitude of 14.34 and a 3.0 μm ice band with $\tau = 0.04$. Using the high sensitivity of an 8 m class telescope (VLT) it is feasible to obtain, within a couple of hours, S/N ≥1000 spectra of such a highly extincted source in the wavelength range under investigation. To estimate the expected OD of a pyrene or pyrene cation ice absorption we use the standard relation:

$$N_{\mathrm{H}}/E(B-V) = 5.8 \times 10^{21} \text{ atoms cm}^{-2} \text{ mag}^{-1} \tag{5.4}$$

from Bohlin et al. [1978]. With $E(B-V) = 2.67$ towards MWC297 [Drew et al. 1997] this results in $N_{\mathrm{H}} = 1.6\times10^{22}$ cm^{-2}. Taking the total PAH abundance in clouds with respect to n_{H} to be $\sim3\times10^{-7}$, this results in a total PAH column density of 9.6×10^{15} cm^{-2}. Assuming that 1% of the total PAHs in space is in the form of pyrene frozen out on grains and of this fraction up to 10% is in its singly ionized state (Py^+), the total column density of Py^+ or Py toward MWC297 is estimated to range between 9.6×10^{12} and 8.64×10^{13} species/cm^2. The OD is defined as

$$\tau = \frac{NA}{\Delta\nu}, \tag{5.5}$$

with N the column density of the absorbers, A the integrated band strength and $\Delta\nu$ the FWHM. For a typical strong allowed vibronic transition, such as the $^1B_{2u}\leftarrow{}^1A_g$ Py and $^2A_u\leftarrow{}^2B_{3g}$ Py^+ transitions, we take $A_{\mathrm{Py}} = 2.9 \times 10^{-13}$ cm molecule^{-1} and $A_{\mathrm{Py^+}} = 2.9 \times 10^{-13}$ cm radical^{-1} in ice with a FWHM=400 cm^{-1} and 300 cm^{-1}, respectively. This yields ODs of $0.01 \leq \tau \leq 0.06$ for Py and Py^+, a range similar to that observed for ice bands.

5.6 Conclusion

This work presents the first results of a spectroscopic and photochemical study of pyrene in water ice upon VUV irradiation under astronomical conditions. Since the spectra are recorded in real time, it is possible to derive photochemical characteristics and to monitor a rich ion-mediated chemistry in the solid state. Such processes are yet to be considered in astrochemical models. Additionally, it is shown that the pyrene cations formed within the H_2O ice by VUV irradiation remain trapped in the ice for an extended period. Successive heating of the ice makes these ions available to diffusing species and hence should be considered in solid-state astrochemical processes.

The new laboratory approach presented here offers a general way to provide astronomically relevant PAH solid-state spectra. Specifically, the spectra discussed here provide an alternative way to search for pyrene features in the ISM/CSM. The derived numbers show the potential of this method, but one has to realize, as pointed out before, that these numbers incorporate our limited knowledge on the actual PAH quantities in space. For different PAHs, with different abundances and different absorption strengths other numbers, both less and more favorable, may be expected. Furthermore, it is possible — in view of the rather effective way in which charged species form and stay in the ice — that the actual abundance of ions may be higher. The results presented here are new and aim at a further characterization of the chemical role of PAHs and PAH derivatives in space.

CHAPTER 6

Photochemistry of the PAH pyrene in water ice: the case for ion-mediated solid-state astrochemistry[1]

Icy dust grains play an important role in the formation of complex inter- and circumstellar molecules. Laboratory studies have mainly focused on the physical interactions and chemical pathways in ices containing rather simple molecules, such as H_2O, CO, CO_2, CH_4, and CH_3OH. Observational studies show that polycyclic aromatic hydrocarbons (PAHs) are also abundantly present in the ISM in the gas phase. It is likely that these non-volatile species also freeze-out onto dust grains and participate in the astrochemical solid-state network, but additional experimental PAH ice studies are largely lacking. The study presented here focuses on a rather small PAH, pyrene ($C_{16}H_{10}$), and aims to understand and quantify photochemical reactions of PAHs in interstellar ices upon vacuum ultraviolet (VUV) irradiation as a function of astronomically relevant parameters. Near-UV/VIS spectroscopy is used to track the in situ VUV driven photochemistry of pyrene containing ices at temperatures ranging from 10 to 125 K. The main photoproducts of VUV photolyzed pyrene ices are spectroscopically identified and their band positions are listed for two host ices, H_2O and CO. Pyrene ionization is found to be most efficient in H_2O ices at low temperatures. The reaction products, triplet pyrene and the 1-hydro-1-pyrenyl radical are most efficiently formed in higher temperature water ices and in low temperature CO ice. Formation routes and band strength information of the identified species are discussed. Additionally, the oscillator strengths of Py, $Py^{\cdot+}$, and $PyH^{\cdot}$ are derived and a quantitative kinetic analysis is performed by fitting a chemical reaction network to the experimental data. The results are placed in an astrophysical context by determining the importance of PAH ionization in a molecular cloud. The photoprocessing of a sample PAH in ice described in this chapter indicates that PAH photoprocessing in the solid state should also be taken into account in astrochemical models.

---

[1] Based on: J. Bouwman, H. M. Cuppen, A. Bakker, L. J. Allamandola, and H. Linnartz Astronomy and Astrophysics, 511, A33+ (2010)

6.1 Introduction

Strong infrared emission attributed to polycyclic aromatic hydrocarbons (PAHs) is characteristic of many galactic and extragalactic objects [Smith et al. 2007, Draine et al. 2007, Draine & Li 2007, Tielens 2008]. While this emission generally originates in optically thin, diffuse regions, PAHs should also be common throughout the dense interstellar medium. There, as with most other interstellar species in molecular clouds, PAHs condense out of the gas onto cold icy grain mantles, where they are expected to influence or participate in the chemistry and physics of the ice. While laboratory studies of interstellar ice analogs have shown that complex organic molecules are produced upon extended vacuum ultraviolet (VUV) photolysis [e.g., Briggs et al. 1992, Bernstein et al. 1995], the photoinduced processes occurring during the irradiation of PAH containing interstellar ice analogues have not yet been studied in detail. In optical, in situ studies of the photochemistry of naphthalene, 4-methylpyrene, and quatterylene containing water ice at 20 K, Gudipati & Allamandola [2003, 2006a,b] and Gudipati [2004] showed that these PAHs are readily ionized and stabilized within the ice, suggesting that trapped ions may play important, but overlooked roles in cosmic ice processes. Beyond this, there is little information about the VUV induced, in situ photochemistry and photophysics of PAH-containing water-rich ices.

Here, we describe a detailed study of the VUV-induced photochemistry that takes place within pyrene (Py or $C_{16}H_{10}$) containing water ices (Py:H_2O=1:10,000–1:5,000). The present study is an extension of Chapter 5 in which the focus was on the new experimental setup and where the use of PAH ice spectra was discussed to search for solid-state features of PAHs in space. In this work, the focus is on a detailed characterization of the chemical processes taking place upon VUV irradiation, particularly as a function of ice temperature ranging from 25 to 125 K. Additionally, measurements on Py:CO ices at 10 K were performed to elucidate the role of water in the reaction schemes and to clarify the formation routes of identified species. A similar study of three small PAHs is now underway to understand the general principles of PAH/ice photochemistry. This is part of an overall experimental program at the Sackler Laboratory for Astrophysics to study the fundamental processes of inter- and circumstellar ice analogues such as thermal [Acharyya et al. 2007] and photodesorption [Öberg et al. 2007b, 2009d], hydogenation reactions [Fuchs et al. 2009, Ioppolo et al. 2008], photochemistry [Öberg et al. 2009c], and physical interactions in interstellar ice analogues [Öberg et al. 2007a, 2009b, and Chapter 2 of this thesis].

The chapter is organized as follows. The experimental technique is summarized in §6.2. Paragraph 6.3 describes the Py:H_2O and Py:CO ice photochemistry, the resulting products and their formation routes. The temperature-dependent photochemistry and derived reaction dynamics are described in §6.4 and astrochemical implications are discussed in §6.5. The main conclusions are summarized in §6.6.

6.2 Experimental technique

We use the new apparatus as described in Chapter 5 which follows the photochemistry in kinetic mode during VUV irradiation by measuring the near-UV-visible absorption spectra of an ice, providing ‘real-time’ tracking of the reactants and photoproducts. Dilute Py:H_2O ice samples (~1:10,000–~1:5,000) and a Py:CO ice sample of comparable concentration are prepared by depositing the vapor from a pyrene sample heated to 40°C together with H_2O vapor or CO gas onto a cold MgF_2 window. The window is cooled to 10 K in the case of CO deposition or 25 K in the case of H_2O deposition. The sample window is cooled by a closed cycle He refrigerator. Pyrene (Aldrich, 99%) and CO (Praxair 99.999%) are used as commercially available. Vapor from water, filtered through a milli-Q purification system and purified further by three freeze-pump-thaw cycles, is used. The sample window is mounted in a high-vacuum chamber ($P \approx 10^{-7}$ mbar). The ice growth rate and thickness are determined with a HeNe laser by monitoring the thin-film interference fringes generated during deposition. Simultaneously, the amount of pyrene is tracked by measuring the integrated strength of the $S_2 \leftarrow S_0$ neutral Py transition at 334 nm. Deposition is typically stopped when the optical depth (OD) of Py approaches ~0.15.

The ice samples are photolyzed with the 121.6 nm Lyα (10.6 eV) and the 160 nm molecular hydrogen emission bands (centered around 7.8 eV) generated by a microwave powered discharge in a flowing H_2 gas with a VUV flux of $\sim 10^{15}$ photons s^{-1} [Muñoz Caro et al. 2002]. This results in a photon flux of $\sim 10^{14}$ photons$\cdot$cm^{-2}s^{-1} at the sample surface [Öberg et al. 2009d].

Absorption spectra of VUV-photolyzed Py-containing ices are measured with a Xe-arc lamp serving as a white light source. Lenses and diaphragms direct the light through the ice sample along the optical axis determined by the HeNe laser beam after which it is focused onto the entrance slit of a 0.3 m spectrometer. A 150 lines mm^{-1} grating, blazed at 300 nm, disperses the light onto a sensitive 1024×256 pixel CCD camera with 16 bit digitization. The camera is read out in vertical binning mode by a data acquisition computer that converts the data to absorbance spectra ($\mathrm{OD} = -\ln(I/I_0)$). This configuration spans the 270 to 830 nm spectral range, which permits simultaneously monitoring of the behavior of the neutral Py parent molecule and photoproduct bands without any adjustment of the elements along the optical path. This is critical to obtaining reliable and reproducible baselines in measuring the optical spectra of ices. The spectral resolution is of the order of 0.9 nm, which is more than sufficient to record broad solid-state absorption features.

The measurements described here were performed on various H_2O:Py ice samples at 25, 50, 75, 100, and 125 K. The CO ice experiments were carried out at 10 K to avoid matrix sublimation at higher temperatures. The sample temperature is maintained using a resistive heater with an accuracy of ±2 K. The measured spectra are converted into units of optical depth by using the spectrum of the freshly deposited, unphotolyzed ice at the appropriate temperature as a reference spectrum (I_0). Recording a single spectrum typically takes about 5 ms, and 229 spectra are generally co-added to improve the S/N of a spectrum, producing one single spectrum every 10 seconds.

The optical configuration of the apparatus is such that spectra are recorded *simultaneously* with photolysis. Thus, the short spectral recording time permits us to monitor photoinduced changes on a roughly 10 s time scale. Figure 6.1 shows the 290 to 490 nm spectrum of a Py:H_2O ice at 125 K after 900 s of in situ VUV photolysis. Because the spectrum recorded before VUV irradiation is taken as a reference (I_0), bands with positive OD values originate from species that are produced by photolysis, while the bands with negative OD correspond to the neutral pyrene that is lost upon photolysis. Comparing the Py and photoproduct absorption bands with the narrow Hβ lamp line at 486.1 nm shows that the instrumental resolution indeed far exceeds the ice band widths. The absolute wavelength calibration is accurate to within ±0.5 nm.

More than 1400 individual spectra are recorded and are reduced in a typical 4 hr experiment. Spectra are individually baseline corrected by fitting a second order polynomial through data points where no absorption occurs and subsequently subtracting the fit from the measured spectrum. Integrated absorbances of absorption features are calculated numerically for all spectra. These are corrected for the contributions of atomic hydrogen lines originating in the H_2 discharge lamp. The data reduction software also allows us to plot correlation diagrams between integrated absorbances of different absorption features. All data handling and reduction is performed with LabView routines.

Integrated band areas are used, in conjunction with oscillator strengths (f), to derive molecular abundances. The oscillator strength is converted to integrated absorbance (cm molecule^{-1}) using the conversion factor 8.88×10^{-13} [Kjaergaard et al. 2000]. The number of molecules per cm^2 (N) is given by

$$N = \frac{\int_{\nu_1}^{\nu_2} \tau \, d\nu}{8.88 \times 10^{-13} f}, \tag{6.1}$$

where τ is the optical depth and ν is the frequency in cm^{-1}.

6.3 Band assignments and band strength analysis

The typical photolysis duration of about 4 hours is the time required for nearly complete loss of the neutral pyrene vibrational progression at 334.0, 329.2, and 319.2 nm. Irradiating the sample ices with VUV light produces a set of new absorption bands in the spectra, indicating active photochemistry. The band positions, FWHM, and assignments of the bands in the Py:H_2O ice at 25 K are listed in Table 6.1. The bands appearing in the Py:CO ice at 10 K are similar to those in the Py:H_2O ice at 25 K, although, with slightly altered band positions and FWHM and with very different relative intensities (see also Table 6.1). Figure 6.1 presents a spectrum from the 125 K Py:H_2O series. This figure illustrates production of the pyrene radical cation ($Py^{\cdot+}$), triplet pyrene (^{3}Py), 1-hydro-1-pyrenyl radical ($PyH^{\cdot}$), and a broad underlying ‘residue’ feature upon VUV irradiation. Additionally, a progression of distinct absorption features is found in the Py:CO experiment, which indicates the formation of the (reactive intermediate) $HCO^{\cdot}$ radical. The identifications of these species and their oscillator strengths are discussed below.

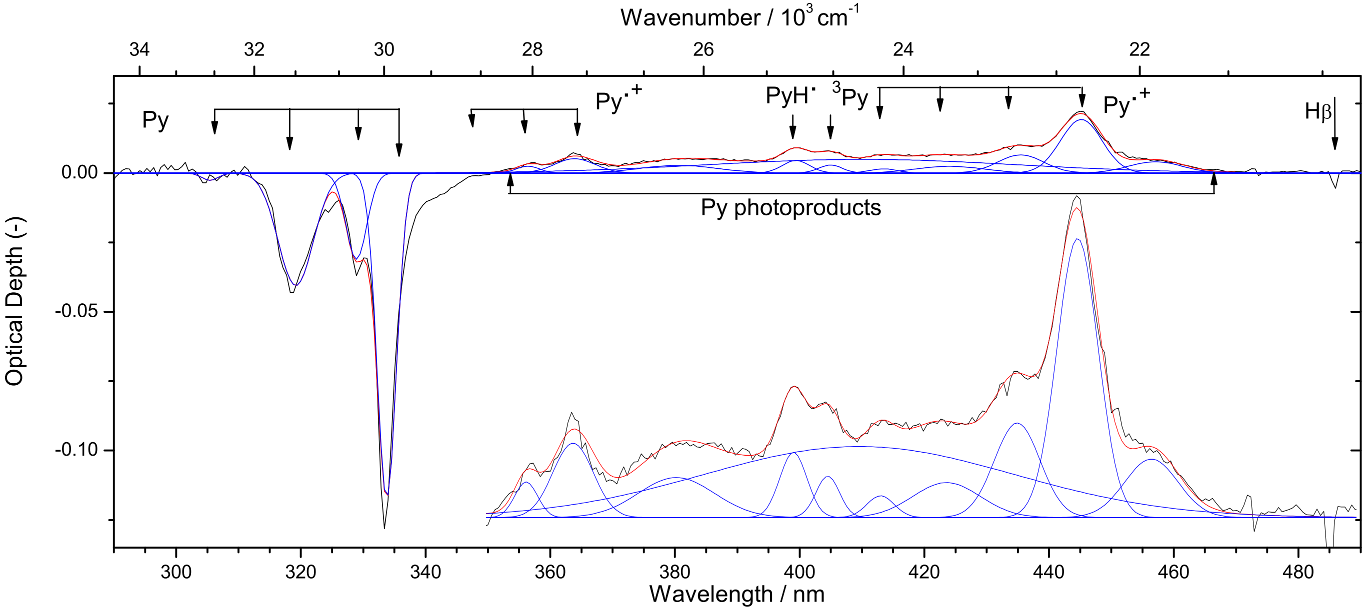

Figure 6.1 The spectrum of a dilute pyrene:H_2O ice after 900 s of VUV irradiation at 125 K. The inset shows a blow-up of the pyrene photoproduct bands. Band assignments are discussed in §6.3. Note the broad feature ranging from about 350 to 470 nm which is indicated by a Gaussian fit. This is attributed to overlapping bands from individual pyrene photoproducts. Bands with negative optical depth indicate species destruction, those with positive optical depth show species formation. The blue bands are Gaussian profiles which co-add to the overall fit shown in red. Note the instrumental resolution indicated by the profile of the H*β* line at 486.1 nm. (This figure is available in color in electronic form)

Table 6.1 Band positions (λ_c) and FWHM in nm for pure pyrene ice at 10 K, pyrene in H_2O ice at 25 K, pyrene in CO ice at 10 K, and photoproduct bands for the Py:H_2O and Py:CO UV processed ices.

Species	Pyrene		Pyrene:H_2O		Pyrene:CO	
	λ_c	FWHM	λ_c	FWHM	λ_c	FWHM
Py $^1B_{2u}$	312.7	7.1	319.2	6.5	319.4	7.5
	325.3	10.0	329.2	3.2	329.2	2.3
	341.5	14.0	334.0	4.4	334.3	4.1
$Py^{\cdot+}$ $^2B_{1u}$	...	...	363.2	3.6	...[a]	...[a]
	...	...	354.0	6.5	...[a]	...[a]
	...	...	344.9	6.2	...[a]	...[a]
$Py^{\cdot+}$ ^2A_u	...	...	445.6	6.6	445.3	7.8
	...	...	435.5	10.2	...[a]	...[a]
	...	...	423.0	12.2	...[a]	...[a]
	...	...	413.8	5.3	...[a]	...[a]
$Py^{\cdot+}$ $^2B_{1u}$	...	...	490.1	10.0	...[a]	...[a]
$PyH^{\cdot}$	...	...	399.4[b]	5.2[b]	400.5	4.2
	...	...	...[a]	...[a]	392.5	6.7
	...	...	...[a]	...[a]	378.4	15.7
^{3}Py $^3A_g^-$	...	...	405.0[b]	4.5[b]	406.2	4.8
$HCO^{\cdot}$ ^2A”	...	...	...	...	513.4	17.5
	...	...	...	...	535.3	12.5
	...	...	...	...	556.3	14.5
	...	...	...	...	583.0	16.8
	...	...	...	...	604.9	10.0
	...	...	...	...	639.2	15.1

[a] Absorption feature was too weak to perform an accurate fit

[b] Features are too weak at 25 K; the 125 K values are indicated

6.3.1 Neutral pyrene bands

As in Chapter 5, the strong, negative bands peaking at 334.0 nm and weaker bands at 329.2 and 319.2 nm in the H_2O ice (see Fig. 6.1), and at slightly shifted positions in the CO ice, are assigned to the $^1B_{2u} \leftarrow ^1A_g$ electronic transition of neutral pyrene ($S_2 \leftarrow S_0$) based on previous studies of pyrene in rare gas matrices [Vala et al. 1994, Halasinski et al. 2005]. To study the chemistry in absolute number densities, a value of $f = 0.33$ is adopted from the literature for the oscillator strength of pyrene [Bito et al. 2000, Wang et al. 2003]. This value is used throughout this paper both for the Py:H_2O and Py:CO experiments. Pure pyrene ice measured at 10 K shows broader absorptions located at 341.5, 325.3, and 312.7 nm (see Table 6.1). We did not perform VUV experiments on the pure pyrene sample.

6.3.2 Pyrene cation bands

Positive bands at 363.2, 354.0, and 344.9 nm appear upon photolysis in the Py:H_2O experiments. This progression is assigned to the $^2B_{1u}\leftarrow{}^2B_{3g}$ vibronic transition of the pyrene cation ($Py^{\cdot+}$) in accordance with the proximity to the band positions reported by Vala et al. [1994] and Halasinski et al. [2005]. This transition for $Py^{\cdot+}$ in H_2O ice was reported in Chapter 5. The $^2B_{1u}\leftarrow{}^2B_{3g}$ transition is too weak to be detected in the Py:CO experiment. A stronger $Py^{\cdot+}$ progression occurs at 445.6, 435.5, 423.0, and 413.8 nm in water ice. Of these bands, only the strongest at 445.3 nm is detectable in the irradiated Py:CO ice. This progression is assigned to the $^2A_u\leftarrow{}^2B_{3g}$ transition of $Py^{\cdot+}$. The much weaker absorption caused by the $^2B_{1u}\leftarrow{}^2B_{3g}$ $Py^{\cdot+}$ transition at 490.1 nm in H_2O is again undetectable in CO.

In these H_2O and CO ice experiments, $Py^{\cdot+}$ formation is the result of direct single photon ionization of the neutral species, following:

$$\mathrm{Py} \xrightarrow{\mathrm{VUV}} \mathrm{Py}^{\cdot+} + \mathrm{e}^{-}. \qquad (6.2)$$

We emphasize that ionization in Py:H_2O ices is far more efficient than in Py:CO ices. Additional measurements on Py:CO:H_2O mixtures indicate that the presence of H_2O indeed enhances the ionization. Hence, it is possible that water contamination in the CO ice is responsible for the formation of some, if not all, of the cation species in the Py:CO

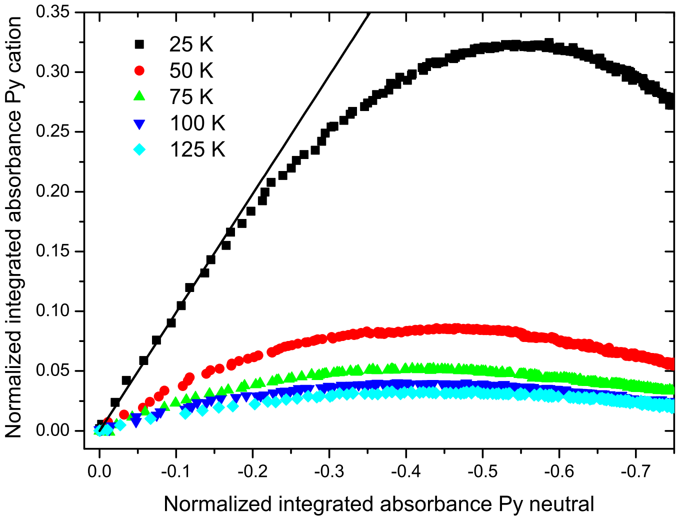

Figure 6.2 Integrated absorbance of the 445.6 nm $Py^{\cdot+}$ band growth plotted against the loss of the 334.0 nm Py band in the 25, 50, 75, 100, and 125 K ices. Ten seconds elapse between subsequent data points. Values are normalized to the maximum integrated absorbance of neutral pyrene. The straight line portion of these plots is used to determine the oscillator strength of $Py^{\cdot+}$ as described in §6.3.2.

experiment. The role of water contamination in CO ice will be discussed in more detail in §6.3.3.

Using baseline corrected spectra as shown in Fig. 6.1, the photochemical evolution is tracked by integrating areas of bands produced by each species in every spectrum and plotting them as a function of photolysis time. The strongest $Py^{\cdot+}$ band at ~445 nm is selected to track the number density evolution of this species. To put the kinetic analysis (§6.4) on a quantitative footing, we determine the oscillator strength of the 445 nm $Py^{\cdot+}$ band as follows. First, the integrated absorbance of the 445 nm $Py^{\cdot+}$ band is plotted versus that of the 334 nm Py band during the course of VUV photolysis at different ice temperatures. These graphs are shown in Fig. 6.2. It should be noted that there is a tight, linear behavior between the loss of neutral pyrene and growth of the pyrene cation during early photolysis times up to 100 s (the first 10 successive datapoints). Inspection of Fig. 6.2 shows that the slope is steepest and the ratio of the integrated absorbance of the $Py^{\cdot+}$ band to the Py band is optimum in the 25 K ice. Since no other photoproduct bands are evident during the linear correlation stage, we conclude that during this phase, neutral pyrene is converted solely into the cation as described previously for naphthalene and quaterrylene [Gudipati & Allamandola 2006a]. The straight-line portion, fitted through the first 10 data points of irradiation at 25 K, is used to determine the oscillator strength of $Py^{\cdot+}$. Given that the ratio of the $Py^{\cdot+}$ to the 334 nm Py band is 0.99 and the oscillator strength of this Py transition is 0.33, the oscillator strength of the 443 nm $Py^{\cdot+}$ band in water ice is also taken to be 0.33. This conclusion is consistent with *ab initio* calculations on pyrene by Weisman et al. [2005]. They calculated that the oscillator strength of the cation is only ~2% stronger than that of the neutral species. As described below, the photolysis of Py in water ices at higher temperatures produces other species in addition to the cation. This explains the different curves in Fig. 6.2.

6.3.3 HCO bands in Py:CO

VUV irradiation of a Py:CO ice also produces a vibrational progression ranging from ~500 to 650 nm. As shown in Fig. 6.3, these absorption bands, located at 513.4, 535.3, 556.3, 583.0, 604.9, and 639.2 nm, are assigned to the $^2\mathrm{A}''(0, v'', 0) \leftarrow \mathrm{X}^2A'(0,0,0)$ $HCO^{\cdot}$ (v''=8–13) transitions based on band positions reported by van IJzendoorn et al. [1983]. The clear $HCO^{\cdot}$ progression indicates a photolytic source of free H atoms in the ice. In addition, it confirms the ability of this setup to record reactive intermediates in the ice.

A possible explanation of the source of H atoms is related to the experimental conditions. The experiments reported here are performed under high vacuum (10^{-7} mbar) conditions. Therefore, background H_2O vapor has ample time to condense onto the sample window while cooling down and growing the ice sample. Water is well known to photodissociate upon VUV irradiation [e.g., Öberg et al. 2009d, Andersson & van Dishoeck 2008] according to

$$\mathrm{H_2O} \xrightarrow{\mathrm{VUV}} \mathrm{OH}^{\cdot} + \mathrm{H}^{\cdot}. \tag{6.3}$$

An experiment on VUV irradiation of a “pure” CO ice indicated that $HCO^{\cdot}$ is also efficiently produced in the absence of pyrene. Therefore, it is likely that water contamination is responsible for the production of HCO$^{\cdot}$ via

$$\mathrm{H}^{\cdot} + \mathrm{CO} \rightarrow \mathrm{HCO}^{\cdot}. \tag{6.4}$$

Another possible formation route could be by means of VUV-induced hydrogen abstraction from pyrene. This pyrene photodissociation reaction, however, is unlikely to occur, since PAHs are generally highly photostable molecules.

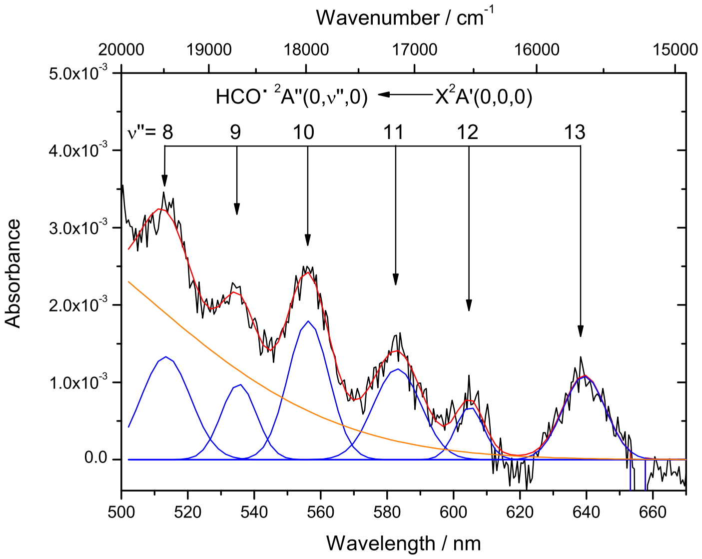

Figure 6.3 Vibrational progression of HCO$^{\cdot}$ generated in a Py:CO ice at 10 K after 600 seconds of VUV irradiation plotted together with a Gaussian fit (red) to the absorption spectrum (black). The individual Gaussians are shown in blue. The orange line indicates the red wing of the underlying broad absorption feature (§6.3.6). (This figure is available in color in electronic form.)

6.3.4 The 400 nm band carrier

Another vibrational progression appears at 400.5, 392.5, and 378.4 nm in the CO ice experiments. As shown in Fig. 6.4, the 400.5 nm band dominates this progression. In contrast, a single band appears at 399.4 nm in the Py:H_2O ice upon VUV irradiation of the samples. The relative intensity of these bands varies with respect to the Py$^{\cdot+}$ bands. The 400 nm bands are more pronounced than the cation bands in the H_2O ice only at *high* temperatures, whereas they are more pronounced in the *low* temperature CO ice.

Two additional measurements were performed to identify the carrier responsible for these transitions. A kinetic experiment was performed on non-VUV-irradiated Py:CO

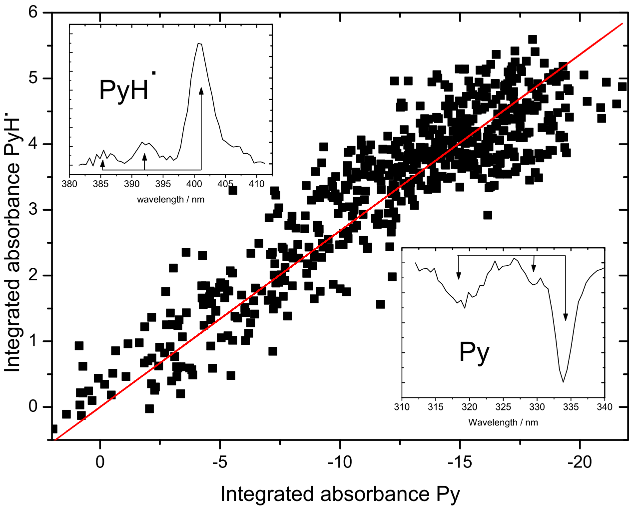

Figure 6.4 Integrated absorbance of the 400 nm $PyH^{\cdot}$ band growth plotted against the loss of the 334 nm Py band in a at 10 K CO ice *after* VUV irradiation is stopped. The straight line directly reflects the relative oscillator strength of both bands as described in §6.3.2. The two insets show the $PyH^{\cdot}$ and Py vibrational progressions in a CO ice 90 minutes after photolysis is stopped.

ice. This ice showed no sign of pyrene ionization by the Xe-lamp, which is used as a spectroscopic light source.The production of $HCO^{\cdot}$ and the formation of the 400 nm band were not observed either. Subsequently, the ice was irradiated by the VUV source for 10 minutes. The steady growth of the 400 nm band with VUV photolysis indicates that the species responsible for the 400 nm band is a product of the VUV processing of the ice. Moreover, when the VUV irradiation is stopped, the 400 nm band carrier *continues* to grow at the expense of the remaining neutral pyrene. This indicates that the chemical reaction leading to the formation of this species is not directly photon-dependent, but rather depends on the diffusion of a photoproduct. A similar experiment on a Py:H_2O ice at 25 K indicates that the same process also takes place in H_2O ice. The detection of $HCO^{\cdot}$ radicals in the ice and the inherent presence of free photolytic H atoms, implies that the growth of the vibrational progression starting at ~400 nm could be the result of the reaction of pyrene with diffusing H atoms

$$\mathrm{Py} + \mathrm{H}^{\cdot} \rightarrow \mathrm{PyH}^{\cdot}. \tag{6.5}$$

This assignment to the 1-hydro-1-pyrenyl radical ($PyH^{\cdot}$) is supported by other experimental studies [Okada et al. 1976, 1980], where progressions at similar band positions are observed upon (laser) flash photolysis.

In contrast to the Py:H_2O experiments where pyrene is also efficiently ionized, the experiment on $PyH^{\cdot}$ formation in CO shows no sign of other reaction products. The integrated absorbance of the growing $PyH^{\cdot}$ transition is plotted versus the integrated absorbance of the diminishing neutral in Fig. 6.4. Growth is tracked over a duration of more than 1.5 hours. Since there is a one-to-one conversion of Py to $PyH^{\cdot}$ in the Py:CO ice (Eq. 6.5), as described in §6.3.2, we derive an oscillator strength of 0.089 for this species by fitting a line through the correlating absorbances in Fig. 6.4.

6.3.5 The 405 nm band carrier

Besides the $Py^{\cdot+}$ and the $PyH^{\cdot}$ bands, another distinct absorption is found in the spectra of VUV irradiated ices. This feature is located at 405.0 nm in the Py:H_2O and at 406.2 nm in the Py:CO experiment. In Chapter 5, we tentatively assigned this absorption to a negative ion, Py^- or PyO^-. The experiments on Py:CO ices presented here enable us to exclude this assignment because of the nearly absent $Py^{\cdot+}$ transitions. Firstly, Py^- is ruled out because a much stronger second Py^- absorption band, expected at 490 nm [Montejano et al. 1995], is absent in our Py:CO experiment. Secondly, PyO^- is also ruled out, because it should exhibit absorption bands down to 350 nm [Milosavljevic & Thomas 2002], bands that are also absent in the Py:CO experiment. Additionally, in Chapter 5 we assumed that PyO^- was a product of PyOH. The formation of PyO^- is also unlikely in the absence of PyOH absorption in these experiments, as discussed below.

The absorption at 405 nm does not correlate with that of the cation, nor with the $PyH^{\cdot}$ band. The band only appears during photolysis and hence is characterized as a VUV-photon-related product. From the literature, it is known that a pyrene triplet-triplet ($^3A_g^- \leftarrow {}^3B_{2u}^+$) transition is expected at this wavelength upon laser excitation of pyrene in solution which populates the lowest member of the triplet manifold [e.g., Hsiao & Webber 1992, Langelaar et al. 1970]. For the 405 nm band to originate from this triplet-triplet transition, the lowest level must be populated and remain so with a long enough lifetime to allow absorption to the $^3A_g^-$ level. In the ice experiments reported here, there are a number of possible routes for pumping the ^{3}Py state. The most obvious route is by means of photoexcitation followed by intersystem crossing

$$^1\mathrm{Py} \xrightarrow{\mathrm{VUV}} {}^1\mathrm{Py}^* \xrightarrow{isc} {}^3\mathrm{Py}. \qquad (6.6)$$

Triplet formation is found to decrease with decreasing temperature in ethanol ice [Stevens et al. 1967]. This translates to our experiment in a nearly absent 405 nm band in the low temperature Py:H_2O experiment, because of the high $Py^{\cdot+}$ formation efficiency. In the high temperature H_2O ice experiments, on the other hand, the 405 nm absorption is much stronger because pyrene is available.

In the CO ice, on the other hand, where $Py^{\cdot+}$ production is low, formation of the 405 nm band carrier appears to be very efficient at low temperatures. The production of the 405 nm band carrier requires VUV photons to be initiated. The pumping of the ^{3}Py state can again occur by means of Eq. 6.6. Moreover, CO has a dipole allowed electronic transition in the VUV. Hence, speculating, pumping of the ^{3}Py state by collisional de-excitation of CO molecules exited by the VUV radiation provides a reaction path of

$$\mathrm{CO} \xrightarrow{\mathrm{VUV}} \mathrm{CO}^*, \tag{6.7}$$

followed by

$$\mathrm{CO}^* +^1 \mathrm{Py} \rightarrow {}^3\mathrm{Py} + \mathrm{CO}. \tag{6.8}$$

In summary, while we cannot identify the carrier of the 405 nm band, the $^3A_g^- \leftarrow ^3B_{2u}^+$ transition seems a plausible explanation.

6.3.6 Broad absorption feature

Finally, besides the narrower bands reported in the previous paragraphs, we discuss a broad underlying feature extending from about 350 to 570 nm, which grows upon photolysis in all cases. This band probably comprises overlapping bands caused by a number of Py/H_2O or Py/CO photoproducts. Part of this Py-residue feature remains even after warming up the sample window to room temperature, whereas all other features disappear at the water desorption temperature.

As discussed above, the very broad feature must be produced by a variety of similar but distinct photoproducts, all containing the pyrene chromophore. Mass spectral analysis of the species produced by the VUV photolysis of a few other PAHs in water ice show that the parent PAH is not destroyed but that OH, O, and H are added to some of the edge carbon atoms [Bernstein et al. 1999]. Given the multiplicity of the side sites on pyrene that can undergo substitution, it is likely that the photoproducts produced in the experiments reported here are multiply substituted, rather than singly substituted. Thus, it is plausible that a mixture of related but distinct Py–X_n species, where X may be H, OH, or O, produce the broad band.

In Chapter 5, we reported the production of a clear and reproducible PyOH band at 344.9 nm in a low temperature H_2O ice. The results presented here do not show evidence of this absorption feature. However, in some instances the absorption was detected upon irradiation or warm-up of the ice. The irregular appearance of the PyOH absorption feature in these experiments indicates that the formation of this species is highly sensitive to the sample's physical parameters, *i*.e., structure of the ice, temperature, and concentration. One possible explanation is that in the experiments reported in Chapter 5, the Py concentration was not controlled and those experiments sampled a very different ice concentration and, by implication, physical ice structure. While we do not have a solution for this discrepancy, we emphasize that both measurement series have been fully reproducible over many independent experiments for periods of months. An experimental program to investigate the role of the PAH:H_2O concentration on ice photochemistry is underway.

6.4 Py:H_2O ice photochemistry at different temperatures

Figure 6.5 shows the spectral evolution of two different Py:H_2O samples at different temperatures. The top frame presents the 280 to 540 nm spectra of the 100 K Py:H_2O ice after 0, 20, 40, 80, and 160 s of in situ photolysis and the bottom frame the corresponding spectra for the 25 K ice. These spectra are snapshots of the more than one thousand spectra collected during 4 hr of photolysis. They illustrate the rapid changes that occur during the early stages in the photochemistry of these ices and the major differences in reaction products at different temperatures.

To probe the VUV-driven photophysics and reaction dynamics for a set of selected temperatures, the production and depletion of species was tracked as a function of irradiation time. To this end, the Py 334 nm, Py$^{\cdot+}$ 445 nm, and PyH$^{\cdot}$ 400 nm bands were integrated for every spectrum. The spectra in Figs. 6.1 and 6.5 show that it is rather straightforward to determine the boundaries needed to integrate these bands. We estimate that the uncertainty in most of these band areas is of the order of 10%.

The integrated absorbances of the neutral Py, strongest Py$^{\cdot+}$, and PyH$^{\cdot}$ bands in H_2O ice at temperatures of 25, 50, 75, 100, and 125 K are plotted versus photolysis time (VUV fluence) in Fig. 6.6. The spectra in Fig. 6.5 and photochemical behavior in Fig. 6.6 show that, upon photolysis, neutral pyrene loss is immediate and rapid. The initial growth of Py$^{\cdot+}$ mirrors the rapid, initial loss of Py. However, while Py steadily decreases, and several other Py photoproduct bands increase during some 4 hours of photolysis, the production of Py$^{\cdot+}$ reaches a maximum and then slowly diminishes. From Fig. 6.6, one can clearly see that ionization of pyrene is most efficient in the low temperature ice. Formation of PyH$^{\cdot}$, on the other hand, is far more efficient at higher temperatures.

For comparison, the integrated absorbances for the irradiated Py:CO ice are plotted as a function of time in the right bottom frame of Fig. 6.6. It should be noted that the PyH$^{\cdot}$ band is multiplied by a factor of 10 in the Py:CO experiment, compared to a factor of 20 in the Py:H_2O experiment. The PyH$^{\cdot}$ band is clearly more prominent in the CO ice experiment than in the H_2O ice experiments. The Py^{+} signal on the other hand is negligible. This indicates that the H_2O ice plays a role in ion formation and stabilization.

To place this behavior on a quantitative footing, the integrated areas for the Py and Py$^{\cdot+}$ bands are converted to number densities using Eq. 6.1. Here, an oscillator strength of 0.33 is used for the 334 nm Py bands. The values used for the oscillator strengths of the Py$^{\cdot+}$ and PyH$^{\cdot}$ bands are 0.33 and 0.089, respectively, as determined in §6.3.2 and §6.3.4. Perusal of Fig. 6.6 shows that Py behaves similarly in all of the ices considered here. Regardless of temperature, its signal drops quickly with the onset of irradiation and continues to diminish with ongoing photolysis. Likewise, Py$^{\cdot+}$ grows rapidly with initial photolysis but peaks after a relatively short time interval corresponding to a fluence of roughly 8×10^{16} photons and then drops continuously. While the Py$^{\cdot+}$ growth and loss curves resemble each other, cation production efficiency is strongest in the 25 K ice. This efficiency remains of the same order at even lower temperatures (not shown here). The photolysis time required for the cation to reach a maximum shortens with increasing

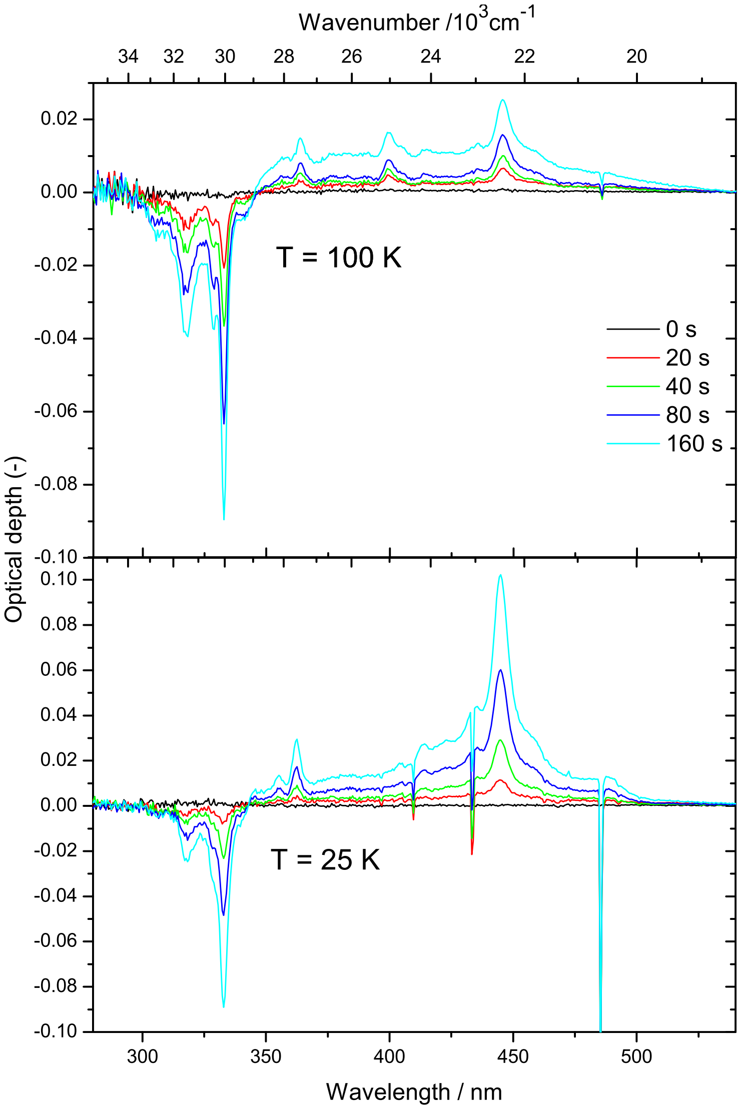

Figure 6.5 The VUV-induced spectroscopic changes in Py:H_2O ice for two different temperatures as a function of photolysis time. Comparing the spectra from the 25 K ice (bottom) with those of the 100 K ice (top) shows the critical role that temperature plays in determining photochemical pathways in a PAH-containing ice. In the 25 K ice, cation formation is favored over production of the pyrene residue and the 400 and 405 nm band carriers. The opposite holds for the 100 K ice.

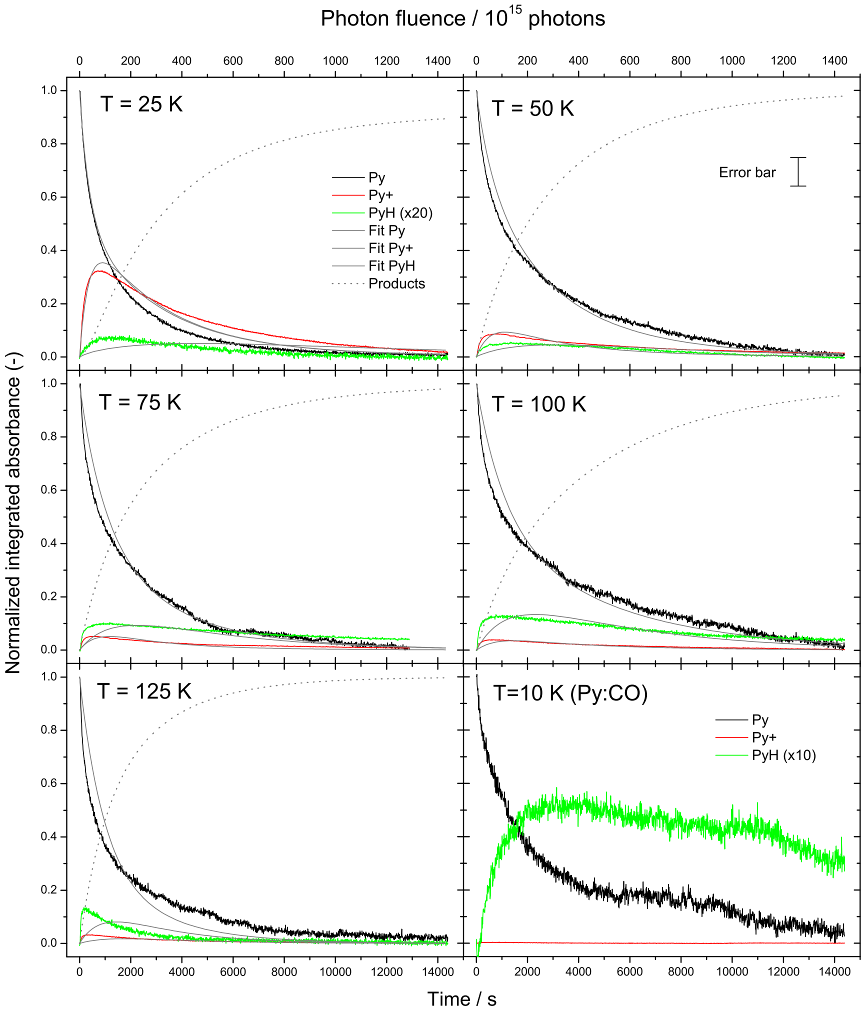

Figure 6.6 The integrated absorbance of the Py 334 nm, $Py^{\cdot+}$ 445 nm, and $PyH^{\cdot}$ 400 nm bands as a function of VUV irradiation in Py:H_2O ices at 25, 50, 75, 100, and 125 K and a Py:CO ice at 10 K plotted together with the fits (grey lines) described in §6.4. Integrated absorbance values are scaled and normalized to the initial value for the Py signal. The $PyH^{\cdot}$ feature is multiplied by a factor of 20 for the Py:H_2O experiments and by a factor of 10 for the Py:CO experiment. The approximate, overall growth of the total Py photoproduct band (P_1+P_2+P_3) is also shown (dotted line). (This figure is available in color in the on-line electronic form.)

temperature. The $PyH^{\cdot}$ band contribution is minor with respect to the $Py^{\cdot+}$ band for ices below 50 K. This reverses between 50 and 75 K, suggesting that there is a change in the dominant Py:H_2O ice photochemical channel in this temperature range.

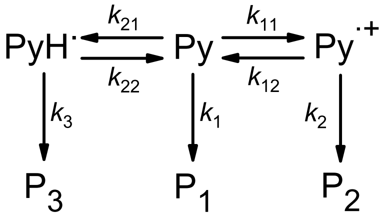

Figure 6.7 Reaction scheme used to fit the experimental data.

A kinetic analysis of the plots in Fig. 6.6 is carried out using the reaction scheme indicated in Fig. 6.7. Here, k_{11} is the photoionization rate of Py to $Py^{\cdot+}$, k_{12} the electron-ion recombination rate of $Py^{\cdot+}$, k_{21} the production rate of the $PyH^{\cdot}$ feature, and k_{22} the rate of the reverse reaction of $PyH^{\cdot}$ to Py. The rates designated k_1, k_2, and k_3 are the production rates for the different products that comprise the Py-residue band. The oscillator strengths for the $Py^{\cdot+}$ and $PyH^{\cdot}$ bands are also fitted, but are restricted to remain within ±10% of the experimentally determined values of 0.33 and 0.089. All reactions are assumed to be first order in the reactant. The relative abundances of “free or solvated electrons” and O, H, and OH radicals in the ice are not considered.

The fits to the growth and decay curves are included in Fig. 6.6 and the temperature dependence of the derived rate constants is presented in Fig. 6.8. The agreement between the fit and the experimental data in terms of curve shape and absolute intensity is good. The fitted oscillator strengths of the $Py^{\cdot+}$ and $PyH^{\cdot}$ bands amount to 0.31 and 0.082, respectively, and hence do not deviate much from the experimentally determined values.

The graph in Fig. 6.8 indicates that the Py photoionization rate (k_{11}) drops rapidly between 25 and 50 K. The electron recombination rate (k_{12}) decreases only slightly, if at all, within the errors over the entire temperature range. As mentioned above, the production of the $PyH^{\cdot}$ becomes more important at higher temperatures. Its formation rate (k_{21}) is low in all ices up to 50 K ($< 4.4 \times 10^{-5}$), but jumps to $> 1\times10^{-4}$ in the ices with temperatures of 75 K and higher. The back channel from $PyH^{\cdot}$ to Py, k_{22}, also shows a temperature dependence. It increases almost linearly in going from cold to warm ices. The formation rate of a photoproduct produced directly from Py (k_1) also seems to jump at 50 K. The formation rate of products originating in the $Py^{\cdot+}$ species, on the other hand, seems to lower with increasing temperature. Finally, the rate of product formation from the $PyH^{\cdot}$ channel is low throughout the entire temperature range. The jump in rate of the formation of P_1 and $PyH^{\cdot}$ with temperature probably reflects the diffusion barrier of radical species ($H^{\cdot}$ and $OH^{\cdot}$) in the ice.

Since published studies of the processes induced by the photolysis of other PAH:H_2O ices are limited, not much information is available with which to compare these results. While, to the best of our knowledge, there are no reports of the photochemistry that takes

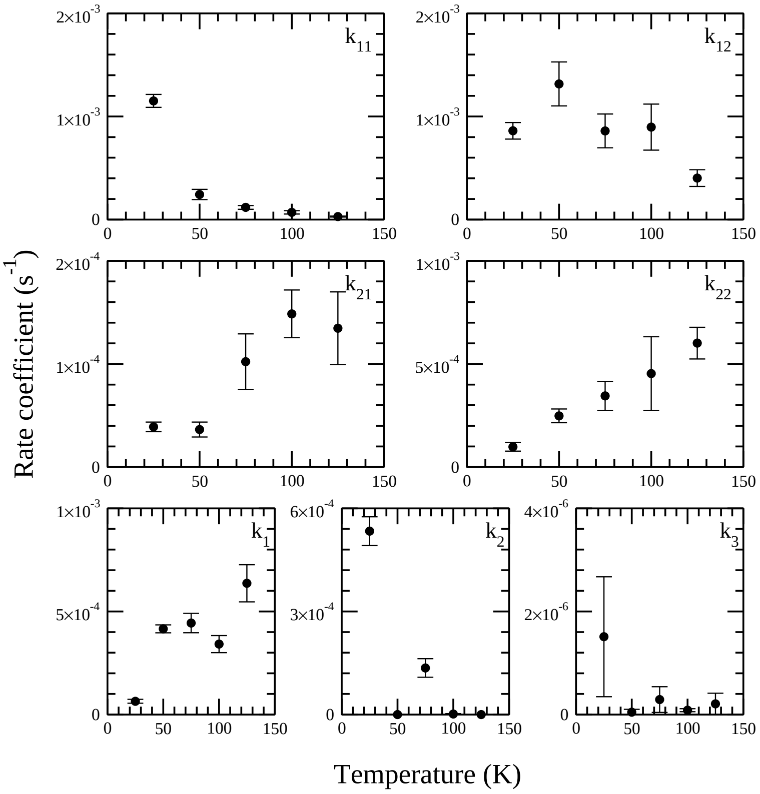

Figure 6.8 Parameters (k_{nm}) as a function of temperature resulting from fitting the reaction scheme (Fig. 6.7) to the kinetic experiments (Fig. 6.6). All rates are indicated in s^{-1}.

place as a function of ice temperature or of long-term fluence, the VUV photochemistry of the PAHs naphthalene, 4-methylpyrene (4MP), and quatterrylene in water ice at 10 K has been studied [Gudipati & Allamandola 2003, Gudipati 2004, Gudipati & Allamandola 2006a,b]. The results obtained are in good agreement with the low temperature (25 K) case reported here. Namely, the parent PAH is easily and efficiently ionized, by quantitative conversion of the neutral species to the cation form. The focus of the earlier studies was on cation production and stabilization and not on long-duration photolysis experiments. In their study of 4MP:H_2O (1:>500) ice at 15 K, Gudipati & Allamandola [2003] utilized a reaction scheme similar to that on the right half of that presented in Fig. 6.7. Table 6.2 compares the reaction rates that they determined with those of the 25 K ice reported here. Except for the production of P_2, which differs by one order of magnitude, there is very good agreement between the rate constants for each step in the two experiments.

The growth and decay curves in Fig. 6.6, taken together with the temperature depen-

Table 6.2 The reaction rates for the VUV photolysis of Py:H_2O (~1:5,000) ice at 25 K compared to those for 4-methylypyrene:H_2O (1:≤500) ice at 15 K [Gudipati & Allamandola 2003].

Rate		This work (s^{-1})	Photon rate[a] ($cm^2 photon^{-1}$)	Gudipati 2003 (s^{-1})
$Py \xrightarrow{VUV} Py^{\cdot +}$	(k_{11})	$(1.2\pm0.1)\times10^{-3}$	1.2×10^{-17}	1.3×10^{-3}
$Py^{\cdot +}+e^- \rightarrow Py$	(k_{12})	$(9\pm2)\times10^{-4}$	9×10^{-18}	8×10^{-4}
$Py \rightarrow P_1$	(k_1)	$(5\pm1)\times10^{-5}$	...	4×10^{-5}
$Py^{\cdot +} \rightarrow P_2$	(k_2)	$(5\pm1)\times10^{-4}$	...	5×10^{-5}

[a] Photon rates are indicated only for reaction channels which are dominated by photon processes.

dence of the reaction rates in Fig. 6.8, show that the VUV-driven PAH photochemistry depends strongly on ice temperature. The influence of the ice morphology on this chemistry was also investigated, to understand the origin of the temperature dependence. An experiment on an ice deposited at 25 K, annealed to 125 K, and subsequently cooled to 25 K before photolysis, showed that the ionization rate and efficiency are similar to that of an unannealed ice. Apparently, it is not the morphology but the temperature of the ice that primarily determines which process dominates. We discriminate between two temperature regimes. One governed by ion-mediated processes that dominate at 25 K and slightly higher temperatures, and a second, presumably radical-driven regime, that becomes increasingly more important at higher temperatures.

6.5 Astrochemical Implications

As shown in the previous paragraphs, ionization and chemistry of a rather small PAH species, pyrene, trapped in H_2O ice turns out to be very efficient in a laboratory setting. Here, we extend these findings to interstellar conditions, with the aim of including the calculated rates in astrochemical models. For this, it is crucial to distinguish pure photochemical processes from diffusion, since the latter will be highly dependent on the number density of radicals and electrons in the ice. As mentioned in the previous paragraph, the photoionization of Py is probably a single-photon process, whereas protonation of Py and the electron recombination of $Py^{\cdot +}$ are the results of both VUV photolysis and diffusion. The mechanism for $PyH^{\cdot}$ deprotonation is unclear, since it can proceed by means of either VUV processing or through hydrogen abstraction by diffusing species. Diffusion of radicals through the ice is a thermally activated process and will therefore increase with temperature. Recombination, however, is largely temperature-independent in our experiments, indicating that the rate of $Py^{\cdot +}$ recombination is not dominated by the diffusion of electrons in the ice. If $Py^{\cdot +}$ loss occurs by means of electron recombination and not $Py^{\cdot +}$ reaction with H_2O or one of its photoproducts, the electron most likely originates from the initial photoionization event after which electrons remain in the vicinity of the recombining $Py^{\cdot +}$ species. Hence, this local process can be, although indirectly, regarded as a single-photon process.

The rates of protonation of Py and deprotonation of $PyH^{\cdot}$ show a temperature dependence and the importance of diffusion can therefore not be excluded. This makes it harder to directly translate the rates (s^{-1}) into photon rates (cm^2 $photon^{-1}$). However, we can determine astrochemical photon rates for both ionization and recombination of pyrene in interstellar H_2O ice (see Table 6.2).

Now, to translate this to the astrochemical situation and with other processes, we assume that PAHs generally have an ionization rate similar to that of pyrene. How do ionization and chemistry compare with other processes such as the photodesorption of the icy grain mantle, in which the PAHs are embedded? To exemplify this, the rate of ionization of a PAH in water ice at 25 K (in $photon^{-1}$) is calculated anywhere in a dense cloud where $A_V = 3$ and compared with the VUV photodesorption rate of H_2O derived by Öberg et al. [2009d]. It is well established that the onset of ice formation occurs in clouds with an edge-to-edge (through the cloud) magnitude of $A_V = 3$ [e.g. Whittet et al. 2001]. Thus, inside our hypothetical dense cloud at $A_V = 3$ (from cloud edge to within the cloud), ices are present.

The experimentally determined PAH ionization rate in H_2O at 25 K, normalized to the total amount of deposited PAH is given by

$$k_{11} = \frac{\mathrm{d}\frac{[\mathrm{PAH}^+]}{[\mathrm{PAH}]_0}}{\mathrm{d}t} = 10^{-3}\ \mathrm{s}^{-1}. \tag{6.9}$$

Consider a typical interstellar grain, covered by a 100 monolayer (ML) thick ice. The number of sites on a grain is 10^{15} cm^{-2}. If we assume that one in every 10^4 particles on the grain is a PAH, the total number of PAH molecules on the grain is $[\mathrm{PAH}]_0 = 100 \times 10^{15} \times 10^{-4} = 10^{13}\ \mathrm{cm}^{-2}$. Furthermore, the VUV photon flux in our laboratory, Φ, is 10^{14} photons $cm^{-2}s^{-1}$. The production rate of PAH cations on an interstellar grain is now given by $[\mathrm{PAH}]_0 \cdot k_{11}/\Phi = 10^{-4}$ $photon^{-1}$. This ionization rate is an order of magnitude lower than the rate of photodesorption ($\sim 10^{-3}$ $photon^{-1}$) [Öberg et al. 2009d].

However, in our dense cloud the number of photons available for PAH photoionization is larger than the number of photons available for photodesorption of H_2O ice. This is because H_2O photodesorption is primarily caused by VUV photons, whereas PAH ionization can occur for much lower energy photons. To quantify the radiation field in a dense cloud at $A_V = 3$ as a function of wavelength (λ), we take the average UV interstellar radiation field (I_ν) from Sternberg [1988] and rewrite the expression to I_λ with units photons $cm^{-2}s^{-1}nm^{-1}$

$$I_\lambda = \frac{1.068 \times 10^{-4} c}{\lambda^3} - \frac{1.719 \times 10^{-2} c}{\lambda^4} + \frac{6.853 \times 10^{-1} c}{\lambda^5}, \tag{6.10}$$

where c is the speed of light in nm s^{-1}. The attenuation of the radiation field by dust as a function of wavelength is given by

$$D_\lambda = \exp\left[\frac{-11.6 A_V}{R_V} \frac{A_\lambda}{A_{1000\text{Å}}}\right], \tag{6.11}$$

from Draine & Bertoldi [1996], where we assume that $R_V = 3.1$ and $A_V/A_{1000\text{Å}} = 0.21$ [Whittet 2003]. This results in

$$D_\lambda = \exp\left[-0.8\frac{A_\lambda}{A_V}A_V\right], \tag{6.12}$$

where the table of A_λ/A_V values is taken from Mathis [1990]. The photon flux per second per wavelength interval is given by

$$P_\lambda = I_\lambda D_\lambda. \tag{6.13}$$

Water ice absorbs photons with wavelengths ranging from 130 to 150 nm [Kobayashi 1983, Andersson & van Dishoeck 2008]. The ionization energy of PAHs on the other hand, is lowered by about 2 eV when in H_2O ice [Gudipati & Allamandola 2004, Woon & Park 2004]. For the wavelength range available for ionization of PAHs, assuming that H_2O blocks all photons below 150 nm, we take 150 to 250 nm [Li & Draine 2001]. By integrating the photon flux in a cloud of $A_V = 3$ over both wavelength intervals a number of photons available for PAH ionization is found that is 6 times larger than the number of photons available for photodesorption of H_2O. Additionally, at $A_V = 3$, the cosmic-ray-induced UV field is negligible compared to the interstellar UV field [Shen et al. 2004]. Therefore, the occurrence of photoionization is of similar order as photodesorption of the main component in the grain mantle in a dense cloud. The ionization rates from Table 6.2 can be directly included in astrochemical models in the form

$$\frac{\mathrm{d}[\mathrm{PAH}^+]}{\mathrm{d}t} = k_{11}\Psi[\mathrm{PAH}], \tag{6.14}$$

where $[\mathrm{PAH}^+]$ is the concentration of the PAH (pyrene) cation in the ice, k_{11} is the photon rate in $\mathrm{cm}^2\mathrm{photon}^{-1}$, Ψ is the photon flux in photon $\mathrm{s}^{-1}\mathrm{cm}^2$, and [PAH] is the PAH (pyrene) concentration in the ice.

In the above calculation, we assume that all PAHs exhibit the ionization behavior of the pyrene chromophore. Of course, more PAHs need to be investigated experimentally before drawing conclusions on their general photochemical behavior in interstellar ices. However, if all PAHs have an ionization rate similar to that of pyrene, photoionization and subsequent chemical reactions of PAHs trapped in ices are important processes in dense clouds. When frozen-out in ices, PAHs have an important impact on the radical and electron budget in solid state chemistry. Hence, the processes described here may be more important than previously assumed in modeling complex interstellar grain chemistry.

6.6 Conclusions

A recently constructed setup has been used to track, on a sub-second timescale, the photochemistry of a PAH in H_2O and CO ices as a function of temperature. The setup used here clearly has advantages compared to relatively slow infrared photochemical ice studies. The conclusions from this work on a PAH, pyrene, trapped in an interstellar ice analogue are summarized below:

1. A set of photochemical reaction products has been identified in both irradiated Py:H_2O and Py:CO ice experiments. The reaction products result from direct photoionization of pyrene, or from a reaction of the parent, pyrene, with free H atoms produced in the matrix. Additionally, an absorption band is tentatively assigned to a triplet-triplet transition of pyrene. A vibrational progression assigned to $HCO^{\cdot}$ is found in spectra of the VUV-irradiated Py:CO ice.
2. Pyrene is easily and efficiently ionized when trapped in H_2O ice. Photoionization is a non-diffusion-related reaction and hence a photon rate of 1.2×10^{-17} cm^2 photon^{-1}, which can serve as input for astrochemical models, is derived.
3. When trapped in CO ice, pyrene ionization is inefficient compared to that in water ice.
4. Electron-ion recombination is independent of ice temperature and is characterized as a non-diffusion-dominated reaction. For this process, a photon rate of 9×10^{-18} cm^2 photon^{-1} is derived, which can be directly used in astrochemical models.
5. There are two distinct reaction paths in the photochemistry of pyrene trapped in H_2O ice. At low temperatures ($<$ 50 K), the chemistry is dominated by ion-molecule interactions and processes. At temperatures above 50 K, reactions are dominated by diffusing radical species.
6. A simple model indicates that, in dense clouds where $A_V = 3$, the rate of pyrene ionization is comparable to the rate of photodesorption in water-rich ices. Hence, chemical reactions involving pyrene and its cation can be important in modeling grain chemistry in these environments.

CHAPTER 7

Ionization of Polycyclic Aromatic Hydrocarbons trapped in H_2O ice [1]

Mid infrared emission features originating from Polycyclic Aromatic Hydrocarbons are present throughout many phases of the interstellar medium. Towards dense clouds, however, these features are heavily quenched. Observations of dense clouds point out that many simple molecules are frozen out on interstellar grains, forming thin layers of ice. It is likely that more complex non-volatile species, such as PAHs, also freeze out on grains and contribute to the chemistry of interstellar ices. The study presented here aims at obtaining reaction rate data for the photochemistry of PAHs in an interstellar H_2O ice analogue. Furthermore, the experimental data are implemented in a chemical model of a dense interstellar cloud in order to study the relevance of PAH:H_2O ice reactions in these interstellar regions. Time dependent near-UV/visible spectroscopy on anthracene, pyrene, benzo[ghi]perylene and coronene containing interstellar H_2O ice is performed at 25 and 125 K, using an optical absorption setup for the study of ices (*OASIS*). Near-UV/VIS absorption spectra are obtained for these four PAHs and their cationic species trapped in H_2O ice. Relative oscillator strengths of the cation absorption bands are derived relative to the oscillator strength of the neutral parent PAH. The number density evolution of species in the H_2O matrix is measured and fitted to a reaction scheme, resulting in rate constants for the corresponding reactions. A freeze-out model is employed to determine on what timescale PAH molecules are incorporated in interstellar ices. The PAH:H_2O photochemical rate constants are used in an astrochemical model, which is used to determine the importance of PAH:H_2O ice photoprocessing in going from a dense cloud to a protostellar object. All four PAHs studied here are found to be readily ionized upon VUV photolysis when trapped in H_2O ice and exhibit similar rates for ionization. The PAH freeze out occurs on rather long time scales in a dense cloud. Thus, PAH photoprocessing will only be important after the PAH containing ices are formed, i.e. during the protostellar phase. In this phase, photoprocessing of PAH containing H_2O ice is indeed an effective process.

---

[1] Based on: J. Bouwman, H. M. Cuppen, M. Steglich, L. J. Allamandola, H. Linnartz, Astronomy and Astrophysics, in prep.

7.1 Introduction

The presence of Polycyclic Aromatic Hydrocarbons (PAHs) in many phases of the interstellar medium is evidenced by their strong and ubiquitous mid-infrared emission features [Smith et al. 2007, Draine et al. 2007, Draine & Li 2007, Tielens 2008]. Mid-IR features are efficiently emitted by a PAH after being excited by an energetic photon. Toward dense clouds, however, the mid-IR features are strongly quenched. Here, most volatile molecules are frozen out on grains forming layers of ice [e.g., Pontoppidan et al. 2004, Boogert et al. 2008, Öberg et al. 2008, Bottinelli et al. 2010]. Under such conditions, PAHs most likely also condense on interstellar grains, incorporating them in interstellar ices.

Experimental studies on the effect of vacuum ultraviolet (VUV) irradiation of interstellar ice analogues have shown that more complex molecules can be formed in the simplest mixed ices [e.g. Gerakines et al. 1995, Öberg et al. 2009c]. The first laboratory studies on VUV irradiated PAH containing ices indicated that PAHs are easily ionized. These experiments also show the formation of new species. Time dependent information on these chemical reactions, however, is largely lacking.

Here, we present the time evolution of the destruction of four PAHs, anthracene (Ant, $C_{14}H_{10}$), pyrene (Py, $C_{16}H_{10}$), benzo[ghi]perylene ($B_{ghi}P$, $C_{22}H_{12}$), and coronene ($C_{24}H_{12}$) in H_2O ice together with the formation and destruction of the ionized PAH^+ species. This chapter aims to quantify and understand the time dependent chemistry of PAH:H_2O ice mixtures upon VUV irradiation and the resulting photoproducts.

The chemical evolution is tracked by means of near-UV/VIS absorption spectroscopy at two extreme temperatures, 25 K and 125 K. This work is an extension of the detailed study of pyrene in H_2O ice presented in Chapter 4 and aims to draw more general conclusions on the PAH photochemistry in ices based on a larger sample set. Furthermore, the present study extends the PAH:H_2O photochemistry to larger and astrophysically more relevant members of the PAH family.

The outline of this paper is as follows. In §7.2 the experimental setup is briefly discussed, together with the details of the theoretical calculations. Paragraph 7.3 describes spectra of the PAH and PAH^+ cations and present their (relative) oscillator strengths and the assignments of the observed transitions. The fitted time dependent data are discussed in detail in §7.4, after which the astrophysical implications are discussed in §7.5. Finally, the conclusions are summarized in §7.6.

7.2 Experimental technique

Here we briefly describe the experimental setup. The system is described in detail in Chapter 5. The setup consists of a high-vacuum ($\sim 10^{-7}$ mbar) chamber. In the center of the vacuum chamber a MgF_2 sample window is suspended, which is cooled by a closed cycle He cryostat to a temperature of 25 K. Temperatures as low as 11 K can be realized. PAH containing H_2O ices are grown onto the sample window by vapor deposition. Milli-Q H_2O is further purified by three freeze-pump-thaw cycles and the PAHs are used as commercially available (Ant, Aldrich ≥99%, Py, Aldrich, 99%, B$_{ghi}$P, Aldrich, 98%, Cor, Aldrich, 99%). The thickness of the samples is monitored by laser interference and the amount of deposited PAH is monitored in absorption, allowing for determination of the samples PAH:H_2O concentration.

The inlet system has been modified for measuring the large PAHs in our sample, B$_{ghi}$P and Cor. A sample container is mounted in the vacuum chamber and located adjacent to the H_2O deposition tube. The sample container is heated with polyimide insulated nichrome heater wire. The H_2O flow to the sample is set such that a certain static pressure is reached inside the vacuum chamber, and the current through the heater wire is chosen such that the rate of deposition results in the desired sample concentration. Additionally, a heat shield is mounted on the sample holder, such that the PAH that vaporizes during heating of the sample container to the desired temperature is collected on the heat shield, rather than on the sample window.

After deposition on the 25 K window, the sample is heated to the desired temperature. Subsequently, the sample is subject to Vacuum Ultra-Violet (VUV) radiation, which is produced by a H_2 flow microwave (MW) discharge lamp. The lamp operates at a static H_2 pressure of 0.4 mbar, and a MW power of 100 W, resulting in an effective VUV flux of $\sim 10^{14}$ photons·cm^{-2}s^{-1} at the sample surface.

Near UV/VIS absorption spectra are taken during VUV processing of the samples. To this end, a Xe-lamp is used as a broadband light source and a spectrometer equipped with a 1024×256 pixel CCD camera is used as detector. The CCD camera is read out in vertical binning mode by a computer on which the raw data are converted into optical depth ($OD = \ln(I/I_0)$). Spectra ranging from ~280 to 800 nm are taken at a rate of 0.1 s^{-1}, which is sufficient to monitor chemical changes in our ice samples. Each spectrum is the result of co-adding 229 individual spectra, resulting in an excellent signal-to-noise ratio.

The integrated absorbances of the deposited neutral PAH signal, $\int \tau_\nu d\nu$, is converted into a PAH column density, $N_{\rm PAH}$, via the oscillator strength of the neutral PAH, f, by:

$$N_{\rm PAH} = \frac{\int \tau_\nu d\nu}{8.88 \times 10^{-13} f}. \tag{7.1}$$

Together with an ice thickness measurement based on the interference pattern in the reflection of a HeNe laser as described in Chapter 5, this allows for a rather accurate determination of the PAH:H_2O concentration. Sample deposition is stopped at thicknesses of ~2 μm, resulting in comparable ice samples.

In a typical experiment of 4 hours, as many as 1400 spectra are obtained. The spectra are all baseline corrected by fitting a second order polynomial through points where no absorptions occur and subsequently subtracting the polynomial. Additionally, absorption band are integrated and, if necessary, corrected for contributions by atomic H-lines originating in the H_2 MW discharge lamp. All the data handling is performed in a LabView program.

In order to support the assignments of measured absorption bands caused by the photo-products, we performed density functional theory (DFT) calculations using the GAUSSIAN09© software [Frisch et al. 2009]. We used the B3LYP functional in conjunction with the 6-311++G(2d,p) basis set to determine the ground state geometry and electronic structure of PAH neutrals and cations. Excited states were investigated within the framework of the time-dependent density functional theory (TDDFT) applying the same level of theory.

7.3 PAH:H_2O spectroscopy

Long duration photolysis experiments are performed on a set of four PAHs (Ant, Py, $B_{ghi}P$, and Cor) in H_2O ice at low (25 K) and high (125 K) sample temperatures. For determining the amount of deposited PAH, oscillator strengths for the neutral PAHs are taken from the literature. The amount of deposited H_2O is measured by laser interference, yielding ice thicknesses of typically ~2 μm. Combining the thickness of the sample and the amount of deposited PAH results in the PAH concentration in the sample. An overview of the used mixture concentrations , the temperature at which the samples are photolyzed, and the oscillator strengths values (f) of the neutral PAH adopted from the literature is given in Table 7.1.

Table 7.1 An overview of the studied PAH species and used PAH:H_2O concentration, sample temperature as well as the wavelength interval of the strongest neutral absorption band system, and the corresponding literature values for the oscillator strengths.

Species	Conc.	T_{Sample} (K)	λ_{range} (nm)	f
Ant	1:2.000	25	316–381	0.1[a]
Ant	1:1.500	25		
Ant	1:900	25		
Ant	1:500	125		
Py	1:5.000	25	295–350	0.33[b]
Py	1:6.500	125		
$B_{ghi}P$	1:2.000	25	320–388	0.21[c]
$B_{ghi}P$	1:1.000	125		
Cor	1:5.000	25	273–314	1.04[d]
Cor	1:4.000	125		

[a] Gudipati [1993] [b] Bito et al. [2000], Wang et al. [2003] [c] Rouillé et al. [2007] [d] Ehrenfreund et al. [1992]

For each of the PAHs under investigation, we determined the oscillator strengths of the cationic species' absorption bands relative to that of the neutral precursor. This allows for a full quantitative study of the formation and destruction, which will be presented in §7.4. Relative oscillator strengths are determined by plotting the time evolution of the integrated absorbance of the cation transition under investigation against the integrated absorbance of the strongest electronic transition of the neutral species (see Fig. 7.1). Both integrated absorbances are normalized to the amount of deposited neutral PAH, which is determined during the preparation of the ice sample. A quantitative conversion of the PAH molecule into its cationic species is assumed to occur during the first photolysis stage:

$$\mathrm{PAH} \xrightarrow{\mathrm{VUV}} \mathrm{PAH}^{+} + \mathrm{e}^{-}. \tag{7.2}$$

Linear fits are made to the first data points, of which the slope directly reflects the oscillator strength of the cation relative to that of the neutral. None of the PAH species in our sample substantially deviates from a one-to-one conversion during the first 100 s of photolysis, making the assumption valid and the resulting relative oscillator strength values reliable vantage points for further analysis.

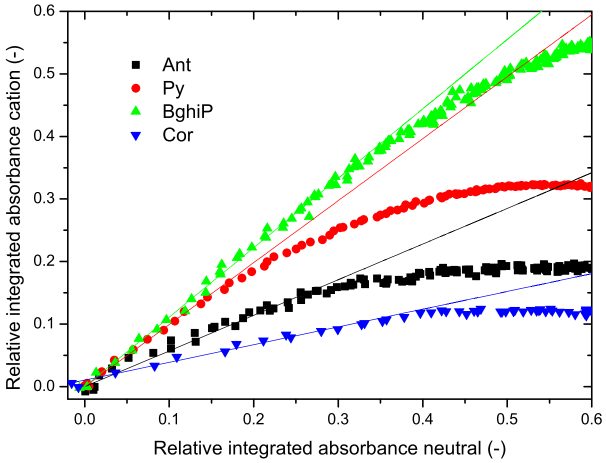

Figure 7.1 The correlation between the amount of produced cation and the amount of used up neutral, both relative to the total deposited amount of neutral PAH.

Typical absorption spectra for the 25 K PAH:H_2O ice mixtures taken at the maximum cation absorption are plotted in Fig. 7.2. The position of the band origin, the range used for integration and oscillator strength value relative to the strongest neutral absorption are listed in Table 7.2. The assignments of the neutral and photoproduct bands is discussed for each individual PAH below.

7.3.1 Anthracene ($C_{14}H_{10}$)

The negative signal between ~310 and 380 nm is caused by the destruction of the neutral Ant molecules and reflects the depopulation of the $^1B_{2u} \leftarrow {}^1A_g$ transition of neutral Ant [Bak et al. 2000]. The positive absorption features throughout the spectrum are caused by species that are produced by photodestruction of the parent PAH. A strong vibronic progression arises between 500 and 760 nm with its maximum at 719.6 nm. This progression has previously been assigned to the $^2A_u \leftarrow {}^2B_{2g}$ transition of the singly ionized Ant species (Ant$^+$) [Szczepanski et al. 1993b]. For this transition we derive an oscillator

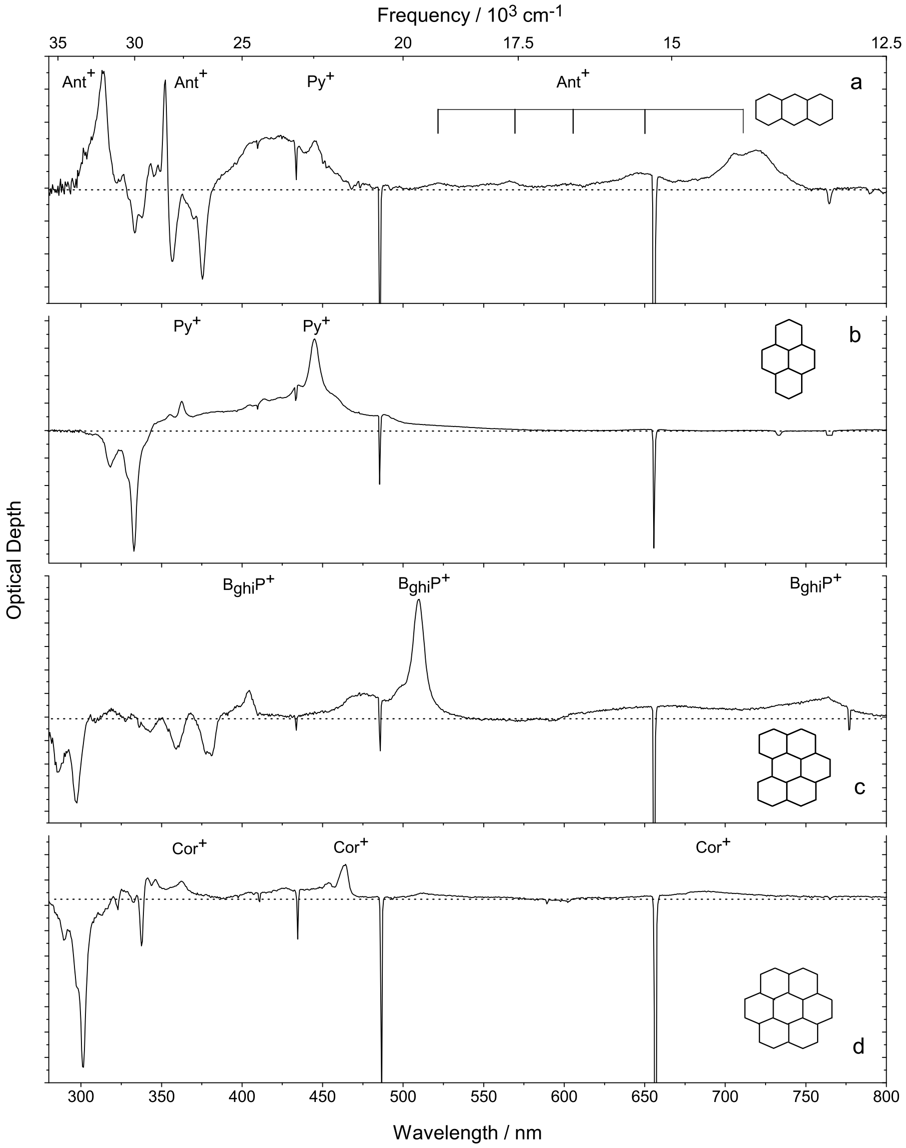

Figure 7.2 The 280 to 800 nm spectra of the PAHs anthracene (a), pyrene (b), benzo[ghi]perylene (c), and coronene (d) in H_2O ice, photolyzed at 25 K. Negative features indicate that a species is destroyed, positive bands indicate that a species is formed. The mixing ratios are 1:700, 1:5.000, 1:2.500, and 1:4.000 (PAH:H_2O) for anthracene, pyrene, benzo[ghi]perylene, and coronene, respectively. The molecular structures are also indicated in the corresponding spectra.

strength value of 0.59 relative to that of the neutral. A sharp and strong absorption feature previously assigned to the $^2B_{1u} \leftarrow {}^2B_{2g}$ transition of Ant^+ appears at 351.1 nm. This absorption has an oscillator strength of 0.15. Likewise, an absorption feature which is assigned to the $^2A_u \leftarrow {}^2B_{2g}$ transition of Ant^+ is found at 313.7 nm.

Table 7.2 Overview of the studied PAHs, state symmetry, position of the band origin, the range over which the transition is integrated, and oscillator strength of the cation species relative to that of the strongest neutral transition.

Species	Symmetry	Origin Pos. (nm)	range (nm)	$f_{rel.}$
Ant	$^1B_{2u}$ $^{(a)}$	375.4	316-385	1.00
Ant^+	^2A_u $^{(b)}$	719.6	505-753	0.74
Ant^+	$^2B_{1u}$ $^{(b)}$	351.1	349-354	0.15
Ant^+	^2A_u $^{(b)}$	313.7	307-318	0.37
Py	$^1B_{2u}$ $^{(c,d)}$	334.0	290-345	1.00
Py^+	$^2B_{1u}$ $^{(c,d)}$	363.2	350-370	0.13
Py^+	^2A_u $^{(c,d)}$	445.6	411-470	0.99
Py^+	$^2B_{1u}$ $^{(c,d)}$	490.1	...	...
$PyH^{\cdot}$	...	399.4	380-410	0.26
$B_{ghi}P$	$^1B_2$ $^{(e)}$	379.8	320-389	1.00
$B_{ghi}P^+$	$^2B_1$ $^{(f)}$	762.2	720-788	0.13
$B_{ghi}P^+$	$^2B_1$ $^{(f)}$	509.7	451-533	1.10
$B_{ghi}P^+$	...	404.3	390-410	0.13
Cor	$^1B_{1u}$	337.6	320-341	0.17
Cor	$^1E_{1u}$	301.4	276-311	1.00
Cor^+	$B_{1,2g}$ $^{(f)}$	687.1	630-760	0.20
Cor^+	$B_{1,2g}$ $^{(f)}$	463.7	389-473	0.23
Cor^+	$^{(f)}$	362.5	352-370	0.16

[a] Bak et al. [2000] [b] Szczepanski et al. [1993b] [c] Halasinski et al. [2005] [d] Vala et al. [1994] [e] Rouillé et al. [2007] [f] indicates a tentative assignment based on theoretical calculations presented here.

Two more absorptions are apparent in the spectra of our photolyzed sample. One sharp absorption appears around 445.8 nm and is probably due to photolysis of small Py contaminations in our ice sample, resulting in a Py^+ absorption. Additionally, a broad feature spanning the range from 380 to 470 nm is found. This band does not correlate with the cation features and is hence thought to be caused by a mixture of Ant+H and/or Ant+OH addition reaction products. These reaction products have previously been mass spectroscopically identified in VUV photolyzed Ant:H_2O (1:≥100) mixtures [Ashbourn et al. 2007].

7.3.2 Pyrene ($C_{16}H_{10}$)

The VUV photolysis of Py:H_2O mixtures has been studied and is described in detail by Chapter 6. Here we only shortly describe the band assignments.

The negative bands that appear between 290 and 345 nm are assigned to the $^1B_{2u}\leftarrow{}^1A_g$ electronic transition of neutral pyrene ($S_2 \leftarrow S_0$) [Vala et al. 1994, Halasinski et al. 2005]. Most of the positive bands that form upon VUV photolysis of the Py containing H_2O ice are ascribed to the Py^+ species. The system ranging from ~411-470 nm is the strongest Py^+ transition and is assigned to the $^2A_u\leftarrow{}^2B_{3g}$ transition. The weaker absorption bands between 350 and 370 nm are assigned to the $^2B_{1u}\leftarrow{}^2B_{3g}$ Py^+ vibronic transition. Finally, the band on the red-wing of the strongest Py^+ transition is due to the $^2B_{1u}\leftarrow{}^2B_{3g}$ transition. Besides the rather strong Py cation absorptions, two more bands are detected around 400 and 405 nm. The band at 400 nm was previously found to originate from an electronic transition in $PyH^{\cdot}$ and the band at 405 nm was tentatively assigned to an electronic transition of ^{3}Py.

7.3.3 Benzo[ghi]perylene ($C_{22}H_{12}$)

The negative bands between ~280 and 390 nm in the spectrum of the irradiated $B_{ghi}P{:}H_2O$ indicate that the neutral species is destroyed upon VUV photolysis. The absorption bands have previously been assigned to the $S_2(^1B_2) \leftarrow S_0(^1A_1)$ transition of $B_{ghi}P$ [Rouillé et al. 2007]. In turn, new bands appear upon VUV photolysis of the $B_{ghi}P$ containing H_2O ice. A very strong absorption, which has previously been assigned to a $B_{ghi}P^+$ absorption by Salama et al. [1995] arises at 509.7 nm. Another, much weaker absorption appears in the mid-IR at 762.2 nm. This band has been assigned in previous matrix work to a low energy electronic transition of the $B_{ghi}P^+$ species [Hudgins & Allamandola 1995a]. Here we report an absorption band at 404.3 nm, which shows a clear correlation with the other $B_{ghi}P^+$ absorptions. We ascribe this band to a higher energy electronic transition of the $B_{ghi}P^+$ species.

An attempt has been made to assign the new observed cation transitions. The optimized geometry of the $B_{ghi}P$ cation is found to be of C_{2v} symmetry. The calculations are based on the molecule in the x-z plane with the z axis coinciding with the C_2 symmetry axis. The electronic ground state is $^2A_2$ making dipole-allowed transitions to A_2, B_2, and B_1 states possible. In the observed wavelength range, several transitions are predicted by the TDDFT calculations. A transition to a $^2B_1$ state is calculated to be at 673 nm ($f_{calc.}$=0.048), which could give rise to the observed band at 762.2 nm. The next strong transition is found at 472 nm ($f_{calc.}$=0.21) relatively close in energy to the strongest observed band at 509.7 nm and we tentatively attribute the corresponding transition to $^2B_1$. The calculations also predict a transition to the $^2A_2$ state around 300 nm, which overlaps strongly with an absorption from the neutral molecule and consequently cannot be assigned experimentally.

7.3.4 Coronene ($C_{24}H_{12}$)

The neutral Cor molecule is of D_{6h} symmetry. From the A_{1g} ground state, dipole-allowed transitions are only possible to electronic states of A_{2u} or E_{1u} symmetry. The observed absorption spectrum in cryogenic matrices strongly resembles the spectrum of hexa-peri-hexabenzocoronene [HBC, Rouillé et al. 2009]. The weak $S_1(^1B_{2u}) \leftarrow S_0(^1A_{1g})$ transition is not seen in our spectrum, but the $S_2(^1B_{1u}) \leftarrow S_0(^1A_{1g})$ transition appears at 337.6 nm. Like in HBC, it gains intensity due to vibronic interaction with the first allowed transition $S_3(^1E_{1u}) \leftarrow S_0(^1A_{1g})$ found at 301.4 nm. The TDDFT calculations predict this transition at 303 nm ($f_{\mathrm{calc.}}$=0.65). The first two transitions are predicted to appear at 386 and 363 nm.

As already noted by Oomens et al. [2001], the degenerate ground state of the coronene cation causes Jahn-Teller interaction and leads to an effective reduction of the point group from D_{6h}, as found for the neutral species, to D_{2h}. It also complicates the assignment of measured absorption bands on the basis of DFT calculations. However, the DFT geometry optimization predicts a slightly elongated structure for the coronene cation with an elongation of only 0.7% of the total diameter. Therefore, we can only provide tentative band assignments assuming D_{2h} to be the correct point group. In that case, the electronic ground state is $^2B_{3u}$. The strongest feature seen in H_2O ice at 463.7 nm could correspond with a transition to an excited state of $B_{1,2g}$ symmetry. This band was found at 462 nm in an Ar [Szczepanski & Vala 1993] and at 459 nm in a Ne matrix with an f-value of 0.012 [Ehrenfreund et al. 1992]. The calculation predicts three states between 390 nm and 460 nm with somewhat higher oscillator strengths between 0.02 and 0.05. Likewise, the broad cation absorption at 687.1 nm could belong to states of $B_{1,2g}$ symmetry. Further dipole-allowed transitions to $B_{1,2g}$ electronic states are predicted around 310 nm, overlapping with the strongest absorption of neutral Cor. These bands are probably very broad, leading to a raise in the baseline around 310 nm as visible in Fig. 7.2.

7.4 PAH ionization rates

In the previous section we derived the oscillator strengths of the cation bands relative to those of the neutral parent PAH. These numbers are now used for quantification of the reaction channels which are involved in the VUV photolysis of PAHs in interstellar ices. In the analysis presented here, the evolution of the column density in the ice is tracked as a function of time. Cation relative oscillator strengths are used to convert the integrated absorbance in a column density relative to the amount of neutral. The analysis is based on the strongest cation bands listed in Table 7.2. The resulting time evolution of the number densities relative to the deposited amount of neutral PAH is shown in Fig. 7.3 for the four systems studied here.

In the analysis we consider a channel for ionizing the PAH with rate k_{11}, a back-channel for recombination of PAH^+ species with electrons with rate k_{12}, a channel for the formation of products P_1 directly from the parent neutral PAH with rate k_1, and the formation of products P_2 from the PAH^+ species with rate k_2. The reaction scheme is schematically displayed in Fig. 7.4. For the Py:H_2O sample, a reaction scheme with one more channel was used in Chapter 6 since this molecule clearly follows an additional reaction path involving $PyH^\cdot$, which can be unambiguously tracked spectroscopically. The contribution of $PyH^\cdot$ to the total amount of reaction products is low and for the sake of analysis and comparison all data, including pyrene, are fitted with the reaction scheme

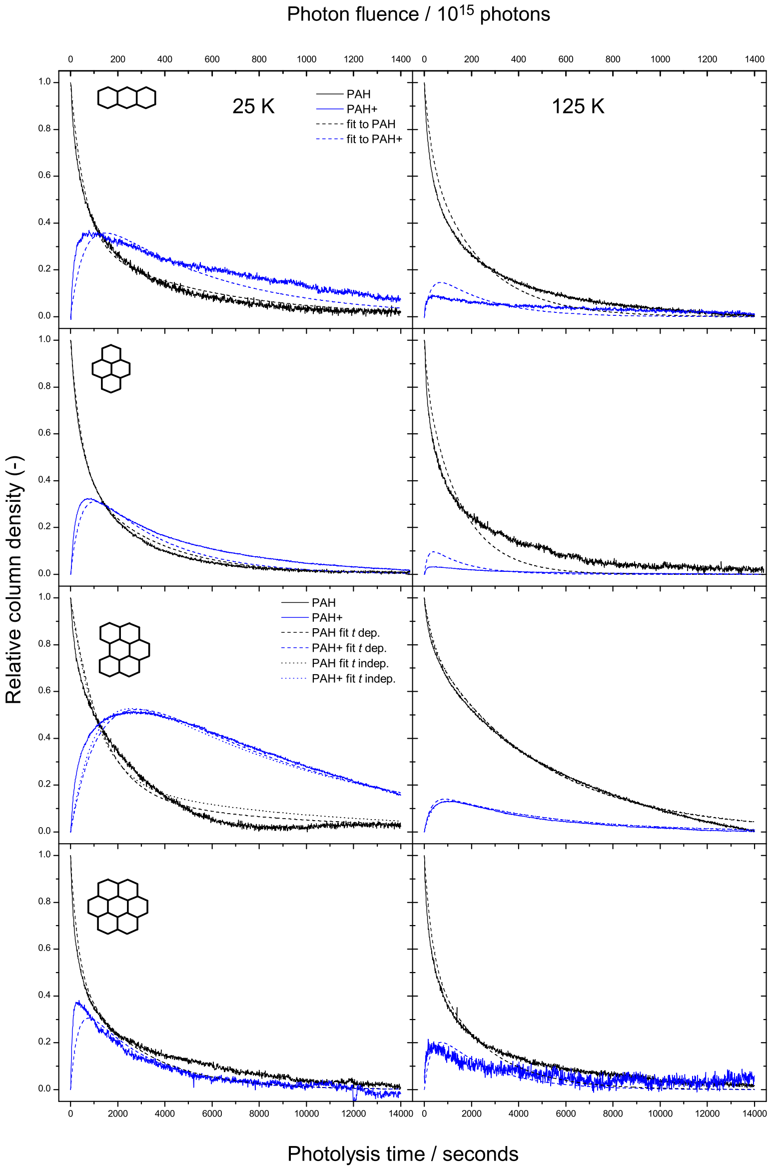

Figure 7.3 The PAH neutral decays and rise and fall of the corresponding cation signal for four PAHs, anthracene, pyrene, benzo[ghi]perylene, and coronene for two different temperatures (25 K and 125 K). The molecule structures and fitted curves are indicated in the plots.

indicated in Fig. 7.4 only, i.e. omitting the formation and destruction of PyH˙.

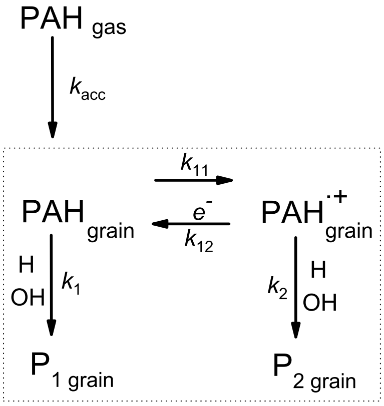

Figure 7.4 The reaction scheme used to fit the experimental time evolution of PAHs and their cations upon VUV irradiation is indicated in the dotted box. The total reaction scheme including the accretion of PAH species from the gas phase into the ice is used for modeling the astrophysical case in §7.5.

The time dependent chemistry of PAHs in H_2O ice is studied for two temperatures, 25 K and 125 K. Fits to the data are co-plotted with the experimental data in Fig. 7.3. Fits to the time evolution curve of the PAH with the strongest cation absorption, $B_{ghi}P$, are made twofold; keeping the ionization channel temperature dependent and independent. This yields insight in the effect of the temperature on the process. In Chapter 6 we noted a temperature dependence in the Py ionization channel. The fits to the data, however, are very sensitive to the integrated cation signal. In the case of Py^+, the signal is very weak and thus an accurate fit is hard to obtain. From the two fits to the $B_{ghi}P$ data in Fig. 7.3 it is clear that temperature actually does not have a large influence on the quality of the fit, and inherently the ionization rate k_{11} turns out to be independent of temperature. The ionization rate k_{11} of the other species, Ant and Cor, also does not exhibit a large temperature dependence. Table. 7.3 gives an overview of the fit parameters which are obtained while keeping all parameters free, i.e. dependent of temperature.

From the fit data constants in Table 7.3 it is clear that the recombination channel, k_{12}, increases with temperature, except for the case of Cor. Additionally, the rate of product formation directly from the parent PAH, k_1, seems to be independent of temperature. The rate of formation of products from the cation species, k_2, on the other hand, drops to zero for all PAHs except for $B_{ghi}P$. What is most striking about the data presented in Table 7.3, is that the ionization rate for *all* PAHs is of the same order.

At the end of an experiment, both the neutral parent PAH and the cation features are destroyed. There are absorptions superposed on the baseline, but there is no clear spectral signature which can be compared to literature data on possible photoproducts. Paper I in this series employed mid-IR spectroscopy to track the spectral changes in VUV

Table 7.3 Fit parameters to the experimental time evolution of the destruction of neutral PAHs and formation of cation species in PAH:H_2O ice following the reaction scheme indicated in Fig. 7.4. All reaction rates are in units of 10^{-4} s^{-1}

Species	Temp (K)	k_{11}	k_{12}	k_1	k_2
Ant	25	8	6	4	0.8
Ant	125	7	20	6	0
Py	25	10	8	4	3
Py	125	8	50	8	0
$B_{ghi}P$	25	7	2	0.8	1
$B_{ghi}P$	125	4	20	2	1
Cor	25	10	20	5	2
Cor	125	9	20	7	0

photolyzed ices of somewhat higher concentration. In that paper, more clear signatures of photoproducts were found, which were tentatively assigned to fundamental vibrations of functional groups in the newly formed photoproduct species (PAH–X_n, with X being H, O, or OH). It is likely that similar photoproducts are formed in the experiments described here.

7.5 Astrophysical implication

As indicated by the rate constants in Table 7.3 in the previous section, PAH chemistry and PAH ionization are rather efficient processes in VUV irradiated PAH containing H_2O ice. This was already known for Py, but is shown here also to be the case several other PAHs. The largest molecule in our sample, Cor, contains 24 carbon atoms, which is still small from an astrophysical viewpoint. However, the experimental study presented here indicates that the rate of ionization is rather size independent in the range of species investigated here. We therefore extend our findings to the astrophysical case, in which larger PAH species ($N_C \geq 50$) are though to be most relevant.

Here, we discuss the relevance of PAH:H_2O ice chemistry in translucent or dark cloud conditions ($A \geq 2$). Whittet et al. [2001] did not observe H_2O ice in clouds with an edge-to-edge visual extinction of $A \leq 3$. We assume that this roughly corresponds to an edge-to-center visual extinction of $A \leq 1.5$ and hence at least H_2O ice will be able to exist under the translucent or dark conditions considered here.

In the interstellar medium, PAHs are initially in the gas phase. The formation of PAH photoproducts on grain mantles therefore consists of two steps: first the neutral PAHs freeze out from the gas phase onto the grains where they can then participate in the solid state reaction network as schemetically indicated in Fig. 7.4. The rate of accretion of PAH species onto the grain, $R_{\mathrm{acc}}^{\mathrm{ISM}}$, is given by

$$\begin{aligned} R_{\mathrm{acc}}^{\mathrm{ISM}} &= v_{\mathrm{PAH}} n_{\mathrm{grain}} \left(\pi a^2\right) n_{\mathrm{PAH}} \\ &= \sqrt{\frac{8k}{\pi}} \frac{n_{\mathrm{grain}}}{n_{\mathrm{H}}} \left(\pi a^2\right) \sqrt{\frac{T_{\mathrm{gas}}}{M}} n_{\mathrm{H}} n_{\mathrm{PAH}} \\ &= 4.57 \cdot 10^{-8} \sqrt{\frac{T_{\mathrm{gas}}}{M}} n_{\mathrm{H}} n_{\mathrm{PAH}} \\ &= k_{\mathrm{acc}} n_{\mathrm{H}} n_{\mathrm{PAH}}, \end{aligned} \tag{7.3}$$

with v_{PAH} the velocity of the PAH molecule in the gas phase, n_{PAH} the gas phase number density of PAHs, n_{H} the total number density of hydrogen, $\frac{n_{\mathrm{grain}}}{n_{\mathrm{H}}}$ the dust to gas number ratio (10^{-12}), a is the standard grain radius (0.1 μm), T_{gas} the gas temperature, M the molecular mass of the PAH molecule (amu), and k_{acc} the accretion rate (cm^{3}s^{-1}). Additionally, all measured PAH reaction coefficients, k, are scaled to the interstellar photon flux and the extinction of the cloud by

$$k^{\mathrm{ISM}} = k^{\mathrm{lab}} \left(\frac{\Psi_{\mathrm{ISM}}}{\Psi_{\mathrm{lab}}} \exp\left[-\gamma A_{\mathrm{V}}\right] + \frac{\Psi_{\mathrm{CR}}}{\Psi_{\mathrm{lab}}} \right), \tag{7.4}$$

with k^{lab} the measured ionization rate constant (s^{-1}), Ψ_{ISM} the interstellar UV flux (photons cm$^{-2}s^{-1}$), Ψ_{lab} the laboratory UV flux (Ψ_{ISM}=$10^{-7}\Psi_{\mathrm{lab}}$), γ a measure of UV extinction relative to visual extinction ($\approx$2) [Roberge et al. 1991], A_{V} the visual magnitude, and Ψ_{CR} the cosmic ray induced photon flux.

An initial total gas phase PAH abundance of 4% with respect to H_2O and an abundance of H_2O of 10^{-4} with respect n_{H} is assumed. We further use the largest PAH investigated in this study, Cor, as a prototype system, which results in $M = 300$ amu, leaving T_{gas}, n_{H}, and A_{V} as input parameters for the model.

The timescales at which PAHs freeze out onto the grains are investigated first. The left panel of Fig. 7.5 plots the gas phase PAH abundance for different initial densities n_{H}. The graph clearly shows that for a dense cloud with $n_{\mathrm{H}} = 10^3$ cm^{-3}, it takes more than 10^7 years for the gas phase to become depleted of PAHs. Densities of 10^5 cm^{-3} and higher need to be reached will PAHs freeze out on a reasonable timescale. The reason for this is that at low densities the frequency with which PAHs encounter a grain is very low, since the grain abundance directly scales with density. Furthermore, the accretion rate scales with the velocity of the species and inherently with its mass. PAH molecules are heavy molecules and thus move slow through the cloud, thereby slowing down their depletion process. Once the PAH does encounter a cold grain, the sticking probability is high and since PAHs are highly non-volatile molecules, they will remain in the ice as long as the ice matrix remains to exist.

The problem is that at such high densities, the interstellar radiation field is almost fully attenuated and only cosmic ray induced photons play a role. This is not enough to get a high processing rate of the PAHs within a reasonable time. In Chapter 4 we have shown for the high mass Young Stellar Object (YSO) W33A and the low mass YSO

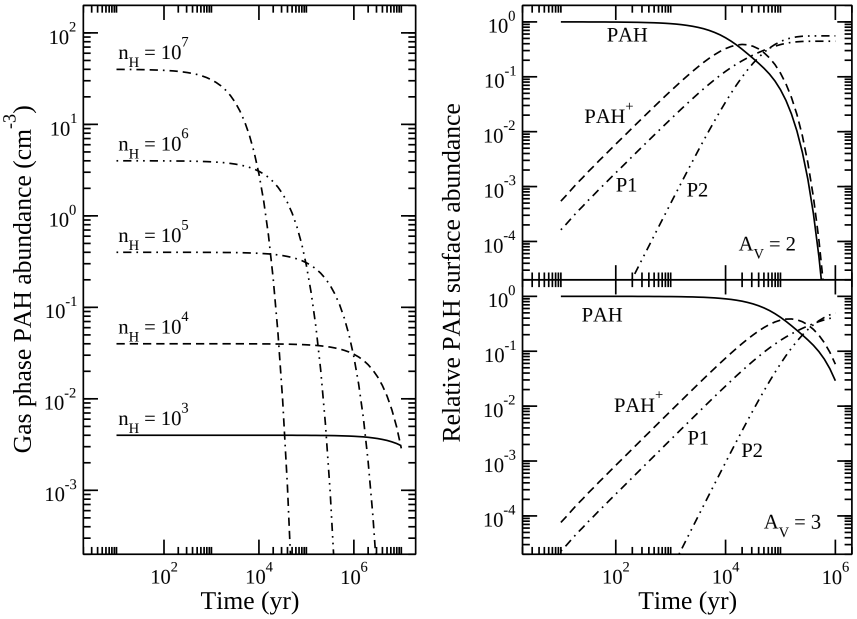

Figure 7.5 *Left panel:* Modeled depletion of PAHs on cold interstellar grains as a function of cloud density. *Right top panel:* Modeled photoprocessing of condensed PAH species in a cloud with a visual magnitude of A_V=2. *Right bottom panel:* Modeled photoprocessing of condensed PAH species in a cloud with a visual magnitude of A_V=3.

RNO 91 that up to 3% of the ice mantle may consist of PAH photoproducts. These high PAH photoproduct concentrations must be formed under the influence of a rather strong radiation field. The two right plots in Fig. 7.5 show the PAH ice chemistry as a function of time under influence of the standard interstellar radiation field at $A_V = 2$ (right top) and 3 (right bottom). The model starts will PAHs frozen out onto the grains. The neutral PAH and the photoproduct abundances are given with respect to the total PAH abundance. For $A_V = 2$ the onset of the formation of photoproducts is after 10^4 yrs; for $A_V = 3$ the onset occurs after 10^5 yrs.

In summary, to explain the high abundances of frozen out PAH photoproducts reported in Chapter 4, grains first need to be in a high density environment after which they are exposed to a high UV field. This corresponds to the following scenario for both the high and low mass YSO's W33A and RNO 91: the PAHs:H_2O ices form in the pre-collapse high density phase. Once the newly formed star starts radiating UV photons, some of the grains will be exposed to the UV field. In a protoplanetary disks a similar situation can occur due to vertical mixing. The ice covered dust grains form in dense regions around the midplane. Vertical mixing brings them closer to the warmer top layer of the disk and back down towards the cold mid-plane of the disk.

7.6 Conclusions

The work presented here describes photolysis experiments on interstellar H_2O ice samples containing four different PAHs. The experiments are performed for two temperatures; one low (25 K) and one high (125 K) temperature. Experimental data are fitted to a reaction model and the resulting rate constants are used in a first order astrochemical model, including freeze-out of species and photoprocessing of ices. The conclusions are summarized below:

1. Near UV/VIS spectroscopy on the photolysis of four PAH species (Ant, Py, $B_{ghi}P$, and Cor) trapped in an interstellar H_2O ice is performed. Photoproduct bands have been assigned to electronic transitions of PAH cation transitions of the respective PAH species.

2. The temporal evolution of the production of cation bands is tracked for the four PAHs at the two temperatures under investigation. Oscillator strengths of the PAH^+ species have been derived for all the PAH^+ electronic transitions relative to those of the neutral parent PAH molecule. Derived relative oscillator strengths of the PAH^+ transitions are used to quantify the temporal evolution of species.

3. It is found that all four PAHs behave similarly upon VUV photolysis in a H_2O ice. The cationic species is efficiently produced in the temperature ices, the number density reaches a maximum and then slowly subsides. The ioniziation efficiency is decreased upon photolysis of PAHs in high temperature H_2O ice. As concluded in Chapter 4 and 6, this behavior can be attributed to PAH-radical or PAH^+-radical reactions being more important due to a larger mobility of radical species (H+OH) in the ice at these temperatures.

4. The experimental PAH and PAH^+ column density time evolution data have been fitted with a model based on a chemical reaction scheme involving PAH ionization and PAH reactions with radical species. Rate constants are derived and reported. All four PAHs exhibit similar reaction rates, allowing for the general conclusion that PAH photoreaction rates are rather size-independent over the range of species studied here.

5. A model to calculate the freeze-out of PAHs on cold interstellar grains in a dense molecular cloud indicates that PAH depletion is rather ineffective on short time scales, because of the PAHs mass and number density. On time scales of the formation of a protoplanetary disk, however, PAHs have efficiently frozen out in ices.

6. The photochemistry of PAH:H_2O ices is modeled for an a protostar. The model results point out that the onset of PAH:H_2O photoprocesing occurs at $t = 10^4$ yrs for a visual magnitude of $A_V = 2$ and at 10^5 yrs for $A_V = 3$. Thus, photoprocessing of PAHs in ices is expected to be of importance in more evolved objects.

CHAPTER 8

Future challenges

Astrophysical laboratory techniques have been and will be of unprecedented value for interpreting and guiding astronomical observations. Spectroscopic data, both in the gas phase and in the solid state, allow to identify species in space and to derive inter- and circumstellar abundances. Experimentally derived rate constants, in addition, serve as input for astrochemical models which can be directly compared to observations. In the last decades, the progress in laboratory based research has boosted the understanding of chemical processes in space. With the further improvement of new upcoming observational facilities and the refinement of chemical models, there is a need for more and more detailed laboratory data. In this chapter experimental challenges are addressed that will be useful for astronomy using *OASIS*, the new setup that has been described here.

In Chapters 5 – 7 it was shown that it is possible to study the photochemistry of PAHs in water ice upon VUV irradiation through optical (i.e. electronic) spectroscopy using direct absorption spectroscopy. The method allows studying reaction products in situ and in real time. As such the technique offers a very versatile and generally applicable tool that is capable of studying other systems as well, both substantially larger and smaller. This provides information needed for identifying species in space as well as insight in possible reaction schemes. The latter point has been addressed in detailed in this thesis, but the use of this work for an astronomical detection of a PAH in the solid state, has only been mentioned in §5.5. The optical PAH ice data, presented in this thesis, basically hold the promise to search for optical solid state PAH signatures in space, as an alternative to electronic gas phase work that has been unsuccessful so far. A kick-off project with the ESO-VLT equipped with the FORS2 spectrometer towards the embedded K0 star DoAr21 has been performed to search for broad absorption features that may be correlated to the absorption bands described for the PAHs and PAH-derivatives in this thesis. The analysis of the data is still in progress and at this stage only the effort to identify PAH in space through their ice spectrum is reported.

It is generally expected that also (and according to several publications, particularly) large PAHs containing 50 carbon atoms or more, the so called GRAND-PAHs, and their photoproducts are present in space. These are expected to be formed in the stellar ejecta of dying stars. Gas phase spectra of such complex PAHs are lacking, mainly because of the experimental challenges that go along with bringing such molecules in the gas phase in the laboratory. The only data available on large PAHs today are from matrix isolation spectroscopy. In such experiments, mainly argon and neon are used as a molecular surrounding, as for such environments matrix interactions are as small as possible. *OASIS* can be used in a similar way, as a regular matrix setup, guiding gas phase studies. Test experiments have been performed on $B_{ghi}P$ ($C_{22}H_{12}$) and hexa-peri-hexabenzocoronene (HBC $C_{42}H_{18}$) using argon instead of water as a matrix. The results are shown in Figure 8.1. The distortion of the PAH energetic structure is proportional to the polarizability of the matrix material. If the purpose of the experiments would be to measure the energy of free PAH molecules, i.e. gas phase species, the experiments are to be performed for more than one matrix material. One could for example measure the spectra in xenon, argon and neon. If the transition energies are now plotted as a function of polarizability of the matrix, it is possible to extrapolate the energy level to zero polarizability, i.e. the electronic energy in vacuum. This is a good indication of the origin of gas phase electronic transitions. This method, subsequently, can be employed to select (GRAND-)PAHs which possibly contribute to diffuse interstellar band absorption features.

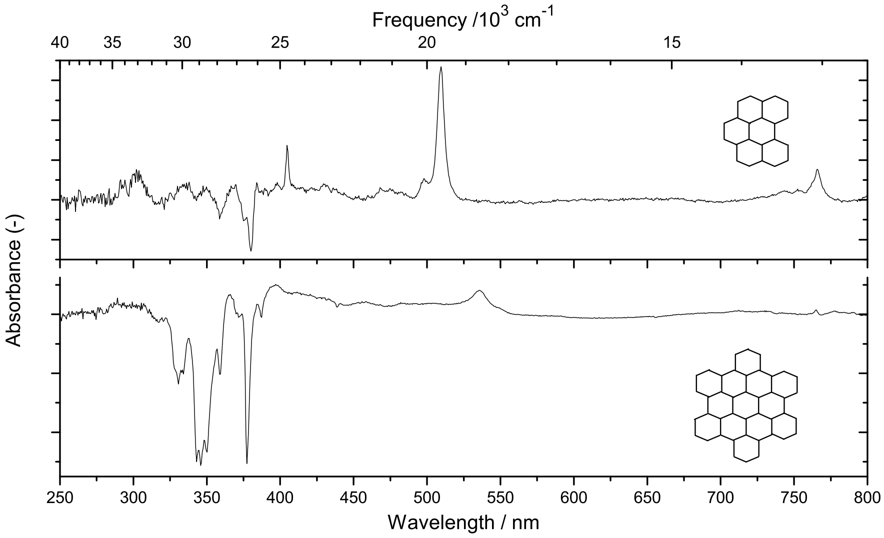

Figure 8.1 The spectrum of matrix isolated Hexa-peri-benzo-coronene and its cation in argon at 12 K (bottom) plotted together with matrix isolated benzo[ghi]perylene and its cation band in argon at 12 K (top)

The general applicability of *OASIS* is also demonstrated with a set of test measurements on a different type of carbon containing molecules, the nano-diamonds adamantane ($C_{10}H_{16}$) and diamantane ($C_{14}H_{20}$). The species are abundantly present in meteorites and are thought to exist in other regions of the interstellar medium as well. Calculations predict that these species are easily ionized by Lyman-alpha radiation and that their cationic species have moderately strong electronic transitions in the optical part of the electromagnetic spectrum [M. Steglich, priv. comm.]. Again, a possibility exists that such species contribute to absorptions in the diffuse interstellar medium. The test measurements performed so far, were done in high concentration matrices and did not exhibit absorption bands that originate from diamondoid ions. Further work is needed.

The next step is to include 'real' prebiotical molecules in the ice. In the last year it was shown that VUV irradiation of a pure methanol ice results in the generation of more complex species such as ethanol, methylformate, acetic acid, glycol aldehyde and ethylene glycol [Öberg et al. 2009c]. That study was based on a long research tradition in Leiden and follows the experiments by Greenberg and coworkers who irradiated astronomical ice equivalents with a VUV broadband light source for many days and identified gas chromatographically amino acids in the resulting organic refractory [Muñoz Caro et al. 2002]. Even though the experiments were performed under quite rough experimental conditions (the residue had to be analyzed outside the vacuum and after warm-up) this has set the tone for this field. An alternative way for this bottom-up approach is a top-down scenario in which the focus is not on the generation of more complex species, starting from simple precursors, but to include real biological systems — e.g. nucleobases, ribonucleotides and their biosynthesis precursors — in the ice and to study their photostability. This can be ideally studied with the new experimental setup and will be a research topic in the next years.

Another interesting subject that can be addressed with *OASIS* is that of the production of small radicals in interstellar ices. In Chapter 6, for example, the observation of $HCO^{\cdot}$ is reported. OH is another interesting object, as the production rate of OH radicals in an interstellar water ice is not yet fully understood. As infrared techniques are generally slow, such methods are not suited to address this question, and the optical equivalent described here offers an alternative. The first test measurements on irradiated pure H_2O ices show that some new very broad absorptions indeed present. This is overcome by doping an argon matrix with H_2O, with a resulting concentration of about 1:100 (H_2O:Ar). A vibronic progression ascribed to the $A^2\Sigma^+(v{=}0)\leftarrow X^2\Pi_{3/2}(v{=}0)$ transition at 308 nm is found [Hancock & Kasyutich 2004]. These test measurements can be extended to more astronomically relevant ices. Ultimately, the diffusion of radical species in the matrix can be studies as a function of temperature.

Finally, *OASIS* was initially designed as *CESSS*: a Cavity Enhanced Solid State Spectrometer. The setup is equipped with two stable and micrometer adjustable mirror mounts on the in and outlet port of the vacuum system. The initial idea was to use an incoherent broad band cavity enhanced detection scheme [Fiedler et al. 2003] to perform the experiments that have been described in this thesis. This did not work in the solid state, presumably because of the light refraction in the ice. Fortunately, a singly pass experiment turned out to be sensitive enough. In the gas phase, however, the system works fine.

A set of mirrors with reflectivities as high as 99.95% can be aligned perpendicular by a HeNe laser. The resulting system behaves like a cavity, which can be excited by intense broad band white light originating from the Xe-lamp. Light will continuously leak out of exit side of the cavity. This light has traversed through the cavity for some time, depending on the reflectivity of the mirrors, resulting in an enhancement of the absorption

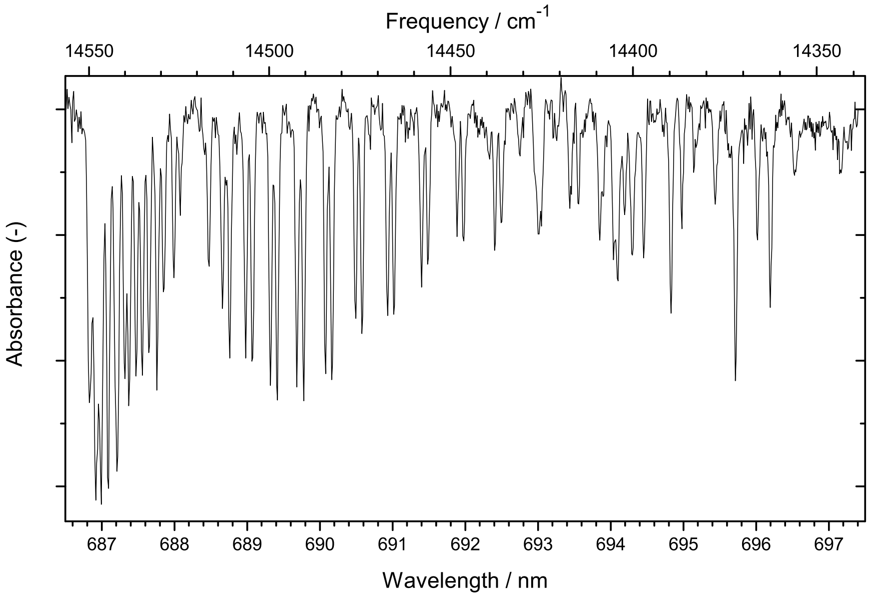

Figure 8.2 The absorption spectrum of the $b^1\Sigma_g^+(v=1)\leftarrow X^3\Sigma_g^-(v=0)$ oxygen transition

path length, which directly reflects the increase in sensitivity of the detection technique [Fiedler et al. 2003]. The power of this arrangement is exemplified by a spectroscopic measurement on the doubly forbidden The forbidden $b^1\Sigma_g^+(v=1)\leftarrow X^3\Sigma_g^-(v=0)$ gas phase oxygen transition can only be observed in the 50 cm long absorption cell, if significant enhancement is achieved in the cavity [O'Keefe & Deacon 1988]. A typical absorption spectrum taken under atmospheric pressure is shown in Fig. 8.2. The example indicates the power of the setup for performing spectroscopic studies on gas phase species. Of course, this technique can be used for measurements on astrophysically relevant species. With minor adjustment of the system, one can sensitively perform spectroscopy on a (plasma) expansion over a large frequency range with moderately high resolution.

In conclusion, *OASIS* has turned out to be a very versatile tool that has proven its use for astronomical research.

Bibliography

Acharyya, K., Fuchs, G. W., Fraser, H. J., van Dishoeck, E. F., & Linnartz, H. 2007, A&A, 466, 1005

Agúndez, M., Cernicharo, J., Guélin, M., et al. 2008, A&A, 478, L19

Al-Halabi, A., Fraser, H. J., Kroes, G. J., & van Dishoeck, E. F. 2004, A&A, 422, 777

Allamandola, L. J., Tielens, A. G. G. M., & Barker, J. R. 1985, ApJ, 290, L25

Allamandola, L. J., Tielens, A. G. G. M., & Barker, J. R. 1989, ApJS, 71, 733

Andersson, S. & van Dishoeck, E. F. 2008, A&A, 491, 907

Ashbourn, S. F. M., Elsila, J. E., Dworkin, J. P., et al. 2007, Meteoritics and Planetary Science, 42, 2035

Bak, K. L., Koch, H., Oddershede, J., Christiansen, O., & Sauer, S. P. A. 2000, J. Chem. Phys., 112, 4173

Barrett, A. H., Ho, P. T. P., & Myers, P. C. 1977, ApJ, 211, L39

Bauschlicher, C. W., Boersma, C., Ricca, A., et al. 2010, ApJS, 189, 341

Bauschlicher, C. W., Peeters, E., & Allamandola, L. J. 2009, ApJ, 697, 311

Bauschlicher, Jr., C. W., Peeters, E., & Allamandola, L. J. 2008, ApJ, 678, 316

Bell, M. B., Feldman, P. A., Travers, M. J., et al. 1997, ApJ, 483, L61+

Bellamy, L. J. 1960, The Infra-Red Spectra of Complex Molecules (Wiley)

Bernstein, M. P., Dworkin, J. P., Sandford, S. A., Cooper, G. W., & Allamandola, L. J. 2002a, Nature, 416, 401

Bernstein, M. P., Elsila, J. E., Dworkin, J. P., et al. 2002b, ApJ, 576, 1115

Bernstein, M. P., Mattioda, A. L., Sandford, S. A., & Hudgins, D. M. 2005a, ApJ, 626, 909

Bernstein, M. P., Sandford, S. A., & Allamandola, L. J. 2005b, ApJS, 161, 53

Bernstein, M. P., Sandford, S. A., Allamandola, L. J., Chang, S., & Scharberg, M. A. 1995, ApJ, 454, 327

Bernstein, M. P., Sandford, S. A., Allamandola, L. J., et al. 1999, Science, 283, 1135

Bernstein, M. P., Sandford, S. A., Mattioda, A. L., & Allamandola, L. J. 2007, ApJ, 664, 1264

Bisschop, S. E., Fuchs, G. W., Boogert, A. C. A., van Dishoeck, E. F., & Linnartz, H. 2007a, A&A, 470, 749

Bisschop, S. E., Fuchs, G. W., van Dishoeck, E. F., & Linnartz, H. 2007b, A&A, 474, 1061

Bito, Y., Shida, N., & Toru, T. 2000, Chem. Phys. Lett., 328, 310

Blake, D., Allamandola, L., Sandford, S., Hudgins, D., & Freund, F. 1991, Science, 254, 548

Blake, G. A., Sutton, E. C., Masson, C. R., & Phillips, T. G. 1987, ApJ, 315, 621

Boersma, C. 2009, PhD thesis, Rijksuniversiteit Groningen

Boersma, C., Hony, S., & Tielens, A. G. G. M. 2006, A&A, 447, 213

Bohlin, R. C., Savage, B. D., & Drake, J. F. 1978, ApJ, 224, 132

Boogert, A. C. A. & Ehrenfreund, P. 2004, in Astronomical Society of the Pacific Conference Series, Vol. 309, Astrophysics of Dust, ed. A. N. Witt, G. C. Clayton, & B. T. Draine, 547–+

Boogert, A. C. A., Hogerheijde, M. R., & Blake, G. A. 2002, ApJ, 568, 761

Boogert, A. C. A., Pontoppidan, K. M., Knez, C., et al. 2008, ApJ, 678, 985

Boogert, A. C. A., Pontoppidan, K. M., Lahuis, F., et al. 2004, ApJS, 154, 359

Boogert, A. C. A., Schutte, W. A., Helmich, F. P., Tielens, A. G. G. M., & Wooden, D. H. 1997, A&A, 317, 929

Boogert, A. C. A., Schutte, W. A., Tielens, A. G. G. M., et al. 1996, A&A, 315, L377

Boogert, A. C. A., Tielens, A. G. G. M., Ceccarelli, C., et al. 2000, A&A, 360, 683

Bottinelli, S., Adwin Boogert, A. C., Bouwman, J., et al. 2010, ApJ, 718, 1100

Bréchignac, P. & Pino, T. 1999, A&A, 343, L49

Bregman, J. D., Hayward, T. L., & Sloan, G. C. 2000, ApJ, 544, L75

Bregman, J. D. & Temi, P. 2001, ApJ, 554, 126

Briggs, R., Ertem, G., Ferris, J. P., et al. 1992, Origins of Life and Evolution of the Biosphere, 22, 287

Brooke, T. Y., Sellgren, K., & Geballe, T. R. 1999, ApJ, 517, 883

Cernicharo, J., Heras, A. M., Tielens, A. G. G. M., et al. 2001, ApJ, 546, L123

Cerrigone, L., Hora, J. L., Umana, G., & Trigilio, C. 2009, ApJ, 703, 585

Cesaroni, R., Churchwell, E., Hofner, P., Walmsley, C. M., & Kurtz, S. 1994, A&A, 288, 903

Cherchneff, I., Barker, J. R., & Tielens, A. G. G. M. 1992, ApJ, 401, 269

Chiar, J. E., Tielens, A. G. G. M., Whittet, D. C. B., et al. 2000, ApJ, 537, 749

Chumbalov, T. K., Chanysheva, I. S., & Muzychkina, R. A. 1967, Journal of Applied Spectroscopy, 6, 570

Collings, M. P., Dever, J. W., Fraser, H. J., & McCoustra, M. R. S. 2003a, Ap&SS, 285, 633

Collings, M. P., Dever, J. W., Fraser, H. J., McCoustra, M. R. S., & Williams, D. A. 2003b, ApJ, 583, 1058

Cuppen, H. M., van Dishoeck, E. F., Herbst, E., & Tielens, A. G. G. M. 2009, A&A, 508, 275

Dartois, E. & d'Hendecourt, L. 2001, A&A, 365, 144

Dartois, E., d'Hendecourt, L., Thi, W., Pontoppidan, K. M., & van Dishoeck, E. F. 2002, A&A, 394, 1057

Dartois, E., Schutte, W., Geballe, T. R., et al. 1999, A&A, 342, L32

D'Hendecourt, L. B. & Allamandola, L. J. 1986, A&AS, 64, 453

Draine, B. T. & Bertoldi, F. 1996, ApJ, 468, 269

Draine, B. T., Dale, D. A., Bendo, G., et al. 2007, ApJ, 663, 866

Draine, B. T. & Li, A. 2007, ApJ, 657, 810

Drew, J. E., Busfield, G., Hoare, M. G., et al. 1997, MNRAS, 286, 538

Eddington, A. S. 1937, The Observatory, 60, 99

Ehrenfreund, P. & Charnley, S. B. 2000, ARA&A, 38, 427

Ehrenfreund, P., D'Hendecourt, L., Verstraete, L., et al. 1992, A&A, 259, 257

Ehrenfreund, P., Rasmussen, S., Cleaves, J., & Chen, L. 2006, Astrobiology, 6, 490

Elsila, J. E., Hammond, M. R., Bernstein, M. P., Sandford, S. A., & Zare, R. N. 2006, Meteoritics and Planetary Science, 41, 785

Evans, II, N. J. 1999, ARA&A, 37, 311

Evans, II, N. J., Allen, L. E., Blake, G. A., et al. 2003, PASP, 115, 965

Federman, S. R., Huntress, Jr., W. T., & Prasad, S. S. 1990, ApJ, 354, 504

Fiedler, S., Hese, A., & Ruth, A. 2003, Chem. Phys. Lett., 371, 284

Fraser, H. J., Bisschop, S. E., Pontoppidan, K. M., Tielens, A. G. G. M., & van Dishoeck, E. F. 2005, MNRAS, 356, 1283

Fraser, H. J., Collings, M. P., Dever, J. W., & McCoustra, M. R. S. 2004, MNRAS, 353, 59

Frenklach, M. & Feigelson, E. D. 1989, ApJ, 341, 372

Frisch, M. J., Trucks, G. W., Schlegel, H. B., et al. 2009, GAUSSIAN 09 Revision A.2, Gaussian Inc., Wallingford CT

Fuchs, G. W., Cuppen, H. M., Ioppolo, S., et al. 2009, A&A, 505, 629

Garrod, R. T. & Herbst, E. 2006, A&A, 457, 927

Genzel, R., Ho, P. T. P., Bieging, J., & Downes, D. 1982, ApJ, 259, L103

Gerakines, P. A., Schutte, W. A., Greenberg, J. M., & van Dishoeck, E. F. 1995, A&A, 296, 810

Gibb, E. L. & Whittet, D. C. B. 2002, ApJ, 566, L113

Gibb, E. L., Whittet, D. C. B., Boogert, A. C. A., & Tielens, A. G. G. M. 2004, ApJS, 151, 35

Gibb, E. L., Whittet, D. C. B., Schutte, W. A., et al. 2000, ApJ, 536, 347

Gillett, F. C., Forrest, W. J., & Merrill, K. M. 1973, ApJ, 183, 87

Greene, T. P., Wilking, B. A., Andre, P., Young, E. T., & Lada, C. J. 1994, ApJ, 434, 614

Gudipati, M. 1993, Chemical Physics, 173, 143

Gudipati, M. 2004, J. Phys. Chem. A., 108, 4412

Gudipati, M. S. & Allamandola, L. J. 2003, ApJ, 596, L195

Gudipati, M. S. & Allamandola, L. J. 2004, ApJ, 615, L177

Gudipati, M. S. & Allamandola, L. J. 2006a, J. Phys. Chem. A., 110, 9020

Gudipati, M. S. & Allamandola, L. J. 2006b, ApJ, 638, 286

Gürtler, J., Klaas, U., Henning, T., et al. 2002, A&A, 390, 1075

Haas, M. R., Davidson, J. A., & Erickson, E. F., eds. 1995, Astronomical Society of the Pacific Conference Series, Vol. 73, Airborne Astronomy Symposium on the Galactic Ecosystem: From Gas to Stars to Dust, volume 73

Hagen, W., Allamandola, L. J., & Greenberg, J. M. 1979, Ap&SS, 65, 215

Hagen, W., Allamandola, L. J., Greenberg, J. M., & Tielens, A. G. G. M. 1980, J. Mol. Struct., 60, 281

Hagen, W. & Tielens, A. G. G. M. 1981, J. Chem. Phys, 75, 4198

Hagen, W., Tielens, A. G. G. M., & Greenberg, J. M. 1983, A&AS, 51, 389

Halasinski, T. M., Salama, F., & Allamandola, L. J. 2005, ApJ, 628, 555

Hancock, G. & Kasyutich, V. 2004, App. Phys. B-lasers and optics, 79, 383

Hayes, D. S., Mavko, G. E., Radick, R. R., Rex, K. H., & Greenberg, J. M. 1973, in IAU Symposium, Vol. 52, Interstellar Dust and Related Topics, ed. J. M. Greenberg & H. C. van de Hulst, 83–+

Herzberg, G. 1945, Molecular spectra and molecular structure. Vol.2: Infrared and Raman spectra of polyatomic molecules (New York: Van Nostrand, Reinhold, 1945)

Hidaka, H., Watanabe, N., Shiraki, T., Nagaoka, A., & Kouchi, A. 2004, ApJ, 614, 1124

Hiraoka, K., Sato, T., Sato, S., et al. 2002, ApJ, 577, 265

Hirata, S., Lee, T., & Head-Gordon, M. 1999, J. Chem. Phys., 111, 8904

Hsiao, J. S. & Webber, S. E. 1992, J. Phys. Chem., 96, 2892

Hudgins, D. M. & Allamandola, L. J. 1995a, J. Phys. Chem., 99, 3033

Hudgins, D. M. & Allamandola, L. J. 1995b, J. Phys. Chem., 99, 8978

Hudgins, D. M. & Allamandola, L. J. 1997, J. Phys. Chem. A, 101, 3472

Hudgins, D. M. & Sandford, S. A. 1998a, J. Phys. Chem. A, 102, 329

Hudgins, D. M. & Sandford, S. A. 1998b, J. Phys. Chem. A, 102, 344

Hudgins, D. M., Sandford, S. A., & Allamandola, L. J. 1994, J. Phys. Chem., 98, 4243

Hudgins, D. M., Sandford, S. A., Allamandola, L. J., & Tielens, A. G. G. M. 1993, ApJS, 86, 713

Ioppolo, S., Cuppen, H. M., Romanzin, C., van Dishoeck, E. F., & Linnartz, H. 2008, ApJ, 686, 1474

Ioppolo, S., Cuppen, H. M., van Dishoeck, E. F., & Linnartz, H. 2010, A&A in prep.

Jenniskens, P. & Blake, D. F. 1994, Science, 265, 753

Jenniskens, P., Blake, D. F., Wilson, M. A., & Pohorille, A. 1995, ApJ, 455, 389

Jiang, G. J., Person, W. B., & Brown, K. G. 1975, J. Chem. Phys, 62, 1201

Joblin, C., D'Hendecourt, L., Leger, A., & Defourneau, D. 1994, A&A, 281, 923

Keane, J. V. 2001, PhD thesis, Rijksuniversiteit Groningen

Keane, J. V., Boonman, A. M. S., Tielens, A. G. G. M., & van Dishoeck, E. F. 2001a, A&A, 376, L5

Keane, J. V., Tielens, A. G. G. M., Boogert, A. C. A., Schutte, W. A., & Whittet, D. C. B. 2001b, A&A, 376, 254

Kemper, F., Vriend, W. J., & Tielens, A. G. G. M. 2004, ApJ, 609, 826

Kerkhof, O., Schutte, W. A., & Ehrenfreund, P. 1999, A&A, 346, 990

Kessler-Silacci, J., Augereau, J., Dullemond, C. P., et al. 2006, ApJ, 639, 275

Kim, H.-S., Wagner, D. R., & Saykally, R. J. 2001, Phys. Rev. Lett., 86, 5691

Kjaergaard, H. G., Robinson, T. W., & Brooking, K. A. 2000, J. Phys. Chem. A, 104, 11297

Knez, C., Boogert, A. C. A., Pontoppidan, K. M., et al. 2005, ApJ, 635, L145

Kobayashi, K. 1983, J. Phys. Chem., 87, 4317

Krelowski, J., Maszkowski, R., & Strobel, A. 1986, A&A, 166, 271

Lacy, J. H., Faraji, H., Sandford, S. A., & Allamandola, L. J. 1998, ApJ, 501, L105+

Langelaar, J., Wegdam-van Beek, J., Ten Brink, H., & Van Voorst, J. D. W. 1970, Chem. Phys. Letters, 7, 368

Langhoff, S. R. 1996, J. Phys. Chem., 100, 2819

Latter, W. B. 1991, ApJ, 377, 187

Lee, J., Bergin, E. A., & Evans, II, N. J. 2004, ApJ, 617, 360

Léger, A., Klein, J., de Cheveigne, S., et al. 1979, A&A, 79, 256

Li, A. & Draine, B. T. 2001, ApJ, 554, 778

Li, A. & Draine, B. T. 2002, ApJ, 572, 232

Linnartz, H. 2009, Cavity ring-down spectroscopy; Techniques and applications, ed. G. Berden & R. Engeln (Wiley), in press

Mathis, J. S. 1990, ARA&A, 28, 37

Mattioda, A. L., Allamandola, L. J., & Hudgins, D. M. 2005a, ApJ, 629, 1183

Mattioda, A. L., Hudgins, D. M., Bauschlicher, C. W., & Allamandola, L. J. 2005b, Advances in Space Research, 36, 156

McCarroll, B. 1970, Rev. Scient. Instrum., 41, 279

Mendoza-Gomez, C. X., de Groot, M. S., & Greenberg, J. M. 1995, A&A, 295, 479

Merrill, K. M., Russell, R. W., & Soifer, B. T. 1976, ApJ, 207, 763

Milligan, D. E. & Jacox, M. E. 1969, J. Chem. Phys., 51, 277

Milosavljevic, B. & Thomas, J. 2002, Photochem. Photobiol. Sci., 1, 100

Min, M., Waters, L. B. F. M., de Koter, A., et al. 2007, A&A, 462, 667

Miyauchi, N., Hidaka, H., Chigai, T., et al. 2008, Chemical Physics Letters, 456, 27

Montejano, H. A., Cosa, J. J., Garrera, H. A., & Previtali, C. M. 1995, J. Photochem. Photobiol. A: Chem., 86, 115

Moore, M. H. & Hudson, R. L. 1998, Icarus, 135, 518

Motylewski, T., Linnartz, H., Vaizert, O., et al. 2000, ApJ, 531, 312

Muñoz Caro, G. M., Meierhenrich, U. J., Schutte, W. A., et al. 2002, Nature, 416, 403

Muñoz Caro, G. M. & Schutte, W. A. 2003, A&A, 412, 121

Murakawa, K., Tamura, M., & Nagata, T. 2000, ApJS, 128, 603

Öberg, K. I. 2009, PhD thesis, Leiden Observatory, Leiden University, P.O. Box 9513,

2300 RA Leiden, The Netherlands
Öberg, K. I., Boogert, A. C. A., Pontoppidan, K. M., et al. 2008, ApJ, 678, 1032
Öberg, K. I., Bottinelli, S., & van Dishoeck, E. F. 2009a, A&A, 494, L13
Öberg, K. I., Fayolle, E. C., Cuppen, H. M., van Dishoeck, E. F., & Linnartz, H. 2009b, A&A, 505, 183
Öberg, K. I., Fraser, H. J., Boogert, A. C. A., et al. 2007a, A&A, 462, 1187
Öberg, K. I., Fuchs, G. W., Awad, Z., et al. 2007b, ApJ, 662, L23
Öberg, K. I., Garrod, R. T., van Dishoeck, E. F., & Linnartz, H. 2009c, A&A, 504, 891
Öberg, K. I., Linnartz, H., Visser, R., & van Dishoeck, E. F. 2009d, ApJ, 693, 1209
Ohno, K., Okimura, M., Akai, N., & Katsumoto, Y. 2005, Phys. Chem. Chem. Phys., 7, 3005
Okada, T., Mori, T., & Mataga, N. 1976, Bull. Chem. Soc. Japan, 49, 3398
Okada, T., Tashita, N., & Mataga, N. 1980, Chem. Phys. Lett., 75, 220
O'Keefe, A. & Deacon, D. A. G. 1988, Review of Scientific Instruments, 59, 2544
Oomens, J., Sartakov, B. G., Tielens, A. G. G. M., Meijer, G., & von Helden, G. 2001, ApJ, 560, L99
Osorio, M., Anglada, G., Lizano, S., & D'Alessio, P. 2009, ApJ, 694, 29
Palumbo, M. E. 2006, A&A, 453, 903
Peeters, E., Allamandola, L. J., Hudgins, D. M., Hony, S., & Tielens, A. G. G. M. 2004a, in Astronomical Society of the Pacific Conference Series, Vol. 309, Astrophysics of Dust, ed. A. N. Witt, G. C. Clayton, & B. T. Draine, 141–+
Peeters, E., Spoon, H. W. W., & Tielens, A. G. G. M. 2004b, ApJ, 613, 986
Peeters, Z., Botta, O., Charnley, S. B., et al. 2005, A&A, 433, 583
Pendleton, Y. J. & Allamandola, L. J. 2002, ApJS, 138, 75
Pontoppidan, K. M. 2006, A&A, 453, L47
Pontoppidan, K. M., Boogert, A. C. A., Fraser, H. J., et al. 2008, ApJ, 678, 1005
Pontoppidan, K. M., Dartois, E., van Dishoeck, E. F., Thi, W., & d'Hendecourt, L. 2003a, A&A, 404, L17
Pontoppidan, K. M., Fraser, H. J., Dartois, E., et al. 2003b, A&A, 408, 981
Pontoppidan, K. M., van Dishoeck, E. F., & Dartois, E. 2004, A&A, 426, 925
Puget, J. L. & Leger, A. 1989, ARA&A, 27, 161
Rapacioli, M., Calvo, F., Joblin, C., et al. 2006, A&A, 460, 519
Roberge, W. G., Jones, D., Lepp, S., & Dalgarno, A. 1991, ApJS, 77, 287
Rodgers, S. D. & Charnley, S. B. 2001, ApJ, 546, 324
Romanini, D., Biennier, L., Salama, F., et al. 1999, Chem. Phys. Lett., 303, 165
Rouillé, G., Arold, M., Staicu, A., et al. 2007, J. Chem. Phys., 126, 174311
Rouillé, G., Steglich, M., Huisken, F., Henning, T., & Müllen, K. 2009, J. Chem. Phys., 131, 204311
Ruiterkamp, R., Peeters, Z., Moore, M. H., Hudson, R. L., & Ehrenfreund, P. 2005, A&A, 440, 391
Salama, F. & Allamandola, L. J. 1991, J. Chem. Phys., 94, 6964

Salama, F., Joblin, C., & Allamandola, L. J. 1995, Planet. Space Sci., 43, 1165

Sandford, S. A. 2002, Planet. Space Sci., 50, 1145

Sandford, S. A. & Allamandola, L. J. 1993, ApJ, 417, 815

Sandford, S. A., Allamandola, L. J., Tielens, A. G. G. M., & Valero, G. J. 1988, ApJ, 329, 498

Sandford, S. A., Bernstein, M. P., & Allamandola, L. J. 2004, ApJ, 607, 346

Savage, B. D. & Sembach, K. R. 1996, ARA&A, 34, 279

Sceats, M. G. and Rice, S., A. 1982, Water: A Comprehensive Treatise, Vol. 7 (Plenum, New York), 83–214

Schmitt, B., Greenberg, J. M., & Grim, R. J. A. 1989a, ApJ, 340, L33

Schmitt, B., Grim, R., & Greenberg, M. 1989b, Spectroscopy and physico-chemistry of CO:H_2O and CO_2:H_2O ices (Infrared Spectroscopy in Astronomy, Proceedings of the 22nd Eslab Symposium held in Salamanca, Spain, 7-9 December, 1988. Edited by B.H. Kaldeich. ESA SP-290. European Space Agency, 1989., p.213), 213–+

Schutte, W. A., Allamandola, L. J., & Sandford, S. A. 1993, Science, 259, 1143

Schutte, W. A., Boogert, A. C. A., Tielens, A. G. G. M., et al. 1999, A&A, 343, 966

Schutte, W. A. & Khanna, R. K. 2003, A&A, 398, 1049

Schutte, W. A., Tielens, A. G. G., & Sandford, S. A. 1991, ApJ, 382, 523

Sellgren, K., Brooke, T. Y., Smith, R. G., & Geballe, T. R. 1995, ApJ, 449, L69+

Sellgren, K., Uchida, K. I., & Werner, M. W. 2007, ApJ, 659, 1338

Shen, C. J., Greenberg, J. M., Schutte, W. A., & van Dishoeck, E. F. 2004, A&A, 415, 203

Silverstein, G. C. & Bassler, R. M. 1967, Spectrometric Identification of Organic Compounds Second Edition (Wiley)

Skinner, C. J., Tielens, A. G. G. M., Barlow, M. J., & Justtanont, K. 1992, ApJ, 399, L79

Smith, J. D. T., Draine, B. T., Dale, D. A., et al. 2007, ApJ, 656, 770

Smith, R. G., Sellgren, K., & Tokunaga, A. T. 1989, ApJ, 344, 413

Soifer, B. T., Puetter, R. C., Russell, R. W., et al. 1979, ApJ, 232, L53

Sonnentrucker, P., Neufeld, D. A., Gerakines, P. A., et al. 2008, ApJ, 672, 361

Speck, A. K. & Barlow, M. J. 1997, Ap&SS, 251, 115

Sternberg, A. 1988, ApJ, 332, 400

Stevens, B., Thomaz, M. F., & Jones, J. 1967, The Journal of Chemical Physics, 46, 405

Swings, P. & Rosenfeld, L. 1937, ApJ, 86, 483

Szczepanski, J., Chapo, C., & Vala, M. 1993a, Chem. Phys. Lett., 205, 434

Szczepanski, J., Drawdy, J., Wehlburg, C., & Vala, M. 1995a, Chemical Physics Letters, 245, 539

Szczepanski, J. & Vala, M. 1993, ApJ, 414, 646

Szczepanski, J., Vala, M., Talbi, D., Parisel, O., & Ellinger, Y. 1993b, J. Chem. Phys., 98, 4494

Szczepanski, J., Wehlburg, C., & Vala, M. 1995b, Chemical Physics Letters, 232, 221

Taban, I. M., Schutte, W. A., Pontoppidan, K. M., & van Dishoeck, E. F. 2003, A&A,

399, 169
Tanaka, M., Nagata, T., Sato, S., & Yamamoto, T. 1994, ApJ, 430, 779
Tanaka, M., Sato, S., Nagata, T., & Yamamoto, T. 1990, ApJ, 352, 724
Tielens, A. G. G. M. 2008, ARA&A, 46, 289
Tielens, A. G. G. M. & Hagen, W. 1982, A&A, 114, 245
Tielens, A. G. G. M., Tokunaga, A. T., Geballe, T. R., & Baas, F. 1991, ApJ, 381, 181
Vala, M., Szczepanski, J., Pauzat, F., et al. 1994, J. Phys. Chem., 98, 9187
van Breda, I. G. & Whittet, D. C. B. 1981, MNRAS, 195, 79
van Broekhuizen, F. A., Groot, I. M. N., Fraser, H. J., van Dishoeck, E. F., & Schlemmer, S. 2006, A&A, 451, 723
van Broekhuizen, F. A., Keane, J. V., & Schutte, W. A. 2004, A&A, 415, 425
van Broekhuizen, F. A., Pontoppidan, K. M., Fraser, H. J., & van Dishoeck, E. F. 2005, A&A, 441, 249
van Dishoeck, E. F. 2004, ARA&A, 42, 119
van IJzendoorn, L. J., Allamandola, L. J., Baas, F., & Greenberg, J. M. 1983, J. Chem. Phys., 78, 7019
Visser, R. 2009, PhD thesis, Leiden Observatory, Leiden University, P.O. Box 9513, 2300 RA Leiden, The Netherlands
Wang, B. C., Chang, J. C., Tso, H. C., Hsu, H. F., & Cheng, C. Y. 2003, J. Mol. Struct. (Theochem), 629, 11
Watanabe, N. & Kouchi, A. 2002, ApJ, 571, L173
Watanabe, N., Nagaoka, A., Shiraki, T., & Kouchi, A. 2004, ApJ, 616, 638
Watson, D. M., Kemper, F., Calvet, N., et al. 2004, ApJS, 154, 391
Weisman, J. L., Mattioda, A., Lee, T. J., et al. 2005, Phys. Chem. Chem. Phys. (Incorporating Faraday Transactions), 7, 109
Wexler, A. 1967, Applied Spectroscopy Reviews, 1, 29
Whittet, D. C. B., ed. 2003, Dust in the galactic environment
Whittet, D. C. B., Bode, M. F., Longmore, A. J., et al. 1988, MNRAS, 233, 321
Whittet, D. C. B., Gerakines, P. A., Hough, J. H., & Shenoy, S. S. 2001, ApJ, 547, 872
Willner, S. P., Gillett, F. C., Herter, T. L., et al. 1982, ApJ, 253, 174
Woon, D. E. & Park, J.-Y. 2004, ApJ, 607, 342

Nederlandse samenvatting

De spectroscopie en de chemie van interstellaire ijs analogen

Het onderzoek dat in dit proefschrift wordt beschreven richt zich op laboratorium experimenten die astrochemische processen nabootsen onder omstandigheden, zoals die in de ruimte voorkomen. Deze omstandigheden zijn extreem. In donkere interstellaire wolken kan de temperatuur zakken tot slechts 10 graden boven het absolute nulpunt, zo'n -263°C. Ook de 'lucht'druk is uitermate gering. Met slechts enkele moleculen per kubieke centimeter zijn interstellaire wolken bijzonder leeg. Lange tijd werd aangenomen, dat de dichtheden in de ruimte te laag zijn voor chemische reacties. De kans dat een aantal deeltjes gelijktijdig botst is immer zeer gering. In 1937 werd echter het eerste molecuul in de ruimte ontdekt: CH, een stabiele binding van een koolstof (C) en waterstof (H) atoom. Deze ontdekking luidde het begin in van een nieuwe onderzoeksdiscipline: de astrochemie. Vandaag, bijna driekwart eeuw later, staat de teller van in de ruimte geïdentificeerde moleculen boven de 150. Hieronder bevinden zich alledaagse substanties — water (H_2O), koolstofdioxide (CO_2) en alcohol (CH_3CH_2OH) —- maar ook meer exotische stoffen, zoals geladen moleculen (HCO^+ en C_6H^-) en het grootste tot nu toe in de ruimte gedetecteerde molecuul: $HC_{11}N$ (de recentelijke publicatie van C_{60} in de ruimte is daarbij nog even buiten beschouwing gelaten). De wijze waarop deze moleculen ontstaan is maar deels begrepen.

De chemische evolutie van moleculen in de ruimte volgt in grote lijnen het stervormingsproces. Een interstellaire wolk (ruwweg 99% gas en 1% stof) stort onder zijn eigen gewicht ineen. De kern van de wolk is 'donker', en bij gebrek aan licht koelt de wolk sterk af. In koude gebieden in de ruimte waar zich zowel gas als stofdeeltjes bevinden, kunnen gas moleculen vast vriezen op het oppervlak, waardoor laagjes ijs ontstaan. In de afgelopen twee decennia is gebleken dat dit ijs, als reservoir voor moleculen en als katalysator, een belangrijke rol speelt bij de vorming van nieuwe moleculen. Chemische reacties worden daarbij geïnitieerd door bestraling met energetisch licht (harde ultraviolette (UV) of kosmische straling) en door een beschieting met atomen (H, N, C, O, S) of electronen en daarbij vormen nieuwe (en meer complexe) moleculen. In een volgend stadium ontstaan in gebieden met nog hogere dichtheid proto-stellaire kernen waaruit uiteindelijk sterren worden geboren. Rondom de nieuwe ster hoopt zich restmaterie op, gas, stof en ijs, in een zogenaamde proto-planetaire schijf. Deze wordt vervolgens met UV licht van de jonge ster bestraald en thermisch verhit, waarbij andere reacties in het ijs plaats vinden. Tevens verdampen ijs moleculen en komen weer in de gas fase terecht waar ze verder kunnen reageren. Het stof en gas van de proto-planetaire schijf vormt uiteindelijk het materiaal waaruit kometen en planeten ontstaan. De chemische evolutie van moleculen in de ruimte is derhalve ook bepalend voor de chemische samenstelling van planeten.

In de ruimte komen moleculen alleen voor in de gas fase of in de vaste stof en zoals hierboven beschreven wisselwerken beide fases, door vastvriezen (accretie) en verdampen (desorptie). De nadruk in dit proefschrift ligt op de studie van inter- en circumstellair ijs. In het laboratorium worden daartoe onder hoog vacuüm condities laagjes ijs gegroeid die bijvoorbeeld met speciale lampen worden bestraald om het harde ultraviolette stralingsveld in de ruimte na te bootsen.

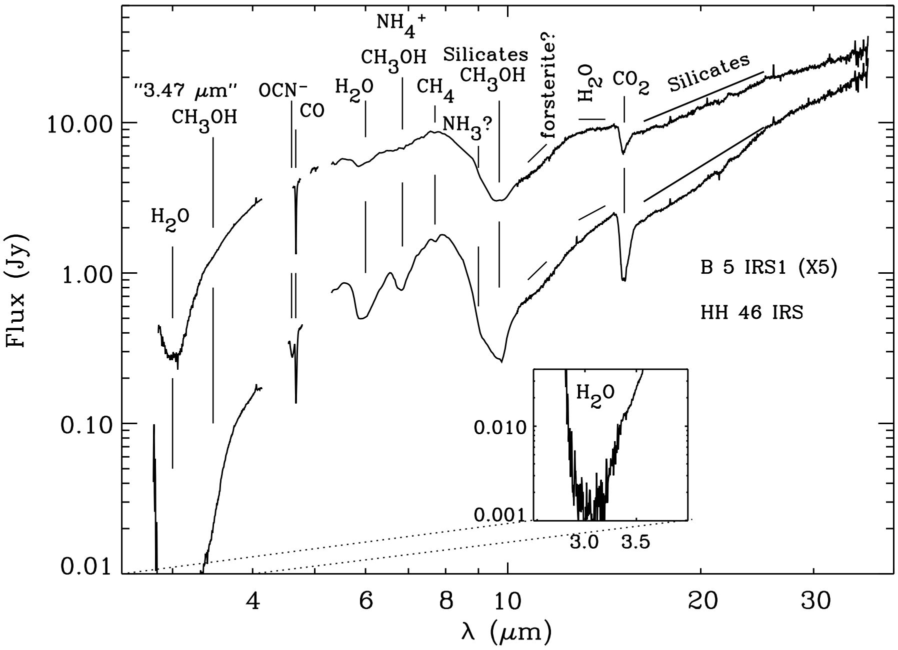

Figuur 1 Een typisch spectrum van infrarood licht genomen richting een ster in wording. Uit de ontbrekende kleuren kan afgeleid worden welke moleculen zich in het ijs bevinden.

Vanaf de Aarde (of vooral met telescopen die rond de Aarde draaien) kunnen we deze dunne ijslaagjes onderzoeken door naar het infrarode licht te kijken, dat door ijs in de ruimte wordt geabsorbeerd. Bepaalde kleuren licht blijken te ontbreken en het resulterende spectrum is typisch voor het voorkomen van bepaalde chemische substanties in het ijs, die bij die specifieke kleuren licht (lees energie) gaan trillen. Door deze astronomische spectra te vergelijken met laboratorium data zoals beschreven in dit proefschrift, is het vervolgens mogelijk om de samenstelling van deze materie op grote afstand te onderzoeken. In Figuur 1 is een infrarood spectrum van een ster in wording weergegeven, waaruit de samenstelling van het ijs kan worden afgeleid. Spectroscopische details (precieze frequenties, band breedtes en intensiteitsverhoudingen) bieden vervolgens verder inzicht in de structuur en temperatuur van het ijs, of en hoe het ijs is gemengd, en welke chemische reacties in het ijs plaats hebben gehad. Dit wordt in dit proefschrift besproken voor ijs bestaande uit H_2O:CO in hoofdstuk 2 en voor NH_3 en CH_3OH houdend ijs in hoofdstuk 3.

In de afgelopen jaren is duidelijk geworden, dat het waarschijnlijk is dat complexe (organische) moleculen in ijs worden gevormd. Dit gebeurt ook bij zeer lage temperaturen. Recentelijk onderzoek, bv. van met ultraviolet licht bestraald puur methanol ijs laat zien, dat vele van de grotere moleculen die al zijn geïdentificeerd in de ruimte, op deze wijze kunnen worden gevormd. Het is echter nog niet duidelijk hoe complex de chemie in interstellair ijs daadwerkelijk kan worden, of bv. de bouwstenen van het leven - aminozuren - in de vaste stof kunnen ontstaan. Dit zal in de komende jaren, o.a. in Leiden, worden onderzocht. Wat wel duidelijk is, dat grote complexe moleculen kunnen vastvriezen in ijs, en dit is een ander onderwerp dat in dit proefschrift wordt besproken.

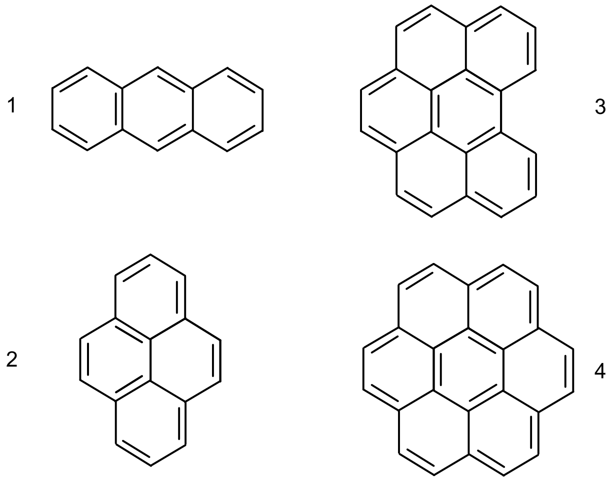

Figuur 2 Polycyclische Aromatische Koolwaterstoffen waaraan in dit proefschrift metingen zijn verricht: 1) anthracene, 2) pyrene, 3) benzo[ghi]perylene en 4) coronene.

Naast het absorberen van infrarode straling, kunnen bepaalde moleculen ook, nadat ze door een energetisch lichtdeeltje zijn aangeslagen, infrarood licht uitzenden. De kleuren van deze emissie zijn net als de kleuren waarbij een molecuul licht kan absorberen, uniek en dus molecuul specifiek. In 1973 werden sterke infrarode emissiebanden in de ruimte ontdekt bij kleuren die specifiek zijn voor koolstof en waterstof houdende moleculen, de zogenaamde PAKs: Polycyclische Aromatische Koolwaterstoffen. Deze stabiele moleculen worden op Aarde vooral gevormd bij verbrandingsprocessen en zijn bekend om hun negatieve invloed op de luchtkwaliteit. Het is waarschijnlijk dat PAKs ook in de ruimte worden gevormd, bijvoorbeeld als bijproduct in verbrandingsreacties in een ster. Dit is in overeenstemming met de gevonden emissie spectra. Typische voorbeelden van PAKs zijn in Figuur 2 weergegeven.

Wanneer PAKs in de ruimte voorkomen, dan is het waarschijnlijk dat zij, net als kleinere moleculen, vastvriezen op stofdeeltjes en bijdragen aan de chemische processen die in het ijs plaats kunnen vinden. Het is slechts deels mogelijk om deze processen met infrarode straling te onderzoeken (zie hoofdstuk 4). De reden hiervoor is, dat PAKs veelal vergelijkbare vibrationele bewegingen uitvoeren en daarom spectroscopisch moeilijk te onderscheiden zijn. Een mogelijke oplossing biedt echter ultraviolette en optische spectroscopie, waarbij de electronische eigenschappen van een molecuul worden bestudeerd en deze zijn voor verschillende PAKs diverser. Derhalve is in de afgelopen jaren een nieuwe opstelling gebouwd — *OASIS* (Optical Absorption Setup for Ice Spectroscopy — (zie hoofdstuk 5), waarmee het mogelijk is PAKs in water ijs met zichtbaar licht te bestuderen (hoofdstukken 6 en 7). Metingen zijn bovendien niet alleen meer molecuul specifiek, maar ook sneller en gevoeliger, waardoor het mogelijk is chemische processen ter plekke vrijwel in ‘real-time’ te volgen.

Dit proefschrift

Dit proefschrift beschrijft een aantal laboratorium experimenten aan inter- en circumstellaire ijs analogen. De metingen zijn verricht met een drietal opstellingen. In Leiden met een Fourier Transform infrarood spectrometer (zie hoofdstukken 2 en 3) en een optische spectrometer (zie hoofdstukken 5, 6 en 7) die beide ijs in een hoog vacuüm opstelling doorlichten en bij NASA Ames met een vergelijkbaar infrarood systeem (hoofdstuk 4). Bij alle drie opstellingen is het mogelijk het ijs met hard UV licht te bestralen. Het infrarode onderzoek is vooral gericht op kleinere moleculen en het optische werk laat met name werk aan PAKs zien. Het doel van het onderzoek is om de spectroscopische vaste stof signatuur te bepalen voor verschillende ijs composities en condities, ook na UV bestraling, zodat astronomische waarnemingen kunnen worden geïnterpreteerd. Verder is gekeken naar mogelijke reactie schema’s in het ijs en daarbij is vooral optische spectroscopie ingezet.

Hoofdstuk 1 geeft een algemeen overzicht en is een inleiding voor het onderzoek dat in dit proefschrift is beschreven. In hoofdstuk 2 wordt de wisselwerking tussen twee belangrijke ijs componenten in de ruimte — CO en H_2O — in detail beschreven. Het onderzoek beschrijft de veranderingen in de absorptie profielen van zowel CO als H_2O bij het inmengen van de partner en voor verschillende temperaturen. Dit geeft inzicht in de interacties in het ijs en biedt verder een mogelijkheid om infrarode astronomische data te interpreteren. In hoofdstuk 3 is dit expliciet uitgewerkt voor metingen aan methanol (CH_3OH) en ammoniak (NH_3) in water ijs en spectra zijn vergeleken met recentelijk verkregen data van de *Spitzer* infrarood ruimte telescoop. In dit hoofdstuk wordt de hoeveelheid ammoniak ijs bepaald die zich bevindt in het ijs rond jonge sterren van lage massa. Verder duiden spectroscopische details aan dat het methanol zeer waarschijnlijk niet met water is gemengd, hetgeen aangeeft dat beide stoffen een verschillende chemische evolutie hebben doorlopen. Het methanol bevindt zich wel in een CO rijke ijslaag en dit stemt overeen met het idee, dat CH_3OH ontstaat uit waterstof atoom addities in CO ijs. Hoofdstuk 4 breidt deze metingen uit naar PAKs in water ijs en laat zien dat na UV bestraling vele nieuwe moleculen worden gevormd. Een groot aantal nieuwe banden is gevonden en deels toegekend, vooral aan geïoniseerde PAKs. De metingen zijn vervolgens gebruikt om astronomische spectra te verklaren die gemeten zijn in de richting van jonge sterren. De belangrijkste conclusie is dat PAKs een deel van de karakteristieke absorptie in het 6.2 micrometer gebied kunnen verklaren.

Het tweede deel van dit proefschrift beschrijft optische ijs spectroscopie. De nieuwe opstelling, *OASIS*, wordt gedetailleerd in hoofdstuk 5 beschreven. De nadruk ligt op de experimentele details en deze worden geïllustreerd aan de hand van metingen aan pyreen ($C_{16}H_{10}$) in zeer koud water ijs. Wanneer het pyreen met hard ultraviolet licht wordt bestraald, verliest het gemakkelijk een electron; het pyreen wordt geioniseerd. De nieuwe opstelling maakt het mogelijk om dit proces tijdsopgelost te bestuderen. Hoofdstuk 6 gaat vervolgens in op de chemische reacties die plaats vinden in een pyreen houdend water ijs, wanneer het met UV licht wordt beschenen. Het ionisatie gedrag en andere chemische reacties zijn gevolgd voor verschillende temperaturen en de resulterende temperatuursafhankelijkheid wordt besproken. Het blijkt dat de snelheid waarmee het pyreen wordt geïoniseerd dusdanig is, dat het ook op tijdschalen in de ruimte een belangrijke rol moet spelen. Verder wordt in dit hoofdstuk getoond, dat het mogelijk is om kleine reactive intermediairs in absorptie waar te nemen, die middels diffusie een belangrijke rol spelen in de chemie van een PAK houdend ijs. Hoofdstuk 7 laat zien dat veel van de processen zoals die voor pyreen in water ijs zijn gevonden, ook plaats vinden voor andere PAKs: anthracene, coronene en benzo[ghi]perylene. De belangrijkste conclusie is, dat PAK chemie niet a priori buiten beschouwing mag worden gelaten in astrochemische modellen en wellicht een belangrijke rol speelt bij de vorming van complexe organische moleculen. Tenslotte bespreekt hoofdstuk 8 het perspectief van het beschreven onderzoek.

Publications

Refereed papers

- *Band profiles and band strengths in mixed H_2O:CO ices*
  J. Bouwman, W. Ludwig, Z. Awad, K. I. Öberg, G. W. Fuchs, E. F. van Dishoeck and H. Linnartz
  Astronomy & Astrophysics, 476, 995-1003 (2007) (Chapter 2)

- *The c2d Spitzer spectroscopic survey of ices around low-mass young stellar objects. IV. NH_3 and CH_3OH*
  S. Bottinelli, A. C. A Boogert, **J. Bouwman**, M. Beckwith, E. F. van Dishoeck, K I. Öberg, K. M. Pontoppidan, H. Linnartz, G. A. Blake, N. J. Evans II and F. Lahuis
  Astrophysical Journal, 718, 1100-1117 (2010) (Chapter 3)

- *Photochemistry of PAHs in cosmic water ice. Part I: Mid-IR spectroscopy and photoproducts*
  J. Bouwman, A. L. Mattioda, H. Linnartz and L. J. Allamandola
  Astronomy & Astrophysics, submitted (2010) (Chapter 4)

- *Optical spectroscopy of VUV irradiated pyrene:H_2O ice*
  J. Bouwman, D. M. Paardekooper, H. M. Cuppen, H. Linnartz and L. J. Allamandola
  Astrophysical Journal, 700, 56-62 (2009) (Chapter 5)

- *Photochemistry of the PAH pyrene in water ice: the case for ion-mediated solid-state astrochemistry*
  J. Bouwman, H. M. Cuppen, A. Bakker, L. J. Allamandola and H. Linnartz
  Astronomy & Astrophysics, 511, A33+ (2010) (Chapter 6)

- *Photochemistry of PAHs in cosmic water ice. Part II: Near UV/VIS spectroscopy and ionization rates*
  J. Bouwman, H. M. Cuppen, L. J. Allamandola and H. Linnartz
  Astronomy & Astrophysics, in prep. (2010) (Chapter 7)

- *High-resolution infrared spectroscopy of the charge-transfer complex* $[Ar-N_2]^+$*: A combined experimental theoretical study*
  H. Verbraak, J. N. P. van Stralen, **J. Bouwman**, J. S. de Klerk, D. Verdes, H. Linnartz and F. M. Bickelhaupt
  Journal of Chemical Physics, 123, 144305 (2005)

Conference Proceeding

- *VUV photochemistry of PAHs trapped in interstellar* H_2O *ice*
  J. Bouwman, H. M. Cuppen, L. J. Allamandola, H. Linnartz, PAHs and the Universe, 2010

Popular article

- *Zwerven door het onderwijs*
  J. Bouwman, Nederlands Tijdschrift voor Natuurkunde, November 2006

Curriculum vitae

I was born on May 3, 1979 in the city of Haarlem, the Netherlands. In the year 1991, I started high school at het Mendelcollege. Here, I finished the MAVO in 1995.

I continued my education at the IJmond Middelbare Technische School in Santpoort-Noord, where I did a technical study dedicated to industrial processing techniques. I started this study in 1995 and after 3 theoretical years, I concluded this study with two half-year long traineeships at Shell Research and Technology Center Amsterdam and at Sigma Coatings Amsterdam. The research aspect of the internship at Shell was very appealing to me and made me decide to pick up a new study rather than starting a career in the industry.

After finishing the IJmond MTS in 1999 I chose to continue at the Technische Hogeschool Rijswijk. Here, a study at the level of Bachelor of Engineering called Technical Physics was offered, which aimed to using physics to solve industrial problems. I chose the specialization Applied Physics and did a one year internship at the Laser Centre Vrije Universiteit. The internship took place at the Department of Physical Chemistry, led by prof. dr. S. Stolte and my daily supervisor was dr. Harold Linnartz. The project consisted of building an electron impact plasma setup, combined with a sensitive high resolution infrared spectrometer with the goal to measure infrared spectra of van der Waals bound ionic complexes. During this project I worked closely together with dr. H. E. Verbraak and dr. J. S. de Klerk. I finished my degree with honors in 2004 on a bachelor thesis entitled “High Resolution Infrared Absorption Spectroscopy of Ionic Complexes”. This work resulted in a publication in a scientific journal.

After finishing my Bachelor degree on a research project at the Vrije Universiteit Amsterdam, the obvious choice was to continue with a Master study. I started the study Chemistry with specialization in Laser Sciences in February 2004. My major research project took place at the Laser Centre, again under supervision of dr. Harold Linnartz. It involved the construction of an experimental setup for performing cavity ring-down spectroscopy on a planar plasma expansion for the spectroscopic detection of diffuse interstellar band carriers. During this project I worked closely together with dr. D. Ityaksov. I graduated on my thesis entitled “High Resolution Electronic Spectroscopy of Molecular

Transients of Astrophysical Interest” in February 2006.

Now, having my Masters degree, I was offered a PhD project in the Raymond & Beverly Sackler Laboratory for Astrophysics, under supervision of again prof. dr. Harold Linnartz. The project comprised the design and construction of a new setup for performing spectroscopy on vacuum ultraviolet processed interstellar ice analogues. This project was financed both by FOM and NOVA. I studied the physical interactions and chemical reactions in interstellar ice analogues, using spectroscopic techniques covering the near ultraviolet to the mid infrared. I worked closely together with dr. L. J. Allamandola from NASA Ames Research Center; a collaboration which led to a two months research visit at NASA Ames. The research focus in this period was on PAH containing ices. During my PhD I guided several bachelor and master students and presented my results at (inter)national scientific meetings and during colloquia in Amsterdam, Groningen, Leiden, Lunteren, Rolduc (the Netherlands), Toulouse (France), Columbus (OH), Berkeley (CA), and NASA Ames Research Center (CA).

November 1st 2010, I will start a postdoctoral research project in prof. dr. S. R. Leone’s group at UC Berkeley, where I will perform gas phase reaction rate and isomer specific reaction product branching ratio measurements.

Nawoord

Een proefschrift kan alleen tot stand komen met steun van anderen. Het was een voorrecht om aan de Sterrewacht Leiden te werken met mensen met een grote verscheidenheid aan nationaliteiten en vakdisciplines. Ten eerste wil ik graag de ondersteunde kracht van de computergroep en het secretariaat noemen. Het bouwen van de opstelling was nooit gelukt zonder de technische ondersteuning van de fijnmechanische werkplaats. Ewie, Gijsbert en Martijn, het was geweldig om samen met jullie de opstelling operationeel te krijgen. De elektronische werkplaats, onder leiding van René, heeft ook zijn aandeel gehad in de het opbouwen en werkend krijgen van de opstelling. Additionally, I am grateful to Andy Ruth for having me in his laboratory at University College Cork. The support from, and interaction with, colleagues from the laboratory and astrochemistry group have played a crucial role in my development, both personally and professionally. Sergio, you have been a great colleague and friend during 4 years of my PhD. Harald, het was fijn om met jou samen te werken, zowel aan de VU in Amsterdam als in het laboratorium in Leiden. Working in the office has been great because of my three roommates Rafael, David and Emily. The other members of the Sackler Laboratory group, Nadine, Edith, Karoliina, and Joseph and the Sackler Lab alumni Guido, Suzanne, Karin and Claire have also been of great support. Zonder Herma's kennis van het modelleren van chemische reacties hadden mijn publicaties lang niet een dergelijk grote impact gehad. Naast de medewerkers van de universiteit heeft ook een aantal studenten — Wiebke, Martha, Daniël, Nienke, Arthur en Michiel — met mij samengewerkt aan het assembleren van de opstelling, reduceren van data, schrijven van software en/of het uitvoeren van metingen. Sandrine, working with you on the ammonia paper was a pleasure. Ook Ewine heeft een zeer belangrijke rol gespeeld bij het voltooien van mijn proefschrift en het vergroten van mijn kennis in de astrochemie. Xander, de gesprekken die wij hebben gehad, hebben een belangrijke bijdrage geleverd aan de uiteindelijke keuze die ik heb gemaakt. Lou, it was an honor and a pleasure to work with you in Leiden. I will never forget our Kasteel afternoons encompassing a perfectly balanced mixture of personal and work-related conversations. Voordat ik als promovendus naar de Universiteit Leiden kwam, heb ik bijzonder veel vertrouwen en steun mogen ontvangen van Harold. Dit heeft er mede toe geleid dat nu dit proefschrift gedrukt voor u ligt. Furthermore, I like to wish my successors, Emily and Steven, the best of luck with the beautiful and well-behaved system!

The two months visit to the astrochemistry group at NASA Ames Research Center has been a life changing experience. The research I have done there seamlessly connects part I and II of this thesis. Lou, Andy and all other (lab) colleagues, thank you for your hospitality, for helping me with the measurements, and for taking me on the great trips through beautiful CA. Additionally, I mention Christiaan and Claire, who have been kind enough to introduce me to Mountain Views night life.

Naast collega's en familie hebben ook mensen uit mijn sociale kring hun bijdrage geleverd. Om te beginnen hebben de spelers van het zaalvoetbalteam van 'de S' mij de nodige inspanning én ontspanning bezorgd. Helaas verdwenen uit het betaald voetbal, maar niet uit mijn hart, HFC Haarlem, en de vele vrienden die ik daar aan over heb gehouden. Het was fantastisch om tweewekelijks onze passie te delen en ik zal nooit onze reisjes door Nederland en daar buiten vergeten.

Graag noem ik mijn vriend en medepromovendus Tom, waar ik bijzonder veel steun aan heb gehad. Het delen van onze passies in het privé leven, gecombineerd met het delen van onze ervaringen in de wetenschap hebben er mede voor gezorgd dat dit mooie proefschrift tot stand is gekomen.

Tot slot wil ik mijn familie noemen, waaronder een aantal mensen in het bijzonder. Marc en Anita, ondanks onze drukke schema's is het ons altijd gelukt tijd vrij te maken voor gezellige avonden! Pap, mam, Jeroen en Suus, die mij altijd mijn eigen keuzes hebben laten maken en mij hebben gesteund door dik en dun! De familie van mijn lieve vrouw, Klaas, Ingrid, Jeroen, Marc en Remco, die mij met hun nuchtere kijk op zaken ook op de rails hebben gehouden. Mijn proefschrift was nooit tot stand gekomen zonder de rust, liefde en steun van mijn lieve vrouw Wendy. Je hebt ervoor gezorgd dat ik ook in drukke tijden mijn focus behield en mijn rustmomenten pakte!